KU LEUVEN

ARENBERG DOCTORAL SCHOOL
Faculty of Engineering Technology

Towards Unmanned Inland Shipping

Gerben Peeters

Supervisors:
Prof. dr. ir. ing. René Boonen
Prof. dr. ir. Peter Slaets
Prof. dr. ir. Maarten Vanierschot

Dissertation presented in partial fulfilment of the requirements for the degree of Doctor of Engineering Technology (PhD)

February 2021

Towards Unmanned Inland Shipping

Gerben PEETERS

Examination committee:
Prof. dr. ir. Bart Lievens, chair
Prof. dr. ir. ing. René Boonen, supervisor
Prof. dr. ir. Peter Slaets, supervisor
Prof. dr. ir. Maarten Vanierschot, supervisor
Prof. dr. ir. Geert Waeyenbergh
Prof. dr. ir. Herman Bruyninckx
Dr. ir. Katrien Eloot
(Flanders Hydraulics Research)
Prof. dr. ir. Marc Vantorre
(Ghent University)
Prof. dr. Edmund Førland Brekke
(Norwegian University of Science and Technology)
Senior research scientist Ørnulf Jan Rødseth
(SINTEF Ocean)

February 2021

Progress Propelled by Problems

 Research funded by Fonds Wetenschappelijk Onderzoek (FWO) — Research Foundation Flanders, grant 1S12517N. Uitgegeven in eigen beheer, Gerben Peeters, 3001, Heverlee (Belgium).

Preface

Although the author would like to put forward a body of evidence for his investigation Towards Unmanned Inland Shipping, a substantial crew was needed. Consequently, to the best knowledge of the author, the following paragraphs seem to make up a non exhaustive list of people of which their, sometimes implicit, contributions significantly altered the end result of this thesis, and thus people the author would like to sincerely thank. It should be readily understood, however, that supportive people who were not explicitly mentioned below, are thanked nonetheless.

First of all, I would like to thank my supervisors for giving me the opportunity and support to conduct my research and to extend my knowledge. You gave me priceless freedom and honest guidance in my search for research answers and their questions. René, thank you for introducing me to the Lagrangian and Hamiltonian mechanics. Maarten, thank you for enabling me to understand parts of the computational fluid dynamics research field. Peter, thank you for the many open-minded discussions, on or off topic, and for housing me in your new research group. Your industrial-application-oriented research approach has significantly impacted and improved this thesis, thank you.

Furthermore, I would like to thank my whole supervisory committee, Edmund, Katrien, Marc, and Ørnulf, for your continuous feedback, for your help in orienting and improving this work, and for our inspiring discussions. In addition, thank you Bart for chairing my defences. Herman, thank you for our asynchronously timed discussions which always provided me with new insights and context. Geert, without our mutual research interest in certain fermentation processes, this PhD would never have started. Thank you for introducing me to this topic, and for your intense support during my start.

Some brave readers will notice the tremendous group effort that made this PhD possible. Although I had the privilege to document and publish many processes, much of the content should be credited to teamwork within our research group.

Therefore, evidently, I would like to thank my team members for our constructive cooperation, our fun after work, and, believe it or not, our occasional fun during work. More precisely, I would like to thank my Coggelleagues for our pleasant time together. Let us never forget our bootcamp in Nieuwpoort, our zuurdesembrood, our cosy winters inside the containers, our field (i.e. fun) trips to Rotselaar lake, and, most importantly, our trailer-induced KU Leuven-blue shins. Chris, Gökay, Marcus, Raheel, Senne, and Tim, thank you! Furthermore, thank you Nicolas and Patrick for upgrading our vessels.

Besides these more marine-oriented research colleagues, I would like to thank some of my earliest colleagues, Ali, Arne, Güven, Mulu, Petros, Robin, and Samrat. Apart from teaching me about a variety of topics, ranging from spider web (development) to sweet potatoes, I would also like to thank you for our coffee conversations with the sporadic conspiracy theory discussion, thank you!

At last, we arrive at the people who did not get paid to support me. On the contrary, these friends, family, and (or?) fools paid to support me, note that their proper categorisation falls out of the scope of the present work. Thank you Anton, Ben, Bregt, Thomas, and Willem for your sincere fake interest in my research, and, perhaps more importantly, for your continuous mental support by letting me win during all our bike rides, time after time again. This is the kind of support only true friendship can offer, thank you!

Nu kunnen we eindigen met de mensen die het meest in mij geïnvesteerd hebben. Hiervoor wil ik graag mijn volledige familie bedanken voor hun steun, advies, en begeleiding doorheen mijn leven in het algemeen. Sommige mensen zien we minder, sommigen zien we nooit meer terug, maar jullie impact op mijn leven zal nooit veranderen, dankjulliewel allemaal! Daarnaast, plaats ik graag nog een extra dankwoordje voor mijn ouders en broer. Dankzij jullie warm nest heb ik mijn vleugels volledig kunnen ontplooien, waarvoor dank. Misschien vlieg ik nu soms wat te ver weg naar jullie zin, zowel fysiek als mentaal, maar weet dat ik altijd terug zal komen.

Finally, Every Excuse might be good to wonder about ones own autonomy. Nevertheless, it is safe to say that Elke provides me with a significant augmentation of my autonomy system. Thank you Elke, for delivering me with continuous software updates and for debugging me on the fly. Having a life partner that understands, accepts, and supports my time-consuming life choices means the world to me. Without your support, care, and love this work would not have been possible, Thank you!

Gerben

Abstract

Road transport dominates the European and Belgian hinterland freight transport sector. Over the last decades, approximately three quarters of the cargo streams passed by road, whilst inland waterway transport seems to offer a more sustainable alternative. Moreover, the larger inland vessels suffer from an excess of supply over demand, and the amount of smaller inland vessels is diminishing. This negative evolution in the inland waterway transport sector does not align well with the European and Belgian governmental ambitions to transfer more freight transport to their waterways. This thesis aims to investigate a solution for this emerging tension field by studying the technological feasibility of unmanned inland cargo vessels. More precisely, three research questions are answered.

The first question explored: "How to design and construct an industrially relevant research vessel for unmanned inland cargo shipping?". To investigate the industrial relevance, the present inland waterway transport sector was examined. Three developments stood out. First, the European Watertruck$^+$ project introduced a novel fleet of modular push boats and barges. Hence, the watertrucks can separate their navigation time from their cargo handling time. Second, Blue Line Logistics built new flat deck vessels with an onboard crane, which enables them to handle their cargo independently from the shoreside infrastructure. These vessels focus on transporting palletized cargo. Finally, smaller urban freight vessels have already successfully transported cargo within several European cities. Next to these industrial developments, the recent research evolution regarding unmanned shipping in general and the specific challenges for inland waterway transport motivated the build of two unmanned research vessels: a scale model self-propelled watertruck barge and a functional scale model of a flat deck barge which focusses on palletized cargo. In addition, both research vessels have a length that facilitates intracity freight transport research.

The second question investigated: “How to model and identify the hydrodynamic motion models of an inland cargo vessel?”. The modelling part focussed mainly on the decoupled equations of motion in the water plane, i.e., the surge, sway, and yaw degrees of freedom. To identify this decoupled model, experimental data were fetched with the research vessel in its real outdoor environment. Two identification procedures were compared. The first one used the instantaneous force balance, and the second one integrated the differential equations of the decoupled motions. Furthermore, two independent data sources were used to validate the identified models: bollard pull test data, measured inside a towing tank, and longitudinal damping data, calculated via computational fluid dynamics.

The third question studied: “How to provide an unmanned inland cargo vessel with perception and motion control?”. For this purpose, four navigational environments were differentiated, based on the presence of known or unknown and static or dynamic objects. These environments influence the requirements for the perception and motion control systems of the vessels: exteroceptive sensors are needed to detect unknown objects, and traffic rules need to be implemented in order to avoid dynamic objects. This thesis demonstrates the first successful missions of an unmanned and autonomous vessel navigating on a river with known static obstacles.

Furthermore, this work provides an alternative answer for the last two research questions, by the construction of an inland shore control centre to remotely monitor or control vessels. Accordingly, the operator performs the perception and motion control tasks for the vessel, and implicitly models and identifies the behaviour of the ship. A shore control centre, however, raises new research questions: can this centre help the operator to construct a feeling of ship sense, and can the operator keep the ship in harmony with the environment from a remote location? The initial experiments, with an operator in this control centre remotely controlling an unmanned vessel, delivered a first answer for these novel questions. In addition, this thesis includes some preliminary results with an augmented remote control system in the control centre. This augmented system offers the operator extra visualisations and measurements of the vessel on its navigational chart.

Evidently, the technological feasibility of the abovementioned research questions alone cannot judge the socio-economic feasibility of unmanned inland shipping in general. Consequently, this work aims to gain insights in order to enable higher resolution socio-economic feasibility studies, with the ambition to guide the course of future investments streams.

Beknopte samenvatting

Vrachtwagenverkeer domineert het Europese en Belgische goederenvervoer in het binnenland. De afgelopen decennia passeerde ongeveer driekwart van de goederenstromen via de baan, alhoewel de binnenvaart een duurzamer alternatief lijkt te bieden. Daarnaast, kampen de grotere binnenvaartschepen momenteel met een overaanbod en vermindert het aantal kleinere binnenvaartschepen. Deze nefaste evolutie in de binnenvaart staat echter in schril contrast met de Europese en Belgische overheidsambities om meer goederenvervoer via hun waterwegen te laten stromen. Deze thesis tracht om een oplossing voor dit spanningsveld te onderzoeken door de technologische haalbaarheid van onbemande binnenvaartschepen te bestuderen. Concreet, worden drie onderzoeksvragen beantwoord.

De eerste vraag luidde: "Hoe kan een industrieel relevant onderzoeksschip voor een onbemande binnenvaart ontworpen en gebouwd worden?". Om de industriële relevantie te onderzoeken, werd de huidige binnenvaart onder de loep genomen. Drie recente ontwikkelingen sprongen in het oog. Ten eerste, introduceerde het Europese Watertruck$^+$ project een nieuwe vloot aan modulaire duwboten en duwbakken. Hiermee ontkoppelen de watertrucks hun vaartijd van hun goederenoverslag tijd. Ten tweede, bouwde Blue Line logistics nieuwe schepen met een plat dek en een eigen kraan waarmee ze onafhankelijk van de kade infrastructuur hun goederen kunnen verladen. Hiermee mikken deze schepen voornamelijk op gepalletiseerde cargo. Tot slot, vervoerden enkele kleinere vrachtschepen reeds succesvol goederen binnenin enkele Europese steden. Naast deze industriële ontwikkelingen, motiveerden de recente algemene onderzoeksevolutie naar onbemande schepen en de specifieke uitdagingen voor de binnenvaart de bouw van twee onbemande onderzoeksschepen: een schaalmodel zelfstandig-aangedreven watertruck duwbak en een functioneel schaalmodel van een plat dek schip dat mikt op gepalletiseerde cargo. Bovendien hebben beide onderzoeksschepen een lengte die onderzoek rond intrastedelijk goederenvervoer mogelijk maakt.

De tweede vraag onderzocht: “Hoe kan de hydrodynamica van een binnenvaartschip gemodelleerd en geïdentificeerd worden?”. Voor de modellering werd er hoofdzakelijk gekeken naar de ontkoppelde vrijheidsgraden voor bewegingen in het watervlak, i.e, schrikken, verzetten, en gieren. De identificatie van dit ontkoppeld model gebruikte experimentele data die buiten werd opgemeten, met het onderzoeksschip in zijn reële omgeving. Hiervoor werden twee identificatie procedures vergeleken. De eerste baseerde zich op het ogenblikkelijke krachtenevenwicht, en de tweede integreerde de differentiaalvergelijkingen van de ontkoppelde bewegingen. Daarnaast werden twee onafhankelijke data bronnen gebruikt ter validatie van de geïdentificeerde modellen: de paaltrekproef, opgemeten in een sleeptank, en de longitudinale demping, berekend via de numerieke stromingsleer.

De derde onderzoeksvraag bekeek: “Hoe kan een onbemand schip de omgeving waarnemen en zich hierin voortbewegen?”. Hiervoor werden de vaargebieden ingedeeld in vier omgevingen, afhankelijk van de aanwezigheid van gekende of ongekende en statische of dynamische objecten. Deze omgevingen beïnvloeden de vereisten voor de perceptie en bewegingscontrole systemen van het schip: om ongekende objecten te detecteren zijn exteroceptieve sensoren nodig, en om dynamische objecten te ontwijken moeten verkeersregels worden geïmplementeerd. Deze thesis toont de eerste succesvolle vaarproeven van een onbemand en autonoom schip varend in een rivier met gekende statische objecten.

Bovendien, voorziet dit werk voor de twee laatste onderzoeksvragen ook nog een alternatief antwoord, via de constructie van een landgebaseerd controle centrum om de schepen van op afstand te besturen of te monitoren. Op deze manier zorgt de operator voor de bewegingscontrole en perceptie van het schip, waarbij het schip impliciet wordt gemodelleerd en geïdentificeerd. Een controle centrum opent echter nieuwe onderzoeksvragen: kan dit centrum de operator helpen bij de constructie van een scheepsgevoel, en kan het schip van op afstand in harmonie met de omgeving gehouden worden? Een initieel antwoord op deze nieuwe vragen wordt gegeven via de eerste experimenten met dit controle centrum, waarbij een onbemand schip van op afstand bestuurd werd. Daarnaast illustreert deze thesis de preliminaire resultaten van een uitgebreid controle centrum, waarbij extra visualisaties en metingen van het schip op zijn navigatie kaart worden getoond aan de operator.

Uiteraard kan de technologische haalbaarheid van bovenstaande onderzoeksvragen alleen de sociaaleconomische haalbaarheid van onbemande binnenvaartschepen in het algemeen niet beoordelen. Daarom tracht dit werk om inzichten te verwerven zodat sociaaleconomische haalbaarheidsstudies op een hogere resolutie kunnen worden bekeken, met de ambitie om toekomstige investeringsstromen op de juiste koers te krijgen.

List of Abbreviations

AAWA Advanced Autonomous Waterborne Applications project. 135, 136

ACD Activity-Centred Design. 136–139

AIS Automatic Identification System. 18, 117, 118

ASV Automated/Autonomous Surface Vessel. 20, 117, 122, 135, 136, 139, 158, 161–166

CBA Cost-Benefit Analysis. 143, 158

CCNR Central Commission for the Navigation of the Rhine. 17, 81, 165

CCW CounterClockWise. 87, 90

CEMT Conférence Européenne des Ministres des Transports (French) inland vessel classification types. 6, 7, 13, 14, 52, 53, 55, 76, 77, 79, 86, 160, 165

CFD Computational Fluid Dynamics. 10, 37, 56, 59, 86, 92, 108–110, 162, 164

COLREG Convention on the International Regulations for Preventing Collisions at Sea, 1972. 117

CW ClockWise. 87, 90

DEM Differential Equation Method. 86, 91, 95, 96, 100, 102, 103, 105, 108

EKF Extended Kalman Filter. 117, 119, 120

FBM Force Balance Method. 86, 90, 94–96, 100, 102, 108

fps Frames Per Second. 121, 130, 147, 153

GCI Grid Convergence Index. 76, 77

GDP Gross Domestic Product. 5

GNSS Global Navigation Satellite System. 27, 87, 89, 116, 119–121, 126, 130, 145, 149, 163

H2H Hull-To-Hull project. 10, 117, 131, 132, 136, 137, 141, 142, 148, 149, 151, 153, 154, 156, 158, 163, 165, 166

I-PC Industrial Computer. 26, 87, 130, 131, 145, 146

IMU Inertial Measurement Unit. 27, 87, 89, 91, 108, 116, 119–121, 126–128, 130, 145, 163

IvP Interval Programming. 123, 124, 126, 127

IWT Inland Waterway Transport. 2, 5–9, 17, 19, 30, 158, 160, 161, 164–166

JCS Joint Cognitive System. 140, 158

KVLCC2 KRISO Very Large Crude oil Carrier 2, designed by the Korea Research Institutefor Ship and Ocean Engineering (KRISO). 52, 53, 55, 76, 77, 79, 110

lidar LIght Detection And Ranging. 27, 117, 121, 128, 130, 132, 145

Mbps MegaBit Per Second. 130, 131

MOOS Mission Oriented Operating Suite. 27, 87–89, 131, 137

MOOS-IvP MOOS-IvP. 27, 117, 123, 137, 163

MOOSApp MOOS Applications. 27, 123, 124

MOOSDB MOOS DataBase. 27, 123, 124

MUNIN Maritime Unmanned Navigation through the Intelligence in Networks. 17, 135

PID Proportional, Integral, and Derivative. 3, 124, 163, 164

PLC Programmable Logic Controller. 26, 27, 124, 137, 145, 146, 153, 163

PPS Pulse Per Second. 87

radar RAdio Detection and Ranging. 117

RTK Real Time Kinematic. 119

SCC Shore Control Centre. 135–140, 142–151, 153, 154, 156–158, 163

SLAM Simultaneous Localisation And Mapping. 117

SP-CEMT Self-Propelled CEMT. 14, 19–21, 26

STAMP Systems-Theoretic Accident Modelling and Processes. 116, 143, 158

TEN-T Trans-European Transport Network. 3, 14, 164

tkm Tonne-KiloMetre. 3, 5

UKC Under Keel Clearance. 79

USV Unmanned Surface Vessel. 9, 13, 17, 20, 26, 37, 41, 50, 59, 114–117, 132, 134–137, 139–147, 149–154, 156–158, 161–166

UTC Universal Time Coordinated. 87–89

WAM-V Wave Adaptive Modular Vessel. 50, 51, 59, 60

List of Symbols

Latin letters

B	Vessel beam, page 20	[m]
C_b	Block coefficient, page 20	[-]
$\mathbf{D}$	Damping matrix, page 38	[-]
D	Experimental data thrust force, page 23	[N]
E	Cost functions, page 62	[-]
I_z	Inertia moment for yaw motion, page 39	[kgm^2]
J	Non dimensional advance ratio, page 43	[-]
K	Nomoto gain factor, page 52	[$\frac{1}{\mathrm{s}}$]
K_T	Nondimensional thrust coefficient, page 43	[-]
L	Vessel length, page 20	[m]
$L^x_{b/s}$	Longitudinal distance from gravity centre bow or stern thruster, page 45	[m]
$\mathcal{M}$	Motion model structure, page 48	[-]
$\mathbf{M}$,$\boldsymbol{M_A}$	Mass matrix, added mass matrix, page 38	[-]
M	Vessel mass, page 39	[kg]
n_h	Hidden neurons in layer, neural network, page 47	[-]

n	Rotational speed propeller, page 23	[rpm]
N_{rrr}, N_{rr}, N_r	Yaw damping coefficients, page 41	[-]
$N_{\dot{r}}$	Yaw acceleration coefficient, page 39	$[\frac{\text{Nms}^2}{\text{rad}}]$
Re	Reynolds number, page 92	[-]
t_e	Thrust deduction due to external hull, page 44	[-]
t_i	Thrust deduction due to internal hull, page 44	[-]
T_m	Model for static propeller speed dependent thrust forces, page 45	[-]
T_{nnn}, T_{nn}, T_n	Thrust force propeller speed dependent coefficients, page 43	[-]
$T_{n_{V_A}}, T_{n_\nu}, T_{nn_\nu}$	Thrust force propeller and vessel speed dependent coefficients, page 43	[-]
T_{th}	Theoretical thrust force, page 43	[N]
T	Nomoto time constant, page 52	[s]
T	Thrust force, page 22	[N]
T	Vessel draft, page 20	[m]
t	Thrust deduction factor, page 44	[-]
u,v,r	Planar surge, sway, and yaw speeds, page 39	[-]
V_A	Axial water inflow speed propeller, page 43	$[\frac{\text{m}}{\text{s}}]$
V, W	Connection matrices, neural network, page 47	[-]
w	Wake factor, page 44	[-]
$\boldsymbol{x_{d_i}}$	Input variables for identification procedure, for $d \in [u, v, r]$, page 90	[-]
X_{uuu}, X_{uu}, X_u	Surge damping coefficients, page 41	[-]
$X_{\dot{u}}$	Surge acceleration coefficient, page 39	$[\frac{\text{Ns}^2}{\text{m}}]$
x	Input vector, neural network, page 47	[-]
x,y,ψ	Planar position and orientation, page 39	[-]

$\boldsymbol{y_{d_i}}$	Output variables for identification procedure, for $d \in [u, v, r]$, page 90	[-]
Y_{vvv}, Y_{vv}, Y_v	Sway damping coefficients, page 41	[-]
$Y_{\dot{v}}$	Sway acceleration coefficient, page 39	$[\frac{\mathrm{Ns}^2}{\mathrm{m}}]$
y	Output vector, neural network, page 47	[-]

Greek Letters

α	Thruster angle, page 22	[°]
β	Bias vector, neural network, page 47	[-]
$\boldsymbol{\beta_d}$	Bias vector for $d \in [u, v]$, page 90	[-]
δ	Rudder input, page 52	[°]
$\boldsymbol{\eta}$	Position and orientation vector, page 38	[-]
$\boldsymbol{\theta_d^x}$	Unknown parameter vector, with $d \in [u, v, r]$, and model candidates $x \in [a, b, c, d, e, f, g, h, i]$, page 48	[-]
$\boldsymbol{\theta_d^{x_x}}$	Subset parameters of $\boldsymbol{\theta_d^x}$ for $\boldsymbol{x_{d_i}}$, page 90	[-]
$\boldsymbol{\theta_d^{x_y}}$	Subset parameters of $\boldsymbol{\theta_d^x}$ for $\boldsymbol{y_{d_i}}$, page 90	[-]
λ	Scale factor, page 20	[-]
$\boldsymbol{\nu}$	Velocity vector, page 38	[-]
ρ	Water density , page 43	$[\frac{\mathrm{kg}}{\mathrm{m}^3}]$
σ	Activation function, neural network, page 47	[-]
$\boldsymbol{\tau}$	Force and moment vector, page 38	[-]

Superscript

0	0 degree angle, page 43
90	90 degree angle, page 43
B	Bounded, page 95
b	Bow thruster (steering-grid), page 48

d	Desired system state, page 27
i	Internal (control angle), page 22
m	Measured system state, page 83
o	Output (thrust angle), page 22
s	Stern thruster (four-channel), page 48
U	Unbounded, page 95
x	Longitudinal component (thrust force), page 24
y	Transversal component (thrust force), page 24

Subscript

0	Initial parameter guess, page 95
b	Bow thruster (steering-grid), page 48
c	Four-Channel thruster, page 24
g	Steering-Grid thruster, page 22
s	Stern thruster (four-channel), page 48

Contents

Abstract iii

Beknopte samenvatting v

List of Abbreviations ix

List of Symbols xiv

Contents xv

List of Figures xxi

List of Tables xxv

Introduction 1
1.1 Research Motivation . . . 2
1.1.1 Historical Waterway Transport . . . 2
1.1.2 Current Inland Waterway Cargo Transport . . . 3
1.1.3 Current Status Inland Waterway Cargo fleet . . . 6
1.2 Research Questions and Objectives . . . 8
1.3 Thesis Outline . . . 9

Design and Build of Industrially Relevant Unmanned Research Vessels 11
2.1 Introduction . . . 13
2.2 Novel Inland Vessel Concepts . . . 13
2.2.1 The European Watertruck Barges . . . 14
2.2.2 The Pallet Shuttle Barges . . . 15
2.2.3 Vessels for Urban Transport . . . 16
2.3 The USV Research Field and Challenges . . . 17
2.3.1 The USV State of the Art . . . 17
2.3.2 Research Challenges For Inland USVs . . . 18

2.3.3 Design Choices Industrially Relevant Research USVs . . 18
2.4 The Cogge — Scale Model Watertruck Barge 19
2.4.1 Vessel Type and Size 19
2.4.2 Actuation System 21
2.4.2.1 Mechanical Design Steering-Grid Thruster . . 22
2.4.2.2 Mechanical Design Four-Channel Thruster . . 23
2.4.3 Component Selection 26
2.4.3.1 Modular Hardware 27
2.4.3.2 Modular software 27
2.5 The Maverick — Scale Model Pallet Shuttle Barge 30
2.5.1 Vessel Type and Size 30
2.5.2 Actuation System 31
2.5.3 Component Selection 31
2.6 Current Exploitation Research Fleet 32
2.7 Conclusion 33

Modelling of Unmanned Inland Cargo Vessels **35**
3.1 Introduction 37
3.2 Decoupled Hydrodynamic Models for a USV 38
3.2.1 Modelling Assumptions 38
3.2.2 Added Mass Models 40
3.2.3 Damping Models 40
3.2.4 Propulsion System Models 41
3.2.4.1 Conventional Propeller Characteristics 43
3.2.4.2 Feedforward Multilayer Network 46
3.2.5 Selected Decoupled Hydrodynamic Motion Models . . . 48
3.3 Transfer Function Steering Models 50
3.3.1 The WAM-V Test platform 50
3.3.2 Transfer Function Modelling of Steering Behaviour . . . 52
3.4 Computational Fluid Dynamics 52
3.4.1 Methodology 53
3.4.2 Geometry and Grid Specifications 53
3.5 Conclusion 56

Identification of Unmanned Inland Cargo Vessels **57**
4.1 Introduction 59
4.2 Transfer Functions WAM-V 59
4.2.1 Methodology 60
4.2.2 Results 60
4.3 Bollard Thrust Model Identification 62
4.3.1 Identification Procedures Bollard Thrust Models 62
4.3.1.1 Conventional Bollard Thrust Model 62
4.3.1.2 Feedforward Multilayer Network Model 63

4.3.2 Results Bollard Thrust Models . . . 64
4.3.2.1 Conventional Bollard Thrust Model . . . 64
4.3.2.2 Feedforward Multilayer Network Model . . . 69
4.3.3 Discussion . . . 74
4.4 Computational Fluid Dynamics Data . . . 76
4.4.1 Grid Studies . . . 76
4.4.2 Deep Water Surge Damping . . . 77
4.4.3 Shallow Water Surge Damping . . . 79
4.4.4 Comparison Deep and Shallow Water Surge Damping . . . 79
4.5 Additional Test Manoeuvres . . . 80
4.5.1 Method . . . 81
4.5.1.1 Existing Vessel Manoeuvres . . . 81
4.5.1.2 Suggested Additional Vessel Manoeuvres . . . 81
4.5.2 Results . . . 83
4.5.2.1 The Crabbing Test . . . 83
4.5.2.2 The Counter Thrust Test . . . 84
4.5.2.3 The Sine Angle Test . . . 85
4.5.3 Discussion . . . 85
4.6 Decoupled Hydrodynamic Motion Models . . . 86
4.6.1 Experimental Design . . . 86
4.6.1.1 Configuration Sensors . . . 87
4.6.1.2 Decoupled Motion Experiments . . . 87
4.6.1.3 Data Post Processing . . . 88
4.6.2 Identification Methods Decoupled Models . . . 89
4.6.2.1 Force Balance Method . . . 90
4.6.2.2 Differential Equation Method . . . 91
4.6.3 Model Structure Comparison and Selection . . . 92
4.6.3.1 Comparisons with External Data . . . 92
4.6.3.2 Comparisons with Experimental Data of this study . . . 94
4.6.4 Results . . . 94
4.6.4.1 Results of Surge Motion Models . . . 95
4.6.4.2 Results of Sway Motion Models . . . 101
4.6.4.3 Results of Yaw Motion Models . . . 104
4.6.5 Discussion . . . 108
4.7 Conclusion . . . 111

Perception and Motion Control of Unmanned Inland Cargo Vessels 113
5.1 Introduction . . . 115
5.2 Perception for Inland USVs . . . 115
5.2.1 Risk and Safety Analyses . . . 115
5.2.2 Navigational Information . . . 116
5.2.3 Environment Perception . . . 117

5.2.4 Selected Sensors for the Cogge . . . 118
5.2.4.1 GNSS . . . 119
5.2.4.2 IMU . . . 119
5.2.4.3 Lidar . . . 121
5.2.4.4 Stereo Cameras . . . 121
5.3 Motion Control for an Inland USV . . . 122
5.3.1 High Level Control . . . 123
5.3.2 Middle Level Control . . . 123
5.3.3 Low Level Control . . . 124
5.4 Results of the First Experiments . . . 124
5.4.1 Open-loop, Rotselaar lake . . . 124
5.4.1.1 Straight Sailing . . . 124
5.4.1.2 Pseudo Spiral Manoeuvre . . . 125
5.4.2 E1 — Known Static Obstacles . . . 126
5.4.2.1 Autonomous Sailing on the Yzer River . . . 126
5.4.3 E2 — Unknown Static Obstacles . . . 128
5.4.3.1 Lidar Scans . . . 128
5.4.3.2 Shoreline Extraction from Lidar Data . . . 129
5.4.3.3 Stereo Camera Images . . . 130
5.4.3.4 In-Operation Communication Data Rates . . . 130
5.4.4 E3 — Known Dynamic Obstacles . . . 131
5.5 Conclusion . . . 132

Design and Build of an Inland Shore Control Centre 133
6.1 Introduction . . . 135
6.2 Motivation for an Inland Shore Control Centre . . . 135
6.3 Concept and Requirements of an Inland Shore Control Centre . . . 137
6.3.1 Line-Of-Sight Control Subsystem . . . 137
6.3.2 Concept of an Inland Shore Control Centre . . . 138
6.3.2.1 Ship Sense and Harmony . . . 138
6.3.2.2 Situation Awareness, Sensemaking, Interaction . . . 139
6.3.2.3 Activity-Centred Design of an Inland SCC . . . 139
6.3.3 Design Requirements of an Inland Shore Control Centre . . . 140
6.3.4 The Hull-To-Hull Navigation Concept . . . 141
6.3.5 Risk and Safety Analysis of an Inland SCC . . . 143
6.4 Design and Construction of an Inland Shore Control Centre . . . 143
6.4.1 Technical Design of an Inland Shore Control Centre . . . 144
6.4.1.1 Design Results for (R-i) . . . 145
6.4.1.2 Design Results for (R-ii) . . . 146
6.4.1.3 Design Results for (R-iii–iv) . . . 147
6.4.2 Construction of an Inland Shore Control Centre . . . 147
6.4.3 Technical Design Hull-To-Hull-Extended Inland SCC . . . 148
6.4.4 Construction of Hull-To-Hull-Extended Inland SCC . . . 149

6.4.5 Design of Experiments . . . 150
6.4.5.1 First USV and Inland SCC tests . . . 150
6.4.5.2 First USV and H2H-Extended Inland SCC tests 151
6.5 Results . . . 152
6.5.1 First USV and Inland SCC tests . . . 152
6.5.2 First USV and H2H-Extended Inland SCC tests . . . 154
6.6 Discussion . . . 156
6.7 Conclusion . . . 158

Conclusion 159
7.1 Research Answers and Deliverables . . . 160
7.1.1 RQ1 — Industrial and Scientific Relevance . . . 160
7.1.2 RQ2 — Modelling and Identification . . . 161
7.1.3 RQ3 — Perception and Motion Control . . . 162
7.1.4 Alternative Answers for RQ2 and RQ3 . . . 163
7.1.5 Overall Conclusion . . . 164
7.2 Future Work . . . 165
7.3 Main Scientific Contributions . . . 166

A Full Components List 167

B Bollard Pull Test Data 170
B.1 Bollard Pull Data Steering-Grid Thruster . . . 170
B.2 Bollard Pull Data Four-Channel Thruster . . . 171

C Identified Bow Thruster Coefficients 172

D Surge Coefficients 174

Bibliography 177

Publications 207

List of Figures

1.1 Man and woman towing a cargo boat . . . 1
1.2 Old Belgian cities and IWT . . . 2
1.3 Global multimodal cargo transportation . . . 4
1.4 Modal split cargo in Europe and Belgium . . . 5
1.5 The inland waterways of Flaners (April 2016) . . . 6
1.6 The thesis outline and chapter cohesion. . . . 9
2.1 Vitruvian Man [275] . . . 11
2.2 A self-propelled watertruck barge [7] . . . 14
2.3 A pallet shuttle barge [30] . . . 15
2.4 Intracity cargo tranport in Utrecht and Amsterdam . . . 16
2.5 The Cogge [199] — a watertruck barge [281] scale model . . . 19
2.6 Hull geometry Cogge . . . 20
2.7 Actuation system configuration Cogge . . . 21
2.8 Mechanical design steering-grid thruster . . . 22
2.9 Bollard pull data steering-grid thruster . . . 23
2.10 Mechanical design four-channel thruster . . . 24
2.11 Bollard pull data four-channel thruster . . . 25
2.12 Main onboard components Cogge . . . 26
2.13 Cogge design drawing and components . . . 29
2.14 The Maverick [206] — a pallet shuttle barge [29] scale model . 30
2.15 Actuation system Maverick . . . 31
3.1 Yin and yang symbol [116] . . . 35
3.2 North-East-Down and body-fixed reference frames . . . 39
3.3 Longitudinal position actuation systems . . . 45
3.4 Multilayer feedforward network with one hidden layer. . . . 47
3.5 The Wave Adaptive Modular Vessel [162] . . . 50
3.6 WAM-V geometry . . . 51
3.7 Geometry KVLCC2 and CEMT–I for deep water. . . . 54
3.8 Computational domain and boundary settings . . . 55
3.9 Grid specifications KVLCC2 and CEMT–I for deep water [195]. 56

4.1 The Egyptian God Horus [219] . . . 57
4.2 Comparison simulated and measured heading . . . 61
4.3 Comparison symmetrical and asymmetrical Nomoto models . . . 61
4.4 Model fits conventional thrust model steering grid, f(α_g^i) . . . 66
4.5 Model fits conventional thrust model steering grid, f(n_g) . . . 67
4.6 Model fits conventional model four-channel thruster . . . 68
4.7 Alternative model fits conventional model four-channel thruster 69
4.8 Results artificial neural networks steering-grid thruster . . . 70
4.9 Results artificial neural networks four-channel thruster . . . 73
4.10 Model comparison for bollard thrust . . . 75
4.11 Thrust capabilites steering-grid thruster . . . 76
4.12 Comparison pressure, elavation, and streamlines . . . 78
4.13 Numerical results surge damping deep and shallow water . . . 79
4.14 The crabbing manoeuvre . . . 84
4.15 The counterclockwise thrust manoeuvre . . . 84
4.16 The sine angle manoeuvre . . . 85
4.17 Input propeller speed profiles . . . 88
4.18 Examplary data surge missions . . . 95
4.19 Comparison FBM and DEM for surge motion . . . 99
4.20 Comparison surge models with CFD [197] and empirical [131] data. 100
4.21 Comparison damping models surge motion . . . 101
4.22 Examplary data sway missions . . . 102
4.23 Comparison thruster models for sway . . . 103
4.24 Comparison damping models for sway . . . 104
4.25 Examplary data yaw missions . . . 105
4.26 Comparison thruster models for yaw motion . . . 106
4.27 Comparison damping models for yaw motion . . . 106
4.28 Neglected roll, pitch, and heave motions . . . 108
4.29 Pseudo advance ratios for surge, sway, and yaw motion . . . 109
5.1 The Statue of Marduk [284] . . . 113
5.2 Working principle of the embedded EKF [230] . . . 120
5.3 Implemented cascaded control hierarchy . . . 122
5.4 Open-Loop straight saiing trajectories . . . 125
5.5 Open-Loop pseudo psiral manoeuvres . . . 126
5.6 Autonomous waypoint following on the Yser river . . . 127
5.7 Static long-exposure lidar scan . . . 128
5.8 Lidar scan from a moving vessel . . . 129
5.9 Shore line extraction from lidar data [269] . . . 129
5.10 Stereo camera images . . . 130
6.1 Geppetto carving Pinocchio [52] . . . 133
6.2 The fromer line-of-sight shoreside infrastructure . . . 138
6.3 H2H augmented remote motion control . . . 142

6.4 Main inland SCC and USV system components 144
6.5 The inland SCC motion control subsystem 146
6.6 Constructed inland SCC 148
6.7 Component position USV 148
6.8 H2H-extended inland SCC and USV components 149
6.9 Current H2H shoreside infrastructure 150
6.10 USV under SCC motion control in a canal (Leuven) 152
6.11 USV under SCC motion control in a lake (Rotselaar) 152
6.12 Measured latency times between onboard and onshore PLCs . . 153
6.13 Results H2H-extended straight line sailing 155
6.14 Images of supplementary videos 155
6.15 Movable motion control SCC subsystem at Rotselaar lake . . . 157
7.1 Cogge, sailing on the Yser reservoir 159

List of Tables

2.1 Geometry Cogge and the self-propelled watertruck barges. . . . 20
2.2 List of components, their description, and their abbreviations. . 28
3.1 The selected decoupled motion model structures of this study. . 49
3.2 WAM-V specifications 50
3.3 Vessel geometry CEMT–I and KVLCC2 comparison for deep water 54
4.1 Summary of the identified model structures within this chapter. 59
4.2 Summary asymmetric Nomoto coefficients 61
4.3 Cost function residuals for the different T_g models 66
4.4 Cost function residuals for the different T_c^x models 67
4.5 Cost function residuals for the different T_c^y models 68
4.6 Residuals neural networks steering-grid thruster 71
4.7 Residuals neural networks four-channel thruster 72
4.8 Deep water results for the KVLCC2 [237] and CEMT–I hulls. . 77
4.9 Shallow water results for the KVLCC2 and CEMT–I hulls . . . 79
4.10 Overview of all decoupled motion model experiments. 88
4.11 Measured, calculated, or estimated parameters of the Cogge. . 93
4.12 Manually chosen validation missions. 94
4.13 Final costs for the surge identification methods. 97
4.14 Identified surge model coefficients for bounded DEM. 97
4.15 Identified sway model coefficients for the bounded DEM. . . . 107
4.16 Identified yaw model coefficients for the bounded DEM. . . . 107
5.1 Selected sensors Cogge 118
5.2 Absolute accuracies for the AsteRx-U Marine [233] 119
5.3 IMU accuracy dependent on GNSS outages [230] 120
6.1 Summary inland SCC design results based on the requirements 144
6.2 Summary of the information group realisations. 145

A.1 Full H2H-extended components list SCC and USV 168
A.1 *Cont.* 169

B.1 Data steering-grid thruster, $D_g(n_g, \alpha^i)$ 170
B.2 Data four-channel stern thruster. 171

C.1 $T_m(n) = T_n n$ 172
C.2 $T_m(n) = T_{nn} n^2$ 172
C.3 $T_m(n) = T_{nnn} n^3$ 173
C.4 $T_m(n) = T_{nn} n^2 + T_n n$ 173
C.5 $T_m(n) = T_{nnn} n^3 + T_{nn} n^2 + T_n n$ 173

D.1 Identified surge model coefficients for the DEM^U. 174
D.2 Identified surge model coefficients for the FBM^B. 175
D.3 Identified surge model coefficients for the FBM^U. 175

Introduction

"Hat man sein *warum?* des Lebens, so verträgt man sich fast mit jedem *wie?* — Der Mensch strebt nicht nach Glück [182]."[1]

Friedrich Nietzsche

Figure 1.1: Man and woman towing a cargo boat through a canal, the Netherlands 1931 [157].

[1]He who has a why to live for, can bear almost any how — Man does not strive for happiness.

1.1 Research Motivation

The Historical Waterway Transport, Current Inland Waterway Cargo Transport, and Current Status Inland Waterway Cargo fleet sections will provide the overarching context for this thesis. Subsequently, the Research Questions and Objectives will be explained, followed by the Thesis Outline.

1.1.1 Historical Waterway Transport

In the ancient world, the Egyptian and Roman empires already used canals to transport cargo and irrigate land. Many centuries later, pre-industrial economies in Europe enhanced rivers and dug canals to increase their Inland Waterway Transport (IWT) [54]. In 1561, the construction of the Brussels–Rupel Maritime Canal offered a 28 km long, 30 m wide, and 2 m deep reliable connection between Brussels and Antwerp [251]. This canal became one of the oldest Belgian and European navigable canals and got extended to the Scheldt in 1997 [288]. In times of horse or wind powered cargo transport, an inland barge offered significant savings in manpower and horsepower: a single horse could pull two tons by wagon, but up to fifty tons by canal barge [65]. However, high initial investments were needed to dig canals or enhance existing rivers [54].

Nevertheless, such investments have been frequently made in the past, resulting in a dense inland waterway network in Western Europe. For example, Figure 1.2a depicts Ghent flourishing in 1791, with evident IWT, and Figure 1.2b shows Bruges with shoreside cargo infrastructure — a manned crane —, in ca. 1525.

(a) Ghent, 1791 [153] (b) Bruges ca. 1525 [17]

Figure 1.2: Old Belgian cities and IWT.

Automating (**RQ3**) an inland vessel (**RQ1**) requires knowledge of its restricted water environment (**RQ2**). The importance of — not having — this knowledge might have had a significant impact on the history of the ancient world. In 2019, Fourdrinoy et al. [92] might have debunked the ship-holder fish myth for the naval battle of Actium. This battle formed the epilogue of the Civil War between the Western Roman world and the Eastern Oriental world in 31 BC. The ships of the latter might not have been able to reach their ramming speed, due to the shallow bathymetry of the battlefield, which did not impact the smaller fleet of the former army. The unexplainable slow motions of the larger vessels, and subsequent battle loss, were attributed to hull-adhering fish that had the power to stop vessels [92]. Finally, it might be interesting to note that the first mathematical description of the well-known Proportional Integral Derivative (PID) controller [290] — also used in the first experiments of this thesis — was derived by observing a helmsman controlling the course of a ship by Minorsky in 1922 [165].

1.1.2 Current Inland Waterway Cargo Transport

The main body of this thesis studies the potential for unmanned vessels in Flanders, Belgium. However, this area should be understood and positioned in its worldwide context. In 2015, vehicles transported an estimated 108×10^{12} tkm of cargo worldwide, of which 70% travelled by sea, 18% by road, 9% by rail, 2% by inland waterway, and less than 0.25% by air [121]. Figure 1.3a draws relative density lines for the global commercial ocean-based shipping of cargo, from 2008 [96]. This figure illustrates that Europe serves as a logistical hub in the world wide multimodal transport web. To facilitate these cargo streams, the European Union has introduced the Trans-European Transport Network TEN-T [79]. Figure 1.3b maps the envisaged TEN-T corridors, consisting of: railway lines, roads, inland waterways, maritime shipping routes, ports, airports, and railroad terminals. These transport corridors aim to remove bottlenecks and technical barriers for the European cargo transport sector.

Flanders has a central position within the European transport network. More precisely, 60% of the European purchasing power is located within 500 km of Flanders [258] and three TEN-T corridors cross Flanders (see Figure 1.3b). Subsequently, Flanders needs and has a dense freight transport infrastructure, detailed by Figure 1.3c. Furthermore, the Belgian Federal Planning Bureau [133] estimates a total cargo growth of +27% (tonnes) in the period between 2015 and 2040, caused by a 5% (tonnes) rise of national transport and a 39% (tonnes) rise of international transport over Belgian territory (under the assumption of unchanged policies). Similarly, they estimate an increase of +32% (tkm) of goods transported over the Belgian inland waterways [133].

(a)

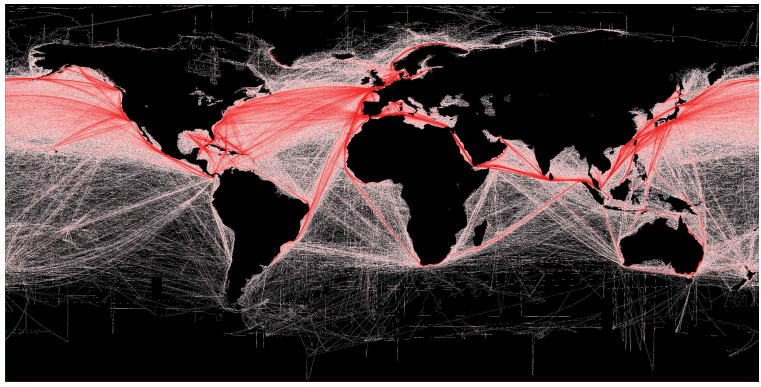

(b)

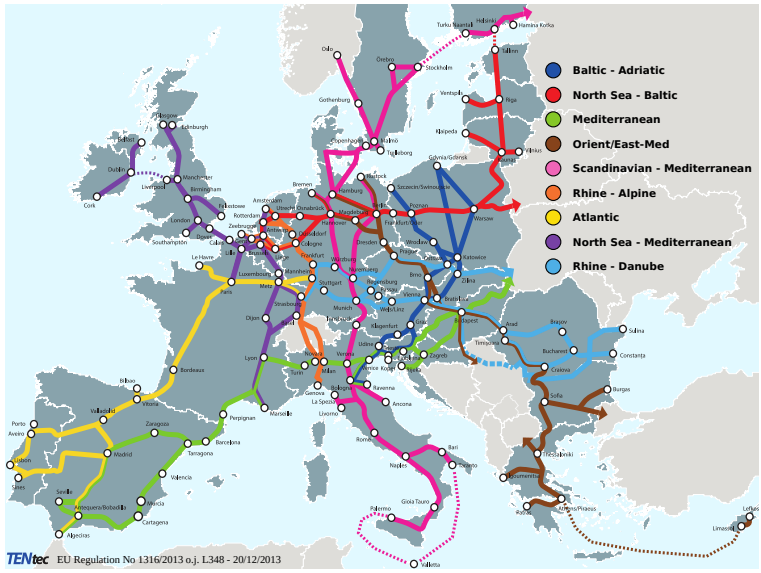

(c)

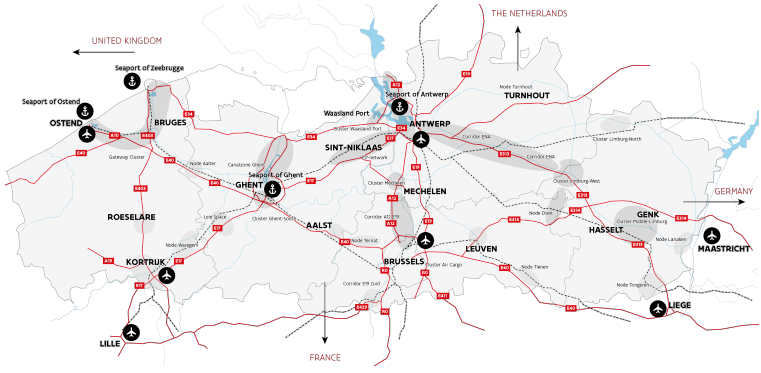

Figure 1.3: Global multimodal transport: (a) relative density of commercial shipping over the oceans [96], (b) the European TEN-T corridors [256], and (c) the freight transport infrastructure of Flanders [84].

These predicted novel cargo flows will further stress the freight infrastructure of Flanders (Figure 1.3c) and Europe (Figure 1.3b). The Belgian and European multimodal cargo division during 2009–2018 can be seen in Figure 1.4a and in Figure 1.4b respectively (excluding maritime transport). For both Europe and Belgium, road-based cargo flows dominate the hinterland freight transport sector. Nevertheless, road-based hinterland freight transport has significantly higher external costs compared to rail or waterway transport. External costs are caused by a transport user on a third party, but not paid for by the transport user [28] (e.g. accidents, air pollution, noise, habitat damage, congestion, and well-to-tank costs). Although at present no scientific consensus exists to determine the exact prices of these external costs [272], several studies [71, 73, 74, 220] concluded that IWT offers a more sustainable alternative than road-based transport.

In 2016, the average European external cost for IWT equalled an estimated 1.9×10^{-2} $\frac{\text{EUR}}{\text{tkm}}$, approximately half the cost of road (heavy goods vehicles) transport which equalled 4.2×10^{-2} $\frac{\text{EUR}}{\text{tkm}}$ [73, 77]. Furthermore, the total external costs for freight transport via road (including light commercial vehicles) amounted for 1.31% of the European (28 countries) GDP, whereas IWT amounted for only 0.02% of the GDP, in 2016 [77]. Subsequently, the European Commission wants to promote IWT as a competitive and resource-efficient mode of transportation [175]. More precisely, they want to push 30% (tkm) of road freight transport, longer than 300 km, to rail and water-borne transport between 2011 and 2030, and similarly transfer 50% (tkm) between 2011 and 2050 [78, 126]. In the same vein, the Flemish Government wants to expand and increase the utilisation of its dense inland waterway infrastructure [286]. In sum, both the regional and European freight transport policies aspire to increase the utilisation of the IWT sector.

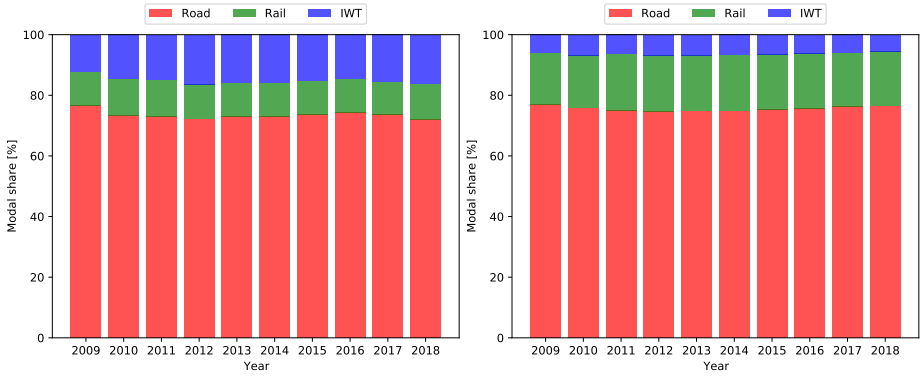

(a) Belgium (b) Europe (28 countries)

Figure 1.4: Hinterland freight transport modal share split (tkm) [80].

1.1.3 Current Status Inland Waterway Cargo fleet

The Conférence Européenne des Ministres des Transports (CEMT, French) divided the European inland waterway fleet into categories ranging from CEMT–I–VI. The smallest categorised vessels have the dimensions of 38.5 m × 5.1 m × 2.5 m, whereas the largest single vessels have a size of 135.0 m × 17.0 m × 4.0 m, note that larger vessel convoys and smaller vessels exist too. Subsequently, the inland waterways can be divided into the same categories, depending on which vessels can enter their waters. Figure 1.5 maps these CEMT classified inland waterways and the associated container terminals for Flanders (2016). The waterways of this dense network pass within 10km of 80% of the Flemish companies [259].

In 2020, approximately 15 200 cargo vessels sailed on the European inland waterways (9 800 in Rhine countries, 3 500 in Danube countries, and 1 900 in other countries) [43]. Vessels older than 75 years still make up 15% of this European fleet. Furthermore, around half of the IWT fleet in Belgium, Germany, and the Netherlands is older than 50 years. In France, nearly 80% of the fleet has this age [44]. Therefore, it could be stated that a relatively old fleet characterizes the Western European IWT market. This characterisation might cast the perception that the IWT lacks innovation, when compared with other transport modes. Nevertheless, this perception need not be true: most vessels frequently undergo upgrades, renovations, and inspections. In addition, these vessels need to stay compliant with novel regulations [272].

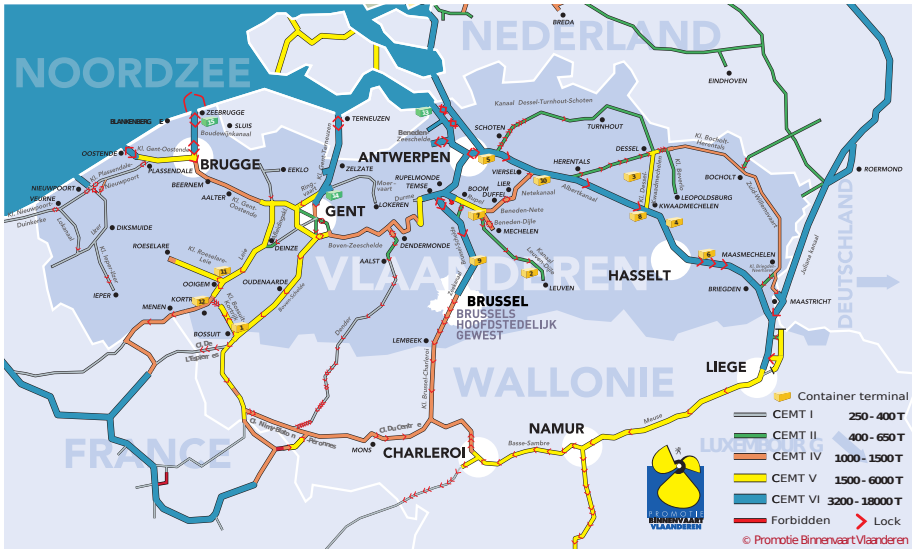

Figure 1.5: The inland waterways of Flanders (April 2016) [216].

The newly constructed vessels consist mainly of larger vessels ($\geqslant$ CEMT–III) [71, 268], although two novel smaller vessel concepts (CEMT–I–II) were recently introduced and constructed: The European Watertruck Barges [281] and The Pallet Shuttle Barges [271]. The former decouples sailing and transshipment times, and the latter has flat deck ships focussing on palletized cargo. In sum, the total capacity of the European IWT fleet is increasing, whereas the number of vessels is decreasing [272]. Moreover, the European IWT sector has a fragmented market structure with intense competition and currently undergoes a surplus of supply over demand. This surplus clusters around the larger waterways [71, 287], since most new vessels are unable to enter the smaller rivers and canals. This excessive supply has a negative impact on the freight rates and thus economic viability for vessel owners [272]. Nevertheless, the European IWT freight capacity itself remains under-exploited.

In addition, the smaller inland waterways witness a net outflow of their fleet, i.e., CEMT type I–II vessels. A non-exhaustive list of the main reasons for this noted outflow [71, 250, 268, 271, 272] seems to be:

(i) Few technological improvements for small inland vessels and waterways.

(ii) Inadequate maintenance of the smaller waterways, which also undermines their full potential.

(iii) The crew costs amount for a larger part of the total transportation costs, when compared with bigger vessels.

(iv) High entry and exit barriers. For example, trucks can be conveniently sold when the market changes, which is not that straightforward for vessels.

(v) A non-attractive investment climate. This climate results in resistance of the banks to provide loans for new vessels, equipment, or technology.

In conclusion, a tension field is growing in the European IWT sector. On the one hand, current policies want to transfer some of the current and predicted future cargo flows from road-based transport towards the more sustainable IWT sector. On the other hand, the larger waterways currently experience an excessive supply and the smaller waterways witness an overall outflow of their fleet. Consequently, the current IWT sector might be evolving into an economically unviable transport mode, whereas this sector presently offers a more sustainable solution for hinterland freight transport than road-based transport. Automated or unmanned inland cargo vessels might induce a paradigmatic change in this tension field. Although the conceptual idea of automated or unmanned vessels itself might be straightforward, it is not clear how these vessels could or should look like. Therefore, this thesis explores the technological feasibility of unmanned inland cargo vessels. This technological focus aims to provide a high resolution research input for researchers, policy makers, and investors.

1.2 Research Questions and Objectives

The abovementioned research context for inland cargo vessels presents only a small piece of the complex industrial- and welfare-economic multi-modal freight transportation puzzle. A full description of the IWT integration in this complex transport chain, perhaps impossible to define, falls out the scope of this thesis. Therefore, the provided context might be prone to selection biases. In order to minimise such biases, this thesis explores the challenges "Towards Unmanned Inland Shipping" from the bottom up, i.e., by studying the technological feasibility of an unmanned inland cargo vessel and its associated infrastructure. More precisely, this work investigates three Research Questions (**RQ**s), listed below, which each have two Research Objectives ($\mathcal{RO}$s). The resultant Deliverables ($\mathcal{D}$s) will help to construct the research Answers (**A**s), detailed in the conclusive chapter of this thesis. The technological achievability of these research objectives alone cannot judge the socio-economic feasibility of unmanned inland cargo vessels in general. On the contrary, the present work aims to provide inputs to enable socio-economic feasibility studies on a higher level of resolution, with the ambition to guide future investment flows.

RQ1. How to design and build an industrially relevant research vessel for unmanned inland cargo shipping? → **A1**

- $\mathcal{RO}$**1.1** Design an industrially relevant unmanned inland cargo vessel. → $\mathcal{D}$**1.1**
- $\mathcal{RO}$**1.2** Design a scientifically relevant unmanned inland cargo vessel. → $\mathcal{D}$**1.2**

RQ2. How to model and identify the hydrodynamic motion models of an inland cargo vessel? → **A2**

- $\mathcal{RO}$**2.1** Model the hydrodynamics of an inland cargo vessel. → $\mathcal{D}$**2.1**
- $\mathcal{RO}$**2.2** Identify the hydrodynamic models of an inland cargo vessel. → $\mathcal{D}$**2.2**

RQ3. How to provide an unmanned inland cargo vessel with perception and motion control? → **A3**

- → $\mathcal{RO}$**3.1** Provide perception for an unmanned inland cargo vessel. $\mathcal{D}$**3.1**
- → $\mathcal{RO}$**3.2** Provide motion control for an unmanned inland cargo vessel. $\mathcal{D}$**3.2**

1.3 Thesis Outline

Figure 1.6 illustrates the overall chapter cohesion of this thesis. With respect to this figure, the remainder of this section will briefly highlight the contents of each chapter. Note that all chapters start with a context providing introduction and end with a conclusion. As visible in Figure 1.6, the present introductory chapter provides the overarching context to position the posed research questions and their objectives.

Chapter 2 investigates the design of industrially relevant (***D*1.1**) research (***D*1.2**) vessels for unmanned inland cargo shipping (**A1**). This chapter starts with explaining three novel vessel concepts for IWT: the watertruck, the pallet shuttle barge, and the smaller intracity cargo vessels. The next section summarises the state of the art of Unmanned Surface Vessel (USV) research in general, followed by a listing of some of the inland-specific research challenges. The combination of these research challenges with the novel industrial vessel concepts resulted in the design and build of two research vessel: a scale model watertruck barge, coined the Cogge [199], and a scale model pallet shuttle barge, coined the Maverick. Finally, their current research exploitation will be pointed out.

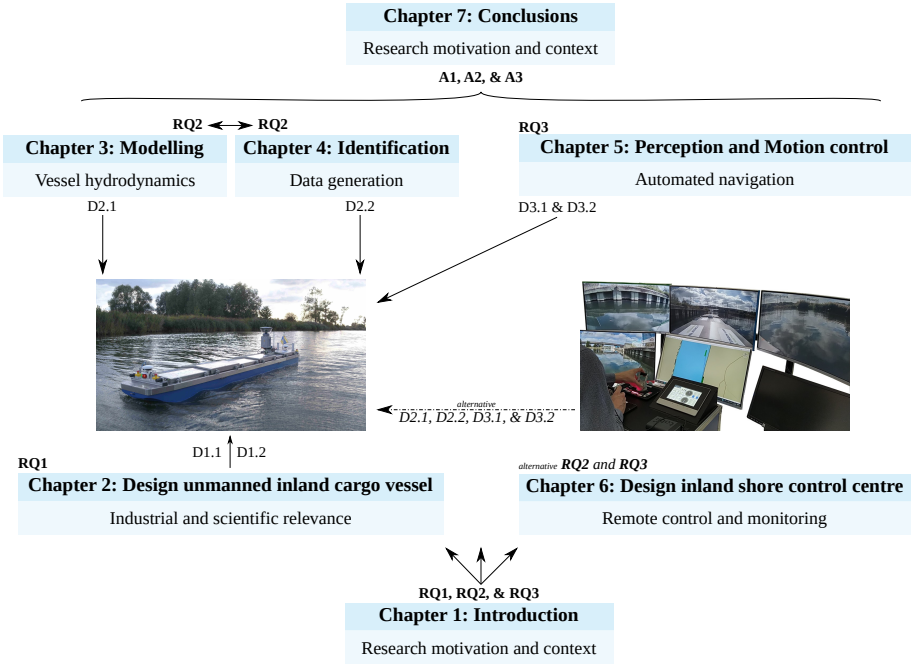

Figure 1.6: The thesis outline and chapter cohesion.

Chapter 3 explores the different modelling possibilities to describe the hydrodynamics (***D*2.1**) of the research fleet. The main part of this chapter investigates the decoupled planar equations of motion for a vessel in surge, sway, and yaw [203] via a modular vectorial model. In addition, a transfer function model [195], a neural network model [194], and a computational fluid dynamics (CFD) approach to model the ambient water [66, 197] will be detailed.

Chapter 4 identifies (***D*2.2**) the models put forward by Chapter 3, note that Table 4.1 lists the main interactions between both chapters (**A2**). Three environments provided the data for the identification procedures: outdoor, indoor, and virtual experiments. The main part of this chapter utilised outdoor generated data to identify the decoupled equations of motion for the Cogge, where a preliminary comparison with indoor bollard pull test and CFD generated surge damping data was made [203].

Chapter 5 analyses the necessary onboard perception (***D*3.1**) and motion control (***D*3.2**) systems for an unmanned or automated vessel (**A3**). This chapter begins with dividing the navigational environments in four parts based on the presence of known or unknown and static or dynamic objects. These environments alter the requirements for the exteroceptive sensors and motion control systems [199]. This chapter ends with listing some of the conducted experiments with the Cogge, e.g., autonomous navigation in a river with known static obstacles.

Chapter 6 provides an alternative answer for the second and third research question, by adding an operator in the loop to remotely control or monitor a vessel. From inside a shore control centre, the operator can perform the perception and motion control for the vessel (**A3**) which requires the implicit modelling and identification of the vessel behaviour (**A2**). This chapter details the design and build of an inland shore control centre [206] and discusses the first remote control experiments conducted via this control centre. In addition, this chapter shows some preliminary results of augmented remote control experiments, performed within the Hull-To-Hull (H2H) project.

Chapter 7 revisits the three research answers **A1**, **A2**, and **A3**, and the alternative answer for the latter two. Thereupon, this chapter draws an overall conclusion regarding the challenges “Towards Unmanned Inland Shipping” and the limitations of the present work. The subsequent future work section aims to provide potential solutions for the present limitations. Finally, the last section briefly highlights the main scientific contributions of this thesis.

Design and Build of Industrially Relevant Unmanned Research Vessels

"Simplicity is the ultimate sophistication [149]."[2]

Clare Boothe Luce

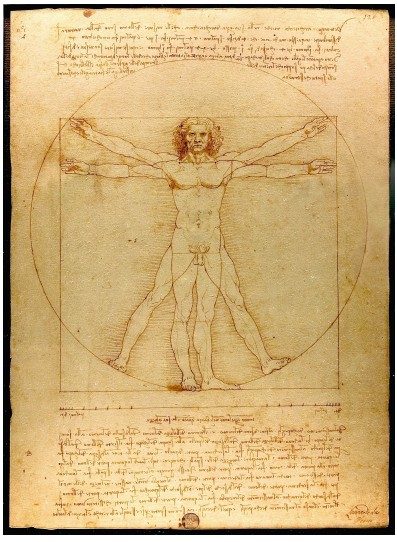

Figure 2.1: Vitruvian Man from Leonardo Da Vinci, circa 1492 [275].

[2]Often described to Leonardo Da Vinci but no written proof has been found yet.

This chapter investigates the first research question (**RQ1**), resulting in the design and construction details of an industrially (***RO*1.1**) and scientifically (***RO*1.2**) relevant vessel for unmanned inland cargo shipping. Parts of this chapter were previously published as:

[199] G. Peeters, M. Kotzé, M. R. Afzal, T. Catoor, S. Van Baelen, P. Geenen, M. Vanierschot, R. Boonen and P. Slaets. "An unmanned inland cargo vessel: Design, build, and experiments". In: *Ocean Eng.* 201.107056 (2020), p. 17. DOI: 10.1016/j.oceaneng.2020.107056

[194] G. Peeters, M. R. Afzal, M. Vanierschot, R. Boonen and P. Slaets. "Model Structures and Identification for Fully Embedded Thrusters: 360-Degrees-Steerable Steering-Grid and Four-Channel Thrusters". In: *Journal of Marine Science and Engineering* 8.220 (2020). DOI: 10.3390/jmse8030220

[196] G. Peeters, T. Catoor, M. R. Afzal, M. Kotzé, P. Geenen, S. Van Baelen, M. Vanierschot, R. Boonen and P. Slaets. "Design and build of a scale model unmanned inland cargo vessel: Actuation and control architecture". English. In: *MTEC/ICMASS 2019*. Vol. 1357. 1. Institute of Physics Publishing, 2019. DOI: 10.1088/1742-6596/1357/1/012016

2.1 Introduction

This chapter explores the design of experimental platforms which have the ambition to explore unmanned inland cargo shipping. This industrially oriented research ambition needs a combination of both industrial and scientific relevance, in order to generate useful data or insights.

Therefore, Section 2.2 first explores the novel vessel concepts on the inland waterways. Both inter- and intracity cargo transport concepts will be discussed. These concepts focus on the smaller inland waterways due to their current outflow of vessels and thus increasing under-exploitation. Next, Section 2.3 lists the current research field regarding unmanned surface vessels (USVs) in general and summarises some of the inland-waterway-specific research challenges for unmanned shipping. In addition, this section aligns the current status and challenges of the USV research field with the novel vessel types from the previous section. This alignment resulted in the made design choices to construct both industrially and scientifically relevant unmanned inland cargo vessels (see Section 2.3.3). In the context of this thesis, the resultant design choices drove the design and construction of two new research vessels. Accordingly, Section 2.4 and Section 2.5 address these design choices for the two newly constructed research vessels.

Afterwards, Section 2.6 reviews the current research application of this novelly constructed fleet. Finally, Section 2.7 provides an overarching conclusion of this chapter.

2.2 Novel Inland Vessel Concepts

The introduction detailed the Current Inland Waterway Cargo Transport and noted an overall outflow of smaller inland vessels (type CEMT–I–II). Nevertheless, novel cargo transport concepts do aim to counter this noted outflow of vessels on the smaller inland waterways, on both an inter- and intracity logistics perspective. For the intercity aim, the European Watertruck$^+$ project [281] introduced a fresh fleet of inland vessels, reviewed by Section 2.2.1. The novel pallet shuttle barges from Blue Line Logistics [29] currently sail on the inland waterways too, discussed in Section 2.2.2. For the intracity perspective, it should be noted that a growing research and industrial interest for urban cargo vessels, and thus intracity logistics, has been triggered in Europe, explained in Section 2.2.3.

2.2.1 The European Watertruck Barges

The European Watertruck$^+$ project [281] aims to revivify the inland waterway transport sector by introducing a novel modular fleet of push vessels and standardised barges of the hull type CEMT–I and II. Note that this project falls under the broader Trans-European Transport Network (TEN-T) framework, (see Section 1.1.2). The barges can be either passive/unpropelled, or active/self-propelled. Furthermore, the vessel–barge convoys can be coupled or decoupled in a truck- or train-like manner. Not only does this modularity provide the on demand configuration of ship fleets, it also decouples sailing and transshipment time, further reducing the onboard crew costs. In its first phase, the Watertruck$^+$ project will introduce 31 new barges and push boats (12 unpropelled barges, 16 self-propelled barges and 3 push boats) of CEMT–I and II. The final ambition aims to expand this fleet to 500 vessels in the CEMT range I to IV.

In addition, this concept aims at introducing a normal working week for the onboard skipper. Therefore, the self-propelled barges do not have any housing accomodation onboard, in contrast to typical inland vessels where the skippers tend to live onboard. For example, the self-propelled-CEMT–I (SP-CEMT–I) barges just provide the skipper with the steering capabilities of the vessel. The actuation systems consists of a 360-degrees-steerable steering-grid in the bow in combination with a 360-degrees-steerable four-channel thruster in the stern of these SP-CEMT–I barges. This unconventional actuation system configuration provides the self-propelled barges with a high level of manoeuvrability, useful in the small spatially restricted inland waterways. Figure 2.2 displays a self-propelled barge sailing on a river.

Figure 2.2: A self-propelled watertruck barge sailing on a river [7]. The skipper and steering interface can be seen at the bow of the vessel.

2.2.2 The Pallet Shuttle Barges

The company named Blue Line Logistics [29] introduced the pallet shuttle barges to the European inland waterways in 2014 [25]. The first two barges have a catamaran-like double hull and a flat deck to facilitate the transportation of palletized cargo. With the main vessel dimensions of 50 m × 6.6 m × 2.2 m, the deck can hold 198 euro pallets per layer (stacked up to 4 m high) and has a cargo capacity of 300 tonnes [289]. Blue Line Logistics named their vessels the Zulus. Note that the third and fourth Zulus have a conventional ship hull, abandoning the catamaran design [271]. The Zulus have no onboard housing accomodation, in contrast with conventional inland vessels. Similarly to the Watertruck$^+$ concept, the Zulu envisages a normal work week where the skipper does not live onboard. Figure 2.3 shows the first Zulu sailing on a canal. This figure shows the bow of the vessel where the skipper and a minimalistic wheelhouse can be seen.

Although the Zulus aim at transporting palletized cargo, this need not be the case: containers can also easily be (and have been) stacked on the deck. Furthermore, the Zulus have their own onboard crane on a rail system. This crane can lift 2 tonnes 9 m far [25] and enables the skipper to load or unload its cargo independently of the shoreside infrastructure. This cargo handling flexibility offers an advantage for the Zulus, given the often lacking shoreside infrastructure on the smaller inland waterways. Furthermore, the skipper does not have to wait on shoreside partners and to start the loading or unloading procedures. Finally, the first two Zulus have a powerful actuator in the stern in conjunction with two bow thrusters, offering a high level of manoeuvrability.

Figure 2.3: A pallet shuttle barge (Zulu 01) sailing on a canal [30]. The skipper and steering cabin can be seen at the bow of the vessel.

2.2.3 Vessels for Urban Transport

In addition to the just-mentioned novel intercity watertruck and Zulu cargo vessels, smaller cargo vessels can provide a novel transportation mode for the intracity logistics. Evidently, a smaller vessel can penetrate deeper into the European hinterland and could thus enter certain urban areas. Nevertheless, road-based transport dominates the urban freight transport in most cities, whereas waterways or railways are seldom used for these purposes [254]. Although urban waterway freight transport remains complex to organise and could benefit from further research [41], smaller-scale cargo transport has been shown to be a workable alternative in urban areas in several European cities by both governmental and private initiatives [122, 154].

In 1996, the city of Utrecht (the Netherlands) introduced the beer boat with the dimensions of 18.80 m × 4.26 m × 1.10 m, depicted in Figure 2.4a. Due to the often narrow roads in Utrecht, trucks tended to block these roads during their cargo loading or unloading. Therefore, the beer boat offered a solution to the increasingly difficult road-based urban city logistics in Utrecht, given that many catering companies are positioned near the dense waterway network of Utrecht. In 2010, approximately 65 catering services were provisioned by the beer boat. In the same year, a second electric boat was introduced due to the success of the first one [154].

In 1997, DHL refurbished a former 17 m long tourist touring boat into a floating service centre in Amsterdam (The Netherlands), shown in Figure 2.4b. In the morning, this centre receives its mail and packages via a DHL van, which picks up the deposited mail and packages in the evening. During the day, the vessel stops at predefined locations where bike couriers perform the last leg of the mail deliveries [122, 154].

(a) The beer boat [62] (b) The DHL floating service centre [164]

Figure 2.4: Intracity cargo transportation in (a) Utrecht and (b) Amsterdam.

2.3 The USV Research Field and Challenges

2.3.1 The USV State of the Art

The advancements in platforms, sensors, onboard computing power, and communication systems have reached critical maturity levels over the last two decades [19]. Complementary improvements occurred for the implementation of guidance, navigation, and control subsystems, which form the intelligent backbone of a USV [63, 89–91, 104, 127, 300]. The combination of these developments gradually unlocks more potential for semi- or fully-autonomous surface vehicles, which has resulted in the growth of five main USV categories for: (i) scientific research, (ii) environmental missions, (iii) ocean resource exploration, (iv) military use, and (v) other applications, as defined by Liu et al. (2016 [148]). In addition, Liu et al. (2016 [148]) noted the scarcity of USVs in the commercial markets, which could be partly explained by their competition with their manned analogues or with other robotic platforms [148, 229].

Nevertheless, in 2016, one of the conclusions of the Maritime Unmanned Navigation through Intelligence in Networks (MUNIN) project [174] was that inland cargo vessels might be plausible first movers for unmanned cargo shipping, if suitable business models can be found. This idea originates from the presumed lower legal and technological complexity of inland cargo shipping compared to maritime shipping [222]. This conclusion was not wrong, as can be seen in the "Listing of pilot and research projects in the field of automation in inland navigation" published by the Central Commission for the Navigation of the Rhine (CCNR) [45], in 2020. In this list, a significant surge in inland waterway automation projects can be noted, over the last three years.

The listed projects investigate potential solutions or augmentations for the IWT sector via a variety of approaches. The ongoing Novimar project [186] investigates the concept of waterborne platooning [51]. The Sensing [232] and Prepare-Ship [213] projects focus on the onboard sensor integration. The FernBin project [83] handles the remote control of a vessel. Similarly, the company Seafar [231] can presently remotely steer manned watertruck barges (with licensed captains) and aims to perform these tests unmanned in the future. The Black box pro [236] and Captain–AI [40] initiatives focus on implementing artificial intelligence in the automation chain. The Autoship project [10] will build and operate an autonomous vessel and its associated infrastructure and shore control centre, aiming at a technology readiness level of seven and higher. Finally, the scale model discussed in Section 2.4 seems to be one of the first scale model inland cargo USVs that conducted unmanned experiments on a river. This scale model and its associated shore control centre (see Chapter 6) aspire to provide inputs for the ongoing projects of the abovementioned list.

2.3.2 Research Challenges For Inland USVs

Although, at first glance, the technological complexity for unmanned inland vessels might seem to be lower than for seagoing vessels, the overall challenges for unmanned inland shipping are not trivial. For instance, inland ships need to sail in spatially more restricted and complex navigational environments, without the help of tugs to manoeuvre [147]. Moreover, the horizontal and vertical confinements of the waterway have a significant influence on the hydrodynamic behaviour of a vessel [210] and bank effects occur when sailing close to a quay or other shoreside infrastructure [137]. The identification of these hydrodynamic effects could help advanced guidance, navigation, and control subsystems. However, these data or models are not (publicly) available for smaller inland vessels [146]. Furthermore the usability of these maritime-originated guidance, navigation, and control subsystems for inland navigation needs to be investigated and further developments might be necessary. Likewise, the perception of the environment of an inland vessel needs to be explored and crucial information will need to be shared over, and fetched, from the Automatic Identification System (AIS) and the River Information Services [265].

2.3.3 Design Choices Industrially Relevant Research USVs

The research vessels of this thesis aim to expand the The USV State of the Art by investigating the Research Challenges For Inland USVs in the context of the already-existing Novel Inland Vessel Concepts. Subsequently, presently two scale models were designed and constructed (see Section 2.4 and Section 2.5) by implementing the following three overarching design choices:

(i) **Vessel type and size** (see Section 2.4.1 and Section 2.5.1): The vessel type should allow the investigation of the automation potential of the novel inland vessel concepts. Preferably, the vessel size should be able to shed light on possible intracity cargo transport.

(ii) **Actuation system** (see Section 2.4.2 and Section 2.5.2): The propulsion systems should be present on current or future real-size inland vessels. Preferably, the system should offer a high level of manoeuvring capabilities for the vessel.

(iii) **Component selection** (see Section 2.4.3 and Section 2.5.3): The installed hardware and software components should be modular, in order to keep the system design flexible and reconfigurable. Where possible, components should be industrial- or marine-grade.

2.4 The Cogge — Scale Model Watertruck Barge

2.4.1 Vessel Type and Size

Given the new fleet of watertruck vessels, on the one hand, and the growing research interest in urban IWT freight transport, on the other hand, the experimental platform, named the *Cogge* [3], has the geometry of a SP-CEMT–I watertruck vessel with a total length of 4.81 m. Figure 2.5a displays a convoy of watertruck barges, and Figure 2.5b, 2.5c, and 2.5d show the Cogge under its three operational modes (autonomous, remote control, open-loop) in its three main test locations (the Yser river, the canal near Leuven, and Rotselaar lake).

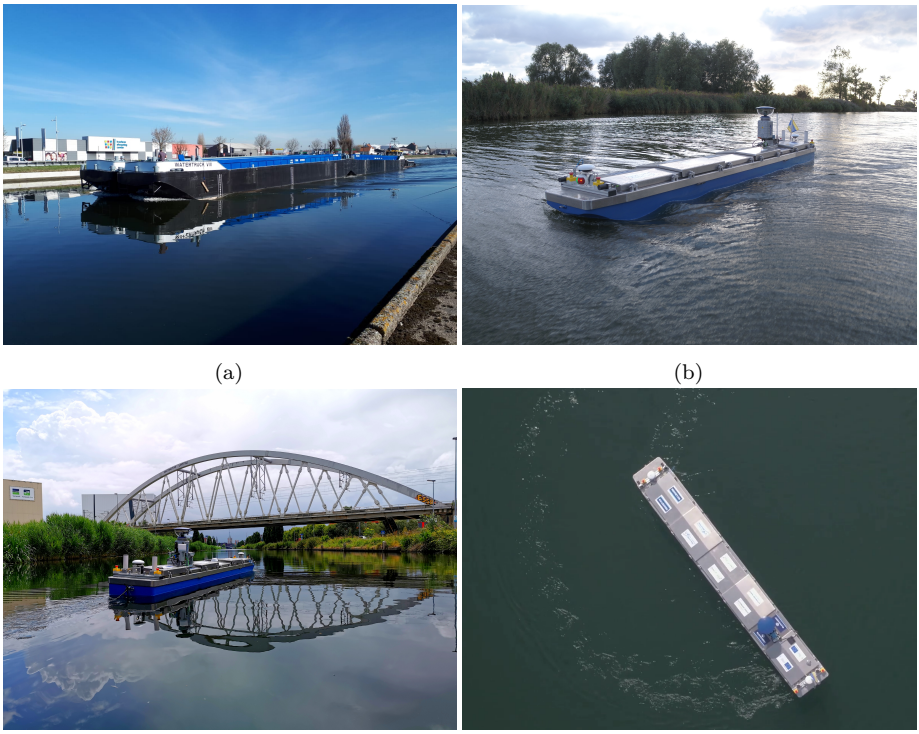

(a) (b)

(c) (d)

Figure 2.5: (a) Four real-size barges, with individual lengths of 38.50 m, and a push vessel from Watertruck$^+$ [281], (b) the 4.81 m long Cogge sailing autonomously on the Yser river [199], (c) the Cogge under remote control operations in the canal near Leuven, and (d) the Cogge performing an open-loop rotational manoeuvre [205] on Rotselaar lake.

[3] As a tribute to Karel Lodewijk Cogge who helped flooding the plains of the Yser during the first World War to keep the German troops at a distance.

Table 2.1 lists the geometrical similarity between the SP-CEMT–I barges and the Cogge. The scale factor of $\lambda = 8$ transforms the vessel into a research platform suitable for studying both the novel SP-CEMT–I fleet and the possibility of urban waterway logistics. Figure 2.6 shows this geometry of the SP-CEMT, or Cogge, together with its body-fixed reference frame where the x-axis points to the bow, y-axis to starboard, and the z-axis downwards.

It is impossible to physically board the Cogge, hence making it a USV by raw definition. Nevertheless, it would be possible to board and steer its real-size counterparts. This discrepancy in operational modes may lead to some confusion between *unmanned* and *autonomous*, as both modes are not mutually exclusive in this context. Similarly, the literature regarding surface vehicles often discusses both ASVs and USVs interchangeably [23, 39, 148, 161]. Moreover, the exact meaning of *autonomous* is often vaguely described as it inherently entails different levels which may be context dependent. For example, Rødseth et al. (2018 [223]) proposed definitions to further clarify this surface-vehicle nomenclature, taking into account both ship specific situations (e.g. having a temporarily unmanned bridge on a manned vessel) and different levels of autonomy, ranging from direct (physical) control by the crew to fully autonomous (i.e. unmanned without supervision). Therefore, the conducted and ongoing research with the Cogge aims to help refine these definitions from a technological bottom-up perspective by investigating the currently feasible operational modes.

Table 2.1: Designed geometry of the Cogge and the self-propelled watertruck barges.

Parameter	Symbol	CEMT–I	Cogge	Units
Scale	λ	1	8^{-1}	[-]
Length	L	38.50	4.81	[m]
Beam	B	5.05	0.63	[m]
Draft$_{full}$	T_{full}	2.80	0.35	[m]
Block coefficient	C_B	0.95	0.95	[-]

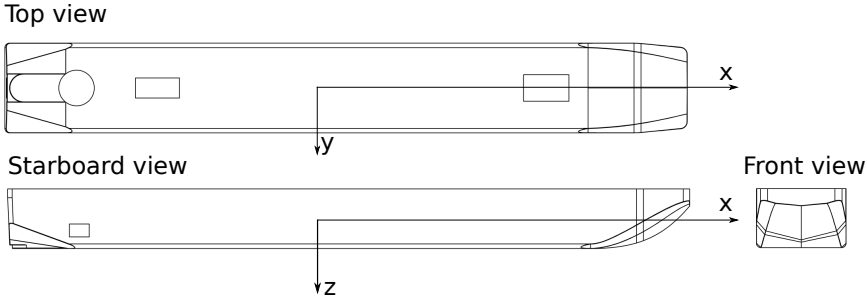

Figure 2.6: Bare hull of a watertruck push barge type CEMT–I. The visible holes enable the full integration of the actuation systems.

2.4.2 Actuation System

The Cogge houses the same non-conventional propulsion system as the first SP-CEMT–I barges, i.e., two 360-degrees-steerable, fully embedded thrusters: a steering-grid thruster in the bow and a four-channel thruster in the stern. Figure 2.7 illustrates their position in the hull of the Cogge. Both thrusters draw in water from underneath the vessel hull and exhaust a water stream according to the orientation of their steering mechanisms. In Figure 2.7c and Figure 2.7d, the body-fixed reference frames of both thrusters are drawn through the origin of their steering mechanisms. Both thrusters have a Kaplan Ka-series propeller without nozzle with a blade area ratio 0.65, and a pitch-diameter ratio of 0.95. The diameter of the steering-grid propeller measures 100 mm, whereas the diameter of the four-channel propeller measures 150 mm. Experimental bollard pull data for both thrusters have been measured in a towing tank facility, in deep water at zero advance speed, and can be found in Appendix B. More details of both thrusters and their bollard data discussion can be found in the subsequent Mechanical Design Steering-Grid Thruster and Mechanical Design Four-Channel Thruster sections.

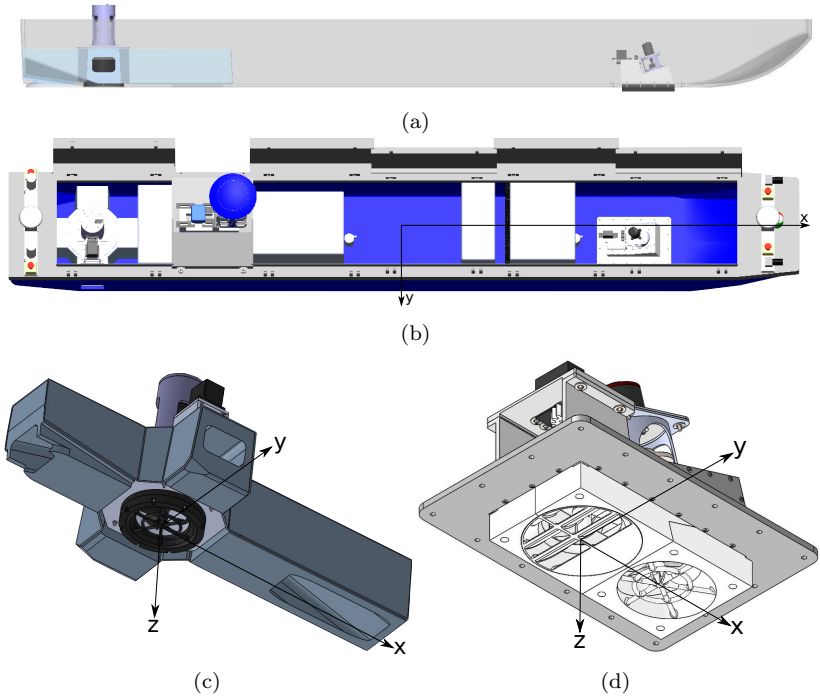

Figure 2.7: Actuation system nested inside the hull (a) and (b), with the four-channel thruster (c) in the stern (see Section 2.4.2.2) and the steering-grid thruster (d) in the bow (see Section 2.4.2.1) of the vessel.

2.4.2.1 Mechanical Design Steering-Grid Thruster

The 360-degrees-steerable steering-grid bow thruster consists of two main parts: the propeller providing the thrust force, and the steering grid which orients the outflow of the water stream and thus provides the steering capabilities. Figure 2.8a shows a longitudinal cut of this thruster, i.e., along the xz-plane through the origin of Figure 2.7d. The propeller and its tilted shaft can be seen on the right side of the cut, where an anti-debris grid covers the inlet hole. The left-hand side shows the axis of the steering grid, but the grid itself is not shown to increase the image readability.

Figure 2.8b draws an abstract top view of the bottom section of this thruster which illustrates the chosen angle convention of the internal control angle of the steering grid, α_g^i. The drawn blue arrows show the orientation of the exiting water flow, which is opposite in direction compared to the thrust force, T_g. It is assumed that internal control angle, α_g^i, equals the output angle, α_g^o, of T_g, i.e., the flow exits the grid in alignment with the grid position in the xy-plane. Therefore, α_g^i immediately gives the orientation of T_g. On top of that, the steering grid has a static angle, γ, of approximately 28° (curved surface, slightly visible in Figure 2.7d) relative to the x-axis in the xz-plane. To illustrate this angle, the drawn blue arrows in Figure 2.8a show the exiting water flow in the xz-plane for $\alpha_g^i = \alpha_g^o = 0°$ which can also be seen in the xy-plane in Figure 2.8b on the left. The steering-grid thruster performed its bollard pull tests as a stand-alone device without enveloping ship hull for $\alpha_g^i \in [0°,\ 180°]$. Hence, symmetry was assumed for the remaining angular domain, although future full domain experiments could uncover potential asymmetrical characteristics. The present data sets can be found in Table B.1.

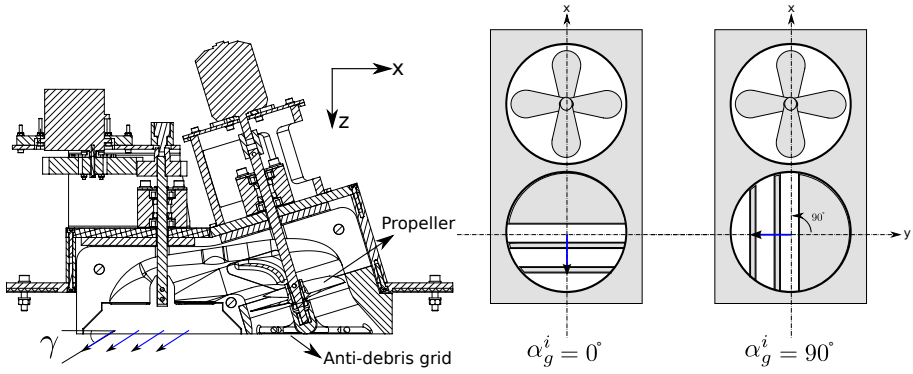

Figure 2.8: 360-degrees-steerable steering-grid thruster: (a) longitudinal cross section at its symmetry plane, and (b) abstract top view of its bottom section for $\alpha_g^i = 0°$ and 90°.

Figure 2.9 shows the measured thrust forces, D_g, linearly extrapolated, at different rotational speeds of its propeller, n_g, and different α_g^i. A significant loss for $D_g(n_g, \alpha_g^i)$ emerges at $\alpha_g^i = \alpha_g^o \in [150°, 180°]$, which might be explained by the potential occurrence of a recirculation zone of water flow — in this steering-grid orientation the exiting water stream is pointed towards the inlet of the thruster.

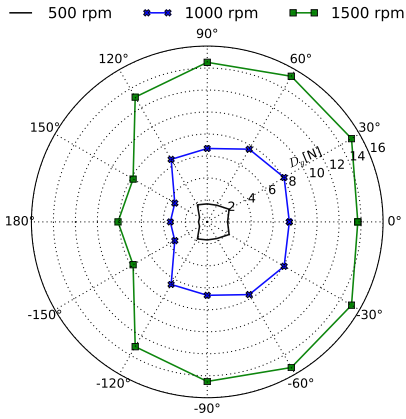

Figure 2.9: Experimental results bollard thrust force steering-grid thruster, D_g, at different α_g^i and n_g. Note that the data were measured for $\alpha_g^i \in [0°,\ 180°]$ (see Bollard Pull Data Steering-Grid Thruster), but the plot assumes symmetry over the x-axis.

2.4.2.2 Mechanical Design Four-Channel Thruster

The 360-degrees-steerable four-channel stern thruster consists of two main parts: its propeller to induce thrust forces, and a 360-degrees-rotatable steering mechanism consisting of half a sphere with an opening of approximately 85° to orient its exiting water flow. Figure 2.10a shows a longitudinal section of this four-channel thruster in the xz-plane, in the origin of its body fixed reference frame of Figure 2.7c. This section shows the propeller and its shaft together with the steering mechanism, which points towards the stern in this figure. This orientation would guide the exiting water flow towards the outlet channel on the left of this figure, which points to the stern of the vessel. The other depicted outlet channel points to the bow, and the remaining two transversal outlet channels cannot be seen in this cut. Notice that the two shown outlets have a downwards angle of approximately 15° relative to the x-axis in the xz-plane, whereas the two transversal outlets have no downwards angle but are positioned a bit higher, directly in line of the internal outlet of the steering mechanism. This height-position difference of the outlets can be seen in Figure 2.7c.

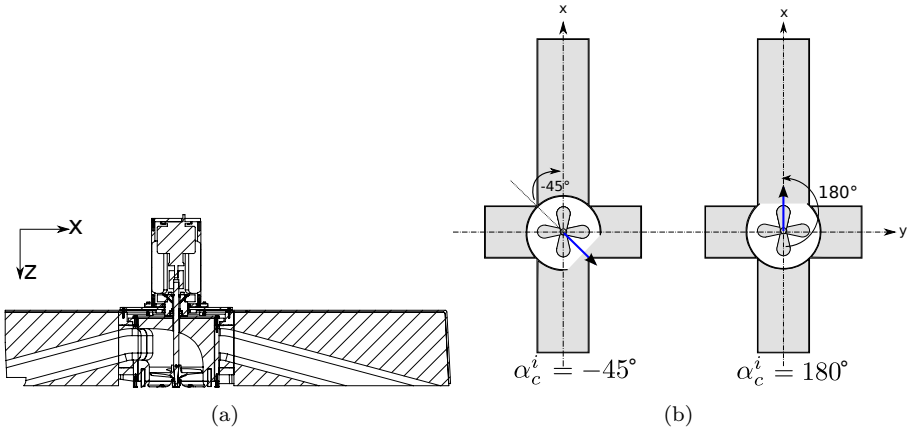

Figure 2.10: 360-Degrees-Steerable four-channel thruster: (a) longitudinal cross section at symmetry plane, and (b) abstract top view of its bottom section for $\alpha_c^i = -45°$ and $= 180°$.

Figure 2.10b depicts the angular convention of the internal control angle of the four-channel thruster, α_c^i, which orients the theoretical outflow of the water stream, denoted by the blue arrows. Due to the geometric differences of the thruster channels, one cannot assume that α_c^i will equal the output angle, α_c^o, of the resultant thrust force, T_c. The main geometric design effects that cause this discrepancy between α_c^i and α_c^o seem to be: (i) the fact that the water flow can only exit through one (e.g. Figure 2.10b at $\alpha_c^i = 180°$), or a superposition of two (e.g. Figure 2.10b at $\alpha_c^i = -45°$) channels simultaneously, (ii) the different channel lengths and shapes (e.g. downwards bends), (iii) internal deflections of the water stream in the xy-plane when $\alpha_c^i \neq 0°$, 90°, 180°, or $-90°$, and (iv) a potentially remaining angular velocity of the water flow as there is no grid to align the water outflow. To study the thrust characteristics of this propulsion system, the resultant four-channel thrust, T_c (and its data sets D_c), can be orthogonally decomposed in longitudinal, T_c^x, and transversal, T_c^y, components for different propeller speeds, n_c, according to:

$$T_c(n_c, \alpha_c^i) = \sqrt{T_c^x(n_c, \alpha_c^i)^2 + T_c^y(n_c, \alpha_c^i)^2}, \quad \alpha_c^o = \arctan\left(\frac{T_c^y}{T_c^x}\right). \tag{2.1}$$

Experimental data were fetched with the four-channel thruster nested inside half a ship hull (transversal cut at midship) at zero velocity in a towing tank, for $\alpha_c^i \in [0°, -180°]$. Here too, symmetry was assumed over the angular domain but further full domain experiments could uncover potential asymmetries. Table B.2 lists all the four-channel thruster data points. Figure 2.11 illustrates these measurements in two different perspectives. Firstly, Figure 2.11a

and Figure 2.11b show the decomposed measured thrust forces for $\alpha_c^i \in [0°, -180°]$ at different n_c. Note that the small fluctuations in n_c, reported in the Table B.2, are accumulated around their mean value in order to plot these data sets with one line, resulting in for example: $n_c = 340 \pm 25$ rpm. Secondly, Figure 2.11d and Figure 2.11c plot exactly the same data but decomposed into α_c^o and D_c, calculated according to (eq. 2.1). Figure 2.11c confirms the nonlinear mapping of α_c^i to α_c^o hypothesis, which appeared to stay consistent over different n_c–sets. This n_c–independent consistency in the angle mapping seems to hint at a structural, geometrical origin of this nonlinearity. The relatively constant α_c^i for $\alpha_c^i \in [-60°, -120°]$ seems to originate from the incapability of the thruster to produce a significant T_c^x within this angular domain allowing the T_c^y to dominate the thrust generation, which results in an almost transversal α_c^i. The inverse seems to be true for α_c^i when $\alpha_c^i \in [-150°, -180°]$. Given the currently available data sets, it remains hard to judge the explicit cause of these nonlinearities.

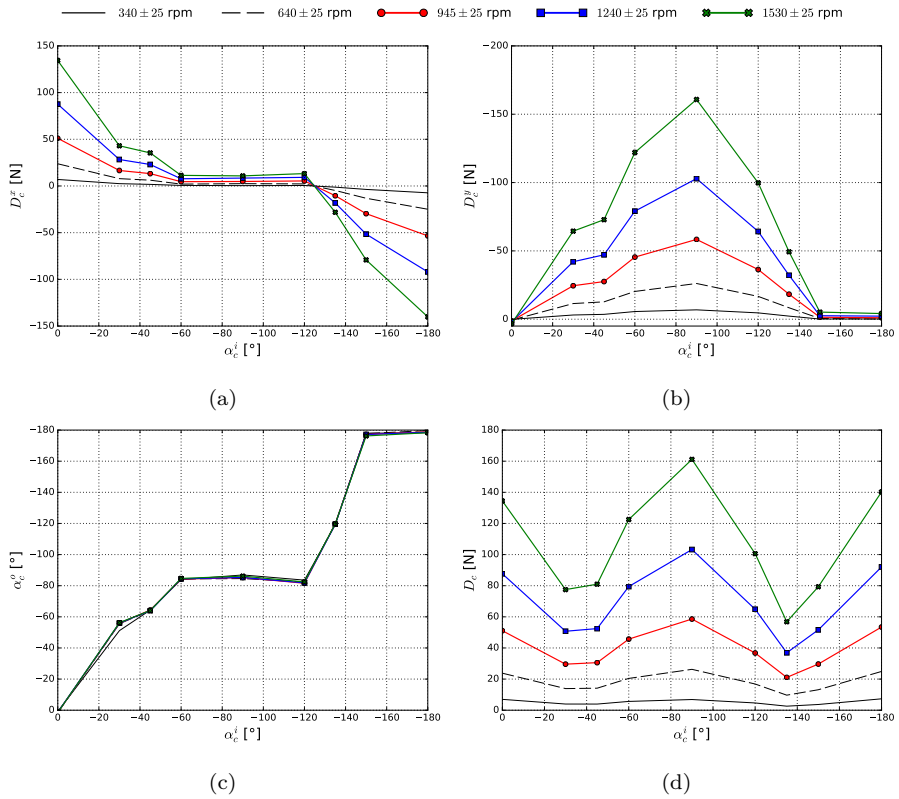

Figure 2.11: Data measurements four-channel thruster for different n_c and $\alpha_c^i \in [0, -180]°$: (a) longitudinal component of D_c, (b) transversal component of D_c, (c) angle mapping between α_c^i and α_c^o, and (d) D_c.

2.4.3 Component Selection

The installed marine-grade and robust components further strengthened the industrial relevance of the Cogge. Accordingly, the component subsystems could be directly transferred to real-size vessels. Furthermore, the modular hardware and software systems aim to keep the USV design flexible. This flexibility should facilitate future design extensions or modifications. Table 2.2 lists the main components and Figure 2.13 shows their onboard location.

Three main subsystems form the overarching hardware and subsequent communication architecture: an actuation, a sensor, and a shoreside subsystem. Figure 2.12 illustrates their vital inter and intra-communication links. Combining the actuation system with the PLC provides the actuation control subsystem, see Section 2.4.3.1. Similarly, connecting the sensors with the I-PC forms the autonomy subsystem, see Section 2.4.3.2. Finally, a discussion of the shown shoreside control subsystem components can be found in Section 6.3.1.

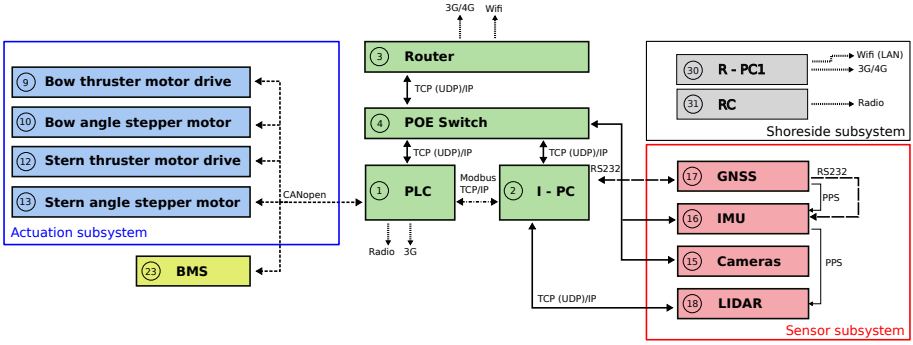

Figure 2.12: Onboard components and their communication links reproduced from [203] with permission from MDPI, 2020.

The energy supply to power all these components consists of two battery systems (1×24V DC — 5000Wh and $1 \times 2 \times 12$V DC — 2×2500Wh). Although the lower energy density of a battery introduces a significant weight and price penalty compared to a fuel-based system, it was judged to be more convenient to use for the scale model for three main reasons: (i) less noise and vibrations, (ii) no local emissions near researchers, and (iii) the vessel can be charged by a 220-230V AC power supply in a few hours. This full electric drive train causes a difference between the Cogge and the first batch of SP-CEMT–I vessels which uses a hybrid system enveloping both batteries and diesel generators to power their electrical engines. This hybrid system aligns with the growing research field looking into hybrid propulsion systems for vessels [125], which might cause a change in the default drive train layouts of future vessels.

2.4.3.1 Modular Hardware — Actuation Control Subsystem

The actuation control subsystem houses a second level of modularity by the nested PLC topology. This PLC controls the lowest level desired actuation system states, i.e., n_g^d, n_c^d, $\alpha_g^{i,d}$, and, $\alpha_c^{i,d}$, and these states can be communicated to the PLC via currently three devices: (i) the remote control over a radio link, (ii) a web-interface over a mobile or a wireless local area network, and (iii) the onboard industrial computer over a Modbus TCP/IP connection. After the reception of these desired system states, the PLC will communicate these states to their appropriate actuation system drivers which will then drive these states to their desired value, using their internal control loops. In this fashion: two motor drives control n_b and n_s and two stepper motors with integrated encoders control α_g^i and α_c^i. This cascaded configuration makes the PLC the heart of the vessel and exploits its industrial robustness to control the desired system states. This lay-out achieves an increased level of operational redundancy, which is paramount for industrial applications.

2.4.3.2 Modular Software — Autonomy Subsystem

The industrial computer forms the core of the autonomy subsystem. On the one hand, it receives the sensor information (currently GNSS, IMU, stereo camera, and lidar), and on the other hand it runs the autonomy software, which can use this sensor information to provide the motion control (see Motion Control for an Inland USV) of the Cogge. Modularity formed the key design choice for the selection of the autonomy software. Therefore an open-source cross-platform software suite was chosen named Mission Oriented Operations Suite (MOOS) [180]. This MOOS software provides internal asynchronous publish-subscribe communication between MOOS Applications (MOOSApps), which are small modular software entities (C++), via its DataBase (MOOSDB), and can be used for robotic research in general. Encompassing this MOOS-core, Benjamin et al. (2010 [20]) wrote a marine-oriented expansion of this software named MOOS Interval Programming, or MOOS-IvP, which takes advantage of the backseat driver paradigm. This backseat paradigm separates the vehicle navigation and control parts from its autonomy system, making the latter research platform independent. This paradigm implementation further increases the modularity and genericness of the control architecture of the Cogge. Furthermore, on the Cogge, this control architecture consists of three cascaded levels coined high, middle, and low level control, which will be discussed in Section 5.3.

Table 2.2: List of components, their description, and their abbreviations.

Nr.	Description	Abbreviation/Name	Type
1	Programmable logic controller	Onboard PLC	Wago PFC200 750-8207
2	Industrial computer	I-PC	Moxa MC-7200-MP-T
3	Power over Ethernet switch	POE switch	Wago 5-port 1000 Base-T
4	Industrial Router USV	Quartz Router USV	Siretta,Quartz-W22-LTE
5	Radio receiver	RR	Danfoss MPCAN
6	Antenna LTE (PLC)	PLC antenna	LTE Antenna for PLC
7	Antenna LTE (Quartz)	LTE antenna	LTE Antenna for Quartz LTE
8	Antenna Wifi (Quartz)	Wifi antenna	Wifi Antenna for Quartz LTE
9	Bow thruster motor drive	Bow motor drive	Roboteq MBL1660A
10	Bow angle integrated stepper	Bow angle quickstep	JVL MIS234S
11	Bow thruster motor	Bow motor	Turnigy RotoMAx 150cc
12	Stern thruster motor drive	Stern motor drive	Roboteq MBL1660A
13	Stern angle integrated stepper	Stern angle quickstep	JVL MIS343
14	Stern thruster motor	Stern motor	Turnigy Aerodrive SK3-6364-245KV
15	Stereo cameras (2x)	Stereo cameras	Custom built, UI-5280FA-C-HQ Vision++
16	Inertial measurements unit	IMU	EKINOX2-E-G4A3
17	Navigational GNSS sensor	GNSS	Septentrio AsteRx-U MARINE
18	Laser scanner	LIDAR	Neptec OPAL-1000
19	Emergency stops (4x)	ESTOP	Twist to reset 40 mm Mushroom
20	Bilge pumps (3x)	Bilge pumps	Rule Bilge pump 800
21	Stern light	Stern light	LED white 12–24 V
22	Directional lights bow	Port/Starboard light	Allpa LED 2 colors 8–30 V
23	Battery monitoring system	BMS	Mastervolt-Amperian interface
24	Battery 24 V	24V DC	Navex
25	Battery 24 V (2 × 12V)	2 × 12V DC	Navex

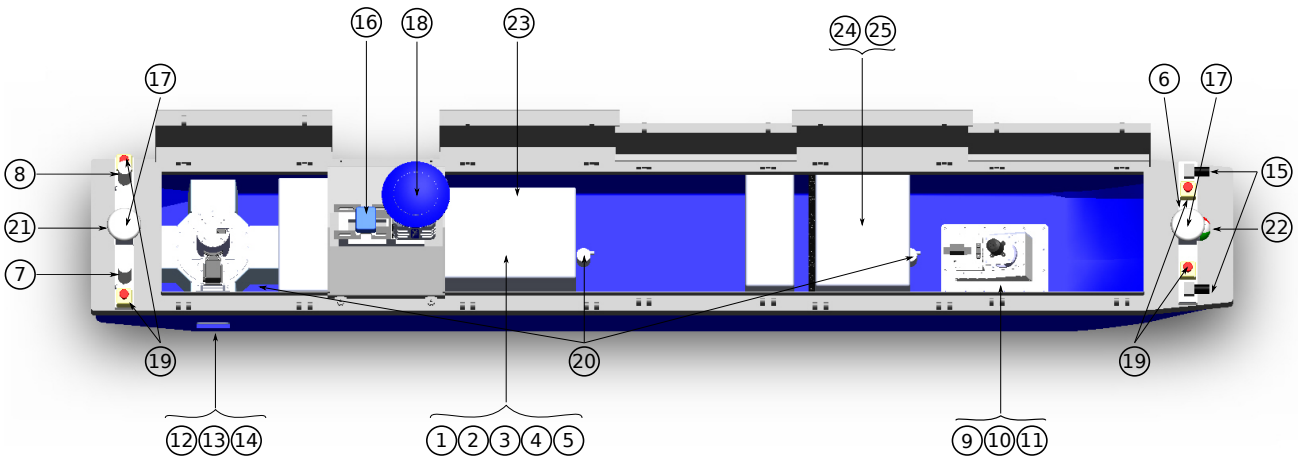

Figure 2.13: Top view 3-dimensional drawing of the Cogge (slightly tilted), stern on the left and bow on the right. The vessel lights, parts nr. 21 and 22 are mounted underneath the visible white GNSS mushroom antennas.

2.5 The Maverick — Scale Model Pallet Shuttle

2.5.1 Vessel Type and Size

Similarly to the Cogge, the design of the second research vessel aims to provide insights for both a novel development on the IWT transport sector and for urban freight transport research. More precisely, this vessel, named the Maverick, is a functional scale model of the new pallet shuttle barges from Blue Line Logistics [29]. Figure 2.14a depicts a pallet shuttle barge independently handling its cargo at a quay. Figure 2.14b shows the Maverick transporting cargo on the canal near Leuven. The maverick has a length of 6 m, a beam of 2 m, and a catamaran-like twin hull. A team of bachelor students constructed the hull in 2017 and installed two combustion outboard motors, visible in Figure 2.14b.

The deck of the Maverick can carry a load of 1 tonne and its flatness should facilitate the transportation of palletized cargo. Evidently, unlike the real-size pallet shuttle barges, the Maverick has no onboard crane. Nevertheless, its one tonne cargo capacity might be interesting for finer urban freight distribution via waterways (see Section 2.6). In 2018, our research group electrified the vessel by replacing the two combustion engines by two electrical motors. This electrification was done in order to be compliant with potential future zero-local-emission policies for intracity cargo transport. Furthermore, during the winter of 2020–2021, these outboard engines will be replaced by two 360-degrees-steerable propulsion systems which should facilitate the further automation of the vessel (see Section 2.5.2 and Section 2.5.3).

(a) (b)

Figure 2.14: The pallet shuttle barges: (a) a real-size Zulu handling cargo at a quay [29], (b) the scale model named Maverick.

2.5.2 Actuation System

From 2017 to 2018, the Maverick had two outboard combustion engines which were replaced by two electrical motors in 2018. The working principle of these electric motor be seen in Figure 2.15a. Both the starboard and port motor orientation angles, i.e., α_p^i and α_s^i, had a mechanically limited steering range of $\alpha^i \in [-42°, 42°]$ and the propellers could provide forwards and backwards thrust, T^p and T^s. Figure 2.15b displays a drawing of the propulsion systems which will be installed during the winter of 2020–2021. Both propulsion systems can rotate 360°, increasing the manoeuvrability of the vessel. In addition, their longitudinal separation of approximately 5 m, see Figure 2.15c, should make the remote control of the vessel more intuitive than the previous transversal configuration, for less experienced operators.

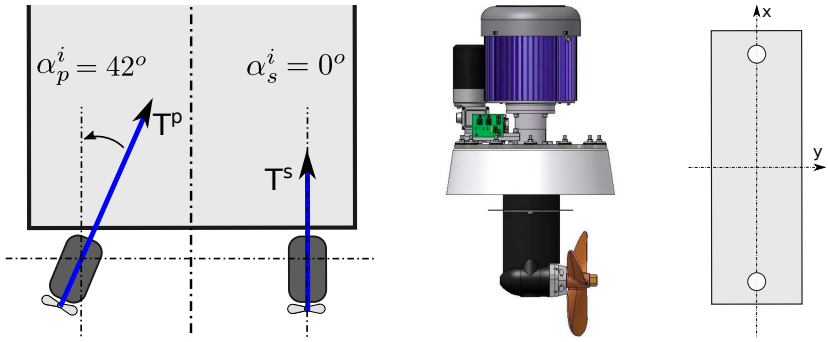

Figure 2.15: Actuation system of the Maverick: (a) the previous outboard motor configuration [206], (b) the newly selected SDK-ED 2.5AC Kräutler electric motors [129], and (c) the envisaged location of the new motors.

2.5.3 Component Selection

The new motors (see Section 2.5.2) and their batteries will offer a more robust and flexible communication (a CAN field bus) with the control architecture, compared with the previous electric system which nested a propriety communication protocol. This control architecture will mirror the cascaded control design of the Cogge (see Section 2.4.3.1). In addition, a sensor subsystem, and by extend an autonomy subsystem, will be installed on the Maverick, based on the blueprints of the Cogge (see Figure 2.12). The exact sensor selection and configuration is presently being investigated, with respect to the research projects in which the Maverick will be operated (see Section 2.6).

2.6 Current Exploitation Research Fleet

The Cogge and the Maverick presently serve as research objects in several doctoral and master theses. In addition, this fleet is or was involved in the following list of regional and international research projects:

(i) "Autonoom Varen in de Westhoek (2017–2019), European Fund for Regional Development [57]" (Dutch for "Autonomous Sailing in the West Corner (region in Belgium)"). This project investigated the technological and legal feasibility of unmanned inland cargo shipping and funded the construction of the Cogge [199].

(ii) "Hull-To-Hull Navigation (2017–2020), European Horizon 2020 [238]". This project investigated the close-proximity manoeuvring of vessels via the sharing of both position data and the vessel geometry [21, 22]. Experiments were conducted with the Cogge for the inland waterway test cases [128, 206, 296, 297], see Section 5.4.4 and Section 6.3.4 for more details.

(iii) "IMEC–SSAVE (2019–2022), Flanders Innovation & Entrepreneurship [248]". This project aims to define methods and technologies for a safe connectivity between marine assets. The KU Leuven partners focus on defining the software architecture to enable data and information sharing between assets. These developments are planned to be deployed on the Cogge for a demonstration.

(iv) "AVATAR (2020–2023), European Interreg North Sea Region [11]". This project aims to deploy automated vessels that provide both intra- and intercity cargo transportation between their respective cargo hubs. The project focus lies on the distribution of palletized goods with zero-local-emission vessels. The current plans involve demonstrations with the Maverick for cargo transportation, although automated intracity navigation with the Cogge could be investigated too.

(v) "IW-NET (2020–2023), European Horizon 2020 [178]". This project aims to produce an "Innovation-driven Collaborative European Inland Waterways Transport Network" (IW-NET) by supplying and developing technological solutions. Both the Maverick and the Cogge are planned to serve as experimental platforms in this project.

(vi) "AUTOBarge (2021–2024), European Horizon 2020 [9]". This project aims to develop a training programme for applying unmanned or autonomous inland vessels, and to investigate their role in the multi-model transport chain in Europe. Both the Maverick and the Cogge are planned to serve as experimental platforms in this project.

2.7 Conclusion

Three main design choices drove the industrially (***RO*1.1**) and scientifically (***RO*1.2**) relevant design and build of two experimental platforms named the Cogge and Maverick:

Vessel Type and Size: Two novel vessel types currently sail on the Flemish inland waterways. First, the watertruck fleet enables the decoupling of sailing time and cargo handling. Second, the pallet shuttle barges focus on palletized cargo via a flat deck and an onboard crane, which allows cargo handling independently of the shoreside infrastructure. In addition to these new vessels, the concept of smaller cargo vessels for urban freight transport gained traction over the recent years. Therefore, the Cogge mirrors the design of a self-propelled watertruck barge, whereas the Maverick is a functional scale model of a pallet shuttle barge. Furthermore, both vessels have a length (4.81 m and 6 m) that unlocks the potential for urban freight transport via narrower waterways.

Actuation System: The Cogge carries the same actuation system as the self-propelled watertruck barges, which consists of two fully embedded 360-degrees-steerable thrusters: a steering-grid thruster in the bow and a four-channel thruster in the stern. This configuration offers a high level of manoeuvrability, and could virtually mimic under-actuated systems, increasing its potential research applications. The Maverick will receive a similar high-manoeuvrable propulsion configuration consisting of two identical fully rotational thrusters, longitudinally separated over the vessel hull.

Component Selection: The modularity of the component selection should facilitate the addition of new components or reconfiguration of the current system. Different autonomy software could control the vessel or different motion control philosophies could run in the current autonomy software. By selecting industrial or marine grade components, the fleet can experiment with a configuration that could be used by real-size inland vessels during their normal operations.

In conclusion, these three design choices answer **RQ1** by augmenting both the industrial and scientific research relevance of the fleet.

Modelling of Unmanned Inland Cargo Vessels

"All models are wrong, but some are useful [32]."

George E.P. Box

Figure 3.1: Yin and yang symbol, ca. 1370 [116].

This chapter investigates the second research question (**RQ2**), by modelling (***RO*2.1**) the hydrodynamics of an inland cargo vessel. Their identification (***RO*2.2**) can be found in Chapter 4. Parts of the present chapter were previously published as:

[203] G. Peeters, S. Van Baelen, G. Yayla, T. Catoor, M. R. Afzal, C. Christofakis, R. Louw, Y. Singh, M. Vanierschot, R. Boonen and P. Slaets. "Decoupled Hydrodynamic Models and Their Outdoor Identification for an Unmanned Inland Cargo Vessel with Embedded Fully Rotatable Thrusters". In: *Journal of Marine Science and Engineering* 8.889 (2020). DOI: 10.3390/jmse8110889

[194] G. Peeters, M. R. Afzal, M. Vanierschot, R. Boonen and P. Slaets. "Model Structures and Identification for Fully Embedded Thrusters: 360-Degrees-Steerable Steering-Grid and Four-Channel Thrusters". In: *Journal of Marine Science and Engineering* 8.220 (2020). DOI: 10.3390/jmse8030220

[197] G. Peeters, A. Eggers, R. Boonen, P. Slaets and M. Vanierschot. "Surge Resistance Identification of Inland Vessels by CFD". in: *OCEANS 2018*. Kobe: IEEE, 2018. DOI: 10.1109/OCEANSKOBE.2018.8559048

[195] G. Peeters, R. Boonen, M. Vanierschot, M. DeFilippo, P. Robinette and P. Slaets. "Asymmetric Steering Hydrodynamics Identification of a Differential Drive Unmanned Surface Vessel." In: *IFAC*. vol. 51. 29. Elsevier, 2018, pp. 207–212. DOI: 10.1016/j.ifacol.2018.09.494

[66] A. Eggers, G. Peeters, P. Slaets and M. Vanierschot. "Shallow water surge resistance identification for inland vessels". In: *5th MASHCON Proceedings*. 2019. URL: http://hdl.handle.net/1854/LU-8624686

3.1 Introduction

Several links in the vessel automation chain can benefit from a hydrodynamic model which describes the motion of the vessel. For example, these models can serve as plant models to verify or tune control algorithms, or as control models, e.g., to construct model predictive controllers [303]. These predictive controllers can also be used with collision avoidance algorithms [72, 132]. Furthermore, Kotzé et al. [128] and Peeters et al. [206] suggested that these motion models could be applied to construct dynamic proximity zones surrounding the vessel hull. These zones could be shared with other ambient vessels or could trigger internal system events.

The literature on the modelling of vessel hydrodynamics seems to hold four main approaches. Firstly, transfer functions can produce response models, e.g., relating yaw-rates with rudder changes [183]. These straightforward black-box models can already provide fruitful inputs for control system designs, e.g., for an adaptive autopilot design [266]. Secondly, Abkowitz (1964 [3]) introduced a third-order Taylor expansion model to mathematically describe the forces acting on a vessel around its equilibrium state [6]. This model can also be found as formal mathematical model [68] or whole ship model [147] in the literature. Thirdly, artificial neural networks have been used to model ship manoeuvres [302]. Fourthly, modular models — such as the modular mathematical model [187] and the robot-like vectorial model [87, 89] — can offer more physical insights in the vessel dynamics.

It should be noted that Norrbin (1971 [185]) added some physical insights to the Abkowitz model. Therefore, the Norrbin model can be regarded as a connection between the formal and modular mathematical models [68]. This thesis models vessels in calm water, in alignment with the Manoeuvring Theory modelling framework [90]. Note that a Seakeeping Theory [90] modelling framework (which has frequency dependent model coefficients) exists too and that a unification of both theories has been made [13, 88].

More precisely, this chapter investigates four modelling approaches (i)–(iv). Section 3.2 models the decoupled planar motions of a USV with (i) a vectorial modular model [90]. This section additionally utilises (ii) a neural network as one of the modelling options for the thruster system. Section 3.3 describes the asymmetric steering behaviour of a USV by (iii) a transfer function model [183]. Section 3.4 models (iv) the ambient water itself by Computational Fluid Dynamics (CFD). This approach enables virtual data capturing that can serve to identify hydrodynamic models. This chapter ends with a conclusion in Section 3.5 and the identified models can be found in Chapter 4.

3.2 Decoupled Hydrodynamic Models for a USV

This section applies the robot-like vectorial model [87, 90] to investigate the hydrodynamics of The Cogge — Scale Model Watertruck Barge. This approach leverages system properties such as symmetry, skew-symmetry, and positiveness of matrices [90], which align with the envisaged future utilisation of the models. At present, the decoupled equations of motion for surge, sway, and yaw have been identified for the Cogge [203] (see Section 4.6). Hence, these three one-degree-of-freedom models describe the behaviour of the Cogge for pure surge, sway, or yaw motion. Their identified coefficients can be used for the diagonal terms in future coupled manoeuvring models which would describe the motions of the Cogge when surge, sway, and yaw occur simultaneously. Accordingly, Section 3.2.1 first relates these decoupled models to the robot-like vectorial model. Thereupon, Section 3.2.2, 3.2.3, and 3.2.4 respectively model the added mass, damping, and actuation forces. Finally, Section 3.2.5 lists the selected decoupled model structures for the identification of the Decoupled Hydrodynamic Motion Models.

3.2.1 Modelling Assumptions

Equation (eq. 3.1) describes the motion for a vessel in calm water (without waves, wind, and current) and thus with frequency-independent coefficients, according to the robot-like vectorial model [87, 90]. Here $\boldsymbol{\nu} = [u, v, w, p, q, r]^\top$ denotes the generalised velocity vector expressed in a body-fixed reference frame with origin, O_b, and $\boldsymbol{\eta} = [x, y, z, \phi, \theta, \psi]^\top$ presents the generalised position and orientation vector of the vessel relative to, and expressed in, an inertial reference frame with origin, O_i. The matrix $\boldsymbol{M_{RB}}$ represents the rigid-body mass matrix, $\boldsymbol{C_{RB}}$ the rigid-body Coriolis and centripetal matrix, $\boldsymbol{M_A}$ the added mass matrix, $\boldsymbol{C_A}$ the Coriolis and centripetal matrix due to $\boldsymbol{M_A}$, $\boldsymbol{D}(\boldsymbol{\nu})$ the damping matrix, $\boldsymbol{g}(\boldsymbol{\eta})$ the gravitational/buoyancy vector, $\boldsymbol{g}_o$ the ballast control vector, and finally, $\boldsymbol{\tau}_{external}$ accumulates all the external forces.

$$\underbrace{\boldsymbol{M_{RB}}\dot{\boldsymbol{\nu}} + \boldsymbol{C_{RB}}(\boldsymbol{\nu})\boldsymbol{\nu}}_{\text{rigid-body}} + \underbrace{\boldsymbol{M_A}\dot{\boldsymbol{\nu}} + \boldsymbol{C_A}(\boldsymbol{\nu})\boldsymbol{\nu} + \boldsymbol{D}(\boldsymbol{\nu})\boldsymbol{\nu}}_{\text{hydrodynamic}} + \underbrace{\boldsymbol{g}(\boldsymbol{\eta})\boldsymbol{\eta} + \boldsymbol{g}_o}_{\text{hydrostatic}} = \boldsymbol{\tau}_{external}. \tag{3.1}$$

The experimental design of this study aimed at solely studying, and thus exciting, the horizontal motions of the vessel, i.e., neglecting pitch, roll, and heave motions, meaning: $\boldsymbol{\eta} = [x,\ y,\ \psi]^\top$ and $\boldsymbol{\nu} = [u,\ v,\ r]^\top$. The remaining motions in the water plane were investigated separately for each degree of freedom,

i.e., $\boldsymbol{\nu} = [u, 0, 0]^\top, [0, v, 0]^\top,$ or $[0, 0, r]^\top$. For these three decoupled motion modes, it will be assumed that the horizontal position of the centre of gravity of the vessel lies in the middle of the vessel in both length and width, given the rather prism-shaped geometry of the vessel and its block coefficient of 0.95. The same assumption will be made for the centres of buoyancy and floatation. Subsequently, no Coriolis, centripetal, buoyancy, or ballast forces were modelled for each one-degree-of-freedom motion model. Furthermore, only thruster related external forces were explicitly modelled, meaning, $\boldsymbol{\tau}_{external} = \boldsymbol{\tau}_{thrust}$, and their dynamic behaviour was neglected. Do note that for the surge and sway models a bias term was added to the external forces, which was intended to implicitly capture any constant wind forces, see Section 4.6.2. In sum, the decoupled model structures for pure surge, sway, or yaw motion turn into:

$$(X_{\dot{u}} + M)\dot{u} + D(u)u = \tau_u, \tag{3.2}$$

$$(Y_{\dot{v}} + M)\dot{v} + D(v)v = \tau_v, \tag{3.3}$$

$$(N_{\dot{r}} + I_z)\dot{r} + D(r)r = \tau_r, \tag{3.4}$$

where M presents the mass of the vessel, I_z the moment of inertia for yaw motion, and $X_{\dot{u}}, Y_{\dot{v}}, N_{\dot{r}}$ the longitudinal, transversal, and rotational added masses. Figure 3.2 shows the reference frames used throughout the identification of these models (see Section 4.6). Accordingly, the body-fixed reference frame, O_b, was positioned at the centre of gravity and its axes aligned with the principal directions of the barge. The position and orientation of the vessel were measured relative to a north-east-down reference frame [90, 224], O_n, which was fixed to the surface of the earth near the first position of the vessel. Hence, the effects on the vessel due to the rotation of the earth and the movement of the earth relative to an inertial reference frame were neglected during the conducted short-duration and short-distance vessel manoeuvres.

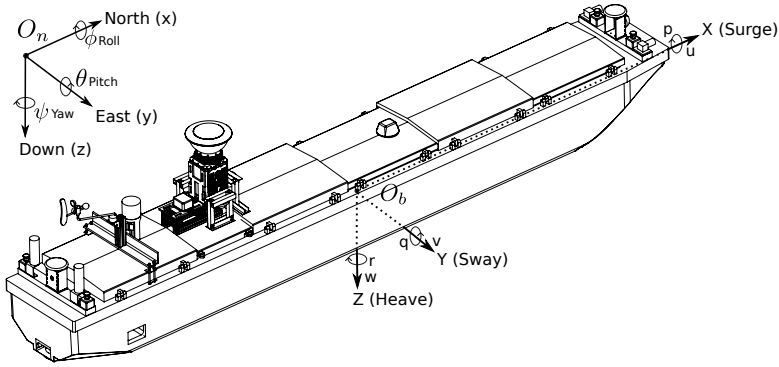

Figure 3.2: North-East-Down (O_n) and body-fixed (O_b) reference frames.

3.2.2 Added Mass Models

In the manoeuvring theory framework [90], the added masses [134] can be modelled by a constant term. Several approaches exist to determine these terms in the absence of well-conditioned towing tank data, by using: (i) less-conditioned outdoor experiments, (ii) empirical methods [50, 304], and (iii) numerical approaches (strip theory [179] or panel methods [279]) which are often based on (iv) theoretical values [117, 179] for common shapes. Liu et al. (2017 [146]) successfully implemented the empirical methods of Zhou et al. (1983 [304]) and Clarke et al. (1983 [50]) on two scale model reference inland vessels for the Yangtze River. Therefore, this study applied the method of Zhou et al. (1983 [304]) for the transversal and rotational added masses, and the method of Clarke et al. (1983 [50]) for the longitudinal added mass, $X_{\dot{u}}$, which equates to:

$$3\% \times M \leq X_{\dot{u}} \leq 6\% \times M. \tag{3.5}$$

Given that the Cogge has a higher C_B than the reference vessels used to derive (eq. 3.5) [50], the upper limit of (eq. 3.5) was selected for $X_{\dot{u}}$. Additionally, Zhou et al. (1983 [304]) suggested that the transversal, $Y_{\dot{v}}$, and rotational, $N_{\dot{r}}$, added masses can be approximated based on the main ship dimensions, listed in Table 2.1, by the following two relations:

$$\begin{aligned} Y_{\dot{v}} = M\Bigg(&0.882 - 0.54C_B\Big(1 - 1.6\frac{T}{B}\Big) - 0.156\Big(1 - 0.673C_B\Big)\frac{L}{B} \\ &+ 0.826\frac{T}{B}\frac{L}{B}\Big(1 - 0.678\frac{T}{B}\Big) - 0.638C_B\frac{T}{B}\frac{L}{B}\Big(1 - 0.669\frac{T}{B}\Big)\Bigg), \end{aligned} \tag{3.6}$$

$$N_{\dot{r}} = Mj_z^2, \quad j_z = \frac{L}{100}\Bigg(33 - 76.85C_B\Big(1 - 0.784C_B\Big) + 3.43\frac{L}{B}\Big(1 - 0.63C_B\Big)\Bigg). \tag{3.7}$$

The geometry of the Cogge differs from the reference vessels used to derive these empirical formulae [50, 304]. Therefore, the estimated $Y_{\dot{v}}$ by (eq. 3.6) and $N_{\dot{r}}$ by (eq. 3.7) were used as the lower limits for the identification procedures of the decoupled motion models, discussed in Section 4.6.

3.2.3 Damping Models

The arising damping forces have many known contributors, e.g., potential damping (due to wave making), skin friction, vortex shedding, and lifting

forces (both due to linear circulation of the water around the hull and due to cross-flow drag). Different modelling assumptions exist to model this complex array of contributors [81, 82, 90, 224]. Given that: (i.) it is not convenient to independently identify all these contributors, and (ii.) this study investigates the decoupled planar motions of the barge, the complexity of the one degree of freedom damping models was chosen to be cubic, quadratic, or linear, respectively represented by the following three equations:

$$\begin{aligned} D(u) &= (X_{uuu}|u|^2 + X_{uu}|u| + X_u)u, \\ D(v) &= (Y_{vvv}|v|^2 + Y_{vv}|v| + Y_v)v, \\ D(r) &= (N_{rrr}|r|^2 + N_{rr}|r| + N_r)r, \end{aligned} \tag{3.8}$$

$$\begin{aligned} D(u) &= (X_{uu}|u| + X_u)u, \\ D(v) &= (Y_{vv}|v| + Y_v)v, \\ D(r) &= (N_{rr}|r| + N_r)r, \end{aligned} \tag{3.9}$$

$$\begin{aligned} D(u) &= X_u u, \\ D(v) &= Y_v v, \\ D(r) &= N_r r. \end{aligned} \tag{3.10}$$

3.2.4 Propulsion System Models

The Cogge, and the self-propelled watertruck barges, navigate with a non-conventional, fully-embedded actuation system configuration consisting of a 360-degrees-steerable steering-grid thruster in the bow in conjunction with a 360-degrees-steerable four-channel thruster in the stern. Conventionally, inland vessels tend to have one or more propellers, regularly ducted to protect them and to increase their performance, which are often placed in combination with multiple rudders to boost their manoeuvrability. Occasionally, the addition of an azimuth or bow thruster further improves their manoeuvrability [146, 147]. In comparison, conventional marine vessels have propeller(s)–rudder(s) configurations positioned at the stern [193], and some marine vessels do carry more exotic propulsion systems such as transversal thrusters, azimuth thrusters, podded propellers, contra-rotating propellers, or even water jets for high speed vessels [90]. In addition, be aware that most small unmanned surface vehicles (USVs) also make use of propeller–rudder configurations [148]. However, some unmanned underwater vessels additionally utilise tunnel thrusters to increase their steering behaviour [192].

In the spectrum of the more conventional propulsion systems, tunnel thrusters [15, 24, 192] and azimuth thrusters [55, 60, 264] might appear to hold the largest similarities with the non-conventional thrusters of the Cogge [206]. The modelling literature for these tunnel and azimuth thrusters does remain scarce and often uses the open-water propeller characteristics model of Blanke (1981 [27]) as its starting point. Furthermore, the present actuation system might look similar to a water jet system, but it was not designed to perform at the conventional higher speed ranges for these systems [5, 93], nor does the overall inlet and outlet design seem to be optimal for these purposes [123]. Do note that some water jet models [112] use the findings of Blanke (1981 [27]) as a modelling starting point, for consistency with the existing hydrodynamic literature.

In sum [194], the main design differences of both thrusters in this work compared to the more conventional thrusters appear to be the simultaneous occurrence of: (i) having the rotational axes of the propellers perpendicular (or almost perpendicular in case of the steering-grid) to the calm water plane, hence the propellers rotate in a plane parallel to the xy-plane, (ii) being completely nested inside the hull and thus not positioned directly in the ambient flow field, (iii) drawing in water from underneath the vessel hull, (iv) having both an inlet and an outlet positioned in the hull, not unlike jet systems, (v) having an internal deflection or rotation of the water stream from inlet to outlet, and (vi) having a 360-degrees-steerable outflow of the accelerated water provided by a steering mechanism, where the propeller itself does not change its position or orientation. Therefore, the present work aims to investigate the adequacy of the open-water propeller characteristics [27] as the kernel of the thrust modelling approach, by:

(i) Adding an internal control angle dependent thrust deduction to the conventional model [27] at zero advance speed, and investigating different propeller-speed dependencies. These constructed models can be found in Bollard Pull Thrust Models, their identification procedure in Conventional Bollard Thrust Model, and their results in Conventional Bollard Thrust Model.

(ii) Offering an additional artificial neural network modelling approach for (i), that might be useful to grip the current, and perhaps future, inherent complex flow phenomena occurring within both thrusters. These models can be found in Feedforward Multilayer Network, their identification procedure in Feedforward Multilayer Network Model, and their results in Feedforward Multilayer Network Model.

(iii) Investigating the speed-dependency of the model of Blanke (1981 [27]), building further on the bollard thrust model results of (i). These models can be found in Wake- and Angle-Dependent Thrust models, their

identification procedure in Identification Methods Decoupled Models, and their results in Results of Surge Motion Models, Results of Sway Motion Models, and Results of Yaw Motion Models.

3.2.4.1 Conventional Propeller Characteristics Thrust Model

The open-water model takes a first order linearised lift force approximation of the propeller blades to calculate their theoretical thrust force [27]. Given the fact that this lift force is a physical characteristic of the blade geometry, it is deemed suitable as a starting point to model both conventional and non-conventional actuation systems. Afterwards, this model will be expanded by adding the more complex flow phenomena that occur in the propulsion systems of the Cogge (see Section 2.4.2). The theoretical thrust force, T_{th}, depends quadratically on the shaft speed, n (for one rotational direction), and bi-linearly on n and the axial inflow speed V_A:

$$T_{th}(n, V_A) = T_{nn} n^2 + T_{n_{V_A}} n V_A. \tag{3.11}$$

It is common to introduce the non-dimensional thrust coefficient, K_T, and non-dimensional advance ratio, J, to express the ship propeller performance, by introducing:

$$K_T = \frac{T_{th}}{\rho n^2 D_p^4}, \tag{3.12}$$

$$J = \frac{V_A}{n D_p}, \tag{3.13}$$

where ρ is the water density and D_p the propeller diameter. Moreover, for the conventional open-water propeller configurations, K_T is often adequately approximated by a linear expression in J:

$$K_T = K_{T_0} + K_{T_J} J. \tag{3.14}$$

Combining (eq. 3.11), (eq. 3.12), (eq. 3.13), and (eq. 3.14) gives:

$$T_{th} = K_{T_0} \rho D_p^4 n^2 + K_{T_J} \rho D_p^3 n V_A, \tag{3.15}$$

which expresses the same information as (eq. 3.11) with:

$$T_{nn} = K_{T_0} \rho D_p^4 \quad , \quad T_{nV_A} = K_{T_J} \rho D_p^3. \tag{3.16}$$

Furthermore, V_A can be written as a fraction of the total speed of the vessel, U, by introducing the wake factor, w, which accounts for the speed reduction of the flow field at the inlet of the propeller:

$$V_A = (1 - w)U. \tag{3.17}$$

In addition, the available thrust force for the vessel, T, is a fraction of the generated T_{th} due to propeller–hull–interaction losses, accounted for by the thrust deduction number, t, which is assumed to be speed-independent:

$$T = (1 - t)T_{th}. \tag{3.18}$$

In conclusion, by accumulating (eq. 3.11), (eq. 3.17), and (eq. 3.18), T becomes:

$$T = (1 - t)\left[T_{nn}n^2 + T_{n_{V_A}}n(1 - w)U\right]. \tag{3.19}$$

Bollard Pull Thrust Models

The bollard pull test data of the thrusters of the Cogge, fetched in a towing tank and listed in Appendix B, will be used by Section 4.3 to identify the speed-independent part of (eq. 3.19). These bollard tests have zero advance speed and thus $K_T = K_{T_0}$. Hence, for the bollard thrust forces, (eq. 3.19) simplifies to:

$$T = (1 - t)T_{nn}n^2. \tag{3.20}$$

These bollard data for the steering-grid thruster and the four-channel thruster show the angle-dependency of their thrust deduction coefficients, i.e., $t = f(\alpha^i)$. Moreover, both internal and external thrust deductions can occur. The water flows over the external hull into the thruster inlet, and then through the embedded thruster — and thus internal hull — itself, resulting in:

$$t = t_i + t_e = f(\alpha^i) = t_i(\alpha^i) + t_e(\alpha^i) = t(\alpha^i), \tag{3.21}$$

where t_i and t_e respectively indicate the internal and external hull-interaction thrust deductions. Hence, (eq. 3.20) can be refined to:

$$T = [1 - t(\alpha^i)]T_{nn}n^2 = \left[1 - \left(t_i(\alpha^i) + t_e(\alpha^i)\right)\right]T_{nn}n^2. \tag{3.22}$$

In order to avoid a model structure bias in the identification results, the Bollard Thrust Model Identification will investigate the propeller speed dependency

of these theoretical thrust forces: $T_{th} = f(n) = T_m(n)$. This approach does not force T_{th} to equal $T_{nn}n^2$ when $U = 0$. Accordingly, this method can thus validate whether the originally derived quadratic propeller-speed dependent thrust model indeed provides the best bollard pull data fit. Ultimately, the thrust forces T to be identified according to the theoretic bollard pull model turn into:

$$T = [1 - t(\alpha^i)]T_m(n). \tag{3.23}$$

Wake- and Angle-Dependent Thrust models

Based on the results of the Bollard Thrust Model Identification [194], the Decoupled Hydrodynamic Motion Models uses (eq. 3.22) for the speed-independent part of the thrust forces. Thereupon, w, will be made velocity-dependent, i.e., $w = w(\boldsymbol{\nu})$, [203]. Hence, (eq. 3.19) transforms into:

$$T(n, \boldsymbol{\nu}, \alpha^i) = \left(1 - t(\alpha^i)\right) \left[T_{nn}n^2 + (1 - w(\boldsymbol{\nu}))\, T_{n\nu} n \boldsymbol{\nu}\right]. \tag{3.24}$$

Note that t and w denote thrust differences between fully open-water tests (only a propeller) and tests with a propeller attached to a hull. Therefore, the static parts of $t(\alpha^i)$ and $w(\boldsymbol{\nu})$ cannot be explicitly identified in this work, but they will be implicitly incorporated in the thrust coefficients. Nevertheless, their respective angle- and speed-dependency can be investigated.

For the Decoupled Hydrodynamic Motion Models, i.e., $\boldsymbol{\nu} = [u, 0, 0]^\top$, $[0, v, 0]^\top$, or $[0, 0, r]^\top$, three thruster angles suffice, $\alpha^i \in [-90°, 0°, 90°]$ (see Decoupled Motion Experiments). Assuming vessel and actuator symmetry around the zx-plane narrows these angles down to $\alpha^i \in [0°, 90° = -90°]$.

Furthermore, the water speed at the inlets of the propellers will be assumed to be purely longitudinal or transversal. For the rotational missions, the inlet transversal speed at the bow or stern thruster depends on their longitudinal distance $L^x_{b/s}$ from the centre of gravity ($v_{inlet} = L^x_{b/s} r$), see Figure 3.3.

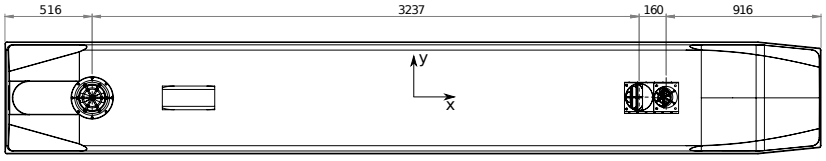

Figure 3.3: Longitudinal position of the thrusters.

In addition, given the axisymmetric water inlet at the bottom of the ship hull and the position of the propeller shaft which stands orthogonal to the calm

water plane, it will be further assumed that the differences in wake effects for a longitudinal or transversal inlet flow will be negligible. This assumption means, $w(\boldsymbol{\nu})$ can be modelled by a single term, $w(\boldsymbol{\nu}) = w_\nu \boldsymbol{\nu}$, where $\boldsymbol{\nu}$ will be assumed to be either pure u or v. Moreover, their magnitudes, $|u|$ and $|v|$ will determine their impact. Combining these assumptions allows for a further simplification of the thruster models:

$$\begin{aligned} T(0°) = T(n, \boldsymbol{\nu} = u, \alpha^i = 0°) &= (1 - t(0°)) \left[T_{nn} n^2 + (1 - w_\nu) T_{n\boldsymbol{\nu}} n u \right] \\ &= T^0_{nn} n^2 + T^0_{n\nu} n |u|, \end{aligned} \tag{3.25}$$

$$\begin{aligned} T(90°) = -T(-90°) &= T(n, \boldsymbol{\nu} = v, \alpha^i = 90°) \\ &= (1 - t(90°)) \left[T_{nn} n^2 + (1 - w_\nu) T_{n\boldsymbol{\nu}} n v \right] \\ &= T^{90}_{nn} n^2 + T^{90}_{n\nu} n |v|. \end{aligned} \tag{3.26}$$

The thruster model of (eq. 3.25) and (eq. 3.26) will be coined the conventional thrust model in the Decoupled Hydrodynamic Motion Models section. In addition, the Decoupled Hydrodynamic Motion Models will explore two other thruster models: (eq. 3.27) the pure bollard thrust model and (eq. 3.28) the direct speed loss thrust model, in order to offer more insights into the potential speed dependency of the thrust forces:

$$T(0°) = T^0_{nn} n^2, \quad T(90°) = T^{90}_{nn} n^2, \tag{3.27}$$

$$T(0°) = T^0_{nn} n^2 + T^0_{nn\nu} n^2 |u|, \quad T(90°) = T^{90}_{nn} n^2 + T^{90}_{nn\nu} n^2 |v|. \tag{3.28}$$

3.2.4.2 Feedforward Multilayer Network Thrust Model

This section describes the architecture of feedforward multilayer neural networks that offer an alternative modelling approach to describe the complex flow phenomena of the thrusters. In general, artificial neural networks have one input layer, a number of hidden layers, and one output layer. However, a multilayer feedforward network with a non-polynomial activation function and only one hidden layer can already serve as a universal approximation for any nonlinear function [140]. This statement means that, regardless of the complexity of the flow phenomena that occur in the actuation system, there will always exist network structures that can approximate the data sets. The capacity of

these neural networks to model nonlinear characteristics drove the decision to add this alternative modelling approach.

In order to describe the general layout of a multilayer feedforward network, imagine the following example. If one takes an input vector, $x \in \mathbb{R}^m$, and an output vector, $y \in \mathbb{R}^l$, separated by one hidden layer with n_h hidden neurons, and connects the hidden layer to y via $W \in \mathbb{R}^{l \times n_h}$ and to x via $V \in \mathbb{R}^{n_h \times m}$ with the addition of a bias vector, $\beta \in \mathbb{R}^{n_h}$, to the latter and an enveloping activation function, $\sigma(\cdot)$, the following matrix–vector expression will describe this model structure:

$$y = W\sigma(Vx + \beta), \tag{3.29}$$

which can also be expressed in an element-wise form, for i = 1, ..., l, according to:

$$y_i = \sum_{r=1}^{n_h} w_{ir}\sigma\left(\sum_{j=1}^{m} v_{rj}x_j + \beta_r\right). \tag{3.30}$$

Figure 3.4 illustrates such a network hierarchy with the following model structure: two inputs (m = 2), one hidden layer of three neurons ($n_h = 3$) of which the bias terms are not explicitly shown, two outputs (l = 2), and interconnection weights w_{ij}, v_{ij}.

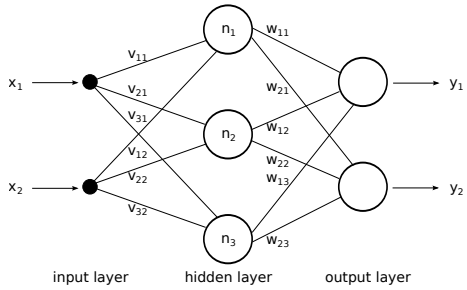

Figure 3.4: Multilayer feedforward network with one hidden layer.

Be noted that these descriptions, (eq. 3.29) and (eq. 3.30), implicitly use a linear activation function for the output layer, although this need not be the case. Furthermore, the $\sigma(\cdot)$ can have any shape, but typically a nonlinear function (e.g. a sigmoid, tangent, or hyperbolic tangent) is used in order to exploit their characteristics. Moreover, similarly to (eq. 3.29), a second hidden layer could be inserted, resulting in:

$$y = W\sigma_2\Big(V_2\sigma_1(V_1x + \beta_1) + \beta_2\Big), \tag{3.31}$$

with n_{h_1} and n_{h_2} neurons in the hidden layers, connection-weight matrices, $W \in \mathbb{R}^{l \times n_{h_2}}$, $V_2 \in \mathbb{R}^{n_{h_2} \times n_{h_1}}$, $V_1 \in \mathbb{R}^{n_{h_1} \times m}$, bias vectors, $\beta_2 \in \mathbb{R}^{n_{h_2}}$, $\beta_1 \in \mathbb{R}^{n_{h_1}}$, and activation functions, $\sigma_1(\cdot)$ and $\sigma_2(\cdot)$.

This hidden-layer insertion can be repeated to add multiple layers in an equivalent manner. The amount of hidden layers, their number of neurons, and the activation function types can all be chosen by the user. These design aspects offer great flexibility on the one hand, but an infinite amount of possible network architectures on the other hand. Accordingly, a few network designs will be shown in Section 4.3, which offers the possibility to compare their performance. These developed multilayer feedforward networks were trained to generate an output vector y (based on their input vector x), which aims to represent the desired output vector, i.e., the measured towing-tank data sets. More details of this network training procedure can be found in Section 4.3.1.2.

3.2.5 Selected Decoupled Hydrodynamic Motion Models

Table 3.1 lists the selected combinations of the aforementioned model structures for the damping and thruster forces. The resultant model structures, $\mathcal{M}(\boldsymbol{\theta_d^x})$, are named by the vector of their unknown parameters, $\boldsymbol{\theta_d^x}$, for each degree of freedom, $d \in [u, v, r]$, and a combination of thruster and damping models, $x \in [a, b, c, d, e, f, g, h, i]$. In order to fully crystallise this convention, (eq. 3.32) expresses the full model of $\mathcal{M}(\boldsymbol{\theta_u^a})$, (eq. 3.33) of $\mathcal{M}(\boldsymbol{\theta_v^e})$, and (eq. 3.34) of $\mathcal{M}(\boldsymbol{\theta_r^i})$, for a forward surge, starboard sway, and clockwise yaw motion, where the sub and superscripts "b" and "s" for the thruster parameters denote the bow (see Section 2.4.2.1) and stern (see Section 2.4.2.2) thruster respectively.

The models of Table 3.1 intend to capture pure surge, sway, or yaw motion (see Modelling Assumptions and Experimental Design) and do not envisage to describe a manoeuvring model for the vessel experiencing coupled motions. For a coupled model, the Coriolis-centripetal forces from both the rigid-body mass and added mass matrices should be added, and the assumption of the position of the centre of gravity should be validated. Furthermore, the off-diagonal matrix terms for the mass, added mass, and damping forces should be investigated too, and the wake fraction and thrust deduction fraction might need further refinement.

Table 3.1: The selected decoupled motion model structures of this study.

Model	Added Mass	Damping	Propulsion
$\mathcal{M}(\boldsymbol{\theta_u^a})$, $\mathcal{M}(\boldsymbol{\theta_v^a})$, $\mathcal{M}(\boldsymbol{\theta_r^a})$	Constant, see (eq. 3.5)–(eq. 3.7)	Cubic, see (eq. 3.8)	Conventional Thrust, see (eq. 3.25)
$\mathcal{M}(\boldsymbol{\theta_u^b})$, $\mathcal{M}(\boldsymbol{\theta_v^b})$, $\mathcal{M}(\boldsymbol{\theta_r^b})$	Constant, see (eq. 3.5)–(eq. 3.7)	Quadratic, see (eq. 3.9)	Conventional Thrust, see (eq. 3.26)
$\mathcal{M}(\boldsymbol{\theta_u^c})$, $\mathcal{M}(\boldsymbol{\theta_v^c})$, $\mathcal{M}(\boldsymbol{\theta_r^c})$	Constant, see (eq. 3.5)–(eq. 3.7)	Linear, see (eq. 3.10)	Conventional Thrust, see (eq. 3.26)
$\mathcal{M}(\boldsymbol{\theta_u^d})$, $\mathcal{M}(\boldsymbol{\theta_v^d})$, $\mathcal{M}(\boldsymbol{\theta_r^d})$	Constant, see (eq. 3.5)–(eq. 3.7)	Cubic, see (eq. 3.8)	Bollard Thrust, see (eq. 3.27)
$\mathcal{M}(\boldsymbol{\theta_u^e})$, $\mathcal{M}(\boldsymbol{\theta_v^e})$, $\mathcal{M}(\boldsymbol{\theta_r^e})$	Constant, see (eq. 3.5)–(eq. 3.7)	Quadratic, see (eq. 3.9)	Bollard Thrust, see (eq. 3.27)
$\mathcal{M}(\boldsymbol{\theta_u^f})$, $\mathcal{M}(\boldsymbol{\theta_v^f})$, $\mathcal{M}(\boldsymbol{\theta_r^f})$	Constant, see (eq. 3.5)–(eq. 3.7)	Linear, see (eq. 3.10)	Bollard Thrust, see (eq. 3.27)
$\mathcal{M}(\boldsymbol{\theta_u^g})$, $\mathcal{M}(\boldsymbol{\theta_v^g})$, $\mathcal{M}(\boldsymbol{\theta_r^g})$	Constant, see (eq. 3.5)–(eq. 3.7)	Cubic, see (eq. 3.8)	Direct Speed Loss, see (eq. 3.28)
$\mathcal{M}(\boldsymbol{\theta_u^h})$, $\mathcal{M}(\boldsymbol{\theta_v^h})$, $\mathcal{M}(\boldsymbol{\theta_r^h})$	Constant, see (eq. 3.5)–(eq. 3.7)	Quadratic, see (eq. 3.9)	Direct Speed Loss, see (eq. 3.28)
$\mathcal{M}(\boldsymbol{\theta_u^i})$, $\mathcal{M}(\boldsymbol{\theta_v^i})$, $\mathcal{M}(\boldsymbol{\theta_r^i})$	Constant, see (eq. 3.5)–(eq. 3.7)	Linear, see (eq. 3.10)	Direct Speed Loss, see (eq. 3.28)

$$\mathcal{M}(\boldsymbol{\theta_u^a}) = (M + X_{\dot{u}})\dot{u} + (X_{uuu}|u|^2 + X_{uu}|u| + X_u)u = T_{nn}^{0,b} n_b^2 + T_{n\nu}^{0,b} n_b|u| + T_{nn}^{0,s} n_s^2 + T_{n\nu}^{0,s} n_s|u| \tag{3.32}$$

$$\mathcal{M}(\boldsymbol{\theta_v^e}) = (M + Y_{\dot{v}})\dot{v} + (Y_{vv}|v| + Y_v)v = T_{nn}^{90,b} n_b^2 + T_{nn}^{90,s} n_s^2 \tag{3.33}$$

$$\mathcal{M}(\boldsymbol{\theta_r^i}) = (I_z + N_{\dot{r}})\dot{r} + N_r r = L_b^x (T_{nn}^{90,b} n_b^2 + T_{nn\nu}^{90,b} n_b^2 |L_b^x r|) + L_s^x (T_{nn}^{-90,s} n_s^2 + T_{nn\nu}^{-90,s} n_s^2 |L_s^x r|) \tag{3.34}$$

3.3 Transfer Function Steering Models

This section exemplifies the transfer function modelling for a USV. More details of this approach can be found in Peeters et al. (2018 [195]).

3.3.1 The WAM-V Test platform

Figure 3.5 depicts the concept of a differentially steered Wave Adaptive Modular Vessel (WAM-V) [162], similar to the one used throughout this section.

Figure 3.5: Exemplary Wave Adaptive Modular Vessel (WAM-V) [162].

Table 3.2 lists the specifications of the WAM-V used throughout this section [195]. The rear of this vessel, approximately one fifth its length, is able to hinge, guaranteeing the inflow of water for the propellers. The sensor platform has a spring-damped mounting on both the cylindrical hulls. In total this generates high flexibility, making the vessel wave adaptive. A Hemisphere Vector v102 GPS Compass series measured the heading at 5 Hz, with a 0.75° accuracy.

Table 3.2: WAM-V specifications

Parameter	Size	Dimension
Length	4.88	m
Beam	2.44	m
Hull diameter	0.40	m
Weight	270	kg
Max payload	80	kg
Cruise speed u_0	1.4	$\frac{m}{s}$
Max. propulsive power	2×2.24	kW
Propeller diameter	0.25	m

The WAM-V has no physical rudder to steer the vessel. Instead, two outboard propellers (Torqueedo Cruise 4.0) at the stern enable the differential steering

of the vessel. Accordingly, a virtual rudder angle can be constructed. By giving each propeller a different amount of thrust, i.e., $T_{left} \neq T_{right}$, a turning moment N arises:

$$N = b \times (T_{right} - T_{left}) = b \times \triangle T, \tag{3.35}$$

where b denotes the lateral distance between both propellers. The thrust of each propeller can be expressed in percentages and bounded by [-100%, 100%]. These bounds represent the maximum backward and forward propeller speeds, given that the propeller shafts can turn in two directions. To induce a differentially steered rudder of 20%, each propeller either gets half of the rudder, i.e., 10% added to or subtracted from its thrust, depending on the desired turning direction. This generates a turning movement similar to a traditional rudder. A traditional rudder would also explicitly generate a lateral force, as the water is deflected on the rudder. This is not the case with a differentially trusted vessels as both thrust forces are parallel to the longitudinal axis of the body-fixed reference frame. Nevertheless, the effect of propeller walk will generate lateral forces and a subsequent turning moment.

When a right-handed propeller turns clock-wise to generate a forward thrust, an additional lateral force arises, named propeller walk [209] (drawn as W in Figure 3.6a). The WAM-V has two right-handed propellers placed at a longitudinal distance d from the centre of gravity of the vessel, shown in Figure 3.6. Hence, together the propellers generate an additional turning moment $N_W = 2 \times (W \times d)$.

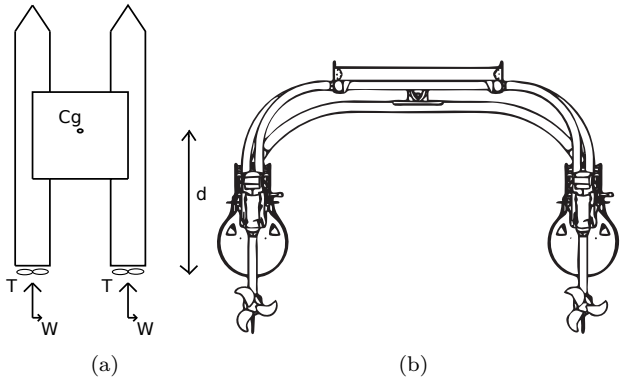

Figure 3.6: Geometry of the WAM-V: (a) concept of the lateral thrust forces, and (b) back view of the vessel.

3.3.2 Transfer Function Modelling of Steering Behaviour

The steering hydrodynamics of a vessel can be modelled by several (linear and nonlinear) first and second order transfer functions [266]. The first and second order models of Nomoto [183] relate the rudder input, δ, to the yaw-rate output, r. The second order transfer function (eq. 3.36) has three time constants T_1, T_2, and T_3, and one gain constant K. Additionally, one can also express a similar transfer function between rudder angle and sway speed, where two constants will be different: $K = K_v$ and $T_3 = T_v$. The first order Nomoto model [183] often adequately replaces this second order model [267]. Accordingly, (eq. 3.36) can be simplified to (eq. 3.37) where $T = T_1 + T_2 - T_3$, which is an adequate assumption because in practice the zero $(1 + T_3 s)$ and pole $(1 + T_2 s)$ tend to cancel each other [267]. Note that the second order Nomoto model can be related to the hydrodynamic coefficients of the vectorial model (discussed in Decoupled Hydrodynamic Models for a USV), by decoupling the sway and yaw steering subsystem from the surge motion at a cruising surge speed [67, 170].

$$\frac{r}{\delta}(s) = \frac{K(1 + T_3 s)}{(1 + T_1 s)(1 + T_2 s)} \tag{3.36}$$

$$\frac{r}{\delta}(s) = \frac{K}{1 + Ts} \tag{3.37}$$

3.4 Computational Fluid Dynamics

Inland and seagoing vessels have different hull geometries. The research field on the latter has well-known dedicated benchmark hulls and their respective towing tank data [237] (e.g. the KVLCC2 hull), to numerically study manoeuvres such as zigzag tests [42] or turning circles [31, 234], in shallow water [257, 262] and when encountering waves [98, 99]. However, little research has been conducted on the identification of inland vessels [145, 146, 225]. Therefore, this work investigates the surge damping for the Cogge in deep [197] and shallow [66] water. The KVLCC2 hull will serve as the validation hull for the numerical Methodology of this work for two main reasons. First, the KVLCC2 has publicly available experimental data [237]. Second, within the publicly available datasets, the KVLCC2 hulls seem to show some of the highest similarities with the CEMT–I hulls. This section continues as follows: first, the Methodology section will detail the numerical approach used for the deep water study. Secondly, the Geometry and Grid Specifications section illustrates the implemented computational grids for this deep water case. More details

on the computational domains can be found in Peeters et al. (2018 [197]) and Eggers et al. (2019 [66]) for the deep and shallow water cases respectively. The results of both can be found in Section 4.4.

3.4.1 Methodology

The second order surge model (see (eq. 3.9)), will model the damping forces:

$$D(u) = X_u u + X_{uu} u^2. \tag{3.38}$$

The OpenFOAM open source toolbox [285] computed $D(u)$ by numerically solving the incompressible, isothermal Reynolds-averaged Navier-Stokes equations. A two equation k-ω shear stress transport turbulence model [138] modelled the Reynolds stress tensor. A volume of fluid approach [109] modelled the free surface, i.e., the water plane. This approach defines a scalar function α which describes the two fluids, i.e., air and water. This scalar function indicates the proportion of the water phase at a certain place within the computational domain. A value of $\alpha = 1$ stands for a cell which is completely submerged in the water phase, whereas $\alpha = 0$ denotes a cell in the air phase. At the interface between both fluids, the cells have a value of $0 < \alpha < 1$. The physical properties of each cell volume can then be calculated by the weighted average of both fluids depending on their volumetric proportion. The calculations started with a local time stepping solver and ended with a transient solver. The former solver used the local Euler scheme for the time discretisation, whereas the latter used the Crank-Nicolson scheme with a coefficient of 0.9. Furthermore, the gradient and divergence schemes were respectively set to a least-squares and a linear-upwind scheme [188].

3.4.2 Geometry and Grid Specifications

Table 3.3 summaries the main characteristics of the real size KVLCC2 vessel together with its scale-model benchmark hull used throughout the deep water calculations. The characteristics of the CEMT–I inland vessel are also listed in this table, together with the specifications of its scale model used in this study. Figure 3.7 visualises their geometrical differences. Figure 3.8 shows an abstract representation of the computational domain, together with its boundary conditions. The three boxes in this figure represent boxes of grid refinement, where the outer box has the coarsest grid, the box closest to the hull the finest, and the box in between both has an intermediate grid refinement. Note that an additional refinement box around the water level is not shown for readability

reasons. However, this refinement box was present in the real computational domain, as it is necessary for the performance of the volume of fluid approach.

Table 3.3: Vessel geometry CEMT–I and KVLCC2 comparison for deep water

	CEMT–I		**KVLCC2**	
	full size	Scale model	full size	scale model
Length, L [m]	38.50	4.813	320.00	6.892
Beam, B [m]	5.05	0.63	58.00	1.249
Draft, T [m]	1.80	0.23	20.80	0.448
Block coefficient, C_b [-]	0.95	0.95	0.81	0.81
Scale, λ [-]	1	8^{-1}	1	46.426^{-1}

(a) KVLCC2 hull side view (with surface grid)

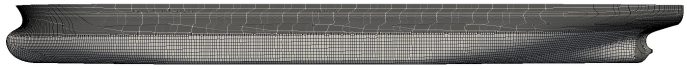

(b) KVLCC2 hull bottom view (with surface grid)

(c) CEMT–I hull side view

(d) CEMT–I hull bottom view

Figure 3.7: Geometry KVLCC2 and CEMT–I for deep water.

Furthermore, as visible in Figure 3.8, the computational domain models only half a ship hull, under the assumption of longitudinal symmetry. The bisected hulls were placed at one ship length from the inlet. The KVLCC2 hull had two ship lengths of fluids behind it and the CEMT I hull had three lengths, due to its longer wake pattern. Underneath the halved hulls, there was an equivalent of five ship heights (not drafts) of computational domain for both vessels, and next to the vessel there existed an equivalent space of four and a halve complete (not halved) ship beams for both hulls.

Within the deep-water study, all surface and volumetric grids were modelled by an unstructured, hybrid mesh. Figure 3.9 illustrates the unstructured surface and volumetric grids for both scale-model vessels. This unstructured approach was chosen to facilitate the grid generating close to the irregular appendices

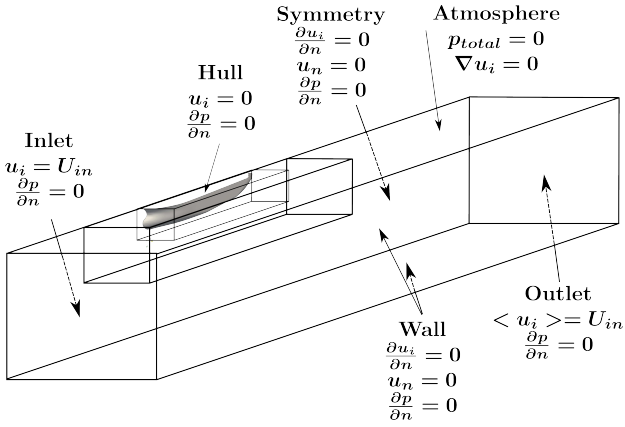

Figure 3.8: Computational domain and boundary settings for the KVLCC2 hull, with u_i the cell velocity components, U_{in} the water inlet velocity, and p the pressure.

of the CEMT–I hull, and to enable the ability to ease the future extension of additional appendices in further research. Nevertheless, hexahedra cells were clustered more structurally at the boundary layer of the hull and at the free surface. This clustering was done to increase the free-surface flow alignment and to resolve the boundary layer.

Figure 3.9a shows part of the quadrilaterally dominant surface grid at the stern of the KVLCC2 vessel in grey (where the hull is depicted in 3D). Additionally, a longitudinal, two dimensional, cut of all the different volumetric grids at the middle of the vessel is shown with a colour legend. The more structured refinement approach with hexahedra cells (in blue) can be seen at the water surface and close to the hull. Figure 3.9b depicts two orthogonal slices of the volumetric grid surrounding the CEMT–I scale model: one in longitudinal direction in blue, and one in transversal direction in grey. The longitudinal cut is approximately at the middle of the vessel, i.e longitudinal symmetry plane. The transversal cut slices the vessel right after the bow of the vessel. Both cuts show the sliced cells in a three dimensional representation.

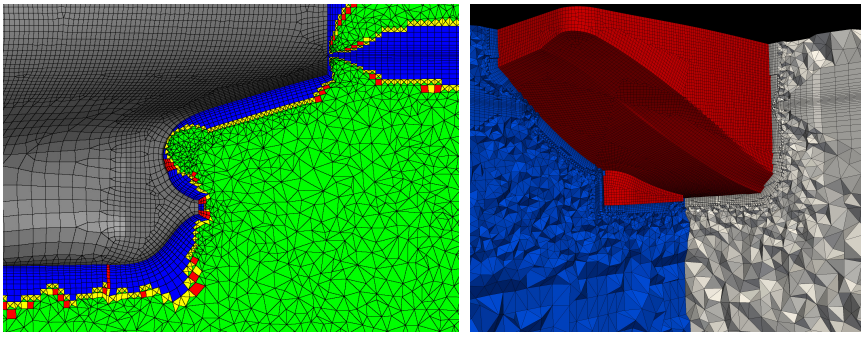

(a) KVLCC2 hull; grey: surface grid, green: tetrahedra, blue: hexahedra, yellow: pyramids, red: triangular prisms.

(b) CEMT–I hull; red: surface hull, blue: longitudinal cut, grey: transversal cut.

Figure 3.9: Grid specifications KVLCC2 and CEMT–I for deep water [195].

3.5 Conclusion

Four modelling approaches (***RO2.1***) have been detailed for inland cargo vessels (i)–(iv):

The decoupled planar motions for the Cogge were modelled via (i) a vectorial model. This model offers physical insights in the occurring hydrodynamics. Given the modularity of this model, (ii) a neural network was suggested and constructed to capture the non-conventional thruster forces of (i). The steering dynamics of a vessel were also modelled by (iii) a transfer function between yaw-rate outputs and rudder inputs. Finally, one can also model (iv) the ambient water via CFD, which enables the capturing of virtual motion data that can be used to identify hydrodynamic models.

These four modelling approaches partly answer **RQ2**. The second part of the answer, their identification (***RO2.2***), can be found in Chapter 4.

Identification of Unmanned Inland Cargo Vessels

> "Thou hypocrite, first cast out the beam out of thine own eye; and then shalt thou see clearly to cast out the mote out of thy brother's eye [163]."
>
> Matthew

Figure 4.1: A relief of the Egyptian god Horus [219].

This chapter investigates the second research question (**RQ2**), by identifying (***RO*2.2**) the hydrodynamic models of an inland cargo vessel. The derivation of these models (***RO*2.1**) can be found in Chapter 3. Parts of the present chapter were previously published as:

[203] G. Peeters, S. Van Baelen, G. Yayla, T. Catoor, M. R. Afzal, C. Christofakis, R. Louw, Y. Singh, M. Vanierschot, R. Boonen and P. Slaets. "Decoupled Hydrodynamic Models and Their Outdoor Identification for an Unmanned Inland Cargo Vessel with Embedded Fully Rotatable Thrusters". In: *Journal of Marine Science and Engineering* 8.889 (2020). DOI: 10.3390/jmse8110889

[194] G. Peeters, M. R. Afzal, M. Vanierschot, R. Boonen and P. Slaets. "Model Structures and Identification for Fully Embedded Thrusters: 360-Degrees-Steerable Steering-Grid and Four-Channel Thrusters". In: *Journal of Marine Science and Engineering* 8.220 (2020). DOI: 10.3390/jmse8030220

[205] G. Peeters, G. Yayla, M. R. Afzal, S. Van Baelen, T. Catoor, M. Vanierschot, R. Boonen and P. Slaets. "Additional Test Manoeuvres for Autonomous Inland Vessels". In: *Proc. of ICMASS 2020*. 2020. DOI: 10.1088/1757-899X/929/1/012024

[197] G. Peeters, A. Eggers, R. Boonen, P. Slaets and M. Vanierschot. "Surge Resistance Identification of Inland Vessels by CFD". in: *OCEANS 2018*. Kobe: IEEE, 2018. DOI: 10.1109/OCEANSKOBE.2018.8559048

[195] G. Peeters, R. Boonen, M. Vanierschot, M. DeFilippo, P. Robinette and P. Slaets. "Asymmetric Steering Hydrodynamics Identification of a Differential Drive Unmanned Surface Vessel." In: *IFAC*. vol. 51. 29. Elsevier, 2018, pp. 207–212. DOI: 10.1016/j.ifacol.2018.09.494

[66] A. Eggers, G. Peeters, P. Slaets and M. Vanierschot. "Shallow water surge resistance identification for inland vessels". In: *5th MASHCON Proceedings*. 2019. URL: http://hdl.handle.net/1854/LU-8624686

4.1 Introduction

This chapter identifies the model structures derived by Chapter 3. In order to identify these models, both experimental data and cost functions are needed. The latter minimise the distance between the model predictions and the experimental data. Table 4.1 summarises where these cost functions and their results are discussed, which models they identify, and how the experimental data was generated. Accordingly, Section 4.2 starts with identifying the asymmetric steering behaviour of the WAM-V deployed as an USV, by using the transfer function models of Section 3.3.

Section 4.3.2.1 and 4.3.2.2 identify the thrust forces of the steering-grid and four-channel thruster of the Cogge. Their bollard pull data were measured inside a towing tank. Section 4.3.2.1 expands the conventional open-water propeller characteristics model with angle-dependent thrust deductions and investigates its propeller-speed dependency, whereas Section 4.3.2.2 investigates the feasibility to model these thrust forces using artificial neural networks.

Section 4.4 utilises CFD to model the surge behaviour of the Cogge in both deep and shallow water. Subsequently, this section identified the surge resistance in these two environments. Finally, Section 4.5 discusses additional test manoeuvres that generated the experimental data for the identification of the decoupled hydrodynamic models in surge, sway, and yaw, discussed in Section 4.6. The latter section also compares its results with the CFD results from Section 4.4.

Table 4.1: Summary of the identified model structures within this chapter.

Discussed in	Identified Model Structure	Data Generation and Vessel
Section 4.2	Transfer function (see Section 3.3)	Outdoor, WAM-V
Section 4.3.2.1	Conventional thruster (see Section 3.2.4.1)	Indoor, actuator Cogge
Section 4.3.2.2	Neural network (see Section 3.2.4.2)	Indoor, actuator Cogge
Section 4.4	Surge damping (see Section 3.4)	Numerical, Cogge
Section 4.5	Additional test manoeuvres (for Section 4.6)	Outdoor, Cogge
Section 4.6	Modular model (see Section 3.2)	Outdoor, Cogge

4.2 Transfer Functions WAM-V

To demonstrate the asymmetric steering characteristics of the WAM-V, three Nomoto first order functions were identified, for: (i) turning left (port), (ii) turning right (starboard), and (iii) the average of turning left and right. First, Section 4.2.1 will summarise the zigzag identification methodology [195] for these transfer functions. Second, Section 4.2.2 will show and discuss their results.

4.2.1 Methodology

In total, three fully-autonomous zigzag tests of each five zigzags were conducted on the Charles river in Boston. Accordingly, for each zigzag test, the WAM-V sped up using 50% of the maximal thrust, meaning $T_{left} = T_{right} = 50\%$. After 10 seconds (ensuring a steady speed regime) the vessels started its configured number of 5 zigzags with virtual rudder changes oscillating between 20% to -20%. These alternating rudder changes resulted in thrust combinations of $T_{left} = 40\%$ and $T_{right} = 60\%$, to turn left, and the other way around to turn right. A completion threshold of 1.00° was programmed equally divided around the desired heading change which triggered a new rudder movement. The first heading change due to a rudder movement δ of every zigzag test has the biggest transient behaviour, as the total speed of the vessels needs to settle. Consequentially the first rudder movement and its heading response are ignored during the identification procedures. The vessel surge speed varied between 1.2 to 1.3 $\frac{\text{m}}{\text{s}}$ [195] during the experiments.

The Nomoto models relate yaw-rate outputs to the rudder inputs. Given that only the heading was measured, their time derivation was needed. Evidently, this need not be the case when a gyroscope would be used. The derived yaw-rates were compared to the first order model in the time domain (eq. 4.1), where $r(k)$ expresses these yaw-rates in the time domain at the measurement time step k. The Nomoto coefficients, T, and K, can be found by minimizing the error between the predicted yaw-rates, i.e., (eq. 4.1), and their measured counterparts [195].

$$r(k) = \underbrace{r_0.e^{-t(k)/T}}_{transient} + \underbrace{K.\delta_r.(1 - e^{-t(k)/T})}_{step} \tag{4.1}$$

4.2.2 Results

Table 4.2 summarises Nomoto coefficients, i.e., time constants T $[s]$ and gains K $[s^{-1}]$, for each zigzag test. To identify the overarching symmetrical behaviour, the average Nomoto gains and time constants were first calculated for each zigzag test separately. Afterwards, the total average of these separate averages was taken, in order to identify the global symmetric Nomoto model, resulting in $T = 1.27$ s, and $K = 0.12$ s^{-1}. Note that this is not simply the average of the left and right turning coefficients as the average uses the consecutive turns as identification data instead of each turn separately.

To show the strength of the asymmetric model, Figure 4.2a illustrates the measured and predicted heading of the third mission for the symmetric Nomoto

model, whereas Figure 4.2b provides a similar plot for the asymmetrical Nomoto model for this mission. These two figures show that the asymmetrical model better captures the vessel behaviour. To further clarify the effect of the two modelling approaches, Figure 4.3a compares their resultant heading predictions, and Figure 4.3b shows their predicted yaw-rates.

Table 4.2: Summary asymmetric Nomoto coefficients

	zigzag1		**zigzag2**		**zigzag3**		**combined**
	left	right	left	right	left	right	symmetry
T	1.36	1.32	1.30	1.45	1.40	1.19	1.27
K	0.13	0.11	0.16	0.11	0.16	0.11	0.12

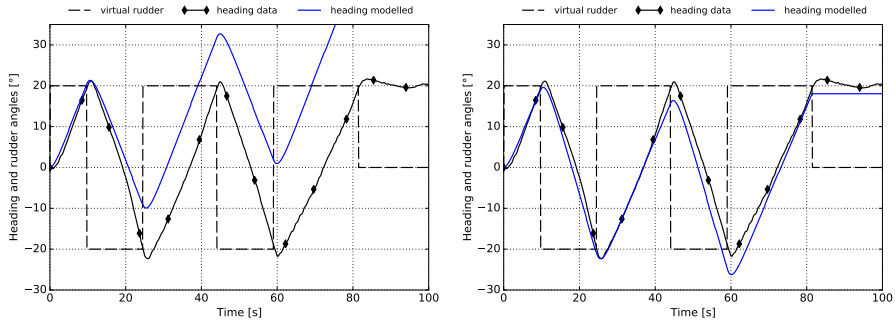

(a) (b)

Figure 4.2: Comparison between simulated heading and measured heading for the third mission: (a) symmetrical Nomoto model, and (b) asymmetrical Nomoto model.

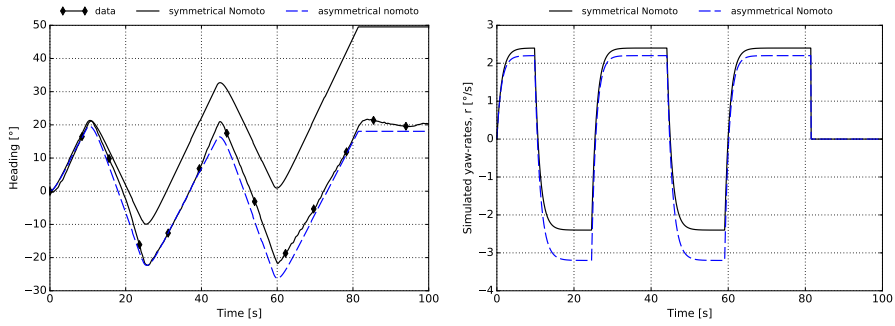

(a) (b)

Figure 4.3: Comparison between the symmetrical and asymmetrical Nomoto modes for mission 3: (a) heading prediction, (b) yaw-rate prediction.

4.3 Bollard Thrust Model Identification

4.3.1 Identification Procedures Bollard Thrust Models

The theoretically derived bollard thrust model, e.g., (eq. 3.23) of the Bollard Pull Thrust Models and the neural networks, e.g., (eq. 3.31) of the Feedforward Multilayer Network provide α^i-dependent and n-dependent model structures for the bollard thrust forces, $T(n, \alpha^i)$, to which their respective experimental data sets, $D(n, \alpha^i)$, see Appendix B, can be fitted. This data fitting can be achieved by minimizing a cost function which calculates the least squares error between the model and the data. Accordingly, (eq. 4.2) exemplifies such a generic cost function between $T(n, \alpha^i)$ and $D(n, \alpha^i)$, for P data points. The Conventional Bollard Thrust Model and Feedforward Multilayer Network Model sections detail the procedures to minimize (eq. 4.2), and thus maximize the model fit, for their model structures. The maximal model complexities were iteratively determined based on their impact on the final residuals.

$$E = \sum_{p=1}^{P} \left(T(n_p, \alpha_p^i) - D(n_p, \alpha_p^i) \right)^2 \tag{4.2}$$

4.3.1.1 Identification Procedure Conventional Bollard Thrust Models

The introduction of (eq. 3.23) into (eq. 4.2) produces the generic cost function for the model structures of the conventional Bollard Pull Thrust Models:

$$E = \sum_{p=1}^{P} \left([1 - t(\alpha_p^i)] T_m(n_p) - D(n_p, \alpha_p^i) \right)^2 . \tag{4.3}$$

Within this study, the maximum polynomial orders for $t(\alpha^i)$ and $T_m(n)$ were respectively chosen to be quintic and cubic; hence, in this situation, E would equal:

$$\begin{aligned} E = \sum_{p=1}^{P} \Big(& \left[1 - (t_5 \alpha_p^{i^5} + t_4 \alpha_p^{i^4} + t_3 \alpha_p^{i^3} + t_2 \alpha_p^{i^2} + t_1 \alpha_p^i + t_0) \right] (T_{nnn} n_p^3 \\ & + T_{nn} n_p^2 + T_n n_p) - D(n_p, \alpha_p^i) \Big)^2 . \end{aligned} \tag{4.4}$$

A Python (version 3.6) script performed the minimization of (eq. 4.4) by using the least_squares() function from the open source SciPy packages [276]. This function determined its step size of the optimization problem, i.e., changing the values of the coefficients of $t(\alpha^i)$ and $T_m(n)$ in order to minimize (eq. 4.4), using a trust region reflective method, based on the algorithm from Branch et al. (1999 [34]).

4.3.1.2 Identification Procedure Feedforward Multilayer Network Models

The term *feedforward* refers to the calculation of y based on x, as these data run through the network of Figure 3.4 from left to right. Afterwards, the cost function (eq. 4.5) can be determined by the insertion of y from, for example (eq. 3.29) or (eq. 3.31), into (eq. 4.2):

$$E = \sum_{p=1}^{P} \left(y_p - D(n_p, \alpha_p^i)\right)^2, \tag{4.5}$$

where y_p represents the network output of the p–th data point, which would be generated by the p–th input point, x_p. Within this study, the deepest developed network structure embodied two hidden layers. Subsequently, its cost function can be defined by:

$$E = \sum_{p=1}^{P} \Big(W\sigma_2\big(V_2\sigma_1(V_1 x_p + \beta_1) + \beta_2\big) - D(n_p, \alpha_p^i)\Big)^2. \tag{4.6}$$

Note that the p inputs for this network, x_p, are the same inputs as for the data points $D(n_p, \alpha_p^i)$; hence, (eq. 4.7) refines to:

$$E = \sum_{p=1}^{P} \left(W\sigma_2\Big(V_2\sigma_1\big(V_1(n_p, \alpha_p^i) + \beta_1\big) + \beta_2\Big) - D(n_p, \alpha_p^i)\right)^2. \tag{4.7}$$

Analogously to the Conventional Bollard Thrust Model, these cost functions (e.g. (eq. 4.7)) need to be minimized. A common way to alter the distance between the data and the network is to use the back-propagation method as first suggested by Rumelhart et al. (1986 [227]). This method derives an analytical expression of the gradient of the cost function for each neuron in the network by means of an iterative calculation from the right to the left in Figure 3.4 (hence the name back-propagation), and uses this gradient to update the weights. Furthermore, one can augment this method by using the

Levenberg–Marquardt algorithm to determine the updates of the connection weights [101]. This augmented back-propagation method was used in this study. Finally, in order to construct a network that generalises well to new inputs, one should avoid the over-fitting of data. Several regularisation methods exist to achieve this generalisation of the network. This work used two regularisation methods: the early-stopping approach [294], and the Bayesian regularisation procedure [150, 151].

The early-stopping regulation divides x into a training, x^t, and a validation, x^v, set. Afterwards, it trains the network with the training data and tests the updated network with the validation data. When the error on the validation set, $E(x^v)$, starts to rise, although the error of the training data, $E(x^t)$, is still decreasing, the iterative algorithm stops. Whereas, like the name suggests, Bayesian regulation uses the principles of the Bayesian probability theory as its regularisation principle. This regularisation is achieved by adding a term that penalises the size of weights, e.g., for a total of j weights w:

$$E_w = \sum_j w_j^2, \tag{4.8}$$

to the cost function (eq. 4.7). In addition, within this approach, the Bayesian probability theory automatically embeds *Ocam's razor* principle by punishing too flexible and too complex module structures based on the *Bayesian evidence* principle [151]. Hence, this approach offers an automatic regularisation method, which boosts the generalisation of the trained networks. A collection of Matlab scripts constructed all the networks within this study. Consequently, the two aforementioned regularisation methods were applied by respectively calling the 'trainlm' [101], and 'trainbr' [86] function calls within the Matlab neural network environment. For the former, a data division of 70% training and 30% validation data was used. Note that this data separation is not necessary for the latter, given its automatic regularisation approach.

4.3.2 Results Bollard Thrust Models

4.3.2.1 Conventional Bollard Thrust Model Identification

Plugging the data sets from Appendix B into the cost function of (eq. 4.4) allows for the identification of the modelled thrust forces according to (eq. 3.23). By varying the order of the polynomials of $t(\alpha^i)$ and $T_m(n)$ up to their respective maximums of quintic and cubic, one can compare the resulting model complexities based on the residuals of their cost functions. This comparison offers a bias–variance trade-off during the eventual model selection [208], where the

final model selection depends on the requirements of its end user. The Steering-Grid Thruster paragraph calculates $T_g(n_g, \alpha_g^i)$ by using $D_g(n_g, \alpha_g^i)$, whereas the Four-Channel Thruster paragraph calculates the orthogonal decomposition of $T_c(n_c, \alpha_c^i)$ into $T_c^x(n_c, \alpha_c^i)$ and $T_c^y(n_c, \alpha_c^i)$ by respectively using $D_c^x(n_c, \alpha_c^i)$ and $D_c^y(n_c, \alpha_c^i)$.

Steering-Grid Thruster

Due to the absence of the hull in the towing-tank experiments listed in the Bollard Pull Test Data, no external hull thrust deductions occurred (except for the small external surface of the thruster itself which will be neglected here), i.e., $t(\alpha_g^i) = t_i(\alpha_g^i)$. This paves the way to identify $t_e(\alpha_g^i)$ by the future increase in thrust deduction when the actuation sits inside its hull by using: $t(\alpha^i) = t_i(\alpha^i) + t_e(\alpha^i)$. Table 4.3 summarises the residuals of the cost functions after performing the aforementioned model fits. The absolute value of these residuals has no meaning; however, their relative size differences indicate the relative model fitness of the underlying model structures. The columns denote the different model structures of $T_m(n_g)$, whereas the rows show the different polynomial orders of $t(\alpha_g^i)$. For example, a cubic-order model for $t(\alpha_g^i)$ in combination with $T_m(n_g) = T_{nn} n_g^2$ can be identified by:

$$E = \sum_{p=1}^{P} \left(\left[1 - (t_3 \alpha_{g,p}^{i^3} + t_2 \alpha_{g,p}^{i^2} + t_1 \alpha_{g,p}^{i} + t_0) \right] (T_{nn} n_{g,p}^2) - D(n_{g,p}, \alpha_{g,p}^i) \right)^2 . \tag{4.9}$$

As visible in Table 4.3, the final cost of the example in (eq. 4.9) would equal 5.38. To further clarify this representation of the results, Appendix C lists all the identified model coefficients for all the model structures of Table 4.3. Table 4.3 seems to validate that taking $T_m(n) = T_{nn} n^2$ generates a simple but robust model which aligns with the theoretically derived propeller-characteristics model of the Conventional Propeller Characteristics, as adding a linear propeller-speed dependency (T_n) or a linear and cubic term (T_n, T_{nnn}) to $T_m(n)$ results in only marginally lower residuals.

Table 4.3: Cost function residuals for the different T_g models. Note that the identified coefficients can be found in Appendix C.

Model $t(\alpha_g^i)$	T_{nnn}, T_{nn}, T_n	T_{nn}, T_n	T_{nnn}	T_{nn}	T_n
Constant	39.26	39.83	64.79	41.24	62.12
Linear	12.77	13.35	39.85	14.84	37.01
Quadratic	5.67	6.12	31.72	7.28	31.88
Cubic	4.11	4.47	29.10	5.38	31.44
Quartic	2.62	2.96	27.32	3.80	30.39
Quintic	0.99	1.50	27.15	2.76	25.45

Given the adequacy of $T_m(n) = T_{nn}n^2$, Figure 4.4a plots the identified quadratic, linear, and constant models for $t(\alpha_g^i)$ with $T_m(n) = T_{nn}n^2$, together with the data points $D_g(n_g, \alpha_g^i)$ to illustrate the model fits. In addition, given the rather constant thrust decrease for $\alpha_g^i \in [150, 180]°$, one could also perform the abovementioned modelling procedure of T_g only for the $\alpha_g^i \in [0, 150]°$ domain, and assume $T_g(n_g, \alpha_g^i) = T_g(n_g, 150°)$ to equal a constant value for $\alpha_g^i \in [150, 180]°$. Figure 4.4b illustrates this second methodology for T_g, using a quadratic fit for $t(\alpha_g^i)$. Figure 4.5 provides another way to visualise these model fits by plotting T_g over its n_g domain for $\alpha_g^i = 0°$, 90°, and 180° by using a quadratic model fit for $t(\alpha_g^i)$ and $T_m(n) = T_{nn}n^2$, for the aforementioned full α_g^i–domain fit in Figure 4.5a, and for the fit which incorporates the constant thrust zone in Figure 4.5b. The latter plot shows the benefit of adding the constant thrust zone as it provides a better fit for $\alpha_g^i = 180°$ compared to Figure 4.5a.

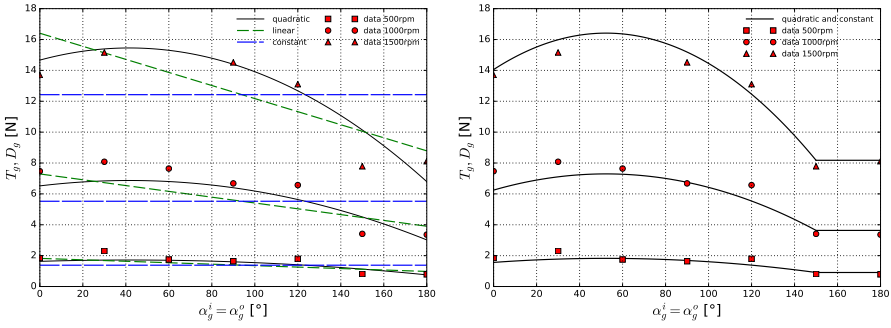

(a) (b)

Figure 4.4: Model fits for T_g by: (a) varying the order of $t(\alpha_g^i)$ with $T_m(n) = T_{nn}n^2$, and (b) a quadratic fit of $t(\alpha_g^i)$ for $\alpha_g^i \in [0, 150]°$ and a constant thrust zone for $\alpha_g^i \in [150, 180]°$ with $T_m(n) = T_{nn}n^2$. Note that there was no data point for, $\alpha_g^i = 60°$ at $n_g = 1500$ rpm, see Table B.1.

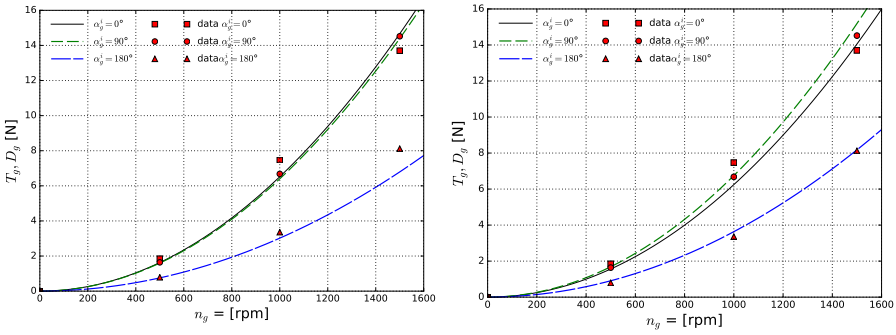

(a) (b)

Figure 4.5: Model fits for T_g with $\alpha_g^i = 0°$, 90°, and 180°, and $T_m(n) = T_{nn}n^2$, based on the identification methodology of Figure 4.4a in (a), and of Figure 4.4b in (b).

Four-Channel Thruster

The four-channel thruster generated its data embedded inside half a hull, making it impossible to diversify between $t_i(\alpha_c^i)$ and $t_e(\alpha_c^i)$ as they both depend on the same angle. Thus, this section identifies the thrust deduction coefficients as a superposition of both external and internal hull losses. Note that future towing-tank experiments without a hull, as have been done for the steering-grid thruster, could identify t_i separately and thus also give t_e. Table 4.4 and 4.5 list the different residuals of the cost functions of the model fitting algorithm for both T_c^x and T_c^y. Both tables give the impression that $T_m(n) = T_{nn}n^2$ forms a simple and robust model structure to represent the theoretical thrust force, which again aligns with the theoretical derivation of the Conventional Propeller Characteristics. Here too, adding T_n (or T_n and T_{nnn}) generates only marginal improvements compared to the quadratic n_c–dependency. Furthermore, these tables seem to indicate that the polynomial order of $t(\alpha_c^i)$ is better modelled by an odd function for T_c^x and by an even function for T_c^y.

Table 4.4: Cost function residuals for the different T_c^x models.

Model $t(\alpha_c^i)$	T_n	T_{nn}	T_{nnn}	T_{nn}, T_n	T_{nnn}, T_{nn}, T_n
Constant	38,795.76	38,795.95	38,796.08	38,795.43	38,795.34
Linear	7292.64	5092.89	5719.02	5085.50	5074.75
Quadratic	7066.95	4860.48	5500.83	4853.59	4843.96
Cubic	3511.66	1267.95	2168.83	1267.48	1267.44
Quartic	3035.18	738.33	1630.70	737.48	737.46
Quintic	2644.39	313.48	1207.49	312.45	312.37

Table 4.5: Cost function residuals for the different T_c^y models.

Model $t(\alpha_c^i)$	T_n	T_{nn}	T_{nnn}	T_{nn}, T_n	T_{nnn}, T_{nn}, T_n
Constant	22,722.75	21,261.84	22,199.03	21,255.83	21,223.65
Linear	22,173.90	20,707.77	21,684.97	20,700.10	20,662.85
Quadratic	7808.53	5129.44	6204.61	5128.91	5128.64
Cubic	6888.01	4515.32	5245.35	4144.76	4144.50
Quartic	3620.45	562.71	1654.30	559.84	559.09
Quintic	3414.50	356.56	1462.72	354.04	353.52

Figure 4.6 illustrates the model fits of T_c^x in Figure 4.6a, and of T_c^y in Figure 4.6b for different polynomial orders of $t(\alpha_c^i)$ with $T_m(n) = T_{nn}n^2$.

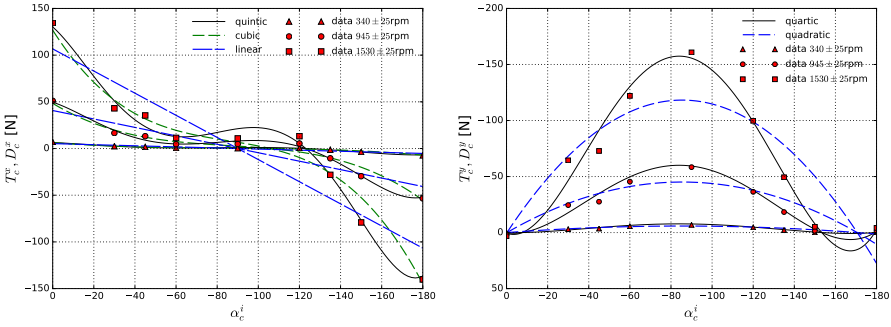

(a) (b)

Figure 4.6: Exemplary model fits for (a) T_c^x and (b) T_c^y.

Given the abovementioned rather constant thrust output of D_c^x for $\alpha_c^i \in [-60°, -120°]$, and of D_c^y for $\alpha_c^i \in [-150°, -180°]$, one could model these regions by a constant value. Subsequently, Figure 4.7a shows a piecewise linear model consisting of a linear fit of T_c^x for $\alpha_c^i \in [0°, -60°]$, a constant thrust zone where $T_c^x = T_c^x(-60°)$ for $\alpha_c^i \in [-60°, -120°]$, and finally again a linear fit for $\alpha_c^i \in [-120°, -180°]$. Whereas, similarly to Figure 4.6b, Figure 4.7b depicts a quartic and quadratic fit of $t(\alpha_c^i)$ for this angle in the $[0°, -150°]$ domain followed by a constant thrust zone where $T_c^y = T_c^y(-150°)$. As can be seen, this constant thrust zone offers a better representation of the data compared to the non-physical polynomial over fitting of Figure 4.6b on the same angular domain.

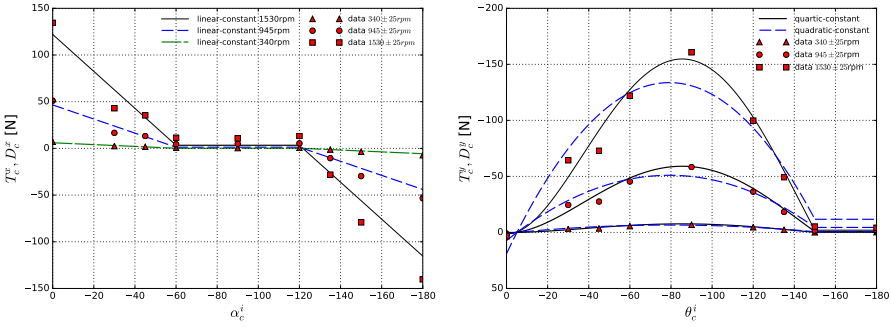

(a) (b)

Figure 4.7: Alternative model fits: (a) piecewise linear model for T_c^x, and (b) constant thrust zone model for T_c^y.

4.3.2.2 Feedforward Multilayer Network Model Identification

Similarly to the Conventional Bollard Thrust Model, this section plugged the data from Appendix B into different feedforward multilayer network designs. Within the subsequent figures and tables, the abbreviations *'br'*, and *'es'* respectively denote a Bayesian regulation and early stopping regulation scheme (see Section 4.3.1.2). These abbreviations will be followed by two numbers which indicate the amount of neurons in each hidden layer: e.g., 'br5-0', will only have one hidden layer with five neurons, whereas 'br3-3' would have two hidden layers with each three neurons. Furthermore, all networks used a tan–sigmoid transfer function, $tansig(\cdot)$, for the activation functions of the hidden layers, i.e., $\sigma(\cdot) = tansig(\cdot)$. Finally, note that all the training procedures of the artificial neural networks within this study were initialised with random weights for the network coefficients. This random initialisation can have an impact on the final results. Therefore, all networks were trained five times and the subsequent tables will show the average, minimum, and maximum final residual cost for each network structure over all five of these training cycles. Analogously to the Conventional Bollard Thrust Model, the model structures can be selected based on a bias–variance trade-off which depends on the requirements of the end user.

Steering-Grid Thruster

The networks for the steering-grid thruster used n_g and α_g^i for the input vector, x, as these inputs also generated the experimental data, i.e., $D_g(n_g, \alpha_g^i)$. The output vector of these networks, y, had only one element which constitutes the

modelled thrust force, i.e., $y = T_g$. To exemplify the cost function calculation and consequently the identification of its neural network, (eq. 4.10) calculates the residual for a network which models the steering grid with one hidden layer of three neurons by plugging (eq. 3.30) into (eq. 4.5), and thus by minimising:

$$E = \sum_{p=1}^{P} \left(\sum_{r=1}^{3} w_r \sigma \left(\sum_{j=1}^{2} v_{rj} x_{j,p} + \beta_r \right) - D(n_{g,p}, \alpha_{g,p}^{i}) \right)^2, \tag{4.10}$$

with $n_h = 3$, $m = 2$, and $l = 1$ (and thus its index is omitted). Accordingly, in matrix notation $W \in \mathbb{R}^{1\times3}$, $V \in \mathbb{R}^{3\times2}$, and $\beta \in \mathbb{R}^{3\times1}$. The two input vector elements, i.e., $x_{1,p}$ and $x_{2,p}$ are $n_{g,p}$ and $\alpha_{g,p}^{i}$, note that the superscript ^{i} from the latter refers to the internal actuation angle and not to an element notation. Depending on the selected training method, equation (eq. 4.10) can calculate the residual for es-3-0 or br-3-0, shown in Table 4.6 which lists the residuals of the final cost functions for all the identified network structures. Figure 4.8a plots the identification results of three different network topologies which only used one hidden layer that had two, three, or five neurons. Moreover, this figure compares the early stopping and Bayesian regulation approaches. Based on this plot, the Bayesian regulation outperformed the early stopping regulation. This performance difference can also be seen in Table 4.6(a). In addition, Figure 4.8b shows similar identification results for two different network architectures which nested two hidden layers. Here too, one can observe the Bayes regulation method outperforming the early stopping approach, on which Table 4.6(b) provides further detail.

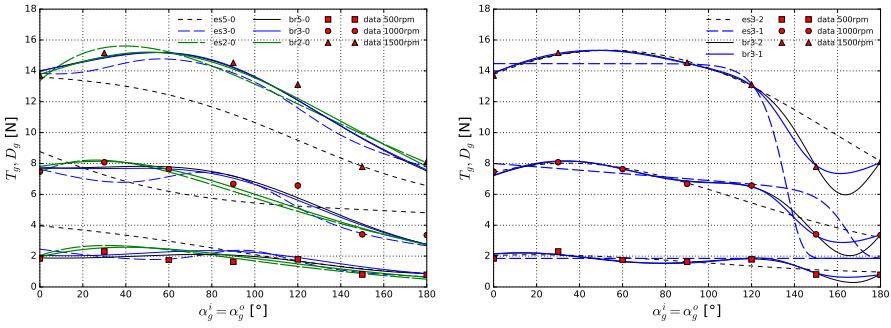

(a) (b)

Figure 4.8: Identification results and regulation comparison multilayer feedforward neural networks for the steering-grid thruster: (a) one hidden layer, (b) two hidden layers.

Table 4.6: Residuals cost functions of the multilayer feedforward neural networks for Figure 4.8: (a) one hidden layer, (b) two hidden layers.

(**a**)			
Model	**Average**	**Minimum**	**Maximum**
es5-0	37.91	12.86	71.26
es3-0	22.82	12.86	51.23
es2-0	22.66	8.33	52.80
br5-0	7.63	7.62	7.63
br3-0	8.38	8.37	8.38
br2-0	10.60	10.60	10.60
(**b**)			
Model	**Average**	**Minimum**	**Maximum**
es3-2	58.54	4.16	192.96
es3-1	80.16	4.16	235.70
br3-2	0.42	0.42	0.42
br3-1	0.37	0.37	0.37
br2-1	8.44	8.44	8.44

Four-Channel Thruster

This section constructs different networks with two hidden layers and a Bayesian regulation approach for the four-channel thruster data. These specific network architectures were chosen based on their performance in the results of the Steering-Grid Thruster. Although all the developed networks used n_c and α_c^i as their input values, three different approaches for the output, y, were selected to illustrate the network-architecture flexibility:

(i) Fitting the orthogonally decomposed thrust forces separately, i.e., constructing two networks with one output each: one for deriving T_c^x based on D_c^x, and analogously one for finding T_c^y based on D_y^c.

(ii) Fitting the orthogonally decomposed thrust forces simultaneously, i.e., constructing one network with two outputs: T_c^x and T_c^y.

(iii) Fitting the resulting thrust force and its orientation simultaneously, i.e., construction one network with two outputs, T_c and θ_c^o.

Table 4.7 compares the final cost function residuals of different network topologies for these three different cases. Firstly, regarding case (i), (a) summarises the residuals for T_c^x and (b) for T_c^y. Secondly, concerning case (ii), (c) shows the residuals of the chosen different network architectures to model this network which has two outputs. Thirdly, for case (iii), (d) shows a variety of model structures that represented this dual-output network. In addition, Figure 4.9 illustrates the fitness of several identified models for cases

(i)–(iii). To plot these identified network structures, one of the five runs of the respective network designs was chosen at random. When one compares case (i) to case (ii), hence comparing the plots Figure 4.9a and Figure 4.9b, with Figure 4.9c and Figure 4.9d, the former seem to have less variance compared to the latter. However, caution should be taken when one compares these plots as they represent different network topologies, have different amounts of neurons, and they are a random selection of one of the five network training cycles performed on each network design.

Table 4.7: Comparison of the identification residuals: (a) for the networks of (i) that model T_c^x, (b) for the networks of (i) that model T_c^y, (c) for the networks of case (ii), and (d) for the networks of case (iii).

(**a**)

Model	Average Cost	Minimum	Maximum
br2-2	17,390.56	2338.70	77,598.00
br3-2	962.83	292.15	1130.50
br3-3	253.10	220.82	301.59
br4-2	31,144.55	211.31	77,597.00
br4-3	192.64	192.64	192.64
br4-4	89.83	28.53	181.78

(**b**)

Model	Average Cost	Minimum	Maximum
br2-2	13,528.72	1252.90	62,631.00
br3-2	13,081.49	693.36	62,634.00
br3-3	299.16	114.91	636.50
br4-2	581.44	521.76	624.52
br4-3	388.45	4.24	518.54
br4-4	194.91	0.42	486.64

(**c**)

Model	Average Cost	Minimum	Maximum
br3-4	703.25	32.14	1279.90
br3-5	299.07	33.31	695.43
br5-3	587.82	558.14	657.58
br4-4	336.92	26.42	575.19
br5-3	587.82	558.14	657.58
br5-4	16.85	3.73	67.21

(**d**)

Model	Average Cost	Minimum	Maximum
br3-4	719.98	585.92	1256.20
br3-5	345.46	116.16	500.89
br5-3	27,349.43	748.15	34,017.00
br4-4	408.67	88.74	513.91
br5-3	27,349.43	748.15	34,017.00
br5-4	33,841.00	33,810.00	33,863.00

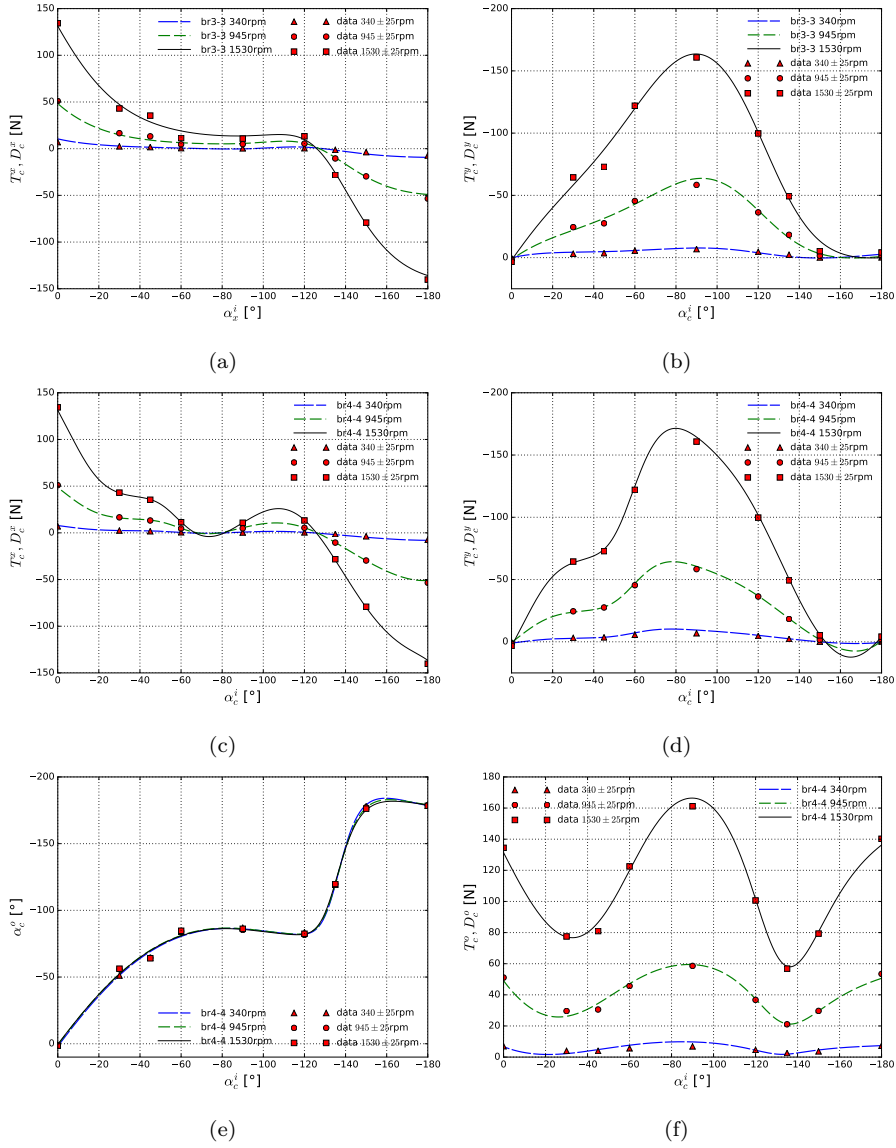

Figure 4.9: Identification results multilayer feedforward neural networks for the four-channel thruster. First, for case (i), the identified T_c^x in (a) and T_c^y in (b) with respective residuals 301.59 and 514.55. Second, for case (ii), the identified T_c^x in (c) and T_c^y in (d) with a network residual of 26.42. Third, for case (iii), the identified T_c in (e) and α_c^o in (f) with a final residual of 412.87.

4.3.3 Discussion

The pure experimental data of Section 2.4.2 could also be used as tabular models within manoeuvring models [68]. These data sets already expose interesting results for both thruster designs. On the one hand, they show the potential occurrence of a recirculation zone of flowing water for certain positions of the steering grid. On the other hand, they highlight the rather biased output angles of the resulting thrust forces of the four-channel thruster. Nevertheless, additional experiments (e.g. with different channel geometries and lengths, propeller diameters, or steering-mechanism designs) could provide complementary insights in the complex flow phenomena arising inside these thrusters. Given the complexity of the flow phenomena at hand, this work offered two model structure methodologies for the bollard thrust forces.

Firstly, the results of the Conventional Bollard Thrust Model validated the theoretical propeller-characteristics thrust model structures, using the Conventional Bollard Thrust Model for both thruster designs by means of a bias–variance trade-off. This trade-off indicates that the quadratic propeller-speed dependency indeed forms a simple but generic description of the resulting thrust forces for both embedded thruster designs at zero advance speed, although more complex model structures could be selected if desired by the end user. Moreover, results of the Conventional Bollard Thrust Model further illustrated the successful modelling approach to capture the internal control-angle dependent thrust deductions that exist in both propulsion systems. Evidently, the aforementioned additional experiments could also help to further refine these propeller-characteristics based thrust models.

Secondly, results of the Feedforward Multilayer Network Model demonstrated the possibility to use the multilayer feedforward networks to grasp the complex water flows, by implementing the Feedforward Multilayer Network Model. Bearing in mind that these networks can serve as universal approximations of nonlinear functions, they offer the capability to model more complex flow phenomena that might occur during future experiments with dynamic propeller speeds or when $U \neq 0$.

Figure 4.10 compares both model structure methodologies for the thrust forces generated by the four-channel thruster. Figure 4.10a depicts the longitudinal modelled forces, T_c^x, whereas Figure 4.10b shows the transversal modelled forces, T_c^y. For T_c^x, a quintic model describes $t(\alpha_c^i)$ in conjunction with $T_m(n) = T_{nn}n^2$ for the propeller characteristics-based model, whereas a Bayesian regulated network of two hidden layers, with three neurons each, forms the neural network structure. A similar approach describes the structures of T_c^y, only here $t(\alpha_c^i)$ has a quartic order. In both cases, i.e., Figure 4.10a and Figure 4.10b, the neural networks seem to outperform the theoretically based models. Particularly

in Figure 4.10b, the theoretical model generates a non-physical fit for $\alpha_c^i \in [-150°, -180°]$ whereas the neural network does not. In Figure 4.10a, for $\alpha_c^i \in [-60°, -120°]$ at $n_c = 1530$ rpm, the theoretical model also offers an incorrect higher thrust force compared to the neural network which is closer to the data points. These differences could origin from the tendency of the higher order polynomials of $t(\alpha_c^i)$ to over fit to the data set, whereas the *Ocam's razor* principle from the Bayesian regulation helps to avoid this situation. Nevertheless, Figure 4.10 offers an arbitrary exemplary comparison between the different modelling methodologies, thus its findings should not be extrapolated.

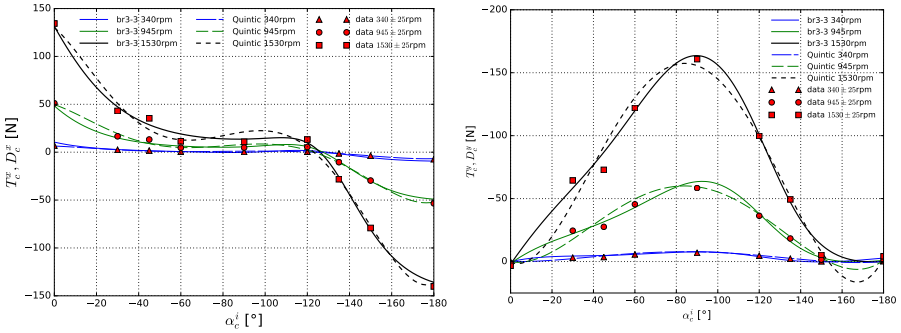

(a) (b)

Figure 4.10: Comparison neural network and propeller-characteristics-based model fits for (a) T_c^x and (b) T_c^y.

Finally, the current and future identified model structures can provide inputs to several applications. For instance, they can illustrate the achievable forces for a certain thruster over its whole control domain as exemplified by Figure 4.11. Furthermore, these models can be used to augment certain links in the automation chain such as thrust allocation methods and motion controllers. For example, an optimal thrust allocation algorithm calculates the optimal thrust magnitudes and orientations for all onboard propulsion systems in order to achieve the desired force and moment output which the motion control calculated [247]. Several implementations of these algorithms exist, such as a quadratic programming approach [144, 282], or by using a linear pseudo-inverse model [4]. However, these approaches tend to model the thrust forces as angle-independent, whereas the models of this work could be used to provide more accurate, control-angle dependent, representations of these forces. In addition, motion controllers could take the aforementioned and modelled constant thrust zones into account, similarly to incorporating dead-zones [155, 226], further improving their performance. Furthermore, model predictive control architectures could also benefit from the suggested physically-based models as they can intrinsically integrate propulsion system limitations and

states into their motion control design [143, 148]. Finally, note that, these predictive controllers could also embed the developed neural networks [168].

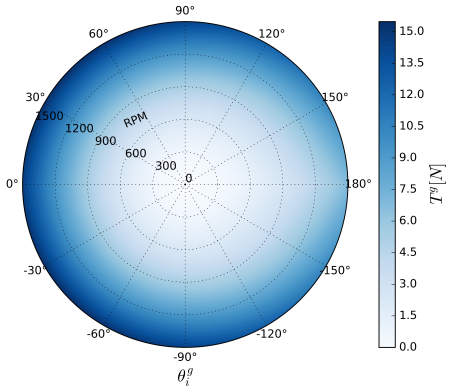

Figure 4.11: Visualisation of the possible magnitudes and orientations of T_g modelled by the quadratic thrust deduction model, i.e., polynomial order of $t(\alpha_g^i)$ equals two, and a pure quadratic n_g–dependency, i.e., $T_m(n) = T_{nn}n^2$, for a continuous area of (α_g^i, n_g) pairs. The outer circumference of this plot shows the same information as the quadratic polynomial at 1500 rpm of Figure 4.4a.

4.4 Computational Fluid Dynamics Data

Section 4.4.1 discusses the implemented grid studies for the deep [197] and shallow [66] water surge damping computations. Thereupon, Section 4.4.2 and 4.4.3 list their results, which Section 4.4.4 compares.

4.4.1 Grid Studies

Two KVLCC2 grids, with a refinement ratio of $r = \sqrt{2}$, investigated the grid convergence for the deep water surge damping [197]. Accordingly, the spatial discretisation error can be calculated by (eq. 4.11). This error can then be used to estimate the Grid Convergence Index (GCI) [221] for both the normal and finer grids (eq. 4.12), with p representing the order of convergence, and F_s a safety factor (often conservatively taken as $F_s = 3.0$ when comparing only two grids and as $F_s = 1.25$ when comparing three or more). The GCI provides an indicative measure of the distance between the calculated value and its asymptotic value. The GCI of the normal KVLCC2 grid (5 156 025 cells) was found to be approximately 7% [197]. The deep water calculations for the CEMT–I hull were done with a slightly more refined grid (7 751 760

cells, but in a longer computational domain, see Section 3.4.2) than the normal KVLCC2 grid, hence the estimated GCI for the latter might be indicative for the CEMT–I results, discussed by Section 4.4.2. For the shallow water identification [66], three KVLCC2 grid refinements, also with $r = \sqrt{2}$, were used. These grids were found to have an oscillatory grid convergence rate [120]. Given that these oscillations seemed to lie in the range of the experimental measurement errors, the medium sized grid was chosen. A similar refinement was used for the CEMT–I results, discussed in Section 4.4.3.

$$|\epsilon_d| = \frac{CFD_n - CFD_f}{CFD_f} \tag{4.11}$$

$$GCI_f = \frac{F_s|\epsilon_d|}{r^p - 1}, \quad GCI_n = \frac{F_s|\epsilon_d|r^p}{r^p - 1} \tag{4.12}$$

4.4.2 Deep Water Surge Damping

The emphasis was put on a conservative speed range: $0 \frac{\text{m}}{\text{s}} \leqslant u \leqslant 1 \frac{\text{m}}{\text{s}}$, in line with the first outdoor experiments with the physical vessel. Table 4.13 summarises the numerical results. Figure 4.12 gives more physical insight in the two outer test cases: $u = 0.200 \frac{\text{m}}{\text{s}}$ and $u = 1.000 \frac{\text{m}}{\text{s}}$, with respective Froude numbers $F_n = 0.03$ and 0.15. This figure compares both speeds on: (a)–(b) the relative pressure of the water surface, (c)–(d) the elevation of this surface, and (e)–(f) the speed and its flow on a longitudinal cut (xz-plane) at the bow of the vessel. One can notice the rather uniform pressure field at $0.200 \frac{\text{m}}{\text{s}}$ evolving in a wave-like pattern at the higher speed $1.000 \frac{\text{m}}{\text{s}}$. The water level elevation also demonstrates the growing wave pattern at the higher speeds, where peaks and bottoms alternate throughout the elevation field. Forty contours further clarify the surface elevation, which has a highest-peak-to-deepest-bottom range of 7 mm for the low speed and 52 mm for the high speed. Due to the low elevation range of the $0.200 \frac{\text{m}}{\text{s}}$ case, most contours are lined around small fluctuations close to the hull, diminishing their visibility.

Table 4.8: Deep water results for the KVLCC2 [237] and CEMT–I hulls.

KVLCC2			**CEMT–I**	
u [m/s]	CFD [N]	% Error	u [m/s]	CFD [N]
0.944	22.64	-1.44%	0.200	1.08
0.981	24.32	-1.54%	0.400	3.72
1.057	27.88	-1.38%	0.600	8.08
1.132	32.02	-0.06%	0.800	14.16
1.208	36.28	0.39%	1.000	22.40
1.283	40.78	0.22%	—	—

Relative pressure on the water surface.

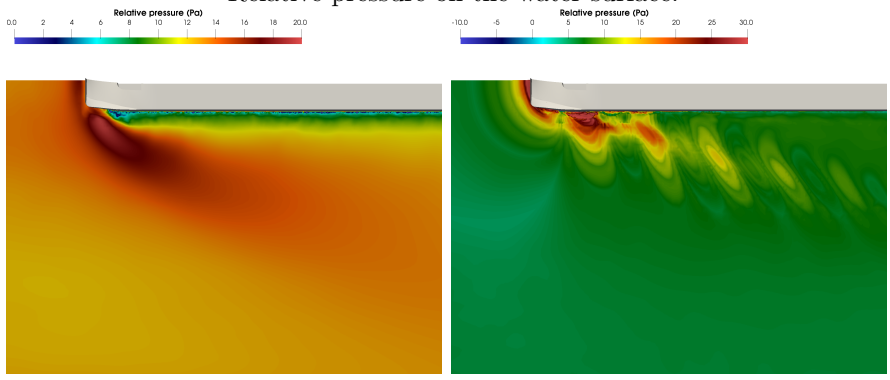

(a) (b)

Elevation of the water surface with contours.

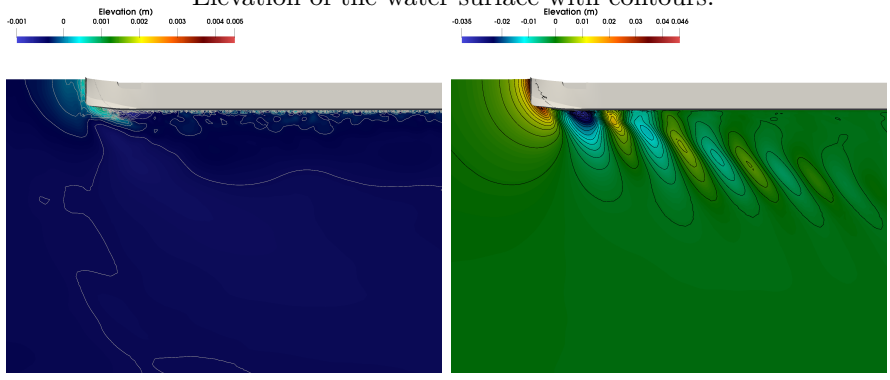

(c) (d)

Longitudinal speed and streamlines at a longitudinal cut at the bow.

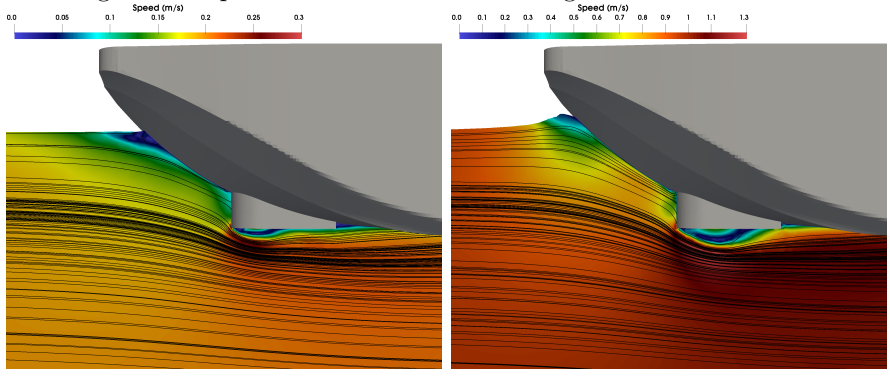

(e) (f)

Figure 4.12: Comparison of pressure, elevation, and speed; left: $u = 0.200\ \frac{\mathrm{m}}{\mathrm{s}}$, $F_n = 0.03$, right: $u = 1.000\ \frac{\mathrm{m}}{\mathrm{s}}$, $F_n = 0.15$.

4.4.3 Shallow Water Surge Damping

The KVLCC2 benchmark hull for the shallow water validation cases had a smaller length (of 4.27 m) than its deep water equivalent. Table 4.9 lists the results for the KVLCC2 and CEMT–I hulls for 50% and 20% under keel clearance (UKC) [66]. For the KVLCC2 hull, the errors between the experimental and computational damping values are also listed.

Table 4.9: Shallow water results for the KVLCC2 and CEMT–I hulls at 20% and 50% UKC [66].

Hull	UKC [%]	Speed [m/s]	CFD [N]	Error [%]
KVLCC2	50	0.416	3.05	-1.4
KVLCC2	20	0.416	3.60	-0.55
CEMT–I	50	0.20	1.31	—
CEMT–I	50	0.40	3.96	—
CEMT–I	20	0.20	1.70	—
CEMT–I	20	0.40	4.40	—

4.4.4 Comparison Deep and Shallow Water Surge Damping

Figure 4.13 compares the deep and shallow water results for the CEMT–I hull. Figure 4.13a plots the CFD data for the deep water calculations together with the identified surge damping model, $D_{CFD}(u) = 0.10u + 22.12u^2$. Figure 4.13b additionally shows the shallow water data. As to be expected, the damping forces rise with decreasing UKC.

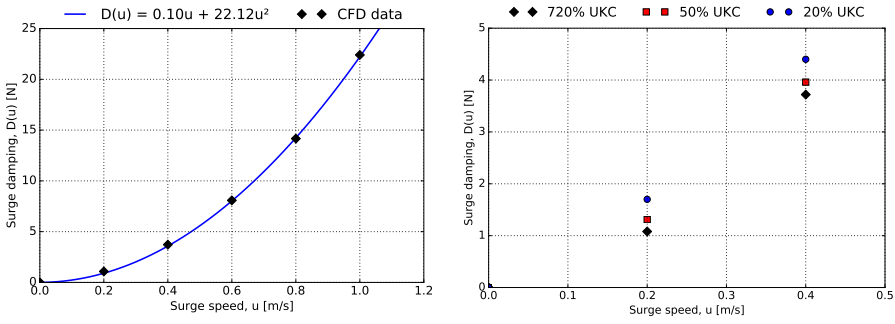

(a) (b)

Figure 4.13: Numerical results surge damping: (a) deep water data and fitted curve $F_{CFD}(u) = 0.10u + 22.12u^2$ for the CEMT–I hull, (b) shallow water data.

4.5 Additional Test Manoeuvres

The existing standardised test manoeuvres aim to reveal the capability of a vessel to perform certain manoeuvres. Hence, these tests allow for the identification of certain hydrodynamic manoeuvring characteristics and metrics. These characteristics can provide an operator with crucial information in order to take correct and timely decisions to safely and effectively navigate the vessel. The International Maritime Organization (IMO) issued the most-known manoeuvrability standards which include checking the manoeuvring performance of a vessel in terms of its inherent dynamic stability, course keeping ability, initial turning and course changing ability, yaw checking ability, turning ability, and stopping ability [118]. Note, however, that these IMO standards should be applied to "ships of all rudder and propulsion types, of 100 m in length and over, and chemical tankers and gas carriers regardless of the length [118]". In Addition, the manoeuvring committee of the International Towing Tank Conference (ITTC) examined 19 manoeuvring tests proposed by various organizations and recommended procedures and guidelines for 14 of them which are able to measure the abovementioned characteristics [119]. Currently, the most widely accepted tests for full scale trials seem to consist of the Turning Circle Test, the 10/10 and 20/20 Zigzag Manoeuvre Test, and the Stopping Test.

However, the typical inland cargo vessel differs significantly from its seagoing counterparts. Firstly, inland vessels tend to operate in spatially restricted shallow or confined water without the help of tug boats. Therefore, they are often built with multiple rudder and/or propeller configurations in order to boost their manoeuvring performance [146]. Even the addition of an azimuth thruster, or a transversal bow thruster, is not uncommon to further increase the manoeuvrability of a vessel [147]. Secondly, the vertical restrictions in the inland waterways usually result in speed regulations in order to avoid the touching of the bottom due to the arising squat effect. Hence, inland vessels usually perform their manoeuvres at low speeds and need to keep course under these conditions. Thirdly, due to the horizontal restrictions such as banks, heavy traffic in access areas, and the necessity of close passages in narrow sections of canals, inland vessels also have to change their courses frequently and usually do a manoeuvre similar to cars changing lanes on the road [145]. Therefore, contrary to seagoing vessels, where course keeping dominates, the initial turning and course changing ability are crucial metrics for inland vessels.

Consequently, smaller vessels which navigate in restricted water with non-conventional propulsion types, do not directly fall under these abovementioned IMO standards [147]. Therefore, some authorities, like the CCNR [46] and the European Commission [75], offered regional standards for inland vessels [217], for example, the stopping and evasive capacity regulations [47, 145]. To offer more insights in the manoeuvring performance of inland vessels in their environment, Liu (2017 [145]) suggested additional manoeuvres and subsequent metrics for inland vessels. This section expands these additional inland manoeuvres and discusses the outdoor executions of some of these existing and newly added manoeuvres with an unmanned autonomous inland cargo vessel. This section continues as follows: section Section 4.5.1 lists some of the existing standardised test manoeuvres, and afterwards it adds three new manoeuvres to this list. Section 4.5.2 details the conducted experiments and Section 4.5.3 provides their overarching discussion.

4.5.1 Method

First, Section 4.5.1.1 briefly discusses the existing manoeuvres which focus on non-conventional propulsion systems of inland vessels. Afterwards, Section 4.5.1.2 introduces additional test manoeuvres tailored for inland vessels with non-conventional propulsion systems.

4.5.1.1 Existing Vessel Manoeuvres

In the proposed guidelines of the ITTC, 2 of the 14 tests mention the use of a lateral thruster: (i) the Thruster Test suggests performing the turning or zigzag manoeuvre with the lateral thruster as a steering input and the rudder at midship, and (ii) the Crabbing Test suggests lateral movements at zero forward speed [119]. Furthermore, in the proposed tests for inland vessels of Liu (2017 [145]), the Hard Turning, T-junction, and Lane Changing tests can use, and benefit from, non-conventional thrusters and their position.

4.5.1.2 Suggested Additional Vessel Manoeuvres

Given the fact that inland vessels tend to use non-conventional propulsion configurations and non-conventional actuators, the here-suggested test manoeuvres assume a generic inland vessel which has two propulsion systems: one at the bow and one at the stern. Moreover, both propulsion systems are presumed to have a controllable thrust force magnitude, T, and orientation, α. Evidently, the maximum thrust force depends on the geometrical design of the system

and the engine powering it, whereas the limits of its orientation lie between $[0°, 360°]$. Alternatively, one can denote this orientation by measuring the angle between T and the longitudinal axis of the vessel which points to the bow and encapsulate this angle between $[-180°, 180°]$ with a positive sign for counter-clock-wise angles. Accordingly, for the remainder of this study, $T \in [0, T_{max}]$, $\alpha \in [-180°, 180°]$, and the subscripts "s" and "b" will be used to denote the stern and bow thruster respectively. Note that, it could happen that the internal control angle of the actuation system, α^i, and the orientation of the resulting output force, α^o, are not aligned. Under these assumptions, the following three additional manoeuvring tests for inland vessels are suggested; the Counter Thrust Test, the Sine Angle Test, and the Simultaneous Zigzag Test.

Counter Thrust Test

This test aims to locally rotate the vessel by covering as little space as possible. For this purpose, both the bow and stern thruster should try to exert an equal but opposite force. If the thrust forces do not equal each other in magnitude, there will be a resulting lateral force which would make the vessel drift during the manoeuvre. Evidently, this manoeuvre could be performed in a clock-wise or counter-clock-wise turning direction, hence:

- $T_b = T_s$
- $\alpha_b^i = 90°$ (or -90°)
- $\alpha_s^i = \text{-}\alpha_b^i$

Sine Angle Test

This test helps to uncover the broad spectrum of achievable turning rates. This test can be performed for both thrusters separately, with the other thruster providing no thrust at all, or another desired value. Furthermore, both thrusters could perform the test simultaneously. The test parameters per thruster consist of its thrust magnitude, the maximum angle of its orientation, and the frequency of the applied sine function:

- $T =$ chosen value
- $\alpha^i = \alpha_{max}^i \sin(2\pi f t)$

Simultaneous Zigzag Test

In line with the suggested additional zigzag manoeuvre from [119], where the lateral thruster provides the steering, one could also instruct both thrusters to work simultaneously. Towards this end, both thrusters should have an opposite angle to cooperatively perform the zigzag manoeuvre:

- T_b = chosen value
- T_s = chosen value
- α_b^i = chosen value (e.g. 30°/-30°)
- α_s^i = - α_b^i

4.5.2 Results

This section shows three of the aforementioned manoeuvres for inland vessels that were performed with the Cogge on a lake in Rotselaar (Belgium). The Cogge conducted all these experiments autonomously with no crew on board. The values of the parameters of these tests were empirically chosen. The superscript ^{m} denotes the measured values. Section 4.5.2.1 discusses an ITTC-suggested manoeuvre, namely The Crabbing Test, whereas Section 4.5.2.2 and 4.5.2.3 respectively handle The Counter Thrust Test and The Sine Angle Test manoeuvres. In order to give an idea of the testing conditions, a top view photo of a counter-clockwise Counter Thrust Test can be seen in Figure 2.5d.

4.5.2.1 The Crabbing Test

Figure 4.14a shows all the system states measured during the 40 s crabbing manoeuvre, i.e., propeller speeds, n, and internal thruster angles, α^i. The vessel performed a starboard crabbing manoeuvre with simultaneously changing propeller speeds for the bow and stern thruster. Ideally, both thrust forces exert an equal but opposing torque on the vessel such that the vessel does not rotate. During the experiment, an empirically derived propeller speed ratio was used to achieve this. Figure 4.14b plots the measured headings (relative to the start heading) and yaw-rates which indicate that the vessel kept a rather straight orientation during the whole manoeuvre. Finally, Figure 4.14c displays the trajectory the main GNSS mushroom covered, positioned at the vessel stern.

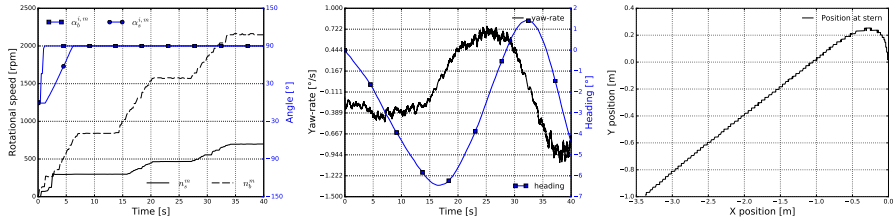

(a) (b) (c)

Figure 4.14: The Crabbing manoeuvre with (a) $\alpha_b^i = \alpha_s^i = 90°$, $n_b = 0$ to 2150 rpm using a staircase profile, and $n_s = 0$ to 700 rpm using a staircase profile, (b) shows the measured headings and yaw-rates, and (c) shows the trajectory of the main GNSS mushroom.

4.5.2.2 The Counter Thrust Test

Figure 4.15a demonstrates the measured system states during the performed counter-clockwise Counter Thrust Test. Here too, a propeller speed ratio was used in order to provide approximately equal thrust magnitudes, similarly to Section 4.5.2.1. As the measured headings of Figure 4.15b illustrate, the Cogge rotated almost twice over the 60 s time span of the manoeuvre. Lastly, Figure 4.15c exposes that the Cogge did not drift far during the experiment, as the position of the main GNSS mushroom, which is placed at the stern of the 4.8 m long vessel, described a spiraled-ellipse shape within a 5.0 m by 5.5 m rectangular box. The spiral shape of the GNSS mushroom antenna indicates that there was a small deviation of the starting position which might be caused by: (i) the error on the experimentally tuned propeller speed ratio which could be diminished in the future, and (ii) external disturbances which might have been present.

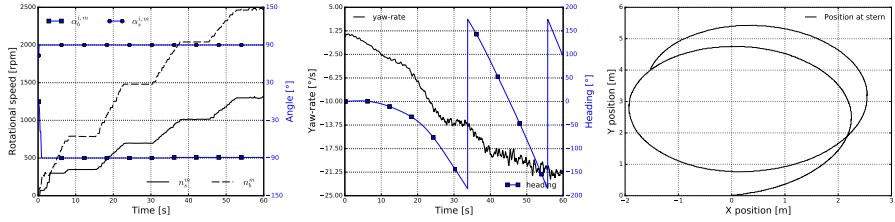

(a) (b) (c)

Figure 4.15: Counter-Clockwise Counter Thrust manoeuvre with (a) $\alpha_b^i = -90°$, $\alpha_s^i = 90°$, $n_b = 0$ to 2450 rpm using a staircase profile, and $n_s = 0$ to 1300 rpm using a staircase profile, (b) shows the measured headings and yaw-rates, and (c) shows the trajectory of the main GNSS mushroom.

4.5.2.3 The Sine Angle Test

Figure 4.16a depicts the measured system states during a Sine Angle Test conducted by the bow thruster, hence the system states for the stern both equalled zero. The bow propeller reached a rotational speed of 2050 rpm and the angle of the steering grid oscillated between [-180°, 180°] over a period of 40 s, which resulted in the measured headings and yaw-rates of Figure 4.16b. These yaw-rates offer an impression of the achievable turning rates of the vessel at low advance speeds. Evidently, the same manoeuvre could be performed over a longer period, giving the yaw-rates more time to settle, or with higher vessel speeds. Finally, Figure 4.16c portrays the distance covered by the main GNSS mushroom during this experiment.

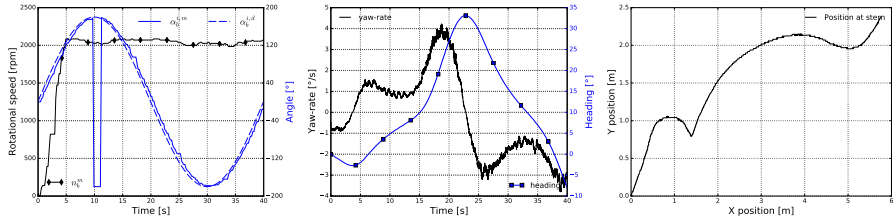

(a) (b) (c)

Figure 4.16: Sine Angle Test with the bow thruster: (a) α_b^i oscillating between $= [-180°, 180°]$ over 40 s, $n_b = 2050$ rpm, $\alpha_s^i = 0°$, and $n^s = 0$ rpm, (b) shows the measured headings and yaw-rates, and (c) shows the trajectory of the main GNSS mushroom.

4.5.3 Discussion

This section suggested additional test manoeuvres focussing on vessels with highly manoeuvrable actuation configurations: (i) the Counter Thrust Test, which can judge the turning capabilities of the vessel in spatially restricted areas, (ii) the Sine Angle Test, which can uncover a wide range of achievable turning rates, and (iii) the Simultaneous Zigzag Test, which can utilise the full capability of the vessel to perform a regular zigzag test. In addition, three manoeuvres were conducted with an unmanned autonomous inland cargo vessel; one existing manoeuvre: The Crabbing Test, and two here-proposed manoeuvres: The Counter Thrust Test, and The Sine Angle Test. The successful execution of these manoeuvres provided fruitful insights in the dynamic capabilities of the vessel at hand. For example, the Counter Thrust Test showed how the vessel can rotate locally with little drift. Presently, the newly suggested manoeuvres have not been tested repeatedly under the same experimental conditions, which should be done in the future to investigate their repeatability.

4.6 Decoupled Hydrodynamic Motion Models

No public hydrodynamic data appear to be available for the CEMT type I–II hulls, and little for inland vessels in general [145, 146, 225]. In addition, the novel self-propelled watertruck barges have a non-conventional propulsion system consisting of two fully nested and 360-degree-steerable actuators: a steering grid thruster in the bow and a four-channel thruster in the stern, for which little or no models or data seem to be available too. Therefore, this section identifies the Selected Decoupled Hydrodynamic Motion Models for surge, sway, and yaw. This decoupling offers insights in the vessel manoeuvrability on the one hand, and enables a focused investigation of the thruster models on the other hand. More precisely, this section used the Cogge to:

(**i**) Provide two identification methods to determine the coefficients of these, or other, manoeuvring models: the Force Balance Method (FBM), and the Differential Equation Method (DEM).

(**ii**) Benchmark the results of the surge models with data from both the abovementioned Deep Water Surge Damping CFD study [197], the empirical approach suggested by Kristensen et al. (2013 [131]), and the bollard pull data of Appendix B [194].

(**iii**) Provide all these experimental data sets, see Supplementary Materials of Peeters et al. (2020 [203]), together with the details of the utilised data logging and processing approaches.

The achievement of these aims provides more understanding of the manoeuvrability of these vessels and the potential hydrodynamic models to predict such movements in surge, sway, and yaw. In addition, these decoupled models present a stepping stone for subsequent coupled models in the future, and the supplemental experimental data unlock the possibility for other researchers to investigate this novel watertruck fleet. This section continues as follows: Section 4.6.1 lists the experimental design for the data generation which served as inputs for the identification procedures of Section 4.6.2. Thereupon, Section 4.6.3 explains the model structure selection procedures of the results of Section 4.6.4. Finally, Section 4.6.5 provides an overarching discussion of these results.

4.6.1 Experimental Design

The Cogge served as the experimental platform of this section. The following subsections will detail its configurations during the conducted experiments.

4.6.1.1 Configuration Sensors

The IMU sensor ran a real-time extended Kalman filter at 200 Hz, where it received corrective steps from the GNSS unit at 5 Hz. A calibration procedure — to find the position and orientation differences between the IMU and GNSS sensors — was conducted using the IMU software; more details and a benchmark of this procedure can be found in Yayla et al. (2020 [297]). In this study, both the GNSS sensor and the IMU internally logged Pulse Per Second (PPS) synchronised data at 50 Hz. The GNSS sensor also sent the Coordinated Universal Time (UTC) to the I-PC, where the MOOS middleware logged these data together with the desired and measured actuation system states which were requested at 20 Hz. Accordingly, the UTC stamps provided the connection for the post-processing synchronisation of all the relevant data; see Section 4.6.1.3.

4.6.1.2 Decoupled Surge, Sway, and Yaw Motion Experiments

In the comparative review of identification papers on ship manoeuvring models in Herrero et al. (2012 [106]), it can be noted that most studies use standard manoeuvres as inputs. In this study, the decoupled motions of surge, sway, and yaw need to be excited independently over a variety of speeds, in order to generate data for the models of the Selected Decoupled Hydrodynamic Motion Models. Table 4.10 shows that the actuation system of the Cogge enables three sub-modes to generate surge motion data: (i) bow thruster only, named "Bow", (ii) stern thruster only, named "Stern", and (iii) both thrusters simultaneously, named "Dual". In addition, the Cogge can sway to the "Left" or to the "Right", not unlike the crabbing test manoeuvres [119]. Finally, a counter thrust test as suggested by Peeters et al. (2020 [199]) can be performed clockwise or counter-clockwise, named "CW" or "CCW", to induce the yaw motion data.

For each of the aforementioned sub-modes, three desired time-dependent propeller speed missions, $n^d_{b/s}(t)$, were requested from the thrusters named "Ramp", "Stairs", and "Step" in Table 4.10, and each mission was conducted twice. Figure 4.17 illustrates the three different desired and measured, $n^m_{b/s}(t)$, time-dependent propeller speed profiles. The first batch of missions, denoted by "m_1", were conducted in calm weather conditions, whereas a slight 1–2 Beaufort wind picked up during the second batch, "m_2", which can also be seen in the Exemplary Data Yaw Missions. For the surge missions, both thrusters had an equal internal angle, $\alpha^i_{b/s} = 0°$, for the sway missions both angles were oriented sideways, $\alpha^i_{b/s} = 90°$ or $= -90°$, and for the yaw missions both thrusters had opposite sideways angles, $\alpha^i_b = -\alpha^i_s = 90°$ or $= -90°$. The requested and measured rotational speeds for all missions can be found in the Supplementary Materials of Peeters et al. (2020 [203]). For the sway and yaw

motions, the $n^d_{b/s}$ were manually determined during the experiments and set to $n^d_b = 2000$ rpm and $n^d_s = 500$ rpm for all their sub-modes. This speed ratio gave good visual results — by watching the vessel motion from inside a supply vessel — for both sway and yaw, but it might have introduced a small discrepancy: since a no-yaw requirement needs equal but counteracting moments of the thrusters, and a no-sway requirement needs equal but counteracting forces of these thrusters. Given the different lever arms of both thrusters, see Figure 3.3, it might be assumed that one cannot achieve both situations, i.e., no yaw during sway and vice versa, with the same propeller speed ratio, although this depends on the potential speed-dependency of the thrust forces which was unknown during the experiments.

Table 4.10: Overview of all decoupled motion model experiments.

	Surge			Sway		Yaw	
$n^d_{b/s}(t)$	**Bow**	**Stern**	**Dual**	**Left**	**Right**	**CW**	**CCW**
Ramp	m_1, m_2	m_1, m_2	m_1, m_2	m_1, m_2	m_1, m_2	m_1, m_2	m_1, m_2
Stairs	m_1, m_2	m_1, m_2	m_1, m_2	m_1, m_2	m_1, m_2	m_1, m_2	m_1, m_2
Step	m_1, m_2	m_1, m_2	m_1, m_2	m_1, m_2	m_1, m_2	m_1, m_2	m_1, m_2

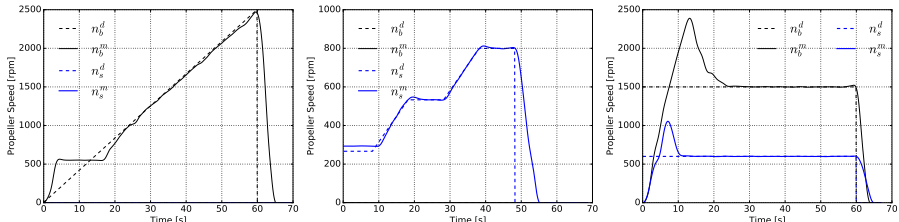

(a) bow–ramp–m_1 (b) stern–stairs–m_1 (c) dual–step–m_1

Figure 4.17: Time-dependent speed profiles, desired, $n^d_{b/s}$, and measured, $n^m_{b/s}$, values: (a) ramp profile for a bow thruster mission, (b) stair profile for a stern thruster mission, and (c) a step profile for a dual thrusters mission.

4.6.1.3 Data Post Processing

Due to the different data logging locations and frequencies (see Configuration Sensors), the relative time vector of the MOOS database needed to be converted to UTC stamps, and the MOOS data needed to be merged with the other sensor data. Consequently, the following manipulations were done to the MOOS data using the Pandas package [260] in Python version 3 [270]: (i) the time vector was converted to a UTC time vector, (ii) the data were clipped to their relevant mission time range, (iii) the offsets in relative time and position were

removed, (iv) the variables were linearly interpolated, given that MOOS allows for asynchronous data logging, and (v) the resultant data were upsampled to 50 Hz. Afterwards, these data were merged with the IMU and GNSS data based on the UTC time vector. The potential time delays between a measurement and its log were assumed negligible and irrelevant compared to the studied vessel dynamics.

The Supplementary Materials of Peeters et al. (2020 [203]) holds the results of these manipulations for the variables used in this study in a file per mission, structured according to the taxonomy of Table 4.10. As a result, each mission file contains: (i) a relative time vector, (ii) the position data of the main GNSS mushroom, which were calculated in the MOOS in real-time using the driver from [167], (iii) the desired and measured $\alpha^i_{b/s}$ and $n_{b/s}$ from the MOOS, (iv) the roll, pitch, and yaw angles from the IMU, (v) the yaw-rate from the IMU, (vi) the northern and eastern speeds from the IMU, and (vii) the surge and sway accelerations from the IMU. Note that the IMU publishes these accelerations in a horizontal ship reference frame where the gravity vector has been taken into account. This horizontal frame aligns with the aforementioned Modelling Assumptions. In combination with the decoupled design of the experiments, and thus by neglecting other motions, one can assume these accelerations to be equal to those at the centre of gravity for the surge and sway experiments.

Based on the logged northern and eastern speeds, the course over ground was calculated which allowed the determination of the drift vector. Thereupon, the surge and sway speeds were calculated based on the total speed and drift vectors. In addition, the yaw-accelerations were calculated using the gradient function from Numpy [102]. Finally, all data — to have similar distortions on each variable — were filtered forward and backward — to avoid phase distortions — using a low pass Butterworth filter of order 2 with desired cutoff frequency of 0.3 Hz and Nyquist frequency of 25 Hz, by using the Scipy package [276]. Note that these calculations and filters were not added or performed on the Supplementary Materials of Peeters et al. (2020 [203]), in order to provide the original as-measured data sets.

4.6.2 Identification Methods Decoupled Models

The offline identification of hydrodynamic vessel models can be roughly divided into frequency and time domain methods [106, 148, 207]. This section uses two different time domain approaches of which the usage need not be restricted to the suggested models. The Force Balance Method uses the instantaneous force balance of the dynamic equations, given that all inputs and outputs

were measured during the experiments. The Differential Equation Method integrates the system dynamics by solving its differential equations. For each model structure $x \in [a, \cdots, i]$ and motion $d \in [u, v, r]$, both methods called the bounded nonlinear least squares function of Virtanen et al. [276], which uses a thrust-region reflective method based on Branch et al. [34] to minimise a cost function, $E_d^x(\boldsymbol{\theta_d^x})$, for k sets of data by altering the values of their parameter vector $\boldsymbol{\theta_d^x}$:

$$E_d^x(\boldsymbol{\theta_d^x}) = \sum_{i=1}^{i=k} E_{d_i}^x(\boldsymbol{\theta_d^x}). \tag{4.13}$$

To each translational training mission, i.e., $d \in [u, v]$, a bias term β_{d_i} was added as an external force, which was intended to capture the static parts of the wind forces. Accordingly, the vector $\boldsymbol{\beta_d} = [\beta_{d_i}, \ \ldots, \ \beta_{d_k}]$ was added to the $\boldsymbol{\theta_d^x}$ vectors of the surge and sway cases. In other words, for these two cases, the k training missions share the unknown parameter vector $\boldsymbol{\theta_d^x}$ but each mission has an individual bias term β_{d_i}. To facilitate the notation of the cost functions in the Force Balance Method and the Differential Equation Method, let the matrices $\boldsymbol{y_{d_i}} = [\boldsymbol{\dot{d}_i}, \boldsymbol{d_i^3}, \boldsymbol{d_i^2}, \boldsymbol{d_i}]$ accumulate all the speeds and their quadratic and cubic values, and the accelerations for each $d \in [u, v, r]$. Similarly, let $\boldsymbol{x_{d_i}} = [\boldsymbol{n_s^m}, \boldsymbol{n_b^m}, \boldsymbol{\alpha_s^m}, \boldsymbol{\alpha_b^m}]$ capture all the measured thruster states. For $\boldsymbol{x_{u_i}}$ and $\boldsymbol{x_{v_i}}$, the outputs $\boldsymbol{u_i}$ and $\boldsymbol{v_i}$ should be added too, given that some thruster models depend on these speeds. Similarly, $\boldsymbol{x_{r_i}}$ needs to be appended with the calculated transversal speeds at the thrusters: $\boldsymbol{v_{b,i}}$ and $\boldsymbol{v_{s,i}}$. Consequently, each parameter vector $\boldsymbol{\theta_d^x}$ can be similarly divided into two parts which accumulate the parameters relevant for $\boldsymbol{y_{d_i}}$ and $\boldsymbol{x_{d_i}}$ respectively: $\boldsymbol{\theta_d^{x_y}}$ and $\boldsymbol{\theta_d^{x_x}}$. Finally, all "left" and "CCW" missions were transformed to "right" and "CW" missions by changing the signs of the measurements.

4.6.2.1 Force Balance Method

Using the knowledge from (eq. 3.2–3.4), i.e., the inertial and damping forces should equal the thrust forces, and by adding the individual potential wind bias term for each translation mission, the following three equations show the cost functions for k training sets for the surge, sway, and yaw methods respectively using the FBM approach:

$$E_u^x(\boldsymbol{\theta_u^x}, \ \boldsymbol{\beta_u}) = \sum_{i=1}^{i=k} E_{u_i}^x(\boldsymbol{\theta_u^x}, \ \beta_{u_i}) = \sum_{i=1}^{i=k} \left(\boldsymbol{\theta_u^{x_y}} \boldsymbol{y_{u_i}} - \boldsymbol{\theta_u^{x_x}} \boldsymbol{x_{u_i}} - \beta_{u_i}\right)^2, \tag{4.14}$$

$$E_v^x(\boldsymbol{\theta_v^x}, \ \boldsymbol{\beta_v}) = \sum_{i=1}^{i=k} E_{v_i}^x(\boldsymbol{\theta_v^x}, \ \beta_{v_i}) = \sum_{i=1}^{i=k} \left(\boldsymbol{\theta_v^{x_y}} \boldsymbol{y_{v_i}} - \boldsymbol{\theta_v^{x_x}} \boldsymbol{x_{v_i}} - \beta_{v_i}\right)^2, \tag{4.15}$$

$$E_r^x(\boldsymbol{\theta}_{\boldsymbol{r}}^{\boldsymbol{x}}) = \sum_{i=1}^{i=k} E_{r_i}^x(\boldsymbol{\theta}_{\boldsymbol{r}}^{\boldsymbol{x}}) = \sum_{i=1}^{i=k} \left(\boldsymbol{\theta}_{\boldsymbol{r}}^{\boldsymbol{x_y}} \boldsymbol{y}_{\boldsymbol{r_i}} - \boldsymbol{\theta}_{\boldsymbol{r}}^{\boldsymbol{x_x}} \boldsymbol{x}_{\boldsymbol{r_i}}\right)^2. \tag{4.16}$$

4.6.2.2 Differential Equation Method

In order to integrate the differential equations of motion, only the measured $\alpha_{b/s}^i$ and $n_{b/s}$ are needed in combination with the initial vessel speed, which provides the start condition. These integrations were done using the "odeint" function from the SciPy python package [276] which calls the "lsode" solver from the FORTRAN library "odepack" [108]. To further clarify this approach, Equation (eq. 4.17) expresses such a differential equation for $\mathcal{M}(\boldsymbol{\theta}_{\boldsymbol{v}}^{\boldsymbol{e}})$ of (eq. 3.33):

$$\dot{v} = \frac{T_{nn}^{b,90} n_b^2 + T_{nn}^{s,90} n_s^2 - Y_{vv} v^2 - Y_v v}{M + Y_{\dot{v}}}. \tag{4.17}$$

Integrating (eq. 4.17) for each time period of 20 ms, where the associated propeller speed and angle measurements are updated accordingly, generates a vector, $\hat{\boldsymbol{v}}$, with the predicted sway speeds for that mission. The vectors $\hat{\boldsymbol{u}}$ and $\hat{\boldsymbol{r}}$ can be calculated analogously. The DEM cost functions aim to minimise the difference between these predicted speeds and the measured speeds by changing the values of $\boldsymbol{\theta}_{\boldsymbol{d}}^{\boldsymbol{x}}$ and $\boldsymbol{\beta}_{\boldsymbol{d}}$, as respectively shown for surge, sway, and yaw speeds:

$$E_u^x(\boldsymbol{\theta}_{\boldsymbol{u}}^{\boldsymbol{x}},\ \boldsymbol{\beta}_{\boldsymbol{u}}) = \sum_{i=1}^{i=k} E_{u_i}^x(\boldsymbol{\theta}_{\boldsymbol{u}}^{\boldsymbol{x}},\ \beta_{u_i}) = \sum_{i=1}^{i=k} \left(\boldsymbol{u_i} - \hat{\boldsymbol{u}}_{\boldsymbol{i}}(t, \boldsymbol{x}_{\boldsymbol{u_i}}, \boldsymbol{\theta}_{\boldsymbol{u}}^{\boldsymbol{x}}, \beta_{u_i})\right)^2, \tag{4.18}$$

$$E_v^x(\boldsymbol{\theta}_{\boldsymbol{v}}^{\boldsymbol{x}},\ \boldsymbol{\beta}_{\boldsymbol{v}}) = \sum_{i=1}^{i=k} E_{v_i}^x(\boldsymbol{\theta}_{\boldsymbol{v}}^{\boldsymbol{x}},\ \beta_{v_i}) = \sum_{i=1}^{i=k} \left(\boldsymbol{v_i} - \hat{\boldsymbol{v}}_{\boldsymbol{i}}(t, \boldsymbol{x}_{\boldsymbol{v_i}}, \boldsymbol{\theta}_{\boldsymbol{v}}^{\boldsymbol{x}}, \beta_{v_i})\right)^2, \tag{4.19}$$

$$E_r^x(\boldsymbol{\theta}_{\boldsymbol{r}}^{\boldsymbol{x}}) = \sum_{i=1}^{i=k} E_{r_i}^x(\boldsymbol{\theta}_{\boldsymbol{r}}^{\boldsymbol{x}}) = \sum_{i=1}^{i=k} \left(\boldsymbol{r_i} - \hat{\boldsymbol{r}}_{\boldsymbol{i}}(t, \boldsymbol{x}_{\boldsymbol{r_i}}, \boldsymbol{\theta}_{\boldsymbol{r}}^{\boldsymbol{x}})\right)^2. \tag{4.20}$$

Thus, this DEM method uses an implementation of the prediction error method philosophy [208]. In comparison to methods using the known predictor equation [12], which only predicts one step ahead based on the previous measurement, the DEM method can predict the speed profile for the whole time range based on $\boldsymbol{\theta}_{\boldsymbol{d}}^{\boldsymbol{x}}$ and $\boldsymbol{\beta}_{\boldsymbol{d}}$. Furthermore, the equations of motion need no linearisation, which often is the case (e.g. [245, 246]), and no direct accelerations need to be used. The extended Kalman filter of the IMU does use these accelerations to calculate its speeds, so they are implicitly nested in the cost functions.

4.6.3 Model Structure Comparison and Selection

Section 4.6.3.1 offers the comparison potential for the surge identification results with external data sets from a CFD study and from an empirical approach. Afterwards, Section 4.6.3.2 briefly lists the comparison possibilities solely using the data of this study.

4.6.3.1 Comparisons with External Data

Peeters et al. (2018 [197]) applied CFD to investigate the surge resistance of the Cogge, see Section 3.4 and 4.4.2 for more details. Figure 4.12 illustrated some of the CFD results where the Cogge had a draft of $T_{CFD} = 0.23$ m and a simulated surge speed of $u = 0.2$ or $u = 1.0$ $\frac{\text{m}}{\text{s}}$. Figure 4.12e and 4.12f demonstrate that, during the initial design phase, the steering-grid thruster at the bow protruded the vessel hull. The physical Cogge has no such protrusion, since its thrusters are fully embedded. In addition, these simulations were done with a total vessel height of 0.35 m, whereas the final hull has a height of approximately 0.43 m, if sensor extensions are neglected. Bearing these assumptions and discrepancies in mind, the CFD calculations resulted in the following second order approximation of the surge damping forces:

$$D_{CFD}(u) = 22.12u^2 + 0.10u. \tag{4.21}$$

Kristensen et al. (2013 [131]) extensively reported on an empirical approach based on the ITTC-1957 method [171] to estimate the damping forces of a vessel. Accordingly, the total resistance coefficient C_T can be approximated by (eq. 4.22), with R_T being the total resistance, S the wetted surface, and the following coefficients: C_F the frictional resistance, C_A the incremental resistance, C_{AA} air resistance, and C_R the residual resistance. Applying the method from Kristensen et al. (2013 [131]), the following estimations and calculations were made: (i) S according to (eq. 4.23), where ∇ denotes the displacement and L_{wl} the waterline length, (ii) C_F by (eq. 4.24), where Re represents the Reynolds number and ν the kinematic viscosity, (iii) $C_A = 0.0004$, given that the hull was not produced according to towing tank standards, and its surface roughness is more in line with larger vessels, (iv) $C_{AA} = 0.00007$ given that the vessel has plenty of extensions on its deck, and finally (v) for the estimation of C_R, Harvald et al. (1983 [103]) provided diagrams based on the length-displacement ratio M_d, prismatic coefficient C_P where C_M denotes the midship coefficient, and the Froude number F_r — see (eq. 4.25) for their definitions. This diagram estimation, C_{R_d}, should be corrected for several factors, $\sum C_{R_{corr}}$: the position of the centre of buoyancy, hull shape and form, bulbous bow shapes, and the $\frac{B}{T}$ ratio — see (eq. 4.26). Based on Appendix I from Kristensen et al. (2013 [131]),

$C_{R_d} = 0.001$, and only a correction for $\frac{B}{T}$ was added by the following equation: $C_{R_{corr,\frac{B}{T}}} = 0.16(\frac{B}{T} - 2.5) \times 10^{-3}$.

$$C_T = C_F + C_A + C_{AA} + C_R = \frac{R_T}{0.5\rho S u^2} \tag{4.22}$$

$$S = 0.99(\frac{\nabla}{T} + 1.9L_{wl}T), \quad \nabla = \frac{M}{\rho} \tag{4.23}$$

$$C_F = \frac{0.0075}{(log(Re) - 2)^2}, \quad Re = \frac{uL_{wl}}{\nu} \tag{4.24}$$

$$M_d = \frac{L_{wl}}{\nabla^{1/3}}, \quad C_P = \frac{C_B}{C_M}, \quad F_r = \frac{u}{\sqrt{gL_{wl}}} \tag{4.25}$$

$$C_R = C_{R_d} + \sum C_{R_{corr}} \tag{4.26}$$

Table 4.11 lists the additional measured, calculated, or estimated parameters of the geometry of the Cogge. The measured draft of 0.22 m would equal a vessel weight of 623 kg, and vice versa, the measured weight of 590 kg would generate a draft of 0.21 m. The latter weight and draft have been used for the calculations in this study. The geometry of the Cogge, with a $C_B = 0.95$, lies outside the boundaries of some parts of the empirical method of Kristensen et al. (2013 [131]). Consequently, it is not straightforward to read, or extrapolate, the right C_{R_d} from the diagrams, or to apply all these suggested C_R corrections; hence, only the $\frac{B}{T}$ correction was added. Considering these limitations, made assumptions, and the neglected additional corrections, the predicted damping forces by this empirical method can thus be reasonably assumed to serve as an underestimation of the actual damping forces. Calculating R_T via (eq. 4.22) with $u = 1.0$ $\frac{\text{m}}{\text{s}}$, $\rho = 997$ $\frac{\text{kg}}{\text{m}^3}$, $\nu = 1.15 \times 10^{-6}$ $\frac{\text{m}^2}{\text{s}}$ was used to define (eq. 4.27), by fitting a quadratic curve through this calculated point.

$$D_{Emp}(u) = 11.82u^2 \tag{4.27}$$

Table 4.11: Measured, calculated, or estimated parameters of the Cogge.

Parameter	Symbol	Measured	Calculated	Estimated	Units
Draft	T	0.22 ± 0.02	0.21	–	[m]
Length waterline	L_{wl}	4.75± 0.02	–	–	[m]
Mass	M	590 ± 10	623	–	[kg]
Midship section coefficient	C_M	–	–	0.99 [131]	[-]
Prismatic coefficient	C_P	–	0.96	–	[-]

4.6.3.2 Comparisons with Internal Data

In addition to the two external data comparisons of Section 4.6.3.1, this section briefly handles three approaches to compare the model structures in this section, based solely on the present experimental data. First, one can use both identification methods of Section 4.6.2 for the same model structures and see whether both methods independently achieve similar results, which might hint at a good underlying model structure. Second, one can compare the final cost of (eq. 4.13) between model structures for an identification method. Note that one should not compare these costs between identification methods, given their different cost function declarations. Third, for both identification methods, all the data have been split into a verification and a validation set. The former groups all the training missions, whereas the latter gathers the missions which were not used during the identification procedure. Table 4.12 lists these manually selected validation missions. These missions were chosen to be the missions with the highest initial conditions, i.e., vessel speeds. Accordingly, a robust test set of data is offered to investigate the model structures and identification methods of this study. This selection should also increase the performance of the FBM, which is more sensitive to the start conditions.

Table 4.12: Manually chosen validation missions.

Surge	**Sway**	**Yaw**
bow–ramp–m_2	left–ramp–m_2	cw–ramp–m_1
bow–step–m_1	left–stairs–m_2	cw–step–m_2
stern–ramp–m_1	right–step–m_2	ccw-stairs–m_1
stern–stairs–m_1		
dual–ramp–m_2		
dual–stairs–m_2		

4.6.4 Results

Section 4.6.4.1, 4.6.4.2, and 4.6.4.3 respectively discuss the results for the surge, sway, and yaw motion models. Each section starts with plotting experimental data, continues with the identification and comparison of their model structures, and ends with a suggested model selection.

4.6.4.1 Results of Surge Motion Models

Exemplary Data Surge Missions

Figure 4.18 summarises the relevant measured data, which were processed according to Section 4.6.1.3, from the first-step mission with both thrusters on. Figure 4.18a reveals that the measured n_b and n_s overshot before they reached their requested values. This behaviour offers a richer data set, and can also be noted in the measured $\dot{u}$. Figure 4.18b, and Figure 4.18c confirm that the sway speeds remained small compared to the surge speeds, and that the heading did not change much during the mission.

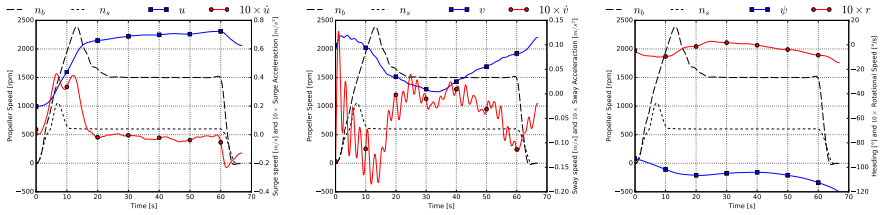

(a) Surge (b) Sway (c) Yaw

Figure 4.18: Data fetched during the first surge dual step mission: (a) surge speed and acceleration, (b) sway speed and acceleration, and (c) heading and yaw-rate.

Surge Model Structures Identification and Comparison

The surge motion sub-mode experiments enabled data to be recorded where the thrusters did not cooperate. These independent operation modes, in combination with the dual modes, might offer the most versatile data sets in this study. For this reason, all the surge models, $\mathcal{M}(\boldsymbol{\theta}_{\boldsymbol{u}}^{\boldsymbol{x}})$, have been identified by both the FBM and DEM, once using physical boundaries on the thruster parameters, and once with unbounded thruster coefficients, denoted by the superscripts ^{B} and ^{U} respectively. For both the bounded and unbounded training runs, the initial guesses $T_{n\nu_0}^{0,b} = T_{nn\nu_0}^{0,b} = T_{n\nu_0}^{0,s} = T_{nn\nu_0}^{0,s} = 0$. The initial guesses for $T_{nn_0}^{0,b} = \frac{13.7}{(1500)^2} \frac{\text{N}}{\text{rpm}^2}$ and $T_{nn_0}^{0,s} = \frac{135}{(1545)^2} \frac{\text{N}}{\text{rpm}^2}$ were calculated based on the towing tank data by assuming a purely quadratic fit to the data points at the highest measured propeller speeds, see Appendix B.

For the unbounded training, $T_{n\nu}^{0,b}, T_{nn\nu}^{0,b}, T_{n\nu}^{0,s}, T_{nn\nu}^{0,s} \in [0, -\infty]$, and $T_{nn}^{0,b}, T_{nn}^{0,s} \in [0, +\infty]$. For the bounded training $T_{nn}^{0,b} \in [0.85 \times T_{nn_0}^{0,b}, 1.15 \times T_{nn_0}^{0,b}]$, and $T_{nn}^{0,s} \in [0.25 \times T_{nn_0}^{0,s}, 1.10 \times T_{nn_0}^{0,s}]$. These boundaries aim to: (i) take into account the data measurement uncertainty of both thrusters [206], (ii) allow some slack, given that higher rotational speeds were used compared to the

towing tank data, (iii) study the now fully embedded steering grid, whereas it was not embedded in Appendix B, and (iv) investigate the installed flow straightener [194] in the stern thruster which was not installed during the towing tank experiments (see Section 5.4.1.1 and Appendix B). Finally, the $T^{0,b}_{n\nu}, T^{0,b}_{nn\nu}, T^{0,s}_{n\nu}, T^{0,s}_{nn\nu}$ had an upper limit of zero, and an lower limit which would induce a thrust reduction the size of the available thrust which was taken to be 85% of the initial guess. More precisely, these lower limits were calculated using the following data of two independent step missions: $n_b = 2700$ rpm, $u = 1.2$ $\frac{\text{m}}{\text{s}}$ for the bow, and $n_s = 1400$ rpm, $u = 0.8$ $\frac{\text{m}}{\text{s}}$ for the stern.

The initial guesses and the boundaries for the added mass and damping models stayed the same throughout all model structures for both the bounded and unbounded methods. The initial guess of $X_{\dot{u}} = 35.4$ $\frac{\text{Ns}^2}{\text{m}}$ equalled the upper limit of (eq. 3.5). To potentially compensate for the weight measurement accuracy, the high C_B, and the geometry of the Cogge, this added mass received the following training boundaries $X_{\dot{u}} \in [25, 75]$. The present damping parameters received an initial value of seven and the training limits $X_{uuu}, X_{uu}, X_u \in [0, 100]$. Evidently, if a damping or thruster parameter was not in $\boldsymbol{\theta}^{\boldsymbol{x}}_{\boldsymbol{u}}$ it was not used during its model fit.

Table 4.13 summarises the residuals of the bounded and unbounded FBM and DEM cost functions for all the surge model structures, i.e., (eq. 4.14) and (eq. 4.18) for $x \in [a, \cdots, i]$. Table 4.14 zooms in on the DEM^B by listing its identified coefficients. The coefficients for DEM^U, FBM^B, and FBM^U, can be respectively found in the Table D.1–D.3. Based on these identified coefficients, Figure 4.19 plots the predicted speed profiles, simulated by the differential equations, for all the model structures with a quadratic damping model, i.e., $\mathcal{M}(\boldsymbol{\theta}^{\boldsymbol{b}}_{\boldsymbol{u}})$, $\mathcal{M}(\boldsymbol{\theta}^{\boldsymbol{e}}_{\boldsymbol{u}})$, and $\mathcal{M}(\boldsymbol{\theta}^{\boldsymbol{h}}_{\boldsymbol{u}})$, for three validation and three verification cases. The bias term for each mission was determined by retraining (eq. 4.14) or (eq. 4.18) for only one mission using the identified coefficients and only allowing β_{u_i} to vary. For both the validation and the verification missions, the FBM^B seems to better capture the data compared to its unbounded alternative. For the bounded and unbounded DEM, there seems to be no significant difference, which can also be noted by the final costs of Table 4.13. In general, when judging the model structures on their ability to capture the shape of the data sets, the speed-independent thruster model, $\mathcal{M}(\boldsymbol{\theta}^{\boldsymbol{e}}_{\boldsymbol{u}})$, looks to perform the worst, which Table 4.13 might be confirming, given that this model structure consistently has a higher final cost compared to $\mathcal{M}(\boldsymbol{\theta}^{\boldsymbol{b}}_{\boldsymbol{u}})$ and $\mathcal{M}(\boldsymbol{\theta}^{\boldsymbol{h}}_{\boldsymbol{u}})$ for all the listed identification approaches.

Table 4.13: Final costs for the surge identification methods.

	$\boldsymbol{\theta}_u^a$	$\boldsymbol{\theta}_u^b$	$\boldsymbol{\theta}_u^c$	$\boldsymbol{\theta}_u^d$	$\boldsymbol{\theta}_u^e$	$\boldsymbol{\theta}_u^f$	$\boldsymbol{\theta}_u^g$	$\boldsymbol{\theta}_u^h$	$\boldsymbol{\theta}_u^i$
FBM^B	44,306.46	44,460.31	50,313.20	79,170.60	80,628.91	121,466.91	59,083.96	59,675.91	63,849.69
FBM^U	43,361.09	43,361.09	44,946.84	144,849.19	85,623.04	228,775.01	59,083.96	45,0793.14	63,572.62
DEM^B	13.69	14.36	18.25	35.64	45.28	92.83	19.13	20.77	23.67
DEM^U	13.69	14.24	15.31	36.19	45.33	92.83	19.14	20.79	23.69

Table 4.14: Identified surge model coefficients for bounded DEM.

	$\boldsymbol{\theta}_u^a$	$\boldsymbol{\theta}_u^b$	$\boldsymbol{\theta}_u^c$	$\boldsymbol{\theta}_u^d$	$\boldsymbol{\theta}_u^e$	$\boldsymbol{\theta}_u^f$	$\boldsymbol{\theta}_u^g$	$\boldsymbol{\theta}_u^h$	$\boldsymbol{\theta}_u^i$
cost	13.7	14.4	18.2	35.6	45.3	92.8	19.1	20.8	23.7
$X_{\dot{u}}$	25.7	25.0	25.0	75.0	75.0	58.6	30.5	39.8	27.7
X_{uuu}	8.11	0.00	0.00	25.0	0.00	0.00	12.8	0.00	0.00
X_{uu}	0.00	11.0	0.00	0.00	36.3	0.00	0.00	13.6	0.00
X_u	14.7	10.8	19.0	15.9	3.77	39.3	17.6	14.0	22.9
$T_{nn}^{0,b}$	6.92×10^{-6}	7.00×10^{-6}	7.00×10^{-6}	6.03×10^{-6}	6.02×10^{-6}	5.42×10^{-6}	5.50×10^{-6}	6.21×10^{-6}	6.99×10^{-6}
$T_{nn}^{0,s}$	2.62×10^{-5}	2.66×10^{-5}	2.75×10^{-5}	1.69×10^{-5}	1.62×10^{-5}	1.68×10^{-5}	2.58×10^{-5}	2.71×10^{-5}	2.81×10^{-5}
$T_{n\nu}^{0,b}$	-7.02×10^{-3}	-7.54×10^{-3}	-8.79×10^{-3}	0.00	0.00	0.00	0.00	0.00	0.00
$T_{n\nu}^{0,s}$	-2.67×10^{-2}	-2.78×10^{-2}	-3.00×10^{-2}	0.00	0.00	0.00	0.00	0.00	0.00
$T_{nn\nu}^{0,b}$	0.00	0.00	0.00	0.00	0.00	0.00	-3.55×10^{-7}	-1.42×10^{-6}	-2.98×10^{-6}
$T_{nn\nu}^{0,s}$	0.00	0.00	0.00	0.00	0.00	0.00	-1.52×10^{-5}	-1.70×10^{-5}	-1.89×10^{-5}

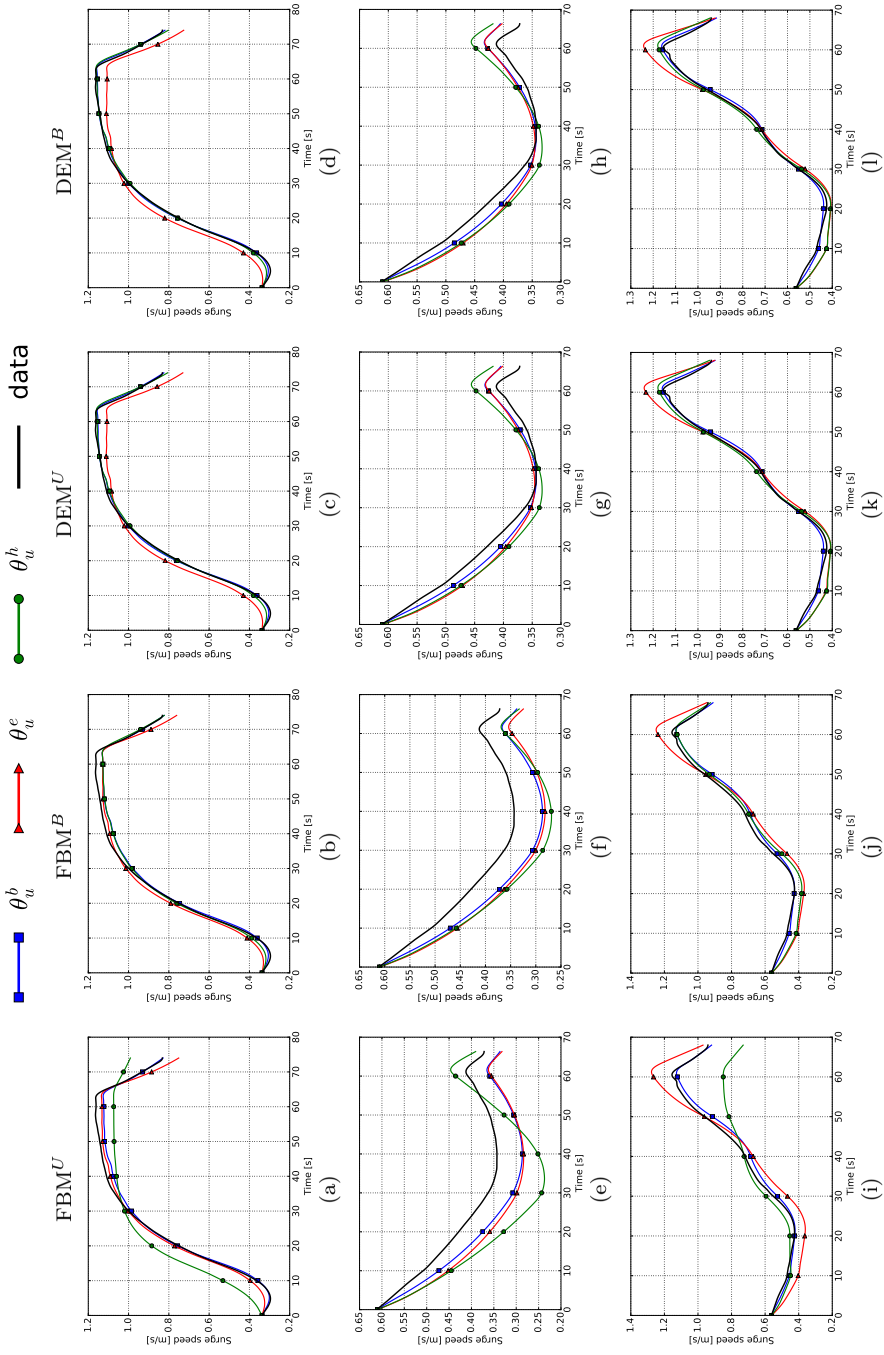
FBM^U
FBM^B
DEM^U
DEM^B
θ_u^b
θ_u^e
θ_u^h
data
Surge speed [m/s]
Time [s]
(a)
(b)
(c)
(d)
(e)
(f)
(g)
(h)
(i)
(j)
(k)
(l)

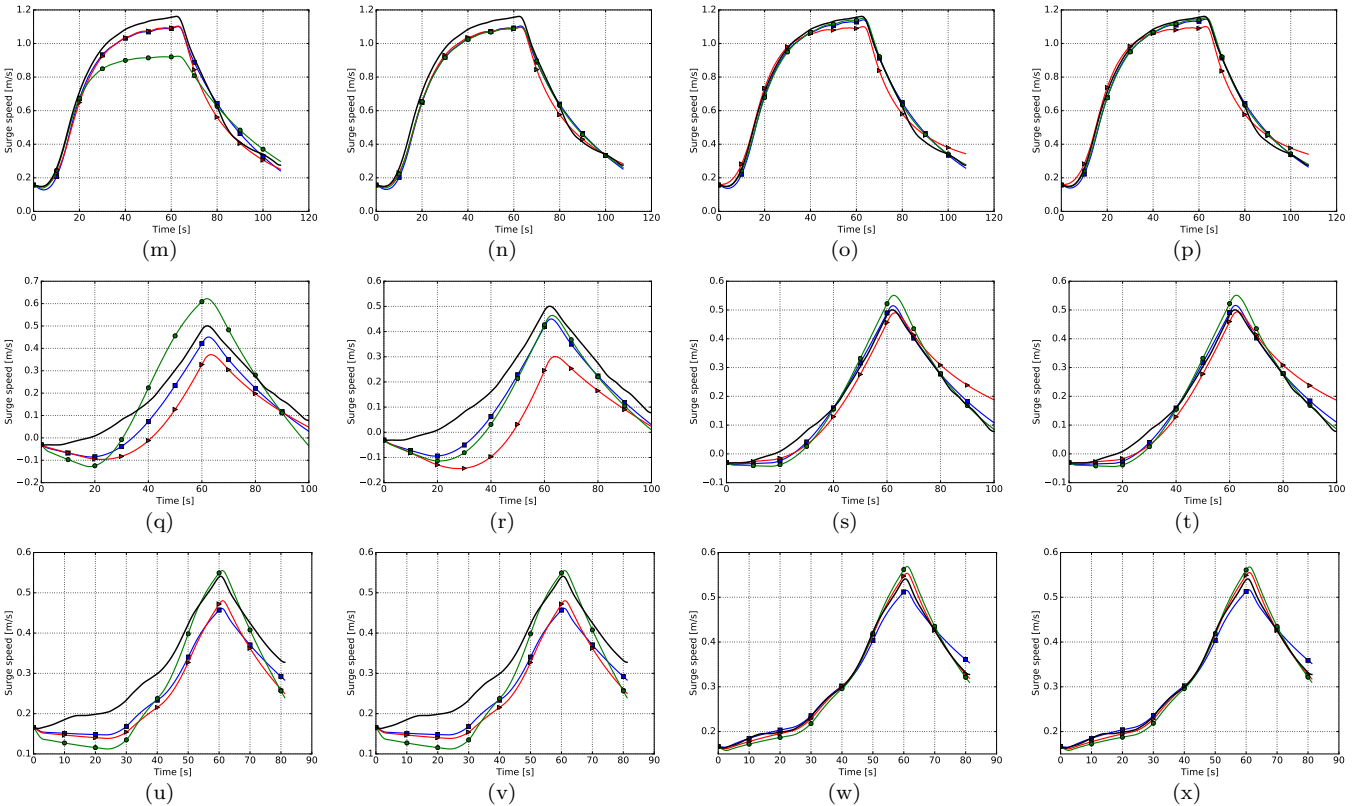

Figure 4.19: Comparison FBM^B, FBM^U, DEM^B, and DEM^U identification methods for the different thruster models with quadratic damping models: (a–d) validation mission: bow–step–m_1; (e–h) validation mission: stern–ramp–m_1; (i–l) validation mission: dual–stairs–m_2; (m–p) verification mission: bow–step–m_2; (q–t) verification mission: stern–ramp–m_2; and (u–x) verification mission: dual–stairs–m_1.

Surge Model Selection

Figure 4.20a–4.20d compares the identified cubic damping models for the three different thruster models, i.e., $\mathcal{M}(\boldsymbol{\theta}_{\boldsymbol{u}}^{\boldsymbol{a}})$, $\mathcal{M}(\boldsymbol{\theta}_{\boldsymbol{u}}^{\boldsymbol{d}})$, and $\mathcal{M}(\boldsymbol{\theta}_{\boldsymbol{u}}^{\boldsymbol{g}})$, with the curves defined by (eq. 4.21) and (eq. 4.27). The damping models for the speed-independent thruster model seem to be consistently too large for both the FBM^{B,U} and DEM^{B,U}. Figure 4.20e–4.20h similarly contrasts the identified bollard thrust forces of the bow thruster, together with its experimental data — where this thruster was not placed in a ship hull. Note that this comparison was not made for the stern thruster due to its installed flow straightener which would make it an unfair benchmark. Evidently, the bollard thrust forces for the bounded FBM and DEM stay close to the experimental data. However, both unbounded methods do stay within a close range too, which might hint at a good model structure and/or identification methodology. Finally, the conventional thruster model seems to perform well according to Table 4.13, Figure 4.19, and Figure 4.20, for both DEM^{B} and DEM^{U}. Furthermore, given the small differences in identified thruster coefficients between DEM^{B} and DEM^{U}, Figure 4.21 illustrates the three different damping models for this thruster model identified by DEM^{B}. In particular, Figure 4.21a–4.21c shows the simulated model responses for the three validation cases, Figure 4.21d compares the damping forces with the curves from (eq. 4.21) and (eq. 4.27), and Figure 4.21e and Figure 4.21f predict the bollard thrust forces.

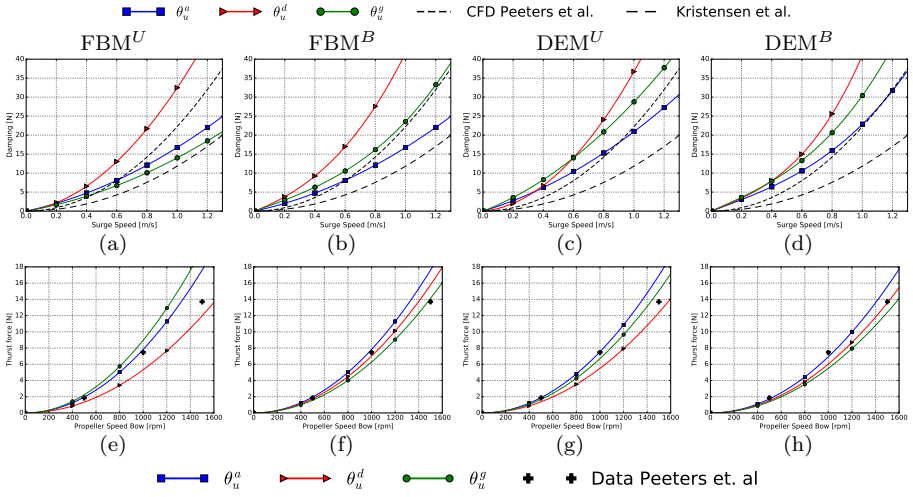

Figure 4.20: Comparison of bounded and unbounded FBM and DEM surge identification methods for the cubic damping models: (a–d) predicted damping models in comparison with Peeters et al. (2018 [197]), i.e., (eq. 4.21) and Kristensen et al. (2013 [131]), i.e., (eq. 4.27); and (e–h) predicted bollard pull forces of the bow thruster in comparison with the towing tank data from Peeters et al. (2020 [206]).

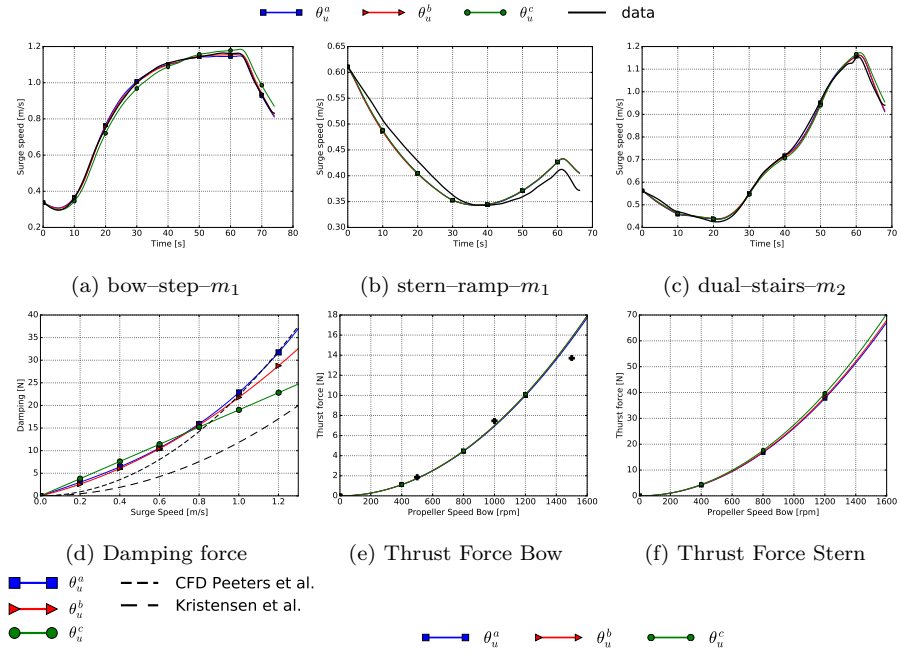

(a) bow–step–m_1 (b) stern–ramp–m_1 (c) dual–stairs–m_2

(d) Damping force (e) Thrust Force Bow (f) Thrust Force Stern

Figure 4.21: Comparisons of different damping models for the conventional thruster model, identified with the DEM^B: (a–c) the three longitudinal validation missions, (d) the predicted damping forces compared with Peeters et al. (2018 [197]), i.e., (eq. 4.21), and Kristensen et al. (2013 [131]), i.e., (eq. 4.27); (e) predicted bollard thrust bow compared with towing tank data from Peeters et al. (2020 [206]), and (f) predicted bollard stern thrust with installed flow straightener; hence the towing tank data was not plotted.

4.6.4.2 Results of Sway Motion Models

Exemplary Data Sway Missions

Figure 4.22 outlines the relevant captured data, which were processed according to Section 4.6.1.3, from the first ramp mission where the vessel swayed to the right. This figure displays that both propellers have a lower limit on their rotational speed, hence the straight parts in the ramp profiles of the propeller speeds. Figure 4.22c reveals that although the heading oscillated a bit during the mission the vessel stayed rather straight. Finally, Figure 4.22a shows a rather small surge speed compared to the sway speed of Figure 4.22b.

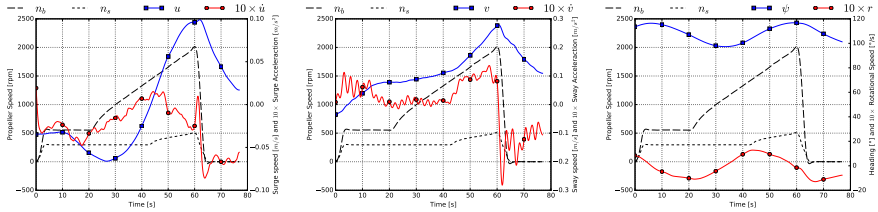

(a) Surge (b) Sway (c) Yaw

Figure 4.22: Data fetched during the first transversal right ramp mission: (a) surge speed and acceleration, (b) sway speed and acceleration, and (c) heading and yaw-rate.

Sway Model Structures Identification and Comparison

Considering the good DEM^B performance in Section 4.6.4.1, similar results for the sway model identifications will be exclusively discussed here. The determination of the initial parameter estimations and their training boundaries happened similarly to the surge model approach. Thus, according to (eq. 3.6), the added mass $Y_{\dot{v}} = 375\ \frac{\text{Ns}^2}{m}$, with the limits $Y_{\dot{v}} \in [365, 583]$ which aim to account for the vessel weight accuracy and its literature-divergent geometry. The damping terms started at 500 and had the boundaries of $Y_{vvv}, Y_{vv}, Y_v \in [0, 1.0 \times 10^4]$.

Taking into consideration that: (i) the surge experiments had the most versatile data sets, (ii) Section 3.2.4.1 assumed the surge or sway wake effect differences to be negligible, and (iii) both the bounded and unbounded FBMs and DEMs identified speed-dependent thruster coefficients in the same order of magnitude, the start estimations for the coefficients, $T^{90,b}_{n\nu_0}, T^{90,b}_{nn\nu_0}$, and $T^{90,s}_{n\nu_0}, T^{90,s}_{nn\nu_0}$, were selected to equal the values of their DEM^b identified $T(0°)$ equivalents for surge; see Table 4.15. In order to consider the angle dependency of the thrust deduction (see Appendix B), t, lower and upper limits of 90% and 110% of their initial value were given to these parameters.

The initial guesses for $T^{90,b}_{nn_0} = \frac{14.52}{(1500)^2}\ \frac{\text{N}}{\text{rpm}^2}$ and $T^{90,s}_{nn_0} = \frac{26.15}{(617)^2}\ \frac{\text{N}}{\text{rpm}^2}$ were calculated based on the towing tank data by assuming a purely quadratic fit to the highest data points closest to the highest propeller speed of the experiments; see Appendix B. Here too, upper and lower limits of 90% and 110% were implemented for both thrusters. These boundaries aimed to: (i) take into account the data uncertainty of both thrusters [206], and (ii) allow some slack, given that higher rotational speeds were used compared to the towing tank data, (iii) and the fact that the steering grid was now inside a hull. Note that there is no flow straightener in the transversal four-channel thruster outlets.

Table 4.15 states the DEM^B identified coefficients for $\mathcal{M}(\boldsymbol{\theta}_{\boldsymbol{v}}^{\boldsymbol{x}})$. Thereupon, Figure 4.23 predicts the sway speed profiles for three validation and three verification missions for the quadratic damping models, i.e., $\mathcal{M}(\boldsymbol{\theta}_{\boldsymbol{v}}^{\boldsymbol{b}})$, $\mathcal{M}(\boldsymbol{\theta}_{\boldsymbol{v}}^{\boldsymbol{e}})$, and $\mathcal{M}(\boldsymbol{\theta}_{\boldsymbol{v}}^{\boldsymbol{h}})$. The bias terms for each mission were determined similarly to the surge speed prediction of Section 4.6.4.1, and the negative initial sway speeds of two of the validation missions were taken into account in their differential equations. Both Table 4.15 and Figure 4.23 indicate minor differences between the different model structures.

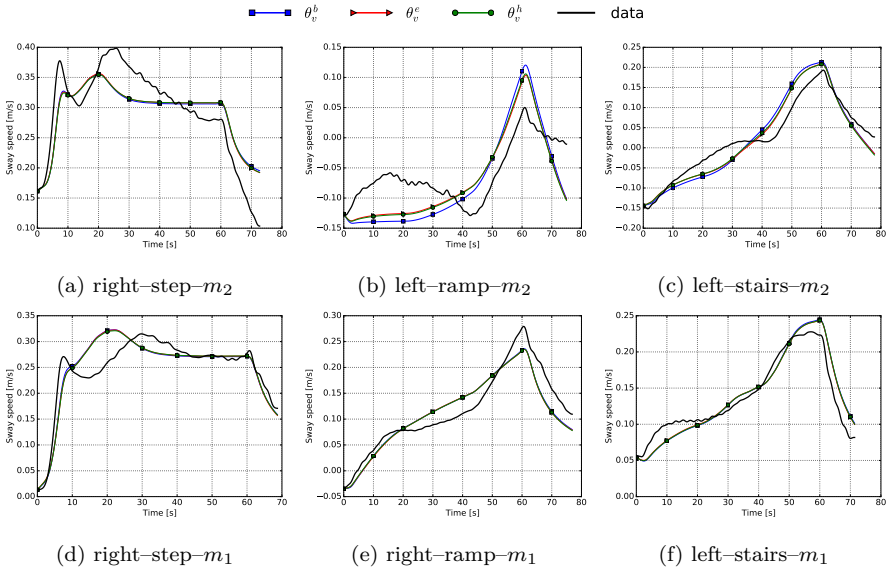

(a) right–step–m_2 (b) left–ramp–m_2 (c) left–stairs–m_2

(d) right–step–m_1 (e) right–ramp–m_1 (f) left–stairs–m_1

Figure 4.23: Comparison of different thruster models using the quadratic damping model: (a–c) the validation missions and (d–f) the verification missions.

Sway Model Selection

With the currently available training data, no model structure seems to outperform its competitors. Figure 4.24a–4.24c depicts the sway speed predictions for three verification missions for the different damping models using the conventional thruster model. These figures indicate little differences between the linear, quadratic, or cubic damping models. Figure 4.24d predicts these damping forces, and Figure 4.24e, and Figure 4.24f evaluate the bollard pull forces for the bow and stern thruster in comparison with their towing tank data.

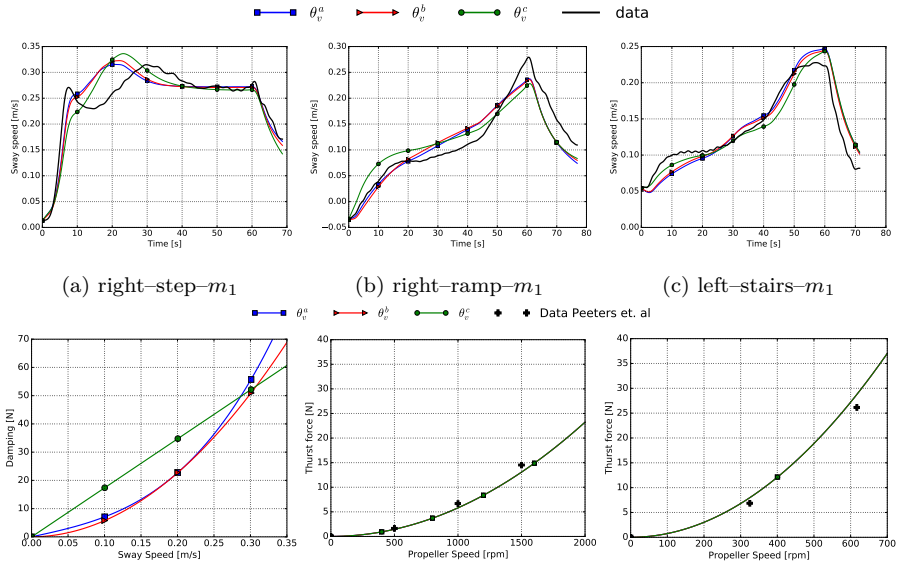

(a) right–step–m_1 (b) right–ramp–m_1 (c) left–stairs–m_1

(d) Damping force (e) Thrust force bow (f) Thrust force stern.

Figure 4.24: Comparisons of different damping models for the conventional thruster model, identified with the bounded DEM: (a–c) the three verification missions, (d) the predicted damping forces, and (e, f) respectively show the identified bollard thrusts of the bow and stern thrusters compared with their towing tank data from Peeters et al. (2020 [206]).

4.6.4.3 Results of Yaw Motion Models

Exemplary Data Yaw Missions

Figure 4.25 gives an overview of the relevant captured data, which were processed according to Section 4.6.1.3, from both stairs missions where the Cogge rotated counter-clockwise. The trajectory plots of Figure 4.25b, and Figure 4.25d demonstrate that there was less wind during the first run of the experiments compared with the second run, given that for the same inputs, the trajectory of the Cogge during m_2 was more spread out in the diagonal XY-direction. Nevertheless, Figure 4.25a, and Figure 4.25c illustrate that similar yaw-rates were achieved during both missions.

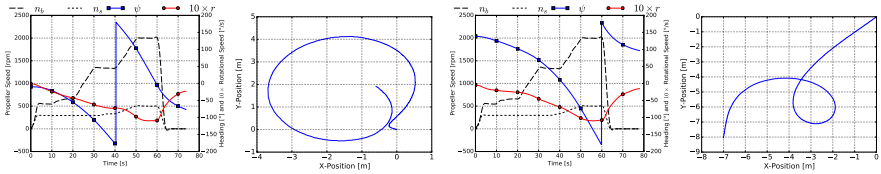

(a) Yaw–m_1 (b) Trajectory–m_1 (c) Yaw–m_2 (d) Trajectory–m_2

Figure 4.25: Data fetched during the first and second rotation counter-clockwise stairs missions: (a,c) heading and yaw rate, and (b,d) position of the stern GNSS antenna.

Yaw Model Structures Identification and Comparison

Since the yaw experiments used the same thruster angles and propeller speed configurations as the sway experiments, the exact same initial conditions and parameter boundaries were used for these thruster coefficients. The yaw moment of inertia was estimated according to $I_z = \mathrm{m}(0.2536\mathrm{L})^2 = 878\ \mathrm{kgm}^2$ [146, 172]. The initial guess $N_{\dot{r}} = 845\ \frac{\mathrm{Nms}^2}{\mathrm{rad}}$, based on (eq. 3.7), received the boundaries $N_{\dot{r}} \in [845, 1245]$ which aim to compensate for the geometry of the Cogge. In addition, all the damping parameters started at 500 and were bounded to $N_{rrr}, N_{rr}, N_r \in [0, 1.0 \times 10^{04}]$.

Table 4.16 lists the coefficients for $\mathcal{M}(\boldsymbol{\theta}_{\boldsymbol{r}}^{\boldsymbol{x}})$, identified by the DEM^B. Subsequently, Figure 4.26 shows simulations of the yaw rates for three validation and three verification missions for the quadratic damping models, i.e., $\mathcal{M}(\boldsymbol{\theta}_{\boldsymbol{r}}^{\boldsymbol{b}})$, $\mathcal{M}(\boldsymbol{\theta}_{\boldsymbol{r}}^{\boldsymbol{e}})$, and $\mathcal{M}(\boldsymbol{\theta}_{\boldsymbol{r}}^{\boldsymbol{h}})$. Note that the yaw missions have no bias terms. In the same vein as the sway results of the Sway Model Structures Identification and Comparison, both Table 4.16 and Figure 4.26 suggest minor differences between the different yaw model structures.

Yaw Model Selection

Comparable with the Sway Model Selection, no $\mathcal{M}(\boldsymbol{\theta}_{\boldsymbol{r}}^{\boldsymbol{x}})$ seems to capture the yaw-rate data better than its alternatives. Figure 4.27a–4.27c compares the conventional thruster model for the three damping models on the three validation missions. These comparisons indicate a better curve fitting for the non-linear damping models. Finally, Figure 4.27d illustrates the different predicted damping moments, and Figure 4.27e and Figure 4.27f plot the computed bollard thrust forces for the bow and stern thruster.

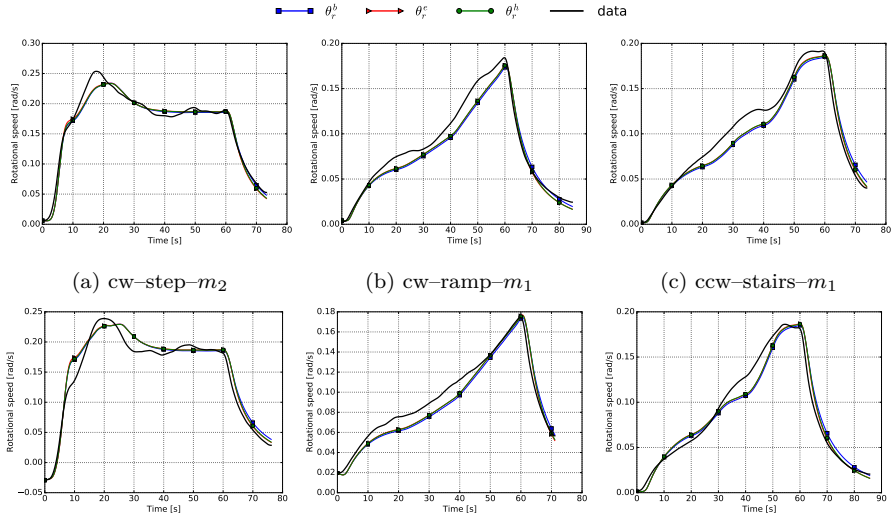

(a) cw–step–m_2 (b) cw–ramp–m_1 (c) ccw–stairs–m_1

(d) ccw–step–m_2 (e) ccw–ramp–m_1 (f) cw–stairs–m_2

Figure 4.26: Comparison of different thruster models for the quadratic damping model: (a–c) the validation missions and (d–f) the verification missions.

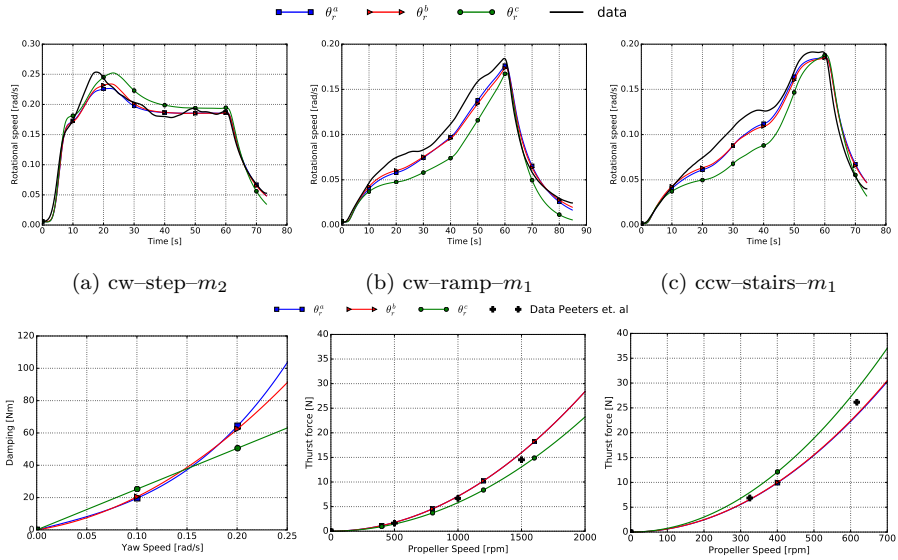

(a) cw–step–m_2 (b) cw–ramp–m_1 (c) ccw–stairs–m_1

(d) Damping moment (e) Thrust force bow (f) Thrust force stern

Figure 4.27: Comparisons of different damping models for the conventional thruster model, identified with the bounded DEM: (a–c) the three validation missions, (d) the predicted damping moments, and (e,f) respectively show the identified bollard thrusts of the bow and stern thruster compared with their towing tank data from Peeters et al. (2020 [206]).

Table 4.15: Identified sway model coefficients for the bounded DEM.

	$\boldsymbol{\theta_v^a}$	$\boldsymbol{\theta_v^b}$	$\boldsymbol{\theta_v^c}$	$\boldsymbol{\theta_v^d}$	$\boldsymbol{\theta_v^e}$	$\boldsymbol{\theta_v^f}$	$\boldsymbol{\theta_v^g}$	$\boldsymbol{\theta_v^h}$	$\boldsymbol{\theta_v^i}$
cost	10.1	10.6	12.8	10.4	11.0	14.1	10.4	10.8	12.6
$Y_{\dot{v}}$	430.26	440.51	583.00	569.82	583.00	583.00	547.97	545.61	583.00
Y_{vvv}	1424.59	0.00	0.00	1732.56	0.00	0.00	1663.00	0.00	0.00
Y_{vv}	0.00	557.57	0.00	0.00	682.70	0.00	0.00	616.06	0.00
Y_v	56.43.7	1.70	173.44	68.62	3.26	226.31	67.87	9.1	195.21
$T_{nn}^{90,b}$	5.81×10^{-6}	5.81×10^{-6}	5.81×10^{-6}	5.81×10^{-6}	5.81×10^{-6}	5.81×10^{-6}	5.81×10^{-6}	5.81×10^{-6}	5.81×10^{-6}
$T_{nn}^{90,s}$	7.56×10^{-5}	7.56×10^{-5}	7.56×10^{-5}	7.56×10^{-5}	7.56×10^{-5}	7.56×10^{-5}	7.56×10^{-5}	7.56×10^{-5}	7.56×10^{-5}
$T_{n\nu}^{90,b}$	-7.72×10^{-3}	-8.29×10^{-3}	-9.67×10^{-3}	0.00	0.00	0.00	0.00	0.00	0.00
$T_{n\nu}^{90,s}$	-2.40×10^{-2}	-2.50×10^{-2}	-3.30×10^{-2}	0.00	0.00	0.00	0.00	0.00	0.00
$T_{nn\nu}^{90,b}$	0.00	0.00	0.00	0.00	0.00	0.00	-3.91×10^{-07}	-1.56×10^{-6}	-3.28×10^{-6}
$T_{nn\nu}^{90,s}$	0.00	0.00	0.00	0.00	0.00	0.00	-1.37×10^{-5}	-1.53×10^{-5}	-1.70×10^{-5}

Table 4.16: Identified yaw model coefficients for the bounded DEM.

	$\boldsymbol{\theta_r^a}$	$\boldsymbol{\theta_r^b}$	$\boldsymbol{\theta_r^c}$	$\boldsymbol{\theta_r^d}$	$\boldsymbol{\theta_r^e}$	$\boldsymbol{\theta_r^f}$	$\boldsymbol{\theta_r^g}$	$\boldsymbol{\theta_r^h}$	$\boldsymbol{\theta_r^i}$
cost	2.64	2.90	7.41	2.4	2.67	10.72	2.39	2.68	8.14
$N_{\dot{r}}$	845.00	845.00	845.00	887.07	877.95	969.59	845.00	845.00	845.00
N_{rrr}	4158.99	0.00	0.00	5278.05	0.00	0.00	4873.16	0.00	0.00
N_{rr}	0.00	1067.49	0.00	0.00	1282.86	0.00	0.00	1218.23	0.00
N_r	153.98	97.57	252.29	175.66	102.54	342.74	173.49	108.28	292.55
$T_{nn}^{90,b}$	7.10×10^{-6}	7.10×10^{-6}	5.81×10^{-6}	7.10×10^{-6}	7.10×10^{-6}	5.81×10^{-6}	7.10×10^{-6}	7.10×10^{-6}	5.81×10^{-6}
$T_{nn}^{90,s}$	6.18×10^{-5}	6.22×10^{-5}	7.56×10^{-5}	6.18×10^{-5}	6.18×10^{-5}	7.56×10^{-5}	6.18×10^{-5}	6.18×10^{-5}	7.27×10^{-5}
$T_{n\nu}^{90,b}$	-6.32×10^{-3}	-6.79×10^{-3}	-9.67×10^{-3}	0.00	0.00	0.00	0.00	0.00	0.00
$T_{n\nu}^{90,s}$	-2.40×10^{-2}	-2.50×10^{-2}	-3.30×10^{-2}	0.00	0.00	0.00	0.00	0.00	0.00
$T_{nn\nu}^{90,b}$	0.00	0.00	0.00	0.00	0.00	0.00	-3.20×10^{-7}	-1.28×10^{-6}	-3.28×10^{-6}
$T_{nn\nu}^{90,s}$	0.00	0.00	0.00	0.00	0.00	0.00	-1.67×10^{-5}	-1.87×10^{-5}	-2.08×10^{-5}

4.6.5 Discussion

When investigating the results of Section 4.6.4, the modelling assumptions and limitations of Section 3.2.1 need to be kept in mind. The provided exemplary mission data sets — see Exemplary Data Surge Missions, Exemplary Data Sway Missions, and Exemplary Data Yaw Missions — already aided to judge the adequacy of these assumptions. In addition, Figure 4.28 sheds more light on the neglected degrees of freedom, i.e., roll, pitch, and heave, for three step missions of the studied motions of surge, sway, and yaw. This figure reveals that the pitch angle did not vary much for these missions. The roll angle varied more compared to this pitch angle, and even changed almost 3° during the rotational manoeuvre. The plotted heave represents the motions of the IMU. Evidently, these neglected degrees of freedom do impact the hydrodynamics of the vessel.

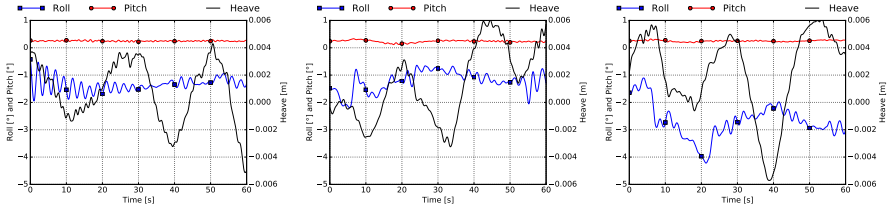

(a) dual–step–m_1 (b) right–step–m_1 (c) cw–step–m_1

Figure 4.28: Roll, pitch, and heave for three step missions in the three different motion modes: (a) dual–step–m_1, (b) right–step–m_1, and (c) cw–step–m_1.

Bearing the just-mentioned assumptions and limitations in mind, the conventional thruster models, i.e., $\mathcal{M}(\boldsymbol{\theta}_{\boldsymbol{u}}^{\boldsymbol{a}})$, $\mathcal{M}(\boldsymbol{\theta}_{\boldsymbol{u}}^{\boldsymbol{b}})$, and $\mathcal{M}(\boldsymbol{\theta}_{\boldsymbol{u}}^{\boldsymbol{c}})$, seem to outperform their alternative thruster models for the surge motion according to: (i) their cost function results for both the FBM and the DEM — see Table 4.13; (ii) their predictions of both validation and verification missions — see Figure 4.19; and (iii) their comparison with the external CFD and empirical methods — see Figure 4.20 and Figure 4.21. This combination of evidence might hint that these model structures best capture the occurring hydrodynamics. However, for the yaw and sway motion, there seems to be no real significant performance difference between the different thruster models. Accordingly, Figure 4.29 attempts to provide more insights into why this might be the case, by plotting the longitudinal or transversal pseudo-advanced speed ratios for surge, sway, and yaw step missions. The vessel speed was taken as advance speed to calculate these ratios; however, the propeller itself does not move in this speed direction, hence the name pseudo-advanced speed ratio. It can be seen that both thrusters achieved higher pseudo-advanced speed ratios in surge than in sway or yaw motion.

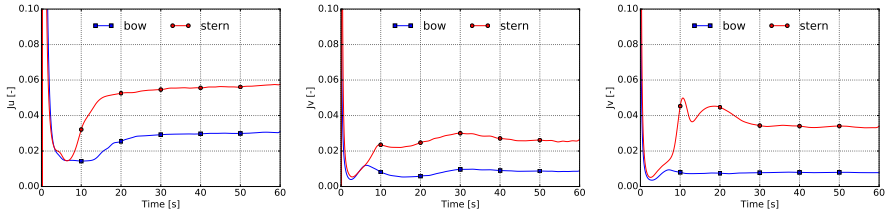

(a) dual–step–m_1 (b) right–step–m_1 (c) cw–step–m_1

Figure 4.29: Pseudo longitudinal, Ju, or transversal, Jv, advance speed ratios, at both thrusters for a three-step mission in the three different motion modes: (a) dual–step–m_1, (b) right–step–m_1, and (c) cw–step–m_1.

Whether or not the conventional thruster models of this study capture the conventional advance speed effect of a normal propeller configuration might not be determinable with the current data. It might also be the case that this conventional model structure succeeds in approximating another physical phenomena. Nevertheless, both speed-dependent thruster models of this study, i.e., (eq. 3.25) and (eq. 3.28), perform better than the speed-independent thruster model, (eq. 3.27), for the surge missions, which did induce higher vessel speeds compared to the sway and yaw cases. For the latter two motion cases, the simpler bollard thrust model (eq. 3.27) seems to suffice to capture the vessel behaviour. For all motions, the damping forces or moments seem to be capturable with only two parameters: a combination of a linear and a quadratic or cubic term. Consequently, it was demonstrated that a variety of model structures can capture the decoupled hydrodynamic behaviour of the Cogge.

Furthermore, the drag equation can offer more insights in the ship resistance of the Cogge:

$$F_{drag} = C_D A \frac{\rho u^2}{2}, \tag{4.28}$$

with F_{drag} the drag force, A the frontal area, and C_D the drag coefficient. For example, the C_D of a sphere and half a sphere respectively equal 0.47 and 0.42 for Re around 10^4 [49]. The surge damping results from this section (e.g. the conventional thruster model with a quadratic damping model, i.e., $\boldsymbol{\theta}_{\boldsymbol{u}}^{\boldsymbol{b}}$ from Table 4.14), the deep water CFD results (see Table 4.8, and (eq. 4.21)), and the empirical method (eq. 4.27), can be used to estimate the C_D of the Cogge. In order to estimate these coefficients, A can be calculated based on the vessel draft and beam, hence the air resistance will be neglected. Note that the CFD results used a draft of 0.23 m, whereas the experiments and empirical method assumed a draft of 0.21 m. For example, at $u = 1.0$ $\frac{\text{m}}{\text{s}}$ and $Re = 4.2 \times 10^6$: the CFD results generate a $C_D = 0.31$ (i.e. based on (eq. 4.21)), the experiments give $C_D = 0.33$ (i.e. based on $\boldsymbol{\theta}_{\boldsymbol{u}}^{\boldsymbol{b}}$), whereas the empirical method predicts $C_D = 0.18$ (i.e. based on eq. 4.27). Hence, a good alignment

between the CFD and outdoor experiments can be found, and the empirical method seems to underestimate the vessel drag. As discussed in Section 4.6.3.1, this empirical method is based on sea-going vessels with different geometries than the Cogge, which has a high block coefficient of $C_B = 0.95$ and length-beam ratio of $\frac{L}{B} = 7.6$. Therefore, not all corrections of the empirical method could be applied and the dimensions of the Cogge fell outside the boundaries of some parts of this empirical method, which might explain this underestimation. In comparison, based on the CFD results of Table 4.8, the KVLCC2 (with $C_B = 0.81$ and $\frac{L}{B} = 5.5$) has a $C_D = 0.09$, with $u = 0.981\ \frac{\text{m}}{\text{s}}$ and $Re = 5.9 \times 10^6$. Therefore, there seems to be room to improve the hydrodynamic design (i.e. decrease the ship resistance) of the Cogge which would decrease its power consumption.

Be noted that, running the sway and yaw models without limitations on their speed-dependent thruster parameters, i.e., $T_{n\nu}^{90,b/s}, T_{nn\nu}^{90,b/s} \in [0, -\infty]$, resulted in similar identification results where the speed-dependent thrust losses became assigned to only one thruster. This assignment might have been caused due to the fact that both propellers received the same shapes of input signals. Future work could add the no-yaw or no-sway constraints to the cost functions of these sway or yaw modes, which might reduce or avoid this identification effect.

Future work could also focus on investigating the coupled equations of motion, where the addition of the roll motion might be beneficial, considering the data of Figure 4.28. Likewise, the propeller dynamics [26, 192, 298] or the potential thruster-thruster interactions [59] could be investigated. These interactions might be present when the outflow of the steering-grid points towards the stern. Adding a wind sensor and explicitly modelling this disturbance should also offer a better performance than the currently implemented bias terms which were included to capture these effects. Based on Figure 4.21, the installed flow straightener seems to have significantly decreased the thrust force of the four-channel thruster. Hence, it might be better to replace this configuration with a rudder in the future. The identification methods used need not be restricted to the suggested model structures or the utilised vessel and its actuators. For example, a similar approach could be applied to the real-size watertrucks, which would eliminate the scale effects [64] that would occur when one extrapolates the presently identified models. The small scale factor of eight, however, should help in decreasing these scale effects [100].

4.7 Conclusion

This chapter identified (***RO*2.2**) hydrodynamic models for inland vessels.

It was shown that virtual rudder inputs, and the measured resultant heading changes, suffice to identify both symmetrical and asymmetrical transfer function models to capture the turning behaviour of a differentially-steered vessel. Furthermore, the theoretical propeller-characteristics based thrust model provided an adequate bollard pull data representation, which got confirmed by means of a bias–variance trade-off, and can be extended with an angle-dependent thrust deduction function for both propulsion systems. In addition, a multilayer feedforward neural network with Bayesian regulation exemplified a second modelling approach, which is inherently capable to model complex nonlinear functions and could offer more protection against the non-physical over-fitting of data.

Finally, additional test manoeuvres were suggested and conducted to help identify the decoupled equations of motion for surge, sway, and yaw of the Cogge, of which all experimental data sets can be found in the Supplementary Materials of Peeters et al. (2020 [203]). Furthermore, the CFD-derived surge damping models, the empirical data, and the bollard pull data served as external validation data sets for the identification of the surge model. The decoupled model identification compared two methods, one based on the instantaneous force balance, and the other one based on the integrating of the differential equations of motion. Subsequently, the conventional thruster model seemed to be a good model structure for the surge motion of the Cogge. Whereas, speed-independent thrust models seem to suffice for the yaw and sway motions. Finally, cubic or quadratic models seemed to suit to predict the damping forces or moments for surge, sway, and yaw.

These identified models partly answer **RQ2**. The first part of the answer, their derivation (***RO*2.1**), can be found in Chapter 3.

Perception and Motion Control of Unmanned Inland Cargo Vessels

"The less you understand the world, the easier it is to make a decision [252]."

Nassim Nicholas Taleb

Figure 5.1: The Statue of Marduk with his servant dragon [284].

This chapter investigates the third research question (**RQ3**), by providing the perception (***RO*3.1**) and motion control (***RO*3.2**) systems for USVs. Parts of this chapter were previously published as:

[199] G. Peeters, M. Kotzé, M. R. Afzal, T. Catoor, S. Van Baelen, P. Geenen, M. Vanierschot, R. Boonen and P. Slaets. "An unmanned inland cargo vessel: Design, build, and experiments". In: *Ocean Eng.* 201.107056 (2020), p. 17. DOI: 10.1016/j.oceaneng.2020.107056

[196] G. Peeters, T. Catoor, M. R. Afzal, M. Kotzé, P. Geenen, S. Van Baelen, M. Vanierschot, R. Boonen and P. Slaets. "Design and build of a scale model unmanned inland cargo vessel: Actuation and control architecture". English. In: *MTEC/ICMASS 2019*. Vol. 1357. 1. Institute of Physics Publishing, 2019. DOI: 10.1088/1742-6596/1357/1/012016

[269] S. Van Baelen, H. Shin, G. Peeters, M. R. Afzal, G. Yayla and P. Slaets. "Preliminary results on increased situational awareness for inland vessels using onboard lidar." In: *Proc. of Oceans 2020*. In press, ISBN: 978-1-7281-5446-6. Singapore, 2020

5.1 Introduction

An unmanned or automated vessel needs to perceive and interact with its environment in order to navigate. Therefore, Section 5.2 details the current perception systems for the Cogge, and Section 5.3 handles its present motion control configuration. Afterwards, Section 5.4 describes the first interactions between both systems, i.e., the first experiments with the Cogge. Finally, Section 5.5 concludes this chapter.

To understand the environmental settings in which the vessel could sail, the following arbitrary differentiation based on the present obstacles could be made: (**E1**) static known obstacles, (**E2**) static unknown obstacles, (**E3**) dynamic known obstacles, and (**E4**) dynamic unknown obstacles. Here, obstacles envelop both the waterway infrastructure (e.g. bridges, locks, quays, and waterway cross-sections), and other nearby vessels. The adjective *known* points to the information (e.g. geometry, pose, and velocity) availability of the objects, whereas the opposite holds for the *unknown* objects. From the moment that one object in the environment is unknown or dynamic, the environment changes to its associated description. It is readily understood that other environmental differentiations could be made, depending on the preferred level of analysis.

5.2 Perception for Inland USVs

These four environments (**E1**–**E4**) seem to demand different sensor capabilities from the vessel on the one hand, and different risk and safety analyses on the other hand. The former should provide the vessel with both navigational information of itself and perceptive information of its ambient environment, respectively discussed in Section 5.2.2 and Section 5.2.3. First, Section 5.2.1 covers the implemented, bottom-up, risk and safety analyses approach. The in-depth investigations of these analyses falls out of the scope of this thesis.

5.2.1 Risk and Safety Analyses

Although there currently exists little research on industrial cargo USVs [148], their risk and safety analyses have been investigated [14, 218, 261, 292]. For example, Thieme et al. (2018 [261]) investigated the applicability of 64 existing ship risk models for ship-ship collisions, ship-structure collisions, and groundings for autonomous marine vessels. Thieme et al. (2018 [261]) concluded that for a more detailed system evaluation more information regarding the USV concept needs to be known. Valdez Banda et al. (2019 [14]) complementarily noted the

major challenge of ensuring the safety of a USV in its operational context given the limited experience with functioning USVs. Therefore, they analysed the safety hazards for two ferries in their current operational modes and in their potential autonomous deployments. Finally, the inclusion of a shore control centre, to monitor or remotely steer a USV, further complicates the risk analyses by introducing human-system interactions. Here too, a deficiency in the amount of research considering such human-system interactions and potential human failures exists [218] (for more information, see Risk and Safety Analysis of an Inland SCC).

Considering that a common denominator over these recent USV risks analyses seems to be the scarcity of operational USV concepts, the developments in this section aim to provide data and insights to nurture future developments in the risk and safety research area. In this research field, the Systems-Theoretic Accident Modelling and Processes (STAMP) [14, 141] might be a good future methodology, given that it reviews the entire socio-technical system [8, 14, 48]. Accordingly, the risk assessments of the present work focused mainly on the lower technical level, i.e., implementing levels of redundancy in the vessel hardware, selecting industrially-robust components, having the ability to remotely control the vessel, and implementing emergency stops. In addition, the relatively small vessel weight and its slow manoeuvring speeds added to a higher safety level, during the conducted experiments. Apart from these technical safety measures, the Flemish waterway administrator, and by extent the Flemish government, have taken an active role in the discussions regarding safety and regulations during the experiments conducted with our scale model vessel. They achieved this role by defining, monitoring, and continuously optimizing a legal framework for testing and demonstration purposes with autonomous inland vessels.

5.2.2 Navigational Information

Presently, a vessel often fetches its navigational information (e.g. its pose and its time derivatives) from a standalone GNSS or IMU sensor, from a GNSS and an IMU separately, or from an integrated IMU–GNSS system. Although the vessel desires a high accuracy from these sensors, the preciseness of their measurements can be influenced in practical applications due to environmental noise, sensor drift, and sensor faults [148]. Moreover, the quality of GNSS signals drops in the vicinity of tall buildings [280]. Or, in the case of inland vessels, imperfect GNSS signals will occur in the neighbourhood of bridges, locks, quays, or other large vessels. Nevertheless, these are the situations where the highest positional accuracy would be desired. A first solution, to diminish the effect of sensor faults and the impact of environmental noise, is to install state-of-the-art marine-grade sensors. Accordingly, the Cogge nests such a GNSS and IMU sensor, of which

the specifications are discussed in Section 5.2.4.1 and Section 5.2.4.2. The fusion of their data forms a second solution to increase their performance. Currently, an Extended Kalman Filter (EKF) based on the vessel kinematics improves the accuracy of the navigational data. Note that the hydrodynamics of the vessel could also be included in an EKF [37, 263].

5.2.3 Environment Perception

Complementary to the necessity of accurate navigational information, USVs or ASVs need to be aware of their environment, e.g., here differentiated by (**E1**–**4**). In the ideal environment of known static obstacles (**E1**), and low or no environmental disturbances, — which evidently does not exist (for long) in reality — a GNSS can suffice to autonomously navigate the vessel. However, in order to perceive unknown static objects and their relative distance (**E2**), exteroceptive sensors (e.g. Stereo Cameras, Lidar, or radar) need to be present. The lidar and/or stereo camera based object detection has been a growing research field for indoor environments and the current research also expands towards, larger, outdoor environments, often forcing the sensors to collect data at a greater distance with a lower density [94]. Although several successful studies have demonstrated the Simultaneous Localisation And Mapping (SLAM) of an agent [38] in a static environment, and some studies implemented SLAM with obstacle avoidance [53, 113, 173, 301], it remains to be investigated which sensor set, and their minimum required specifications, is deemed necessary to achieve this goal on the inland waterways for cargo vessels (**E2**). Moreover, a supplementary challenge arises with the addition of dynamic known (**E3**) or unknown (**E4**) objects.

An implementation of a COLREG compliant collision avoidance for known dynamic objects (**E3**) can be found in Benjamin et al. (2017 [18]): the (autonomous) fleet can share navigational information with other (autonomous) vessels using the same nested MOOS-IvP software, hence making all the dynamic objects known. Given the fact that the Cogge currently runs the MOOS-IvP software, the usability of its obstacle avoidance implementation for inland waterways can be investigated in the future. Given the modularity of the software design, other collision avoidance strategies could also be implemented. Another example of an environment with known dynamic objects (**E3**) can be found in the Hull-to-Hull (H2H) navigation project [21, 128] which also involves test cases with the Cogge. In this project, vessels share their navigational information and its uncertainty over a proprietary communication channel in order to perform close proximity encounters (more details can be found in The Hull-To-Hull Navigation Concept section). In addition, some navigational information of known dynamic obstacles can be fetched from the AIS data.

Nevertheless, in reality, not all vessels use their AIS, nor do all vessels have such a system, and different smaller waterway users can enter the operational environment of an unmanned vessel, unlocking the need for the detection and tracking of unknown dynamic objects (**E4**). In comparison with their terrestrial and aerial robotic counterparts, there seem to be two main differences. On the one hand, most of the to-be-tracked objects tend to be larger in size exhibiting slower dynamics which could lower the complexity of tracking these objects. On the other hand, however, this larger size means that the objects have higher inertias and thus slower response times so the collision avoidance algorithms will need to operate and predict over a longer time horizon. These non-trivial dynamic tracking and collision avoidance tasks need to build their foundation on the results of (**E1**–**3**), and consequently their investigation falls out of the scope of this thesis.

5.2.4 Selected Sensors for the Cogge

During the first research stages, good weather conditions are presumed for the sensor selection. Later on, the additional complexity of bad weather conditions can be added. Keeping this assumption in mind, and based on the ongoing research mentioned above, Table 5.1 lists the envisaged sensor sets to investigate the different environments (**E1**–**4**). Thereupon, the following sections describe the selected onboard sensors (GNSS, IMU, Lidar, and Stereo Cameras). Their first in-situ experimental results can be found in Section 5.4. The remote motion control H2H experiments are discussed thoroughly in Section 6.5.2, and, currently, there is no AIS system installed. Therefore both systems will not be discussed in detail in the present chapter. On top of these sensor selections, it is not unlikely that additional sensors will be added in the future, depending on the findings and possible limitations of the current sensor sets. Finally, note that the achieved results in these environments can also help the development of more automated manned vessels. For example, these developments in the perception of the environment could guide, augment, or replace certain tasks currently performed by the onboard crew.

Table 5.1: Envisaged sensor settings for the first experiments with the Cogge

Env.	Obstacles	Minimal sensor set	Status
E1	Known, static	GNSS, IMU	Successful, see Section 5.4.2
E2	Unknown, static	GNSS, IMU, Lidar, Stereo Cameras	In progress, see Section 5.4.3
E3	Known, dynamic	GNSS, IMU, AIS or other asset communication	In progress, see Section 5.4.4
E4	Unknown, dynamic	GNSS, IMU, Lidar, Stereo Cameras, AIS or other asset communication	Future work

5.2.4.1 GNSS

The installed AsteRx-U Marine GNSS sensor [233] can operate in -30 to 65°C and has an IP67-rated housing, making it a robust sensor for inland vessels. On the Cogge, it uses two mushroom antennas (separated by a baseline of approximately 4.43 m [297]) to receive multi-frequency and multi-constellation GNSS signals. This way, it can benefit from the more accurate European Galileo constellation while still being able to use additional constellations to boost its convergence time and accuracy [142]. Furthermore, it includes a ultra high frequency radio, Bluetooth, WiFi, and a cellular modem. This cellular connection allows for the reception of Real Time Kinematic (RTK) corrections [136] for the GNSS signals, improving the accuracy of its navigational data. Table 5.2 visualises the impact of these RTK corrections on the performance of this sensor, together with other accuracies. As shown, the correction accuracy depends on the distance between the sensor and the nearest RTK base station. For example, for the horizontal position the absolute accuracy results in 0.6 cm + $0.05\frac{\text{cm}}{\text{km}}$ of distance from an RTK base station. Flanders currently has 45 base stations installed, ensuring a dense coverage, and freely provides these RTK corrections over mobile internet via the Flemish Positioning Service [85].

Table 5.2: Absolute accuracies for the AsteRx-U Marine [233]. Using the twice the distance root mean square accuracy: the distance between the true and computed parameter is lower than the stated accuracy with at least a 95% probability.

Parameter	Accuracy
Horizontal position, standalone	1.2 m
Vertical position, standalone	1.9 m
Horizontal position, RTK	0.6 cm + 0.5 ppm
Vertical position, RTK	1.0 cm + 1 ppm
Velocity, standalone	0.03 m/s
Heading, 1m baseline	0.15°
Heading, 10m baseline	0.03°
Pitch, 1m baseline	0.25°
Pitch, 10m baseline	0.05°

5.2.4.2 IMU

The Ekinox-2-E IMU sensor can operate in the temperature range of -40 to 75°C and has an IP68 rating (24 hours submersible at 2 m) [230]. This IMU uses three accelerometers and three gyroscopes to measure the linear accelerations and angular velocities of the vessel. Moreover, it can provide additional information regarding the position, orientation, and linear speeds of the vessel by means of single or double time integration. An internal kinematic EKF can be used to

compensate for the IMU drift, shown by Figure 5.2. The internal EKF predicts states at 200 Hz, based on the integration of its gyroscopes and accelerometers, and these states get a corrective step at 5 Hz provided by GNSS data from the GNSS. An embedded software module first checks the integrity of this GNSS data and sends it through its proprietary error model before sending it to the EKF.

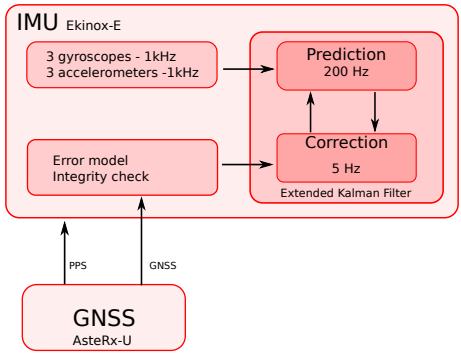

Figure 5.2: Working principle of the embedded EKF, based on [230].

The line of sight between the tracked satellites and the GNSS mushrooms will be disturbed and potentially blocked when passing a bridge. Consequently, it is of paramount importance for an unmanned vessel to still receive reliable navigational information during this time span. Table 5.3 demonstrates two examples of the importance of the EKF by listing its accuracy in function of the elapsed time since a corrective GNSS signal was received (0 s, 10 s, and 30 s). Logically, the accuracy diminishes the longer a GNSS outage lasts. Nevertheless the IMU is still capable to produce useful data during these shorter outages which align with the typical time of passing under a bridge. Furthermore, the IMU computes and publishes the accuracies of its predicted states so that an autonomy system could take this information into account.

Table 5.3: IMU accuracy (one standard deviation) dependent on GNSS outages [230]

Parameter	**Accuracy**
Horizontal velocity, 0 s	0.02 m/s
Horizontal velocity, 10 s	0.05 m/s
Horizontal velocity, 30 s	0.25 m/s
Heading (baseline $>$ 4 m) 0 s	0.05°
Heading (baseline $>$ 4 m) 10 s	0.08°
Heading (baseline $>$ 4 m) 30 s	0.13°

5.2.4.3 Lidar

The OPAL 1000 lidar has no external moving parts, sits in an IP67 housing, and can operate in a temperature range of -40 to 40°C [177]. The laser scanner measures a panoramic field of view of 360° in the horizontal plane, and 45° in the vertical plane, at a maximum rate of 300 000 pulses per second, with a maximum range of 1000 m. It can penetrate obscurants such as dust, snow, rain, fog, and smoke by using its patented algorithm, which uses seven pulses to measure one point. Moreover, it can also be connected to and synced with the IMU and GNSS in order to perform scans when the vessel moves.

5.2.4.4 Stereo Cameras

A computer vision technology company named Vision++ provided the tailored stereo camera system [277] for the Cogge. This system consists of two industrial cameras positioned on the port and starboard side of the bow sensor rail. Most conventional, commercially available, systems have a maximum distance of 40 cm between both cameras, whereas on the Cogge, they have a baseline of 60 cm, which provides an optimal depth sight at a distance of approximately 15-20 m, i.e., 3–4 times the length of the Cogge. These cameras have a frame rate of 22 frames per second (fps), a pixel class of 5 megapixel, and a power-over-Ethernet connection, which simplifies the power and communication requirements. When creating stereoscopic images, it is crucial that the images provided by both cameras are taken simultaneously. Hence, in the current set-up, the cameras are connected to each other via a proprietary wire, which allows one camera to trigger the other one. The camera software suite controls the cameras and allows the user to fine tune the settings of the cameras to optimize their exposure. In addition, the software supplied by Vision++ enables the extraction of 3-dimensional-point cloud data from a stereo camera image, specifically configured for an inland waterway environment. This cloud can be used in conjunction with the point cloud data produced by the lidar. The camera images can also be used to aid the perception and obstacle detection.

5.3 Motion Control for an Inland USV

Presently, three control levels provide the motion control of the vessel, when it operates as an ASV. Figure 5.3 provides an overarching view of these three control levels coined “low”, “middle”, and “high” level control. This figure illustrates their main interactions when the Cogge follows a list of waypoints. The following High Level Control, Middle Level Control, and Low Level Control sections provide more details, referring to Figure 5.3.

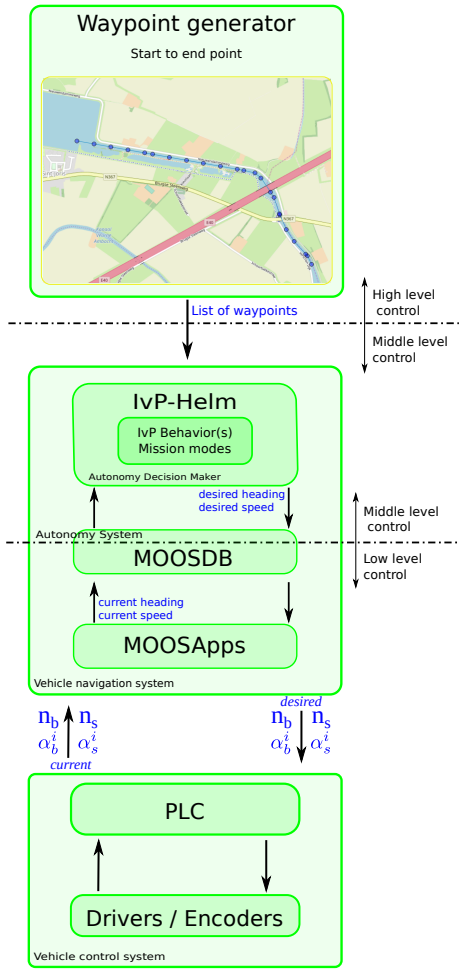

Figure 5.3: Implemented cascaded control hierarchy

5.3.1 High Level Control

The high level control covers the top-level route planning, for example the determination of the route to be taken between two cities. Currently, an in-house developed (by Senne Van Baelen) waypoint generator forms a static list of waypoints between a chosen start and endpoint on a river or canal. This developed generator uses the OpenStreetMap [189] database in order to fetch the global coordinates from the chosen waterway. The generator places waypoints in the middle of the waterway, and the maximum distance between two consecutive waypoints can be specified by the user. Finally, the result can be downloaded as a plain text file and be used as to-be-tracked waypoints by the Middle Level Control.

5.3.2 Middle Level Control

Currently, the MOOS-IvP autonomy system provides the foundation for the middle level control of the Cogge. Three main components form the core of this autonomy system: a collection of MOOSApps, the autonomy decision making system named the IvP-Helm (which is a MOOSApp on its own), and the MOOSDB for their communication. To configure this IvP-Helm, the user can write or use a set of behaviours that the vessel should follow, for example: follow waypoints and maintain a certain speed. These behaviours have user-defined IvP-functions which span over their decision space (e.g. heading and speed). Moreover, the user can also decide when a particular behaviour should occur by configuring the mission modes. The IvP-Helm will then calculate the desired system states depending on the different active behaviours, and their IvP-functions [20].

Continuing with the illustrative configuration of Figure 5.3, the IvP-Helm could be configured to, for example, solely follow waypoints by using the MOOS-IvP waypoint-following behaviour. This behaviour needs a list of waypoints to follow, which in this case will be provided by the aforementioned High Level Control. Next, the IvP-Helm needs navigational information, e.g., the current heading and speed, to calculate the desired heading and speed for the vessel to reach the following waypoint. This information flow illustrates the backseat control paradigm from the MOOS-IvP software: the autonomy decision making IvP-Helm only needs navigational information from the vessel at hand, which it can treat as a black box. The IvP-Helm will then, based on its internal behaviour configuration, provide the desired systems states for the vessel. Nevertheless, in the control architecture of the Cogge, the navigation and control modules are no black boxes but currently also consist of several MOOSApps, such as drivers for the sensors, and the low level motion controller. Therefore, the virtual

hierarchical separation line between middle and low level control has been drawn at the level of the MOOSDB as some part of the autonomy system (the IvP-Helm and its surroundings) form the middle level control and other parts (low level motion controller and sensor drivers) form the Low Level Control.

5.3.3 Low Level Control

The low level control diminishes the error between the desired and current system states, e.g., the heading and speed. The former states are produced by the Middle Level Control and the latter are provided by the GNSS and IMU sensors. Currently, a conventional Proportional Integral Derivative (PID) controller (implemented as a MOOSApp) can control the heading and speed of the vessel. The PID controller is a well-known, simple, and robust controller, often used in maritime applications [63, 90] and can be tuned by pole placement algorithms [90, 169, 293]. Evidently, more sophisticated control techniques can be used in the future which take into account the vessel kinematics and kinetics [67, 72, 132, 143, 303]. Nevertheless, the performance of the implemented PID controller can be used as a benchmark for the future implementation of more sophisticated control philosophies. Finally, the onboard PLC (see Section 2.4.3.1) receives the output of the PID controller, i.e., the desired control system states $n_b^d, n_s^d, \alpha_b^{i,d}, \alpha_s^{i,d}$, sends back their measured values. In addition, this PLC diminishes the error between these lowest-level system states.

5.4 Results of the First Experiments

This section analyses some of the first experiments conducted with the Cogge. First, Section 5.4.1 demonstrates a few open-loop experiments to uncover some of the basic hydrodynamic capabilities of the vessel. These trials were performed on the small lake of Rotselaar, Belgium. Afterwards, the subsequent sections discuss a few different environment interactions for the aforementioned differentiated cases **E1**, **E2**, and **E3**.

5.4.1 Open-loop, Rotselaar lake

5.4.1.1 Straight Sailing

During the first open-loop tests, the Cogge showed an asymmetric course behaviour. When the vessel was commanded to sail straight (e.g. giving solely the stern an rpm, i.e., $n_s^d \neq 0$ and $n_b^d = \alpha_b^i = \alpha_s^i = 0$) it seemed to show a

repetitive asymmetric behaviour which turned the vessel to starboard. Presently, it is hard to discover the exact cause of this behaviour. A first empirical solution was to place a honeycomb-like flow-straightener in the longitudinal direction of the stern-side outlet of the stern thruster to straighten its exiting water flow when sailing straight ahead. Figure 5.4 displays the effect of this flow-straightener on the straight line sailing capacity of the vessel. The black lines show the first experiments without flow-straightener, whereas the red lines show similar experiments but with the flow-straightener inserted in the stern outlet. Note how the black lines show a high curvature due to the asymmetric behaviour, whereas the red lines show a more straight sailing behaviour over longer spatial slots. The differences in length between all curves are due to different requested propeller speeds and time spans of the missions. The installation of this flow straightener significantly improved the straight line stability of the vessel — which can be felt when remotely controlling the vessel.

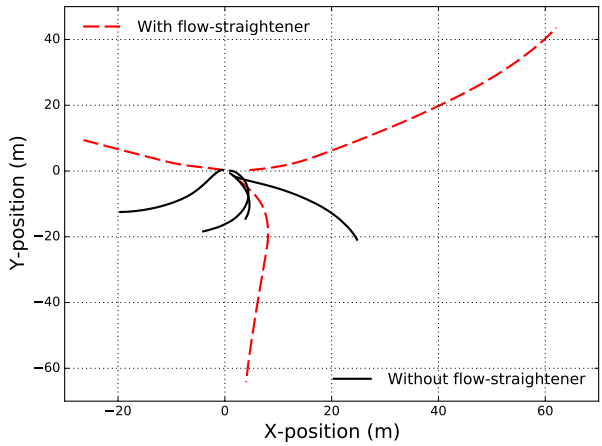

Figure 5.4: Sailed trajectories for open-loop straight sailing with and without flow-straightener, the positions were measured by the GNSS placed at the stern.

5.4.1.2 Pseudo Spiral Manoeuvre

To investigate the possible turning rates of the Cogge, a pseudo spiral manoeuvre was performed. This manoeuvre differed slightly from the Dieudonné spiral manoeuvre [61], as the vessel only turned into one direction and there was a constant settling time between the rudder impulses. The uncertainty of the spatial necessities for a full spiral manoeuvre pushed the decision to initially only perform the pseudo spiral manoeuvre. The manoeuvre was performed fully autonomously with the following desired settings: $n_s = 1000$ rpm, $\alpha_s^i = 0°$,

$n_b = 2500$ rpm, and α_b^i varying between $[4°, 8°, 20°, 40°, 60°, 80°]$. Hence the stern thruster was oriented to propel the vessel forward (with the flow-straightener installed) and the bow thruster was used to steer the vessel, by using a constant propeller speed but changing its outlet angle. Figure 5.5a lists these desired system states during the whole mission. As visible, an arbitrarily settling time of 10 seconds was used, this time span was chosen to be rather short in order to have the space to perform the full mission, but it can be increased in future tests. For the same reason, the first angle change occurred right from the start, introducing some start-up effects in the data as the vessel itself also needed to accelerate. In the future a longer start-up time could be introduced. Figure 5.5b plots the measured heading from the GNSS and the recorded yaw-rates from the IMU. The latter were filtered with a centered moving average filter of window size 50. Finally, Figure 5.5c plots the sailed trajectory.

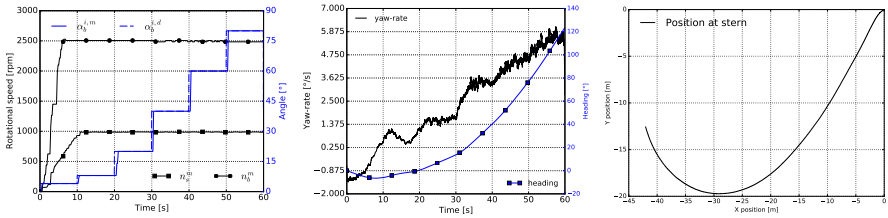

(a) (b) (c)

Figure 5.5: Open-Loop pseudo spiral manoeuvre: (a) manoeuvre inputs, (b) relevant system outputs, and (c) elapsed trajectory, the positions were measured by the GNSS placed at the stern.

5.4.2 E1 — Known Static Obstacles

5.4.2.1 Autonomous Sailing on the Yzer River

The first autonomous, unmanned, closed-loop tests were performed on the Yser (river in Nieuwpoort, Belgium), in the context of the EFRO (European Fund for Regional Development) project "Autonoom Varen in de Westhoek [57]". This EFRO project investigated the legal and technical necessities to perform a pilot demonstration of autonomous sailing with a scale model of an inland vessel in a confined demonstration area. Afterwards the project conducted such demonstrations of which the described tests in this section were the first ones. These preliminary tests used the control hierarchy described in Section 5.3. Moreover, the map shown in the waypoint generator of Figure 5.3 actually shows some of the generated waypoints for these experiments. After the generation of the waypoints list, and the configuration of the IvP-Helm to follow these

consecutive waypoints, the low level controller needs to be configured. The angle of the bow thruster provided the steering mechanism for the vessel, whereas the stern thruster was kept a static neutral angle with a constant propeller speed. This set-up aligns with the configuration of the Pseudo Spiral Manoeuvre, and had the following settings: $n_s \approx 1250$ rpm, $\alpha_s^i = 0°$, $n_b \approx 2400$ rpm, and $\alpha_b^i \in [-90°, 90°]$ as the control variable. The IvP-Helm provided the desired heading to follow the waypoints and the IMU gave the current heading. The error between both headings was controlled with a manually tuned PI-control on α_b^i, with a proportional gain factor $K_P = 2$ and an integral gain factor $K_I = 0.2s^{-1}$ with an integral limit of 0.7 in order to avoid integral wind-up.

Figure 5.6 summarises two parts of autonomous sailing on the Yser: (a), (b), and (c), show a fragment of a straight part on the Yser; whereas (d), (e), and (f), show a sample of a bend of the Yser, whilst passing underneath a bridge. These two trajectories are also visible on the map of Figure 5.3 where the red line is the highway bridge under which the vessel sailed in (d). The plotted waypoints of (a) and (d) have a higher density than the waypoints of Figure 5.3, as for the latter the amount of visible waypoints was decreased to increase the readability of the figure. Next, plots (b) and (e) show the measured propeller speeds on the one hand, and the measured control angle α_b^i on the other hand. Finally, (c) and (f) show the desired heading, determined and published by the IvP-Helm, and the current heading, fetched from the IMU. As demonstrated by these six subplots, the vessel was able to follow the waypoints on both a straight and curved trajectory which passed underneath a bridge.

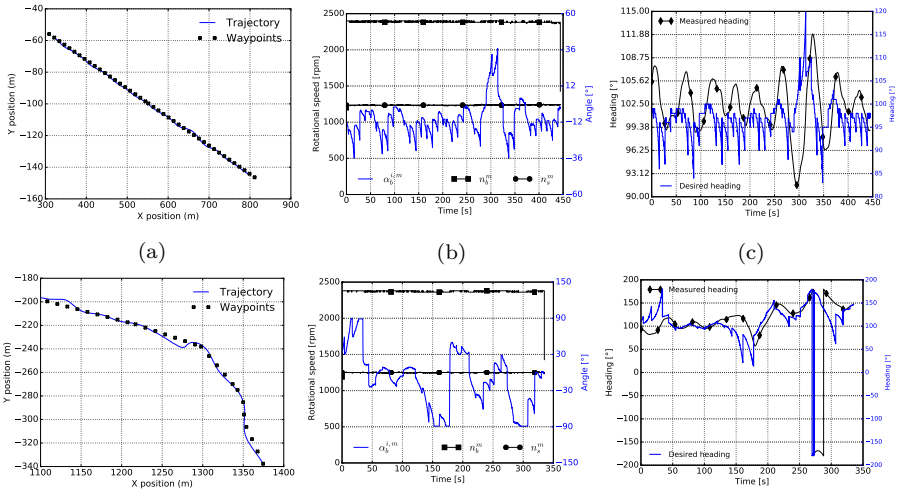

Figure 5.6: Closed-loop waypoint following on the Yser. Straight trajectory on the first row (a–b–c), and a curved trajectory on the second row (d–e–f), position measured at stern.

5.4.3 E2 — Unknown Static Obstacles

5.4.3.1 Lidar Scans

Figure 5.7 illustrates a static scan with an exposure of 5 minutes at the small inland leisure harbour of Leuven, Belgium, where the lidar was placed on the shoreside. On the left side of this image, a few moored leisure craft can be seen. Whereas, Figure 5.8 shows the accumulated data of an approximately one minute scan while the vessel was slowly sailing. The left hand side plots the raw lidar data using a colour code from red to blue to denote the decreasing intensity of the measured points, and thus increasing distance relative to the lidar. The right hand side of the figure plots the manual overlay of the lidar data (now in black) on the local geographical map of the lake of Rotselaar where these data were fetched. Hence for this configuration the lidar was mounted on the vessel and had access to the IMU data. During the exposure time, a wind-surfing class was present on the water which resulted in the ghost points on the water close to the top of the image.

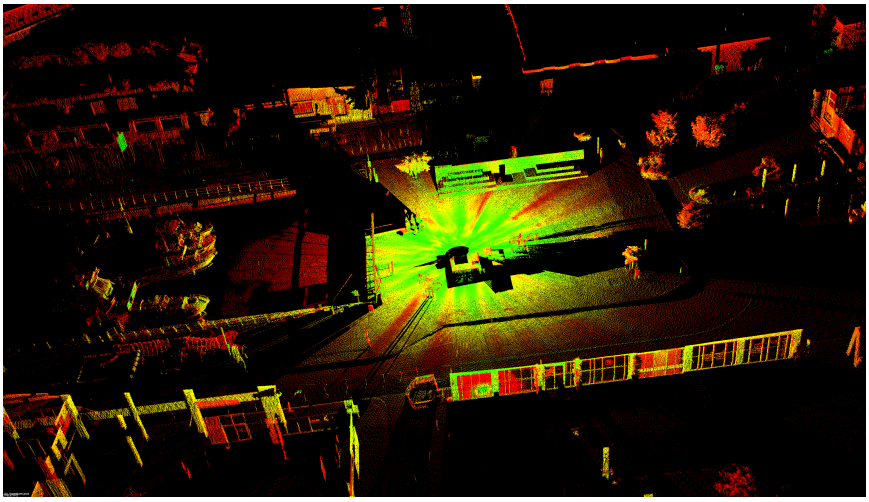

Figure 5.7: Lidar cloud after 5 minutes of exposure time. The shown area is approximately 50 m by 100 m, on the left the bow of a few leisure vessels can be seen and on the right some trees. The top and bottom show the contours of the neighbouring buildings.

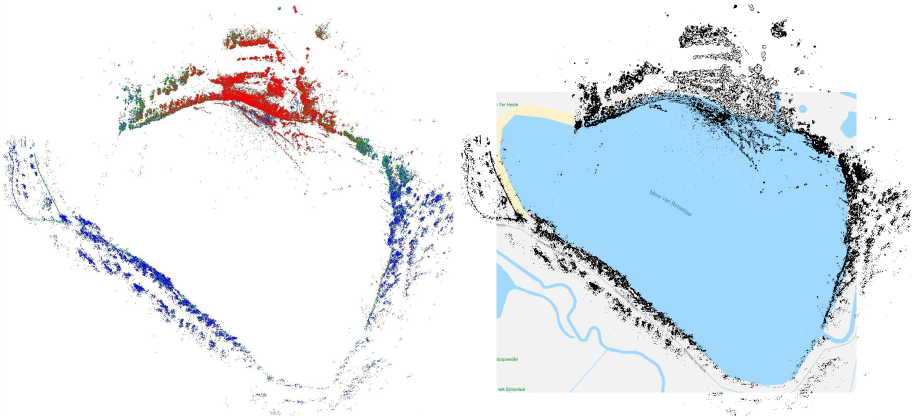

Figure 5.8: Lidar data from an approximately one minute scan while the vessel was moving: (left) intensity data points, (right) manual overlay of data on geographical map.

5.4.3.2 Shoreline Extraction from Lidar Data

Van Baelen et al. (2020 [269]) compared three methods to extract a shoreline from lidar data. Figure 5.9 illustrates the working principle for such a shoreline extraction. The methods were performed offline based on a lidar scan conducted with the Cogge, which Figure 5.9a partly shows. Figure 5.9b depicts a resulting shoreline extraction. This extraction can then be compared with the available inland navigation charts, see Figure 5.9c.

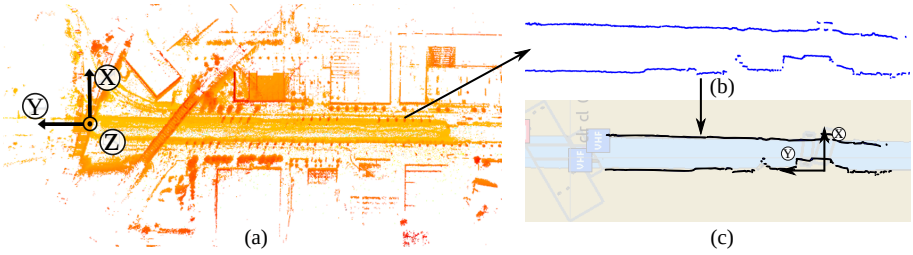

Figure 5.9: Shore line extraction from lidar data, adapted from Van Baelen et al. [269]: (a) lidar data set, (b) shore line extraction, and (c) extracted shoreline and inland navigation chart shoreline comparison.

5.4.3.3 Stereo Camera Images

Figure 5.10 depicts two, simultaneously-taken, images of the stereo camera system. The visible railway bridge lies at the coordinates (50° 54′ 01.5″ N, 4° 42′ 23.9″ E). As mentioned in section Section 5.2.4.4, these images can be used to extract depth data of the surrounding environment. The images were taken on a rainy day where water droplets eventually made it onto the lenses, resulting in the blurred result. This effect of the weather shows the importance of using more than one perception system and hints at the future research challenges when the effects of bad weather conditions are added.

(a) (b)

Figure 5.10: Stereo camera images: (a) image of the left camera, (b) image of the right camera, at the same time stamp.

5.4.3.4 In-Operation Communication Data Rates

The following data rates indicate the measured data consumptions during the first experiments. Evidently, these rates depend on the configuration of certain sensor parameters. In order to avoid confusion, two separate network loops can be detailed: (i) the local network, i.e., communication between the sensors and the onboard I-PC, and (ii) wireless vessel-to-shore communication, i.e., where certain data could be transmitted between the onboard I-PC and the rugged shoreside laptop. In the first case, both the GNSS and IMU consume less than 1 Mbps (Megabit per second). The lidar uses approximately 5 Mbps when it spins on one-sixth of its maximum frequency. And, given that each camera can produce 5 megapixel images at 22 fps, they could theoretically each approximately produce a maximum data rate of 330 Mbps, which they each transmit over a category seven Ethernet cable.

In the second case, when one wants to stream some of these data wirelessly to another device, there are currently two options available via the onboard router: using the cellular network or using a wireless local area network. Note that this router has a theoretical maximum bandwidth of 150 Mbps. On top of that, the current cellular 4G network has a claimed maximum bandwidth of 100 Mbps. However, this number is highly environment-dependent and a conservative bandwidth of 5–15 Mbps has been noticed to be more representative for the possible regime data rates at our testing locations. During the experiments, there was always a wireless communication between the onboard MOOS processes and the MOOS processes on a remote laptop which triggered and monitored the onboard counterparts. The frequency and the content of these vessel-to-shore communications can be chosen and was never larger than 1 Mbps, hence it was always possible to transmit these data over the cellular network. It might be beneficial to add a second separated local network to route all the data coming from the perception sensors, together with a second I-PC to process all these data, and a second router to transmit these data to the shore in the future.

5.4.4 E3 — Known Dynamic Obstacles

In the European Horizon 2020 project "Hull-to-Hull (H2H) [21, 22, 128, 297]", vessels will sail in an environment with known, i.e., H2H-compliant, dynamic objects. This H2H concept uses uncertainty zones to visualise the relative positioning between H2H-compliant vessels. Presently, H2H-experiments have been conducted with the Cogge remotely controlled from the shore, see First USV and H2H-Extended Inland SCC tests, for more details. Future work could focus in integrating this received H2H-information from other vessels into the motion control of the Cogge. This integration would need the addition of traffic rules to the present motion control system [18, 72].

5.5 Conclusion

This chapter detailed the perception (***RO*3.1**) and motion control (***RO*3.2**) systems for USVs, by differentiating four navigational environments (**E1**–**E4**) according to the presence of static or dynamic, and known or unknown objects.

In these environments, the USV needs navigational information of itself (e.g. pose and velocity) in order to perform meaningful manoeuvres. Dependent on in which environment the USV operates, it needs different environment perception information fetched by exteroceptive sensors such as lidars and stereo cameras. Subsequently, the currently envisaged onboard sensor selection was listed together with the specifications of these sensors, for the Cogge operating in these four environments.

Currently, the associated motion control system has a hierarchical structure of three levels coined high, middle, and low level control. This structure controlled the Cogge during its autonomous sailing missions in the Yser river, under the assumption of static and known obstacles (**E1**). In addition, the present onboard status of the exteroceptive sensors for unknown static object (**E2**) recognition was detailed. And finally, the first explorations towards navigating in the vicinity of known dynamic objects (**E3**) were briefly discussed with respect to the H2H experiments on which Chapter 6 will provide more details.

Together, the present perception and motion control systems provide a preliminary answer to **RQ3**. The results of future experiments might adapt certain parts of the current answers.

Design and Build of an Inland Shore Control Centre

"De beste stuer-luy sijn aen lant [182]."[4]

Jacob Cats

Figure 6.1: Geppetto carving Pinocchio, 1902 [52].

[4]The best helmsmen stand on shore

This chapter provides an alternative answer to the second and third research questions (**RQ2** and **RQ3**), by putting a remote operator in the loop. This operator can implicitly model (***RO*2.1**) and identify (***RO*2.2**) the USV, in combination with providing its perception (***RO*3.1**) and motion control (***RO*3.2**). Parts of this chapter were previously published as:

[206] G. Peeters, G. Yayla, T. Catoor, S. Van Baelen, M. R. Afzal, C. Christofakis, S. Storms, R. Boonen and P. Slaets. "An Inland Shore Control Centre for Monitoring or Controlling Unmanned Inland Cargo Vessels". In: *Journal of Marine Science and Engineering* 8.758 (2020). With joined first authors G. Peeters and G. Yayla. DOI: 10.3390/jmse8100758

6.1 Introduction

Although a spectrum of definitions for automated or autonomous can be found [16], they are often entangled with, or separated by, a level of human interference. This interference might hint at a human mediator in juxtaposition with an increasingly automated and independent cargo fleet as a technologically-feasible inland waterway transport concept in the near future. Consequently, one of the key components of this envisaged concept could be an inland Shore Control Centre (SCC) capable of remotely monitoring and controlling several USVs or ASVs simultaneously. Therefore, Section 6.2 details the motivation to build an inland SCC. Afterwards, Section 6.3 discusses the inland SCC design concept together with its design requirements, which resulted in the inland SCC design of Section 6.4. Thereupon, Section 6.5 handles on the first in-situ experiments, Section 6.6 discusses their results, and Section 6.7 concludes this section.

6.2 Motivation for an Inland Shore Control Centre

Over the last few years, the investigation of autonomous or unmanned vessel concepts has grown rapidly. The Finnish Advanced Autonomous Waterborne Applications project (AAWA) [1] proposed preliminary designs for advanced ship solutions. The first autonomous cargo vessel, the Norwegian Yara Birkeland, is on its way [291], whereas a Belgian scale model of an unmanned inland cargo vessel, the Cogge, already performed preliminary unmanned experiments [194]. Additionally, the European Maritime Unmanned Navigation, through the Intelligence in Networks MUNIN project [130], investigated a dry bulk carrier for intercontinental trade. Most of these just-mentioned concepts rely heavily on an SCC that can monitor or steer the vessels. The MUNIN project went into great detail for the technological concept of a complete SCC: they included operators, back-up operators, watch keepers (supervisors, engineers, and captains), planners (voyage and maintenance), and administrative staff in their design [130, 152]. Accordingly, they estimated a necessary total staff of 169 people to continuously monitor a fleet of 90 vessels dedicated to one SCC wherein an operator monitors six vessels at once. Such a novel SCC design also gives rise to human factor challenges, where other domains (e.g. aviation, cars, and subway systems) can provide useful insights [278]. Furthermore, the operational context between an onboard bridge and onshore SCC differs significantly, i.e., one can most likely not just move the bridge to shore and expect it to work, given that the user–environment interactions, and thus the actual work, would change [159, 160].

Consequently, this chapter used an activity-centred design (ACD) approach [184] to construct an inland SCC for five main reasons. Firstly, given that the final businesses model for a USV or ASV for inland cargo transport is not yet clear, the emphasis was put on the activity, i.e., remotely controlling or monitoring a USV or ASV via the inland SCC, which will most likely need to be performed independently of the final concept. Secondly, Man et al. (2018 [160]) noted that, when having to remotely monitor and control simulated unmanned cargo vessels via an SCC, operators tend to use the familiar navigational and collision avoidance technologies but in a different way. Therefore, this study offers a flexible combination of different technologies that should enable the activity of monitoring or controlling USVs. Thirdly, the first potential business models for short sea shipping and ferries seem to focus on short, local routes [291], not unlike inland cargo shipping, hence the focus on an inland SCC. Fourthly, one of the concluded next steps in the AAWA project stresses the need for the development and testing of specific technological solutions [1], such as the here-constructed inland SCC. Finally, most of the existing SCC design research focusses on sea-going vessels and stays rather theoretical [1, 130, 152, 211, 291], although some studies have investigated the SCC design by controlling or monitoring simulated vessels [159, 160], whereas this work paves the way to studying real ship-shore interactions. In sum, this chapter aimed to:

I. Use an ACD approach [184] to develop an inland SCC concept which provides its operator with interaction possibilities with a USV, where interaction denotes the remote access of the USV actuation system and overall system settings. Accordingly, this inland SCC aims to serve as a tool to enhance the situation awareness [70] and sensemaking [156] capabilities of the remote operator. Thus, the inland SCC unlocks research on the impacts on ship sense [215] and harmony [214] when remotely monitoring or controlling a USV.

II. Translate this inland SCC concept into four design requirements: (R-i) provide the relevant information groups suggested by Porathe et al. (2014 [211]), (R-ii) provide interaction with the USV, (R-iii) select industrial components, and (R-iv) keep the design modular.

III. Provide technological details of the merged inland SCC and USV system design in accordance with these four design requirements.

IV. Offer preliminary data of an operator remotely controlling a USV via the inland SCC, to investigate the system and operator performance.

V. Illustrate the modular design philosophy by extending the inland SCC design within the Hull-To-Hull (H2H) project [238] which augments the remote motion control of a USV via the inland SCC. The change in operator performance due to this extension was also investigated.

The successful accomplishment of these five research aims will offer insights for potential paradigm shifts in the transport sector on the one hand, and for human factor research within the mechatronic innovations in the inland waterway sector on the other hand. In addition, the modular, industrially-relevant, bottom up approach will enable future cost-benefit analyses of the inland SCC system design by means of an engineering estimate approach [166].

6.3 Concept and Requirements of an Inland Shore Control Centre

Section 6.3.1 summarises the already-existing line-of-sight control subsystem components [199], which unlocked a potential for human monitoring and controlling a USV. Together with the Motivation for an Inland Shore Control Centre, this potential inspired the ACD concept of an inland SCC, handled by Section 6.3.2. Thereupon, Section 6.3.3 lists the design requirements to achieve this concept, and afterwards Section 6.3.4 discusses the H2H navigation concept [238] which extends this inland SCC by providing augmented motion control of the USV. Finally, Section 6.3.5 addresses the inland SCC risk and safety analysis.

6.3.1 Line-Of-Sight Control Subsystem

Figure 6.2 reveals the three main external devices which were used, either on shore or on a support vessel, during the unmanned operations of the Cogge documented in Peeters et al. (2020 [194]). A wearable remote control, see Figure 6.2b, was used to position or manoeuvre the vessel in between missions when desired. This remote has a screen which can access a mobile-friendly version of the PLC web-interface. Both the industrial computer on the Cogge and the shoreside monitoring rugged laptop, see Figure 6.2b, ran the MOOS [180], allowing the latter to monitor the MOOS processes on the former, which also ran MOOS-IvP [20] processes, to provide the vessel with an autonomy system [194]. Finally, Figure 6.2c depicts the web-based interface accessible via any internet-connected device to monitor the relevant onboard PLC parameters and to remotely control the vessel if necessary, not unlike the developments in Osga et al. (2013, 2015 [190, 191]).

(a) (b) (c)

Figure 6.2: The previous line-of-sight shore side control components (summer 2019): (a) wearable remote controller with web-interface, (b) the rugged computer (R-PC) running MOOS-IvP, and (c) an additional laptop monitoring the PLC web-interface.

6.3.2 Concept of an Inland Shore Control Centre

First, Section 6.3.2.1 explains the concepts of ship sense and harmony, and the influence on them when an operator remotely controls a vessel. Afterwards, Section 6.3.2.2 looks at these concepts from another perspective. Finally, Section 6.3.2.3 forms the ACD concept of the inland SCC based on these previous two sections.

6.3.2.1 Ship Sense and Harmony

Conventionally, onboard crew members acquire a certain degree of ship sense [215] with which they handle the ship in order to keep harmony [214] between the ship and its environment. Ideally, this harmony results in a safe and pleasant journey for the vessel, crew, cargo, and passengers [214]. Parts of these ship sense and harmony seeking concepts might be compatible with embodied sensemaking [56], which in addition to the more-studied cognitive and linguistic sensemaking literature [228] also investigates the effects of intuitions, sensations, and emotions on how one interprets and acts in the environment [56, 156]. These potential compatibilities can be seen in the three harmony sub-categories: (i) environmental prerequisites (context and situation), (ii) vessel-specific prerequisites (inertia and navigational instrumentation), and (iii) personal requisites (spatial awareness, theoretical knowledge, and experience) [214]. Evidently, an operator in a remote SCC loses a direct ship sense, and thus the subsequent harmony with the environment [158], which complicates the ship handling. Therefore, to study the necessities for adequate situation awareness in an SCC, Porathe et al. (2014 [211]) interviewed six bridge officers and uncovered 165 pieces of necessary information which they bundled into nine groups: (i) voyage (e.g. voyage plan), (ii) sailing (e.g. heading data),

(iii) observations (e.g. video cameras), (iv) safety and emergencies (e.g. bilge pumps status), (v) security (e.g. video of ship itself), (vi) cargo stability and strength (e.g. stability system status), (vii) technical (e.g. engine parameters), (viii) shore control centre (e.g. voice communication with other vessels), and (ix) administrative (e.g. log books). Furthermore, Man et al. (2015 [159]) performed several scenario-based trials with an SCC monitoring virtual vessels to study the aforementioned harmony model and the adequacy of these nine information groups for situation awareness. Two of their main conclusions were the importance of a proper alarm management system and the fact that a SCC should not mimic the bridge layout. This latter conclusion was again emphasised in Man et al. (2018 [160]) which noted the tight coupling between the user and the environment that could be taken into account by means of an ecological design approach [274].

6.3.2.2 Situation Awareness, Sensemaking, and Interaction

At a different level of analysis, these concepts of ship sense and harmony seem to span the areas of situation awareness, sensemaking, and interaction. Situation awareness and its different levels are understood as, "The perception of elements in the environment within a volume of time and space, the comprehension of their meaning, and the projection of their status in the near future [70]", note that Endsley (2015 [69]) clarified some of the common misconceptions or misunderstandings of this definition. Likewise, sensemaking refers to: "The interplay of action and interpretation rather than the influence of evaluation of choice [283]", or alternatively: "sensemaking is the process through which people work to understand issues or events that are novel, ambiguous, confusing, or in some other way violate expectations [156]". Finally, within this study, interaction indicates both the possibility of remote motion control actions from an operator and the option of changing onboard operational settings. These three concepts are not mutually exclusive; on the contrary, they seem to have codependent sub parts all centring around the human operator.

6.3.2.3 Activity-Centred Design Concept of an Inland Shore Control Centre

The ACD approach of this study focusses on providing a tool, i.e., the inland SCC, to remotely control or monitor an ASV or USV, whereas a human-centred design approach would focus more on making the tool invisible [184]. Nevertheless, given that the current users, i.e., the researchers, are also the designers of the inland SCC, user- and human-centred design choices were often implicitly incorporated. The inland SCC should offer the possibility

of interaction with the USV in order to help its operator to develop certain levels of situation awareness and sensemaking (see Section 6.3.2.2). Given that the first experiments and usage (see Section 6.4.5) of this inland SCC focus on (continuously) remotely controlling a USV, situation awareness is herein understood as a cognitive construct, although this definition can be criticised [58]. When future experiments focus more on the monitoring activity, the inland SCC concept will shift further towards a joint cognitive system (JCS) [110, 111]. In this socio-technical system, redefining the situation awareness towards a distributed situation awareness [249] might be more suited. Finally, Section 6.3.3 will translate these concepts of interaction, situation awareness, and sensemaking into design requirements for the inland SCC.

6.3.3 Design Requirements of an Inland Shore Control Centre

Four main design requirements (R-i–iv) were judged necessary in order to realise the inland SCC concept of Section 6.3.2.3. Together, they aim to provide a fully-operational, industrially-relevant, experimental set-up enabling both current research on inland SCCs and on mechatronic innovation for the inland waterway transport sector, whilst attempting not to block future potential expansions thereupon:

(R-i) Generate and communicate elements of the following information groups [211]: (ii) sailing, (iii) observations, (iv) safety and emergencies, (v) security, and (vii) technical to the inland SCC. These groups will enhance the situational awareness and sensemaking abilities of the remote operator.

(R-ii) Provide interaction possibilities with the USV in order to remotely alter the USV motion and its system configurations. This interaction will also assist the sensemaking and situation awareness capabilities of the operator.

(R-iii) Install industrial, marine-grade components for both the extensions on the USV and the inland SCC system design. This requirement should make the overall system safer and transferable to a potential real SCC.

(R-iv) Keep the system design modular and flexible, where possible. This flexibility should smoothen the likely design iterations and extensions.

These requirements illustrate the activity-centred, bottom-up design focus for constructing the USV and inland SCC ecosystem. As emphasised by (R-iv), this focus allows for design iterations and provides a foundation for future extended designs. Some of the known design limitations are the disregard of the remaining information groups [211]: (i) voyage, (vi) cargo stability and strength, (viii) shore control centre, and (ix) administrative; during the first experiments, a

voyage plan, transporting cargo, communicating with other vessels, and overall administration are not deemed crucial. Furthermore, the accountability for the different control modes [97] (e.g. an unmanned, automated, or remotely-controlled, surface vessel) has not yet been implemented: under the assumption that, during the first experiments, the operator is fully aware of the goal of the tests, and that these different modes (their definition and their impact) remain part of the ongoing research.

In addition, the current design makes an abstraction of the potential onboard social hierarchy of the crew [130, 152, 159], as there is only one operator, and of the complexity of managing a fleet [130, 152] as only one USV will be controlled. Finally, no explicit design focus has been put on ergonomics. Given the flexible physical system lay-out, this design can be tuned during experiments, fitting it to the human, and not the other way around [95]. Likewise, mental work load [299] information could be fetched during experiments, which could induce design iterations. These potential iterations and the design flexibility, will help to avoid the unadvised mimicking of a bridge lay-out [159, 160].

6.3.4 The Hull-To-Hull Navigation Concept

The H2H project offers a first conceptual extension of the Concept of an Inland Shore Control Centre. This H2H project fits within the European Horizon 2020 program, and aims to provide the hull-to-hull distance between H2H objects, which can be either stationary (e.g. a dock), or dynamic (e.g. a vessel) [21, 22], in combination with the uncertainty of this distance and of the positions and orientations of these H2H objects. Figure 6.3a draws an exemplary uncertainty zone in red around a moving H2H object. This zone, together with the dynamics of the ship and its operational mode, could also be used for cascaded, dynamically-changing uncertainty zones, shown in orange and green [128, 297], that could trigger certain messages or system events when interactions with other vessels occur.

Within this H2H project, each H2H object has an H2H System which normally consists of: (i) position and movement sensors, (ii) 2D or 3D geometry models, (iii) an H2H engine to perform calculations, (iv) a data communication link, and (v) an H2H application or user interface. This overarching H2H System design should facilitate close proximity manoeuvring between H2H objects. Accordingly, our research group will test this H2H design philosophy for inland vessels by two types of experiments: single-handed sailing and single-handed docking. Here, the underlying hypothesis would be that the H2H System should allow a vessel operator to single-handedly perform close proximity manoeuvres when using the H2H Application.

Figure 6.3b illustrates such a docking manoeuvre, where the numbers indicate the sequence of envisaged waypoints. Accordingly, the vessel will arrive near the dock, initiate a starboard docking manoeuvre, continue sailing, turn around, and finally perform a second docking manoeuvre from port side. Since it is physically impossible to board the Cogge, the USV would conduct these experiments while being remotely controlled by a human operator in the inland SCC.

Given this unmanned nature of the Cogge and the fact that this USV should only avoid (straight sailing) or encounter (docking) the shoreline, a modification in the H2H system design has been made, depicted by Figure 6.3c, that leverages our modular inland SCC design. Instead of having two H2H engines, i.e., one for the USV and one for the dock, both engines have been combined into one. In order to achieve this design, the USV needs to send its H2H-engine-relevant data to the combined engine. Furthermore, given that the human will use the H2H-application, this information needs to be sent from the H2H-combined engine to our inland SCC where it will be shown on a display. The motion control and monitoring parts of the inland SCC will be used as discussed in Section 6.4.3 and demonstrated in Section 6.4.4.

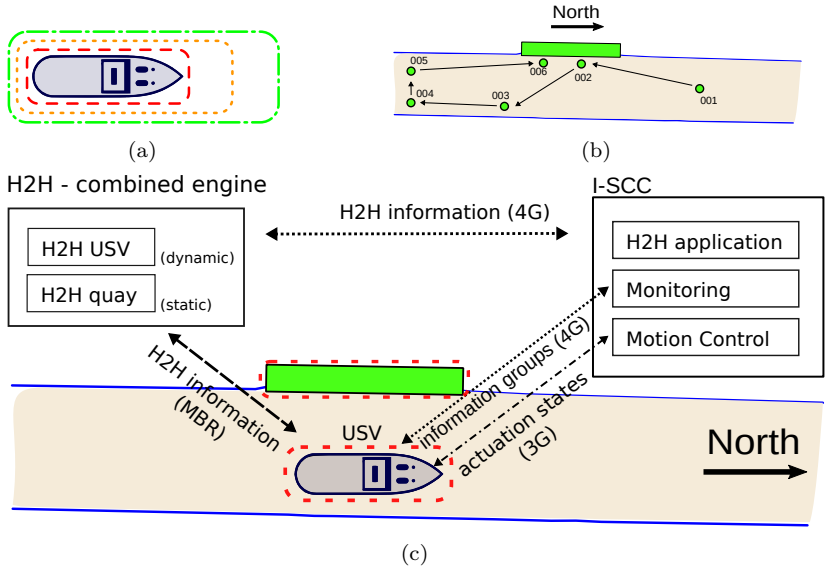

Figure 6.3: Augmented remote motion control and monitoring within the H2H project: (a) proximity zones, (b) envisaged design docking manoeuvre experiments, and (c) design philosophy of the H2H-extensions on the Inland SCC design.

6.3.5 Risk and Safety Analysis of an Inland Shore Control Centre

Despite the scarcity of research regarding industrial cargo USVs [148], their potentially complimentary SCCs [56, 130, 152], and thus their subsequent operational modes or business cases, several studies investigated the potential risks, hazards, and safety concerns for these concepts [14, 218, 261, 292], and their integration in the existing International Maritime Organisation regulations [235]. Nevertheless, the usefulness of having more operational USV and SCC concept data remains a common conclusion in most analyses. Therefore, in line with the suggested engineering estimate approach for the potential future CBAs and the overall activity-based, bottom-up, modular system design, the risk assessment concentrates on the lower technical level (e.g. selecting industrially-robust components, having multiple interaction possibilities with the vessel, having onboard safety stops).

Consequently, the inland SCC and its induced experimental data can nurture the just-mentioned risk and safety analyses, for which the Systems-theoretic Accident Modelling and Processes (STAMP) [14, 141] seems to be a good future methodology as it reviews the entire socio-technical system [8, 14, 48], which will be of paramount importance given the envisaged human–machine interactions. Finally, note that the Flemish waterway administrator continuously defines, monitors, and optimises a legal framework for testing and demonstration purposes with USVs, generating mutually beneficial discussions regarding USV safety and regulations.

6.4 Design and Construction of an Inland Shore Control Centre

First, Section 6.4.1 summarises the resulting technical inland SCC design based on its concept and requirements, i.e., nurtured by the Activity-Centred Design of an Inland SCC and the Design Requirements of an Inland Shore Control Centre, and Section 6.4.2 depicts its physical construction. Similarly Section 6.4.3 shows the technical details of the H2H-extended inland SCC and Section 6.4.4 illustrates its physical construction. Finally, Section 6.4.5 discusses the design of the performed experiments.

6.4.1 Technical Design of an Inland Shore Control Centre

Figure 6.4 represents the full inland SCC design in conjunction with the USV of Section 2.4, i.e., the Cogge. The additions to this USV, in order to accomplish the inland SCC design requirements together with the inland SCC design itself, are detailed in the following three sections, as summarised by Table 6.1, with reference to the full components list of Table A.1.

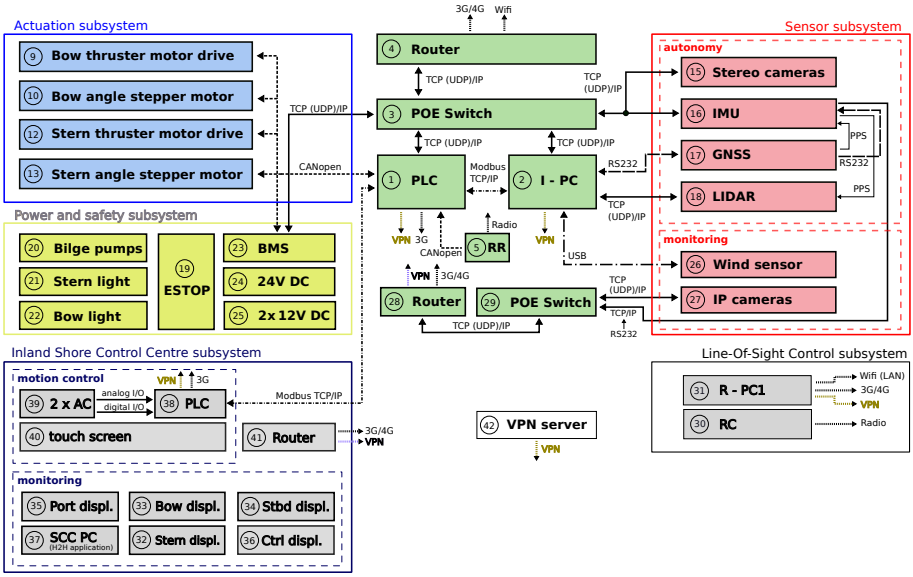

Figure 6.4: Main inland SCC and USV components and their communication links.

Table 6.1: Resulting inland SCC design based on the design requirements of Section 6.3.3.

	Requirement	Design Result	Discussed in
(R-i)	Information Groups	Figure 6.4: sensor and Inland SCC subsystem, PLC	Section 6.4.1.1
(R-ii)	USV Interaction	Figure 6.4: inland SCC subsystem	Section 6.4.1.2
(R-iii)	Marine-Grade, Industrial Components	Table A.1	Section 6.4.1.3
(R-iv)	Modular and Flexible Design	Figure 6.4	Section 6.4.1.3

6.4.1.1 Design Results for Requirement One (R-i)

Table 6.2 details the USV and inland SCC components or subsystems that provide the necessary data for the selected information groups, with reference to Figure 6.4. Comparing this figure with the components of the Cogge as a USV, i.e., Figure 2.12, demonstrates that some of the already-onboard components, namely, the autonomous part of the sensor subsystem and the PLC (number 1), can now be used for multiple purposes.

More precisely, the GNSS and IMU sensors, which normally feed the autonomy software nested in the I-PC, can now stream their data to the inland SCC, thus providing sailing information. Similarly, the stereo cameras and the lidar can produce observation information, if desired. Furthermore, the onboard PLC monitors all wanted parameters and alarms to provide both technical, and safety and emergency information to the inland SCC. The PLC web interface accumulates this information, similarly to Figure 6.2c. In addition to these reused components, the USV has four new cameras installed: port, bow, starboard, and stern orientation. Their images offer security information on the one hand, and given the small USV size, these can also be used as observation information on the other hand.

Three mobile internet connections can pipe these just-discussed information sources to the inland SCC and its display screens: the (i) PLC transmits its technical, and safety and emergency information via a dedicated 3G connection, (ii) the Quartz router (number 4) is capable of streaming the observation information, and (iii) the Pepwave router (number 28) streams the security information. Note that an offshore VPN server (number 42), in conjunction with nested VPN clients shown on some components, facilities the data routing and provides remote access to all these services.

Table 6.2: Summary of the information group realisations.

Information Group	Design Result
Sailing	Figure 6.4: autonomy sensor subsystem
Observation	Figure 6.4: autonomy and monitoring sensor subsystems
Safety and Emergency	Figure 6.4: PLC
Security	Figure 6.4: monitoring sensor subsystem
Technical	Figure 6.4: PLC

6.4.1.2 Design Results for Requirement Two (R-ii)

With the accomplishment of (R-i), the operator should have a degree of situation awareness and sensemaking capabilities, which both can potentially be improved by interaction with the vessel. This interaction in the form of remote motion control, i.e., when remotely steering the vessel, is self-evident: one needs to be able to send desired actuation states to the actuation subsystem of Figure 6.4. A human–machine interface consisting of two azimuth controllers and a touch screen provides this service, shown by Figure 6.5. The latter depicts the current internal steering angles, α^i, and propeller speeds, n, for both actuators, along with their operator-requested values.

Similarly to the onboard actuation layout, see Figure 2.7, the bow controller is placed in front of the stern controller. Both controllers are 360-degrees-steerable and have a lever to control the propeller speed. Consequently, a one-on-one mapping describes the relation between α^i and the azimuth-controller-angle for both actuators. Likewise, the maximum position of the lever represents the maximum propeller speeds of the actuators.

Figure 6.5: The inland SCC motion control subsystem: two azimuth controllers on the left and a touch screen on the right.

The motion control part of the inland SCC subsystem in Figure 6.4 shows the full design of Figure 6.5. Accordingly, a shoreside PLC (number 38) orchestrates all the desired actuation system states and has a dedicated 3G mobile internet connection with its onboard counterpart at the heart of the USV. Next to this enabled motion control interaction, the onboard PLC (number 1) web interface allows the enabling or disabling of components or settings. Similarly, processes can be started or stopped on the I-PC via a secure shell connection, further augmenting the spectrum of interaction possibilities with the vessel.

6.4.1.3 Design Results for Requirement Three and Four (R-iii–iv)

The component enumeration in Table A.1 exemplifies their accordance with the industrial-robustness requirement, i.e., (R-iii). This selection procedure means that these components should also be serviceable on a real-scale vessel or control centre in their operational environments. The details in the previous two result sections, which handled (R-i) and (R-ii), demonstrate the applied modular system design approach. For instance, the multi-purpose utilisation of the USV autonomy sensors, and the nesting of this full USV system design inside the inland SCC concept in general, see Section 6.4.1.1, reveal the envisaged scalability and component-interchangeability of this modular design. In addiction, Section 6.4.1.2 expanded the inland SCC remote motion control on the already-existing cascaded motion control hierarchy nested inside the USV. Finally Section 6.3.4 presented an additional propagation of the inland SCC, further demonstrating its modularity and adequacy as an experimental set-up.

6.4.2 Construction of an Inland Shore Control Centre

Figure 6.6 displays a picture of the first operational status of the inland SCC, with component numbers referring to Table A.1. As shown, the motion control part of the inland SCC subsystem of Figure 6.4 was fully installed, whereas the stern-view camera (number 27) and complimentary display (number 32) were not yet installed. The other three cameras (number 27) provided a live stream of observation and security data while the USV was under remote motion control. These three IP cameras have a variable data throughput depending on their available bandwidth. They can alter this data rate by changing their configuration parameters, e.g., their quality, resolution, or frames per seconds (fps). Figure 6.7 illustrates the positions of the USV components, where their numbers refer to Table A.1.

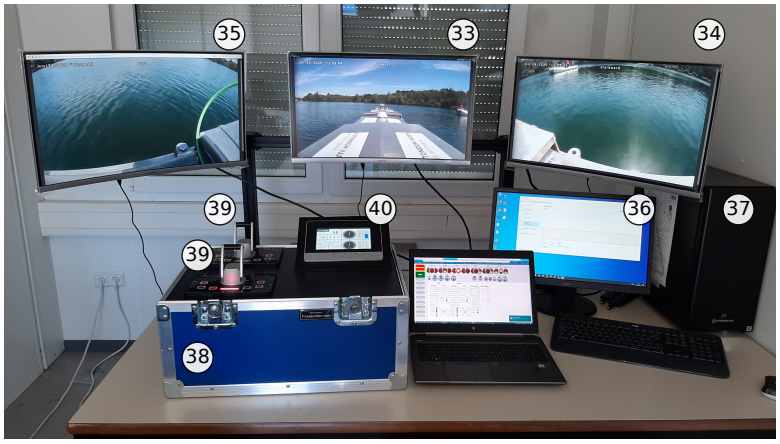

Figure 6.6: Constructed inland SCC streaming video data from the USV sailing on the Rotselaar lake (see Section 6.5.1), part numbers refer to Table A.1.

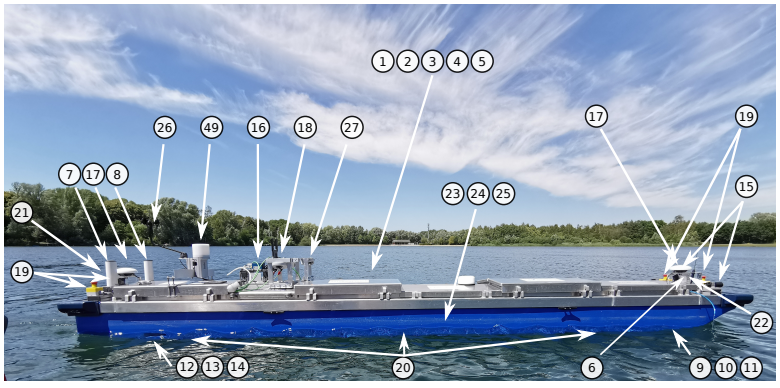

Figure 6.7: Positions of the main onboard USV components, referring to Table A.1. Note that the LIDAR (number 18) was not mounted, but can be seen in Figure 2.5.

6.4.3 Technical Design Hull-To-Hull-Extended Inland Shore Control Centre

Figure 6.8 summarises the current H2H-extended inland SCC system design of this paper. Note that the ongoing H2H project does not have a fully finalised design yet. Consequently, the final H2H-extended system design might still have small adaptions compared to this current design.

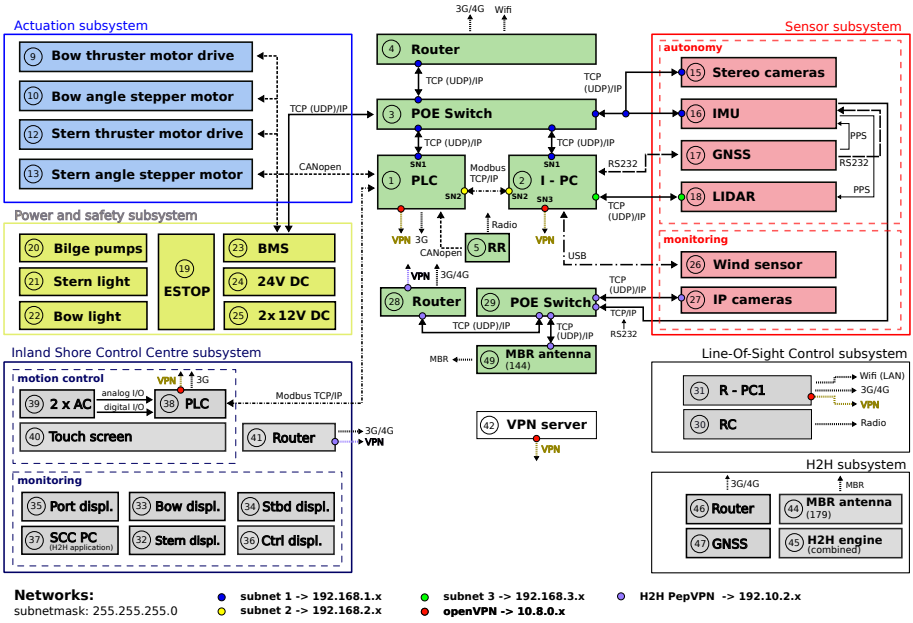

Figure 6.8: H2H-extended inland SCC and USV system design: main components and their communication links.

6.4.4 Construction of Hull-To-Hull-Extended Inland Shore Control Centre

In order to further clarify the H2H-concept (Section 6.3.4) and its technical design details (Section 6.4.3), Figure 6.9 depicts some core parts of the current H2H-extended inland SCC experimental configuration. Figure 6.9a presents the combined H2H engine, from Figure 6.3c, which receives navigational information from the USV and has an own GNSS antenna (number 47, not shown) which is placed on a pre-calibrated position which, together with its 3D drawing, represents the quay, i.e., a static H2H object. The middle screen (number 32) on the bottom of Figure 6.9b visualises the output of the H2H application, which receives information from the combined H2H engine, see Figure 6.3c. This H2H application ran on a laptop (not listed), to facility the first mobile tests.

(a) (b)

Figure 6.9: Current H2H-extended inland SCC configuration: (a) the combined H2H Engine, and (b) the H2H application running in the inland SCC.

6.4.5 Design of Experiments

In order to test the designs and constructions of Section 6.4.1 – Section 6.4.4, the experiments of this study aimed to measure the performance of the overall USV and inland SCC system and the situation awareness of its operator. The system performance was measured by conducting successful experiments and thus implicitly stress testing its overall design. In addition, indicative communication data rates and latencies were explicitly measured to provide more insights in the system performance. The situation awareness of the operator was assessed by both performance measurements and process indices, similarly to the situation awareness assessments techniques present in aviation research [181].

6.4.5.1 First USV and Inland SCC System Stress Tests and Experiments

An operator inside the inland SCC was instructed to remotely control the USV in two different locations, a canal and a lake, on two different days. In the first experiment, the USV was positioned in a canal near Leuven, in the vicinity of the inland SCC, although there was no line of sight for the operator. In the second experiment, the USV sailed on a lake in Rotselaar and its operator was positioned in the inland SCC in Leuven, which separates them by approximately 7 km. For both experiments, the focus was put on the activity, i.e., continuously remotely controlling the USV via the inland SCC. During the canal mission, the operator was asked to sail past two bridges, turn around, and sail back. During the lake mission, the operator received full freedom to sail around. Consequently, both experiments mainly focus on stress testing the full USV and inland SCC system design. Given their loosely defined mission goal, the situation awareness of the operator was not explicitly measured with the just-discussed assessment tools of this study. The results of both missions can be found in Section 6.5.1.

6.4.5.2 First USV and H2H-Extended Inland SCC System Stress Tests and Experiments

The first experiments with the H2H-extended inland SCC system had two goals: to offer a stress test of the complete extended system, and to provide preliminary data on the impact of the H2H-navigation system on the activity of continuously remotely controlling a USV. Hence, these data can also serve to assess the situation awareness of the operator using the H2H-extended inland SCC system. More precisely, an eye-tracker served as process index and the performance measures framework for unmanned systems [114, 115] was used as a guideline for performance measurements. This set of first experiments falls under a larger set of scheduled experiments which aims to test the single-handed sailing and docking hypotheses (see Section 6.3.4) within the H2H project. In this larger set of experiments, both skippers and students will be asked to single-handedly sail the USV via the inland SCC during both straight sailing and docking manoeuvres, once with and once without the H2H-extended interface.

Five performance metrics were selected: time, energy, accuracy, safety, and reliability, in accordance with the commonly used performance dimensions of effectiveness and efficiency, which respectively denote requirement fulfilment and resource consumption [176]. The former two metrics measure efficiency and the latter three effectiveness. Within these experiments, the time metric denotes the elapsed time of a mission, energy the power consumption of the actuation system, accuracy the deviation from the desired trajectory, safety the avoidance of collision, and reliability the overall effectiveness of the tool, i.e., was the participant able to achieve the envisaged goal [297]. Two main sources of performance measure variance [253] will be used and modelled as continuous variables, coined domain knowledge and gamer experience. The former variable could explain a performance increase, given that a person with skipper experience might better understand the propulsion system of the vessel or make better sense of the vessel movements in its environment. The latter variable might explain a performance increase due to more experience in virtually remotely controlling objects in a gaming universe [139], or a better understanding of the motion control system layout.

In this study, two students, with no former knowledge of the USV and the inland SCC, were asked to sail a straight line, back and forth, in the middle of the canal in Leuven. Each participant was given this task twice: once without the H2H-interface, meaning they had to estimate the middle of the canal based on the camera feedback, and once with the H2H-interface which showed a top view visualisation of the vessel in the canal and the target line in the middle of this canal. The order of these experiments was changed between the students. Their results can be found in Section 6.5.2.

6.5 Results

6.5.1 First USV and Inland SCC System Stress Tests and Experiments

Figure 6.10 and Figure 6.11 respectively present data of the canal (Leuven) and lake (Rotselaar) experiments which Section 6.4.5.1 designed. Figure 6.10a and Figure 6.11a plot the position of the main GNSS antenna mushroom positioned at the stern of the vessel, hence they indicate the sailed trajectories. The USV course can be seen in Figure 6.10b and Figure 6.11b in conjunction with the measured steering angles of both actuators. Be aware that these steering angles should be viewed in combination with their propeller speeds, shown in Figure 6.10c and Figure 6.11c, given that these determine the thrust size. As can be seen on Figure 6.10b, the bow thruster was mainly used for small course corrections, whereas both thrusters were used during the more complex manoeuvres. Throughout the less-spatially-restricted lake mission, Figure 6.6, more complex manoeuvres occurred, often involving rotations of both actuators.

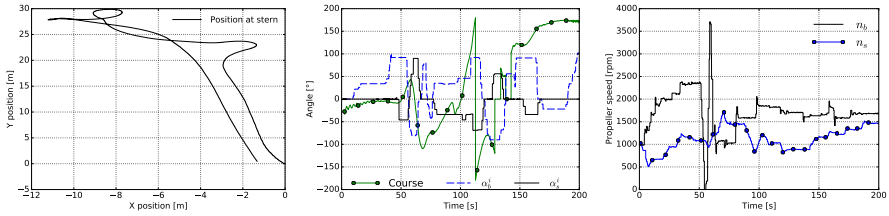

(a) (b) (c)

Figure 6.10: USV under inland SCC motion control in a canal (Leuven): (a) sailed trajectory, (b) internal actuation angles and SCC course, and (c) actuation rotational speeds.

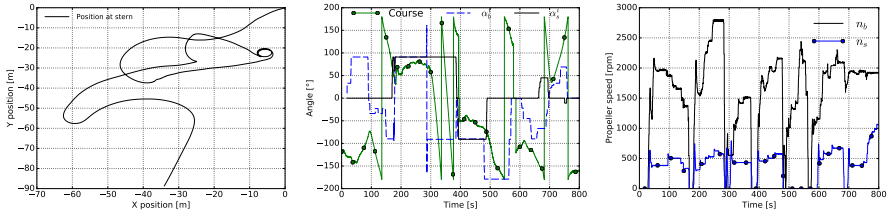

(a) (b) (c)

Figure 6.11: USV under inland SCC motion control in a lake (Rotselaar): (a) sailed trajectory, (b) internal actuation angles and USV course, and (c) actuation rotational speeds.

Figure 6.12 offers the calculated time delays between the USV and inland SCC PLCs for both experiments. This calculation goes as follows: the shoreside PLC transmits its clock-time to the onboard PLC which relays this time to the shoreside PLC. At the reception of this relayed clock time, the shoreside PLC subtracts this time from its current clock time and assumes the half of this difference to be the latency time between both PLCs. Figure 6.12 seem to indicate a similar median latency between the onboard and onshore PLCs which use a 3G connection to communicate. In the former mission, two latency peaks larger than 1 s can be noted. These canal tests were performed in the vicinity of two large bridges, whereas the lake missions had no noticeable nearby obstacles, which might explain these peaks. Next to these motion control latency measurements, some indicative video stream delays of 300–500 ms were manually measured. Here, a timer was placed in the field of view of the camera and pictures were taken of the captured video stream together with this timer, hence providing the latency. Note that a new 5G network might be deployed in Belgium in the foreseeable future, which could enhance the streaming capacity and quality.

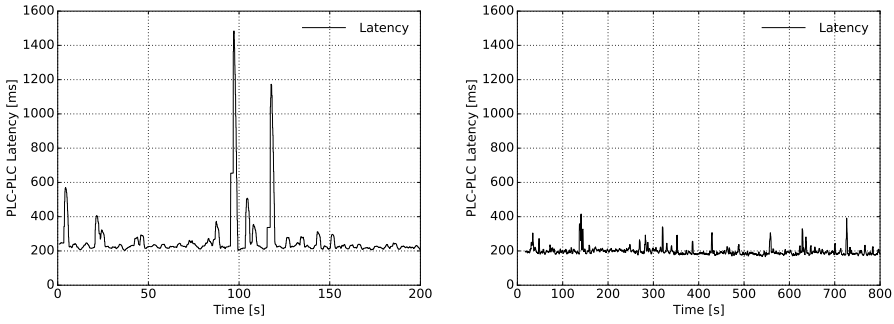

(a) (b)

Figure 6.12: Latency time between PLCs for the (a) canal and (b) lake mission.

In order to fully crystallise the working principle of the USV and inland SCC system, Video S1 shows the Cogge whilst a human operator remotely controls it via the inland SCC, with no line of sight. Note that this video was shot on another testing day than the one producing the data of Figure 6.10, but on the same location. Furthermore, it can be seen that inside the inland SCC the monitor for the stern camera (number 32) was installed but used to visualise the H2H application, which ran on a low frequency during its first live operation, but was not present during the experiments of Figure 6.10 and Figure 6.11. Furthermore, a combined data consumption of 6 to 9 Mbps was noted when requesting a video stream with a resolution of 1024×720 at 24 fps with a normal image quality. Given the average upload speed of 11 Mbps in the Belgian mobile

network [33], the selected Pepwave router (number 28) can pipe this data rate since it has two modems capable of bandwidth fusion with redundant SIM card slot features.

6.5.2 First USV and H2H-Extended Inland SCC System Stress Tests and Experiments

Figure 6.13a and Figure 6.13b respectively show the first run of participant one with the H2H-application and the second run of this participant without the H2H-application. Similarly, but reversed, Figure 6.13c and Figure 6.13d plot the first run of participant two without the H2H-application and the second run of this participant with the H2H-application. These results show that, with or without the H2H-application, the activity of remotely controlling the USV was achievable. It should be noted that, due to their small quantity, these results serve as indicators of how the future larger sets of experiments (see Section 6.4.5.2) can be analysed. Only when more experiments will be conducted in the future, can significant conclusions be made. Nevertheless the current experiments already indicate some interesting findings. Bearing these limitations in mind, Figure 6.13a and Figure 6.13d seem to indicate that the H2H-application helped both participants to stay in the middle of the canal as they show a smaller offset with regard to this middle of the canal (line between both plotted waypoints) compared to Figure 6.13b and Figure 6.13c. Note that the canal is approximately 25 m wide in this test region. In addition, for both participants, the recorded mission durations were shorter when using the H2H-application.

A more in depth analysis of these two performance metrics (time and accuracy), the three remaining performance metrics (energy, safety, and reliability), and the eye-tracker data, falls out of the scope of the current chapter, but will be performed in the H2H project. Although, it can already be noted that all the experiments shown concluded without any collisions and the participants were able to reliably achieve their mission goals. In order to further clarify the operational working principle of the H2H-extended inland SCC, the supplementary Video S2 shows a participant single-handedly preparing a docking manoeuvre with and without the H2H-application. A snapshot of this video can be seen in Figure 6.14a. During these experiments, and the straight-sailing experiments, the participants each wore an eye-tracking device from which a recorded feed can be seen in Video S3. In Video S3, the participant turned the USV during a single-handed straight sailing mission, e.g., Figure 6.13, and the video shows that the participant made use of the H2H-application to orient the USV. A snapshot of this video can also be seen in Figure 6.14b.

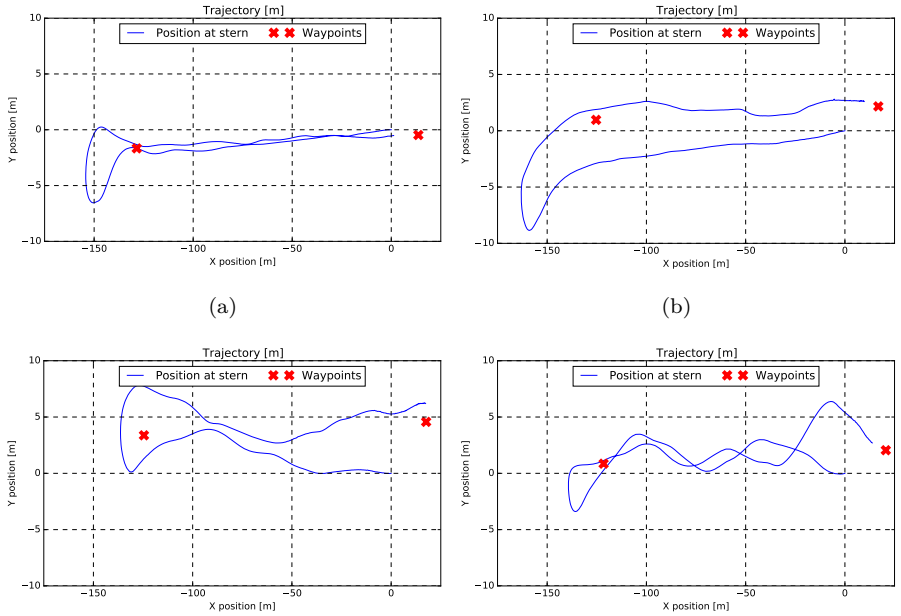

Figure 6.13: H2H-extended inland SCC straight sailing experiment with the USV in a canal (Leuven): (a) participant one, first run, with H2H-application ≈ 8.5 min, (b) participant one, second run, without H2H-application ≈ 10 min, (c) participant two first run, without H2H-application ≈ 7 min, and (d) participant two, second run, with H2H-application ≈ 6 min.

Figure 6.14: Single-handed sailing with the USV and inland SCC system on a canal (Leuven): (a) Video S2: docking manoeuvres from a participant (left) with the H2H-application, and (right) without the H2H application; (b) Video S3: tracking of the eye movements of a participant during the 180° turn of a straight sailing experiment.

6.6 Discussion

The first loosely-defined experiments of Section 6.5.1 offered a thorough stress test of the total USV and inland SCC system. Although the situation awareness of the operator was not explicitly measured, it can be noted that the inland SCC helped the operator to develop a sufficient level of situation awareness and sensemaking during the requested activity of remotely controlling the USV. Hence, these experiments offered a first verification of the ACD concept of the inland SCC from Section 6.3.2.3. Subsequently, the first USV and H2H-extended inland SCC experiments in Section 6.5.2 put forward three main findings. Firstly, they stress tested the H2H-extended inland SCC and USV system, further verifying the possibility to continuously remote control a USV via the inland SCC. Secondly, their goal-oriented mission design allowed to assess the situation awareness of the operator by means of performance measurements and process indices. Thirdly, these assessment tools enable the investigation of the performance impact of the H2H-Extension. For example, both participants seemed to have benefited from this H2H-application, given that it decreased their mission time and track error, compared to the normal inland SCC set-up.

The two analysed performance metrics of Section 6.5.2 seem to indicate an improved level of situation awareness for both participants when using the H2H application, although one needs be careful with such preliminary conclusions: a good performance need not be indicative of a better situation awareness, and vice versa [181]. Additionally, similar caution should be taken when processing the eye-tracker data, given its potential limitation due to the "looked but failed to see [35]" phenomenon [181]. Therefore, in future work, it would be interesting to implement some of the other situation awareness assessment tools of Nguyen et al. (2019 [181]), in order to complement the more basic assessment tools used throughout this study. For example, the freeze-probe technique, would randomly freeze some displays. Afterwards, the participant could be asked to estimate the current system states, such as position, speed, and orientation, or environmental states, such as objects or infrastructure in the neighbourhood. Evidently, the freeze-probe technique would intrude on the activity of controlling the USV. In comparison, a non-intrusive post-trial self-rating technique such as the situation awareness rating technique [255] could also be added.

The cascaded growth of the inland SCC, such as the addition of the H2H-application, further demonstrates that the underlying activities mainly shape the developed tools. Nevertheless, the used ACD approach does also rely heavily on the UCD approach [184]. This connection was rather straightforward given that the researchers act both as product designers and users, thereby often implicitly incorporating their user requirements into the design, which might

give rise to biases. The additions to the inland SCC also emphasise the envisaged modularity of the overall system design, handled by Section 6.4.1.3. In this regard, the currently implemented components of Section 6.4.1.1 provide the integrated USV and inland SCC with a first iteration of information groups in order for its operator to develop levels of situation awareness and sensemaking. Evidently, these selected components are indicative and will most likely be modified and extended based on the feedback of future experiments, which might decrease the aforementioned potential design biases.

Figure 6.15 further exemplifies the overall SCC design modularity, by depicting the motion control subsystem at the lake in Rotselaar, where it only needed a power supply. The shown laptop was connected to a mobile router enabling access to the video stream of the bow-oriented camera. Considering the operator had clear line of sight, this was not necessary but further tested the overall design flexibility. On the top of the picture, a part of the lake can be seen together with the Cogge, a support vessel, and a few researchers. This follow-up vessel was used during all the discussed experiments and had the wearable controller (number 30) onboard. This vessel can also be seen on the bow and starboard oriented video streams on Figure 6.6.

Figure 6.15: Moveable motion control subsystem of the inland SCC system.

Furthermore, this motion control subsystem could also be used to remotely control other types of USVs such as Maverick discussed in Section 2.5. Given that this vessel will have a similar onboard PLC as the Cogge, this should not demand many adaptations. For its old actuator configuration (see Figure 2.15a), it might be more intuitive to change the position of the azimuth controllers, in order to avoid mode confusion [107]. Furthermore, when handling vessels with a larger mass, haptic feedback [2] might be favourable.

The Cogge can already be deployed as an unmanned vessel, capable of autonomously following waypoints [194]. Future work could thus investigate the impact of this operational mode, i.e., monitoring an autonomous inland USV

in its spatially restricted waters [147]. In such a JCS [110, 111] the situational awareness will become more distributed [249] and perhaps extensions such as the H2H-application might help in providing a representation of the current system state and its limitations [160, 274]. Although it is not trivial to define and measure the performance of such a complex system [124, 135], the usability, usefulness, and understandability of such a JCS should be measured [212]. Such future experiments, and the currently scheduled experiments within the H2H project, will allow a further bottom-up investigation of the impact on ship sense and harmony when remotely handling a USV under different operational modes. Although these first data sets will be embryonic, originating from conditioned but real outdoor environments, they hopefully provide essential information for future socio-technical IWT CBAs [166] and STAMP [14, 141] analyses.

6.7 Conclusion

With the intention of providing a finer level of resolution in the feasibility studies regarding unmanned or automated inland cargo shipping, this chapter discussed the design and build of an inland SCC in order to remotely control or monitor a USV or ASV.

Preliminary experiments verified that the operator had sufficient interaction possibilities with the USV in order to continuously remotely control the vessel. Accordingly, the inland SCC had the potential to support the development of situation awareness and sensemaking for its operator, within these first experiments. However, additional situation awareness assessment tools would be advised to further probe the achieved level of situation awareness in the future. Similarly, experiments where the USV is remotely monitored instead of controlled could further validate these findings and help to study the impact on ship sense and harmony when monitoring an autonomous USV. A stepping stone in this direction might be achieved during the discussed H2H navigation experiments which investigate the enhanced remote motion control of a USV. This enhancement could serve as a monitoring tool in the future. Evidently, the technological feasibility of this inland SCC system and its potential design iterations or extensions do not prove its socio-economic viability. For such a viability estimation, future CBAs would be better suited for which this chapter aims to provide fruitful input.

This chapter provides an alternative answer to **RQ2** and **RQ3**, by putting a remote operator in the loop.

Conclusion

> "The line separating good and evil passes not through states, nor between classes, nor between political parties either — but right through every human heart — and through all human hearts. This line shifts, inside us, it oscillates with the years [244]."
>
> Alexander Solzhenitsyn

Figure 7.1: Cogge, sailing on the Yser reservoir, photo courtesy of Marcus Kotzé.

7.1 Research Answers and Deliverables

This section revisits the main research questions of this thesis and provides more insights on their current answers. Afterwards, this section elaborates on the alternative answers for the last two research questions. Finally, an overarching conclusion of the present answers concludes this section.

7.1.1 RQ1 — Industrial and Scientific Relevance

A1. The design and build of an industrially relevant research vessel for unmanned inland cargo shipping (← **RQ1**).

This thesis intends to provide data and insights to investigate the automation potential of the inland waterway fleet. This intention resulted in the design and construction of two industrially relevant (***D*1.1**) research (***D*1.2**) vessels (Chapter 2). The resultant automation potential of these two designs depends on the onboard perception and motion control systems (**A3**) which can benefit from modelling and identifying the vessel hydrodynamics (**A2**).

***D*1.1** An industrially relevant unmanned inland cargo vessel (← ***RO*1.1**).

The introduction (Chapter 1) highlighted the present situation of the IWT sector which undergoes an outflow of small CEMT–I–II vessels and has an overcapacity problem on the larger waterways. Nevertheless, the present governmental policies aim to transport more freight via this IWT sector. Two novel smaller vessel designs might offer part of the solution for this envisaged IWT utilisation discrepancy. First, the new watertruck barges enable the decoupling of sailing and cargo handling time, by introducing a modular fleet of push boats and propelled or unpropelled barges. Second, the onboard crane of the pallet shuttle barges unlocks cargo handling, independently of the shoreside infrastructure. Furthermore, their flat deck facilitates the transportation of palletized cargo. Both concepts seem to have an automation potential which, when properly exploited, might increase their competitiveness and attract more cargo to the IWT sector. Therefore, these novel vessel types served as the blueprints for the research (***D*1.2**) fleet construction. Furthermore, most intracity cargo transport still goes over road, although a few European cities have demonstrated their potential for urban freight transport via waterways. Here too, increasing the automation level of smaller urban vessels might unlock a competitive freight transport alternative.

$\mathcal{D}$1.2 A scientifically relevant unmanned inland cargo vessel (← **$\mathcal{RO}$1.2**).

The state of the art of USV or ASV research further crystallised the design of the research fleet, in addition to the industrial developments in the IWT sector (**$\mathcal{D}$1.1**). Some of the specific research challenges for inland cargo vessels were listed and provided inputs for orienting **A2** and **A3**. Consequently, three design choices integrated the industrial relevance perspective into the design of two experimental platforms. First, the Cogge is a geometrical sale model of a self-propelled watertruck barge, and the Maverick is a functional scale model of a pallet shuttle barge. In addition, both vessels have a length that should enable intracity freight transport research. Second, both vessels have a highly manoeuvrable actuation system which could virtually mimic more constrained actuation systems. Furthermore, the Cogge carries the same non-conventional propulsion system as its real-size counterparts. Third, the modular software and hardware design should facilitate future system extensions or reconfigurations. Moreover, industrial and robust system components were selected in order to facilitate their potential future transfer to real-size vessels (**$\mathcal{D}$1.1**).

7.1.2 RQ2 — Modelling and Identification

A2. The modelling and identification of hydrodynamic motion models of an inland cargo vessel (← **RQ2**).

Understanding the hydrodynamics of the new research fleet (**A1**) can increase the performance of the perception and motion control systems (**A3**). However, given that no model is correct but some are useful, caution should be taken when selecting a model and its subsequent assumptions and limitations. Hence, deciding "what" to model and "how" depends on the requirements of the end-user. Subsequently, this thesis offers a selection of models (Chapter 3, **$\mathcal{D}$2.1**) and their identification procedures (Chapter 4, **$\mathcal{D}$2.2**).

$\mathcal{D}$2.1 Hydrodynamic models for an inland cargo vessel (← **$\mathcal{RO}$2.1**).

The hydrodynamic models of this thesis (Chapter 3) focussed on modelling the decoupled planar motions via a modular vectorial model, since this model offers physical insights in the occurring hydrodynamics. Moreover, given the modularity of this model, an alternative neural network was suggested and constructed to capture the non-conventional thruster forces of the Cogge. In addition, a transfer function model, which relates the yaw-rate outputs to the rudder inputs, can offer a straightforward model for the steering behaviour of a

vessel. Finally, CFD can model the water in which a vessel navigates, in order to construct a virtual hydrodynamic data generation environment.

***D*2.2** Identified hydrodynamic models for inland cargo vessels (← ***RO*2.2**).

This thesis divided the data generation for the identification (Chapter 4) of the hydrodynamic models (***D*2.1**) into three sources: outdoor, indoor, or virtual experiments. The virtual environment might offer the most conditioned environment, given that all the conditions need to be specified by the user. The indoor towing tank offers a second well-conditioned testing facility, whereas the outdoor environment will be most prone to known and unknown disturbances. However, outdoor experiments generate data of the vessel in its operational environment and can thus provide insights in the usability of the modelling assumptions and limitations. Therefore, outdoor data sets for the decoupled planar motions of the Cogge were generated, some based on newly defined additional testing manoeuvres. The subsequently identified surge motion models were compared with bollard pull towing tank data, and with both empirically- and CFD-generated surge damping data. These comparisons seem to hint at a good underlying derived model structure (***D*2.1**) and the physical plausibility of the identified parameters. Finally, the outdoor measured heading and virtual-rudder angles sufficed to identify the asymmetrical steering dynamics of a differentially steered vessel.

7.1.3 RQ3 — Perception and Motion Control

A3. The perception and motion control systems for an unmanned inland cargo vessel (← **RQ3**).

A USV or ASV (**A1**) needs to perceive (***D*3.1**) in order to act in (***D*3.2**) its environment. Both perception and motion control systems can benefit from the hydrodynamic models of the vessels in their environment (**A3**). This study (Chapter 5) defined four environments based on the presence of known or unknown and static or dynamic objects. Furthermore, the perception system envelopes both own navigational information (e.g. pose and speed) and exteroceptive information (sensing the objects in the neighbourhood). The motion control system was further refined into low, middle, and high level control. Evidently, all made refinements are arbitrary and can be altered dependent on the desired research interest.

$\mathcal{D}$3.1 Perception for an unmanned inland cargo vessel (← **$\mathcal{RQ}$3.1**).

Autonomous and unmanned navigation in an environment with solely known and static obstacles was demonstrated with a GNSS sensor in combination with an IMU for the Cogge on a river. This configuration could also suffice for known dynamic objects. Nevertheless, environments with only known static or dynamic objects remain scarce. Therefore, the present work showed the preliminary work on the offline detection and extraction of a shoreline as a stepping stone towards the online detection of a shoreline or other static unknown obstacles.

$\mathcal{D}$3.2 Motion control for an unmanned inland cargo vessel (← **$\mathcal{RQ}$3.2**).

The present highest level of control calculated waypoints between two points of interest. Thereupon, the middle level control followed these waypoints by means of the waypoint following MOOS-IvP behaviour, which could run in combination with other behaviours. Finally the low level PID heading controller commanded the desired actuation control system changes, handled by the onboard PLC. For the avoidance of dynamic objects, traffic rules will need to be implemented.

7.1.4 Alternative Answers for RQ2 and RQ3

A2 and **A3** revisited by putting a remote operator in the loop.

Two main findings drove the design of an inland shore control centre (Chapter 6). First, since it is physically impossible to board the Cogge, a wearable remote controller was used during the initial outdoor experiments. The capability of this wearable controller to position the vessel in between missions, significantly facilitated these experiments. Second, the manual remote control of a USV or ASV could unlock alternative industrial applications. Subsequently, an inland shore control centre to remotely control or monitor USVs or ASVs was designed and constructed. In this shore control centre, a human operator indirectly performs the perception (**$\mathcal{D}$3.1**) and motion control (**$\mathcal{D}$3.2**) for the vessel (**A3**). Furthermore, the operator implicitly models (**$\mathcal{D}$2.1**) and identifies (**$\mathcal{D}$2.2**) the vessel hydrodynamics (**A2**) when interacting with the vessel. The first remote control experiments with this SCC seem to confirm the capability of this SCC to aid the remote operator in the construction of situational awareness and sensemaking. This situational awareness seemed to have been improved during the first preliminary H2H-extended SCC experiments.

7.1.5 Overall Conclusion

Present answers and their limitations Towards Unmanned Inland Shipping.

The constructed vessels balance industrial and scientific relevance. The vessel designs did not study the optimal dimensions [105] for an unmanned inland vessel. The present fleet rather aims to provide data and insights for such calculations, given that current USV or ASV economically viable business models still need to be defined [222, 272]. Currently, most IWT focussed TEN-T related investments seem to focus on facilitating the hinterland navigation for large vessels [76]. However, urban freight transportation via IWT might additionally offer a sustainable urban cargo transportation alternative, for several European cities. This potential will be investigated in the ongoing Avatar [11] and IW-Net [178] projects, in which the constructed fleet will serve as experimental platforms. Multimodal logistical hubs [268] might be crucial for these urban freight transport developments, which might need significant private or public IWT investments, as did happen frequently and successfully in the past [54] (see Figure 1.2).

The identified decoupled motion models for the Cogge [203] focussed on using data generated outdoor with the vessel in its operational environment [205]. Although this approach tests the models where they will be used, it does lack a ground truth for the identified coefficients. Presently, the longitudinal surge damping coefficients derived via CFD [197] and the bollard pull towing tank data [194] offered two Cogge-specific external data benchmarks. However, conducting additional experiments with the Cogge inside a towing tank would provide additional physical insights, and would unlock a complete outdoor, indoor, and virtual data-based model identification comparison. Although CFD based data generation might offer the most conditioned environment, these conditions need to be correctly set by the user, i.e., a converging CFD solution does not need to indicate a physically correct solution.

External disturbances such as wind, current, and waves [90] were presently not explicitly modelled. Nevertheless, for the envisaged smaller freight vessels and current research fleet, these disturbances will have a relatively large effect and should thus be taken into account. Similarly, for the larger vessels, the horizontal and vertical spatial restrictions will influence the hydrodynamic vessel behaviour [68, 145, 210], as they did in the past.

At the lowest control level, the old helmsmen-inspired PID controller can still suffice for autonomous navigation in certain environments [90, 199]. However, the identified hydrodynamic models could be used to develop model predictive controllers which might offer a performance increase. Moreover, the overall control performance could also be increased by injecting additional information

and context in the higher levels of the control hierarchy, with the potential integration of formalised collision avoidance algorithms [72, 132].

In the same vein, the onboard exteroceptive sensors will need information and context to provide online obstacle detection [38], whereas only their offline performance was presently briefly investigated. These context injections should pave the way towards future explainable and composable USV or ASV system integrations [36]. Furthermore, these exteroceptive sensors would enable relative-position-based motion control for the vessels. This control mode might be crucial in the vicinity of infrastructure where the availability and accuracy of global positioning data decreases (e.g. bridges, locks, and quays).

The constructed inland shore control centre [206] offers an intermediate solution for these perception and motion control challenges, by enabling a remote operator to perform these tasks. Nevertheless, this solution raises questions regarding the feasibility for the remote operator to construct a feeling of ship sense [215] and to keep the ship in harmony [214] with its environment, for which the present H2H experiments aim to provide some preliminary insights [295, 296].

In conclusion, this thesis resulted in two experimental platforms and an associated shore control centre, to investigate the automation potential of the present and future inland cargo fleet. Evidently, the technologically oriented validations of the abovementioned research questions alone do not prove their socio-economic viability. Accordingly, this work aims to provide fruitful insights for higher resolution socio-economic feasibility studies. Note that over the last three years, this broader socio-economic scope of automated vessels has become an important aspect of some of the projects classified by the CCNR list of "automation in inland navigation [45]". Moreover, this overview [45] confirms the pioneering role of the present thesis with its construction and experimentation of unmanned, scale model, inland cargo vessels and their associated shore control centre. Finally, the results of this work need not be restricted to unmanned vessels but could also guide automation developments for manned vessels.

7.2 Future Work

With the present vessel design blueprints, their first implementation, the resultant first outdoor experiments, and their limitations, an iteration on the price estimation for potentially unmanned or automated inland cargo vessels could be made [272, 273], focussing on the vessel sizes ranging from urban freight transport up to CEMT–I–II. Similarly, the cost for a minimally viable urban IWT cargo flow could be roughly estimated [11, 178]. Both estimations might help to orient private or public IWT-related investments.

The coupled hydrodynamic motion models should be identified, in addition to their present decoupled counterparts. The present work focussed on modelling and identifying inland vessels in calm water, without explicitly modelled disturbances. However, the wind disturbance [90] should be modelled and measured or estimated for the smaller size vessels, given its large relative effect. The effects of shallow water or banks could also be investigated with the research fleet [68, 137, 210]. Evidently, these effects increase for larger vessels navigating in the same waterways. Furthermore, if the vessels operate in a river, the water current could be modelled [90]. In most inland waterways, wave effects might be neglected, however, they could be added [13, 88, 90], if deemed necessary. The identification procedures in this work focussed on the hydrodynamics of the Cogge, but they could also be applied to the Maverick.

A first model predictive control implementation [72, 303] could be formed based on the already identified motion models. The present offline shore detection should be modified towards an online equivalent [38]. This would enable relative-position-based navigation, in environments with static obstacles. In combination, these control and perception upgrades would provide a foundation for a more contextual navigation of USV or ASVs, which would make the behaviour of the vessels more explainable [36]. This explainability might be crucial in the potential future vessel–vessel or vessel–human interactions, in a more automated IWT sector.

7.3 Main Scientific Contributions

Three main contributions will be briefly highlighted, a complete overview of the scientific contributions can be found in the publication list of the author.

(i) The build of a scale model unmanned inland cargo vessel (Chapter 2) and its first experiments (Chapter 5) [199]. These design blueprints presently serve to overhaul a second research vessel which will be used to investigate urban freight transport [11, 178].

(ii) The build of an inland shore control centre (Chapter 6) to remotely control or monitor vessels [206]. This centre enabled the H2H experiments and can be used in other ongoing [11, 178, 248] and future projects.

(iii) The modelling (Chapter 3) and identification (Chapter 4) of the decoupled equations of motion for the self-propelled watertruck barge scale model, of which all experimental data are publicly available in the Supplementary Materials of Peeters et al. (2020 [203]).

Appendix A

Full Components List

Table A.1: List of H2H-extended Inland SCC and USV system components: their descriptions, abbreviations or names, and specific types.

Nr.	Description	Abbreviation/Name	Type
1	Programmable logic controller	Onboard PLC	Wago PFC200 750-8207
2	Industrial computer	I-PC	Moxa MC-7200-MP-T
3	Power over Ethernet switch	POE switch	Wago 5-port 1000 Base-T Industrial Eco Switch
4	Industrial Router USV	Quartz Router USV	Siretta,Quartz-W22-LTE, 4G/LTE, WiFi, 2 LAN/2 SIM Port
5	Radio receiver	RR	Danfoss MPCAN
6	Antenna LTE (PLC)	PLC antenna	LTE Antenna for PLC
7	Antenna LTE (Quartz)	LTE antenna	LTE Antenna for Quartz LTE
8	Antenna Wifi (Quartz)	Wifi antenna	Wifi Antenna for Quartz LTE
9	Bow thruster motor drive	Bow motor drive	Roboteq MBL1660A
10	Bow angle integrated stepper	Bow angle quickstep	JVL MIS234S
11	Bow thruster motor	Bow motor	Turnigy RotoMAx 150cc
12	Stern thruster motor drive	Stern motor drive	Roboteq MBL1660A
13	Stern angle integrated stepper	Stern angle quickstep	JVL MIS343
14	Stern thruster motor	Stern motor	Turnigy Aerodrive SK3-6364-245KV
15	Stereo cameras (2x)	Stereo cameras	Custom built, UI-5280FA-C-HQ Vision++
16	Inertial measurements unit	IMU	EKINOX2-E-G4A3
17	Navigational GNSS sensor	GNSS	Septentrio AsteRx-U MARINE
18	Laser scanner	LIDAR	Neptec OPAL-1000
19	Emergency stops (4x)	ESTOP	Twist to reset 40 mm Mushroom
20	Bilge pumps (3x)	Bilge pumps	Rule Bilge pump 800
21	Stern light	Stern light	LED white 12–24 V
22	Directional lights bow	Port/Starboard light	Allpa LED 2 colors 8–30 V
23	Battery monitoring system	BMS	Mastervolt-Amperian interface
24	Battery 24 V	24V DC	Navex
25	Battery 24 V (2 × 12v)	2 × 12V DC	Navex

Table A.1: *Cont.*

26	Wind Sensor	Wind Sensor	Rugged NMEA0183 Wind Transducer WND100
27	Network cameras (4x)	IP cameras	Panasonic WV-S3531L
28	LTE Router	Pepwave LTE Router	Pepwave MAX Transit MAX TST DUO LTEA W T
29	12 Port Switch	Zyxel Switch	Zyxel 12-port GbE Managed PoE Switch RGS200-12P
30	Wearable remote control	RC	IK3 Danfoss
31	Rugged shoreside laptop	R-PC	Dell latitude rugged 7204
32	Monitor stern	Stern displ.	Samsung C27F591FDU Color Display Unit
33	Monitor bow	Bow displ.	Samsung C27F591FDU Color Display Unit
34	Monitor starboard	Stbd displ.	Samsung C27F591FDU Color Display Unit
35	Monitor port	Port displ.	Samsung C27F591FDU Color Display Unit
36	Monitor information	Ctrl displ.	HP LD5512 UHD 4K Conferencing Display
37	Monitoring Computer	SCC PC	Intel i9X based PC
38	Programmable logic controller	Shore PLC	Wago PFC200, 750-8207
39	Azimuth controllers (2x)	AC	Verhaar Omega IVOP-BS-01
40	Motion control touch screen	Touch screen	Wago Touch Panel 600, 762-4103
41	Industrial Router SCC	Quartz Router SCC	Siretta,Quartz-W22-LTE, 4G/LTE, WiFi, 2 LAN/2 SIM Port
42	VPN server	VPN server	OpenVPN
43	LTM942 Antenna	Multi Band Antenna	Mobilemark Dual Carrier MIMO Multi-Band LTM942
44	MBR Antenna 179	MBR 179 Antenna	Kongsberg Maritime Broadband Radio MBR 179
45	H2H Combined Engine	H2H Engines (combined)	Kongsberg Rack, 2x DPS R+ HMI, 2x DPS 232 R+
46	4G LTE Router	Pepwave Router	Pepwave MAX BR1 Embedded 4G LTE Automatic Failover
47	GNSS Antenna shore	NovAtel Antenna	NovAtel GPS-713-GGG-N , GNSS & GPS Antenna
48	Dynamic positioning systems	DPS (2x)	2x Kongsberg DPS 232 R+
49	MBR Antenna 144	MBR 144 Antenna	Kongsberg Maritime Broadband Radio MBR 144

Appendix B

Bollard Pull Test Data

Table B.1 lists the towing tank data for the steering-grid thruster. This thruster performed its bollard pull tests as a stand-alone device without enveloping ship hull hence only the internal angle-dependent hull losses occurred. In addition, the thrust forces were measured in alignment with the control angle of the steering grid, i.e., assuming $\alpha_g^i = \alpha_g^o$, using a planar beam load cell of the type LCPB series of OMEGA with a maximal error of 1% [194]. Table B.2 lists the four-channel thruster bollard tests, measured by a UDW3 force/torque sensor from AMTI, with a maximal error of 3% per component (mainly due to the possibility of cross-talk). These tests were performed inside half a ship hull, which was split in the transversal direction, i.e., cut in the yz-plane at midship. The data were measured in the x- and y-direction of the vessel. The listed resulting total thrust force, D_c, and its orientation, α_c^o, were calculated based on these xy-decomposed measurements [194]. Note that there was no flow-straightener used during these bollard pull experiments (see Section 5.4.1.1).

B.1 Bollard Pull Data Steering-Grid Thruster

Table B.1: Data steering-grid thruster, $D_g(n_g, \alpha^i)$

α_g^i [°]	500 rpm	1000 rpm	1500 rpm
0	1.85	7.47	13.70
30	2.30	8.08	15.16
60	1.75	7.64	15.30 [1]
90	1.64	6.68	14.52
120	1.79	6.57	13.11
150	0.81	3.41	7.79
180	0.79	3.36	8.12

[1] data point calculated based on Table C.2 with a quadratic fit for $t(\alpha)$.

B.2 Bollard Pull Data Four-Channel Thruster

Table B.2: Data four-channel stern thruster.

α_c^i [°]	n_c [rpm]	D_c^x [N]	D_c^y [N]	D_c [N]	α_c^o [°]
0	354	6.98	0.10	6.98	0.82
−30	348	2.49	−3.09	3.97	−51.14
−45	328	1.71	−3.56	3.95	−64.34
−60	330	0.60	−5.62	5.65	−83.91
−90	325	0.37	−6.86	6.87	−86.91
−120	336	0.52	−4.63	4.66	−83.59
−135	337	−1.27	−2.27	2.60	−119.23
−150	334	−3.68	−0.13	3.68	−177.98
−180	360	−7.32	−0.22	7.32	−178.28
0	660	23.78	0.68	23.79	1.64
−30	653	7.85	−11.46	13.89	−55.59
−45	628	6.20	−12.72	14.15	−64.01
−60	626	2.01	−20.33	20.43	−84.35
−90	617	2.48	−26.15	26.27	−84.58
−120	630	2.22	−16.69	16.84	−82.42
−135	628	−4.82	−8.38	9.67	−119.91
−150	636	−13.15	−0.52	13.16	−177.74
−180	665	−24.91	−0.13	24.91	−179.70
0	960	51.06	1.26	51.08	1.41
−30	952	16.60	−24.50	29.59	−55.88
−45	930	13.23	−27.56	30.57	−64.36
−60	925	4.61	−45.45	45.68	−84.21
−90	925	4.83	−58.38	58.58	−85.27
−120	938	5.39	−36.35	36.75	−81.57
−135	935	−10.45	−18.30	21.07	−119.73
−150	934	−29.63	−1.44	29.66	−177.22
−180	966	−53.43	−1.06	53.44	−178.86
0	1255	87.64	1.99	87.66	1.30
−30	1248	28.34	−42.07	50.73	−56.03
−45	1219	23.00	−47.14	52.45	−63.99
−60	1216	7.72	−79.07	79.45	−84.42
−90	1215	8.45	−102.88	103.23	−85.30
−120	1226	9.23	−64.20	64.86	−81.82
−135	1226	−18.17	−32.13	36.91	−119.49
−150	1226	−51.58	−2.57	51.64	−177.15
−180	1260	−92.01	−2.24	92.04	−178.61
0	1545	134.40	3.36	134.44	1.43
−30	1538	43.05	−64.44	77.50	−56.25
−45	1515	35.41	−72.83	80.98	−64.07
−60	1510	11.36	−121.99	122.52	−84.68
−90	1510	10.80	−160.79	161.15	−86.16
−120	1515	13.26	−99.74	100.62	−82.43
−135	1515	−28.21	−49.33	56.83	−119.76
−150	1515	−79.17	−5.21	79.34	−176.23
−180	1550	−140.19	−4.15	140.25	−178.30

Appendix C

Identified Bow Thruster Coefficients

Table C.1: $T_m(n) = T_n n$

Order t(θ)	Cost	t_5	t_4	t_3	t_2	t_1	t_0	T_n
Quintic	25.45	3.68×10^{-10}	1.61×10^{-07}	-2.43×10^{-05}	1.48×10^{-03}	-2.98×10^{-02}	1.33×10^{-02}	8.40×10^{-03}
Quartic	30.39	0	-5.25×10^{-09}	1.72×10^{-06}	-1.39×10^{-04}	2.36×10^{-03}	1.69×10^{-02}	8.57×10^{-03}
Cubic	31.44	0	0	-1.67×10^{-07}	7.23×10^{-05}	-4.87×10^{-03}	-7.75×10^{-03}	8.18×10^{-03}
Quadratic	31.88	0	0	0	2.61×10^{-05}	-1.72×10^{-03}	-1.94×10^{-02}	8.29×10^{-03}
Linear	37.01	0	0	0	0	2.58×10^{-03}	4.81×10^{-03}	9.36×10^{-03}
Constant	62.12	0	0	0	0	0	2.14×10^{-02}	7.22×10^{-03}

Table C.2: $T_m(n) = T_{nn} n^2$

Order t(θ)	Cost	t_5	t_4	t_3	t_2	t_1	t_0	T_{nn}
Quintic	2.76	-1.86×10^{-10}	7.75×10^{-08}	-1.11×10^{-05}	6.85×10^{-04}	-1.63×10^{-02}	7.76×10^{-03}	6.37×10^{-06}
Quartic	3.80	0	-6.58×10^{-09}	2.01×10^{-06}	-1.32×10^{-04}	-5.03×10^{-04}	8.35×10^{-04}	6.36×10^{-06}
Cubic	5.38	0	0	-3.52×10^{-07}	1.30×10^{-04}	-9.39×10^{-03}	5.85×10^{-03}	6.23×10^{-06}
Quadratic	7.28	0	0	0	3.06×10^{-05}	-2.55×10^{-03}	8.08×10^{-03}	6.57×10^{-06}
Linear	14.84	0	0	0	0	2.60×10^{-03}	-6.83×10^{-03}	7.24×10^{-06}
Constant	41.24	0	0	0	0	0	7.35×10^{-06}	5.52×10^{-06}

Table C.3: $T_m(n) = T_{nnn}n^3$

Order t(θ)	Cost	t_5	t_4	t_3	t_2	t_1	t_0	T_{nnn}
Quintic	27.15	-8.28×10^{-11}	3.04×10^{-08}	-3.75×10^{-06}	2.34×10^{-04}	-8.61×10^{-03}	1.52×10^{-02}	4.40×10^{-09}
Quartic	27.32	0	-7.20×10^{-09}	2.15×10^{-06}	-1.31×10^{-04}	-1.74×10^{-03}	-9.32×10^{-04}	4.34×10^{-09}
Cubic	29.10	0	0	-4.42×10^{-07}	1.58×10^{-04}	-1.17×10^{-02}	-1.29×10^{-02}	4.17×10^{-09}
Quadratic	31.72	0	0	0	3.30×10^{-05}	-2.95×10^{-03}	-3.40×10^{-03}	4.48×10^{-09}
Linear	39.85	0	0	0	0	2.56×10^{-03}	-4.04×10^{-03}	5.03×10^{-09}
Constant	64.79	0	0	0	0	0	2.24×10^{-08}	3.83×10^{-09}

Table C.4: $T_m(n) = T_{nn}n^2 + T_n n$

Order t(θ)	Cost	t_5	t_4	t_3	t_2	t_1	t_0	T_{nn}	T_n
Quintic	1.50	-2.00×10^{-10}	8.44×10^{-08}	-1.23×10^{-05}	7.56×10^{-04}	-1.71×10^{-02}	9.49×10^{-02}	5.74×10^{-06}	1.70×10^{-03}
Quartic	2.96	0	-6.65×10^{-09}	2.05×10^{-06}	-1.38×10^{-04}	-1.56×10^{-04}	-3.61×10^{-02}	5.28×10^{-06}	1.19×10^{-03}
Cubic	4.47	0	0	-3.41×10^{-07}	1.27×10^{-04}	-9.15×10^{-03}	-3.46×10^{-02}	5.11×10^{-06}	1.21×10^{-03}
Quadratic	6.12	0	0	0	3.43×10^{-05}	-2.78×10^{-03}	-1.36×10^{-01}	4.78×10^{-06}	1.31×10^{-03}
Linear	13.35	0	0	0	0	2.58×10^{-03}	3.29×10^{-04}	5.87×10^{-06}	1.91×10^{-03}
Constant	39.83	0	0	0	0	0	-7.91×10^{-02}	4.11×10^{-06}	1.35×10^{-03}

Table C.5: $T_m(n) = T_{nnn}n^3 + T_{nn}n^2 + T_n n$

Order t(θ)	Cost	t_5	t_4	t_3	t_2	t_1	t_0	T_{nnn}	T_{nn}	T_n
Quintic	0.99	-2.43×10^{-10}	1.03×10^{-07}	-1.51×10^{-05}	9.27×10^{-04}	-2.06×10^{-02}	-4.62×10^{-02}	-2.34×10^{-09}	1.01×10^{-05}	-1.05×10^{-03}
Quartic	2.62	0	-9.61×10^{-09}	2.97×10^{-06}	-2.02×10^{-04}	2.27×10^{-05}	-5.09×10^{-01}	-1.31×10^{-09}	6.50×10^{-06}	-5.91×10^{-04}
Cubic	4.11	0	0	-3.32×10^{-07}	1.24×10^{-04}	-8.93×10^{-03}	-3.87×10^{-02}	-1.91×10^{-09}	9.31×10^{-06}	-8.55×10^{-04}
Quadratic	5.67	0	0	0	5.45×10^{-05}	-4.38×10^{-03}	-8.26×10^{-01}	-1.29×10^{-09}	5.82×10^{-06}	-5.85×10^{-04}
Linear	12.77	0	0	0	0	2.51×10^{-03}	2.83×10^{-02}	-3.14×10^{-09}	1.30×10^{-05}	$-1.44e-03$
Constant	39.26	0	0	0	0	0	1.44×10^{-01}	-2.75×10^{-09}	1.13×10^{-05}	-1.29×10^{-03}

Appendix D

Surge Coefficients

Table D.1: Identified surge model coefficients for the DEM^U.

	$\boldsymbol{\theta}_u^a$	$\boldsymbol{\theta}_u^b$	$\boldsymbol{\theta}_u^c$	$\boldsymbol{\theta}_u^d$	$\boldsymbol{\theta}_u^e$	$\boldsymbol{\theta}_u^f$	$\boldsymbol{\theta}_u^g$	$\boldsymbol{\theta}_u^h$	$\boldsymbol{\theta}_u^i$
cost	13.7	14.2	15.3	36.2	45.3	92.8	19.1	20.8	23.7
$X_{\dot{u}}$	26.60	35.41	75.00	75.00	25.00	62.60	43.46	74.96	56.80
X_{uuu}	8.30	0.00	0.00	25.85	0.00	0.00	13.14	0.00	0.00
X_{uu}	0.00	9.01	0.00	0.00	33.08	0.00	0.00	13.45	0.00
X_u	14.7	11.9	18.2	16.0	3.60	39.5	18.0	15.3	24.0
$T_{nn}^{0,b}$	6.88×10^{-6}	7.53×10^{-6}	9.03×10^{-6}	6.28×10^{-6}	5.49×10^{-6}	5.46×10^{-6}	5.55×10^{-6}	6.70×10^{-6}	7.29×10^{-6}
$T_{nn}^{0,s}$	2.62×10^{-5}	2.70×10^{-5}	2.93×10^{-5}	1.67×10^{-5}	1.48×10^{-5}	1.69×10^{-5}	2.63×10^{-5}	2.86×10^{-5}	2.95×10^{-5}
$T_{n\nu}^{0,b}$	-6.84×10^{-3}	-9.22×10^{-3}	-1.41×10^{-2}	0.00	0.00	0.00	0.00	0.00	0.00
$T_{n\nu}^{0,s}$	-2.67×10^{-2}	-2.86×10^{-2}	-3.23×10^{-2}	0.00	0.00	0.00	0.00	0.00	0.00
$T_{nn\nu}^{0,b}$	0.00	0.00	0.00	0.00	0.00	0.00	-2.80×10^{-07}	-1.71×10^{-6}	-3.07×10^{-6}
$T_{nn\nu}^{0,s}$	0.00	0.00	0.00	0.00	0.00	0.00	-1.56×10^{-5}	-1.81×10^{-5}	-1.98×10^{-5}

Table D.2: Identified surge model coefficients for the FBM^B.

	$\boldsymbol{\theta}_u^a$	$\boldsymbol{\theta}_u^b$	$\boldsymbol{\theta}_u^c$	$\boldsymbol{\theta}_u^d$	$\boldsymbol{\theta}_u^e$	$\boldsymbol{\theta}_u^f$	$\boldsymbol{\theta}_u^g$	$\boldsymbol{\theta}_u^h$	$\boldsymbol{\theta}_u^i$
cost	44,306.5	44,460.3	50,313.2	79,170.6	80,628.9	121,466.91	59,084.0	59,675.91	63,849.7
$X_{\dot{u}}$	25.00	25.00	25.00	25.00	25.00	25.00	25.00	25.00	25.00
X_{uuu}	4.42	0.00	0.00	16.60	0.00	0.00	9.36	0.00	0.00
X_{uu}	4.97	11.98	0.00	5.18	31.12	0.00	0.00	13.46	0.00
X_u	9.43	6.52	15.35	10.10	0.00	31.07	14.22	8.92	19.04
$T_{nn}^{0,b}$	7.00×10^{-6}	7.00×10^{-6}	7.00×10^{-6}	5.18×10^{-6}	5.18×10^{-6}	5.18×10^{-6}	6.27×10^{-6}	6.50×10^{-6}	7.00×10^{-6}
$T_{nn}^{0,s}$	2.41×10^{-5}	2.41×10^{-5}	2.54×10^{-5}	1.47×10^{-5}	1.49×10^{-5}	1.56×10^{-5}	2.37×10^{-5}	2.38×10^{-5}	2.50×10^{-5}
$T_{n\nu}^{0,b}$	-8.79×10^{-3}	-8.85×10^{-3}	-1.02×10^{-2}	0.00	0.00	0.00	0.00	0.00	0.00
$T_{n\nu}^{0,s}$	-2.47×10^{-2}	-2.51×10^{-2}	-2.83×10^{-2}	0.00	0.00	0.00	0.00	0.00	0.00
$T_{nn\nu}^{0,b}$	0.00	0.00	0.00	0.00	0.00	0.00	-2.13×10^{-6}	-2.47×10^{-6}	-3.54×10^{-6}
$T_{nn\nu}^{0,s}$	0.00	0.00	0.00	0.00	0.00	0.00	-1.47×10^{-5}	-1.51×10^{-5}	-1.66×10^{-5}

Table D.3: Identified surge model coefficients for the FBM^U.

	$\boldsymbol{\theta}_u^a$	$\boldsymbol{\theta}_u^b$	$\boldsymbol{\theta}_u^c$	$\boldsymbol{\theta}_u^d$	$\boldsymbol{\theta}_u^e$	$\boldsymbol{\theta}_u^f$	$\boldsymbol{\theta}_u^g$	$\boldsymbol{\theta}_u^h$	$\boldsymbol{\theta}_u^i$
cost	43,361.1	43,361.1	44,946.8	144,849.2	85,623.0	228,755.0	59,084.0	450,793.1	63,572.6
$X_{\dot{u}}$	25.00	25.00	25.00	35.45	29.47	35.42	25.0	35.40	25.00
X_{uuu}	0.00	0.00	0.00	12.58	0.00	0.00	9.36	0.00	0.00
X_{uu}	8.10	8.10	0.00	13.38	26.78	0.00	0.00	7.00	0.00
X_u	8.63	8.63	13.78	15.68	5.64	18.25	14.22	7.00	18.85
$T_{nn}^{0,b}$	7.82×10^{-6}	7.82×10^{-6}	8.48×10^{-6}	7.01×10^{-6}	5.32×10^{-6}	6.36×10^{-6}	6.27×10^{-6}	8.96×10^{-6}	7.33×10^{-6}
$T_{nn}^{0,s}$	2.42×10^{-5}	2.42×10^{-5}	2.47×10^{-5}	1.82×10^{-5}	1.55×10^{-5}	1.12×10^{-5}	2.37×10^{-5}	5.64×10^{-5}	2.48×10^{-5}
$T_{n\nu}^{0,b}$	-1.17×10^{-2}	-1.17×10^{-2}	-1.46×10^{-2}	0.00	0.00	0.00	0.00	0.00	0.00
$T_{n\nu}^{0,s}$	-2.55×10^{-2}	-2.55×10^{-2}	-2.73×10^{-2}	0.00	0.00	0.00	0.00	0.00	0.00
$T_{nn\nu}^{0,b}$	0.00	0.00	0.00	0.00	0.00	0.00	-2.13×10^{-6}	-7.49×10^{-6}	-3.88×10^{-6}
$T_{nn\nu}^{0,s}$	0.00	0.00	0.00	0.00	0.00	0.00	-1.47×10^{-5}	-6.65×10^{-5}	-1.63×10^{-5}

Bibliography

[1] AAWA. *Remote and Autonomous Ships: The next steps*. Tech. rep. Advanced Autonomous Waterborne Applications (AAWA) partners, 2016. URL: http://www.rolls-royce.com/~/media/Files/R/Rolls-Royce/documents/customers/marine/ship-intel/aawa-whitepaper-210616.pdf.

[2] D. A. Abbink, M. Mulder and E. R. Boer. "Haptic shared control: smoothly shifting control authority?" In: *Cognition, Technology & Work* 14.1 (Mar. 2012), pp. 19–28. ISSN: 1435-5566. DOI: 10.1007/s10111-011-0192-5.

[3] M. Abkowitz. *Lectures on Ship Hydrodynamics - Steering and Maneuverability*. Tech. rep. Report No. Hy-5. Lyngby: Hydro- og Aerodynamisk Laboratorium, May 1964. URL: http://resolver.tudelft.nl/uuid:d511bd6b-ca2e-4f10-ad9f-6c881eb1e9f8.

[4] A. Ahani and M. J. Ketabdari. "Alternative approach for dynamic-positioning thrust allocation using linear pseudo-inverse model". In: *Appl. Ocean Res.* 90 (May 2019). ISSN: 01411187. DOI: 10.1016/j.apor.2019.101854.

[5] M. Altosole, G. Benvenuto, M. Figari and U. Campora. "Dimensionless Numerical Approaches for the Performance Prediction of Marine Waterjet Propulsion Units". In: *International Journal of Rotating Machinery* (2012). DOI: 10.1155/2012/321306.

[6] V. Ankudinov, P. Kaplan and B. K. Jacobsen. "Assessment and principal structure of the modular mathematical model for ship maneuverability prediction and real-time maneuvering simulations". English. In: *International conference on marine simulation and ship manoeuvrability (MARSIM)*. Canada, 1993.

[7] Antwerp Management School. *Watertruck+: Towards a taxi service of barges*. Mar. 2020. URL: https://blog.antwerpmanagementschool.be/en/toward-a-taxi-service-of-barges.

[8] R. Aps, M. Fetissov, F. Goerlandt, M. Kopti and P. Kujala. "STAMP-Mar based safety management of maritime navigation in the Gulf of Finland (Baltic Sea)". In: *2016 European Navigation Conference (ENC)*. May 2016, pp. 1–8. DOI: 10.1109/EURONAV.2016.7530538.

[9] AUTOBarge. *European training and research network on Autonomous Barges for Smart Inland Shipping*. Horizon 2020, Topic: MSCA-ITN-2020, Type of action: MSCA-ITN-ETN. 2021.

[10] AUTOSHIP. *Autonomous Shipping Initiative for European Waters*. online. 2020. URL: https://www.autoship-project.eu/.

[11] AVATAR. *The Avatar Project*. Online. AVATAR is a project co-funded by the North Sea Region Programme 2014–2020. 2020. URL: https://northsearegion.eu/avatar/.

[12] J. P. Avila, D. C. Donha and J. C. Adamowski. "Experimental model identification of open-frame underwater vehicles". In: *Ocean Engineering* 60 (2013), pp. 81–94. ISSN: 0029-8018. DOI: 10.1016/j.oceaneng.2012.10.007.

[13] P. Bailey, W. Price and P. Temarel. "A unified mathematical model describing the manoeuvring of a ship travelling in a seaway." In: *Transactions of the Royal Institution of Naval Architects* 140 (1998). Part B, pp. 131–149.

[14] O. V. Banda, S. Kannos, F. Goerlandt, P. H. van Gelder, M. Bergström and P. Kujala. "A systemic hazard analysis and management process for the concept design phase of an autonomous vessel". In: *Reliability Engineering and System Safety* 191.106584 (2019). DOI: 10.1016/j.ress.2019.106584.

[15] S. I. Baniela. "The performance of a tunnel bow thruster with slow speed ahead: A revisited issue". In: *J. Navig.* 62.4 (Oct. 2009), pp. 631–642. ISSN: 03734633. DOI: 10.1017/S0373463309990166.

[16] J. M. Beer, A. D. Fisk and W. A. Rogers. "Toward a framework for levels of robot autonomy in human-robot interaction." eng. In: *Journal of human-robot interaction* 3.2 (2014), pp. 74–99. ISSN: 2163-0364. URL: https://dl.acm.org/doi/10.5898/JHRI.3.2.Beer.

[17] S. Bening. *The large city crane, nearby the "Cranebridge"*. Painting. Circa 1525. URL: https://commons.wikimedia.org/wiki/File:Simon_Bening_-_Oktober.jpg.

[18] M. R. Benjamin. *Autonomous COLREGS Modes and Velocity Functions Autonomous COLREGS Modes and Velocity Functions*. Tech. rep. MIT-CSAIL-TR-2017-009. MIT, 2017. URL: http://hdl.handle.net/1721.1/109146.

[19] M. R. Benjamin. *Trends in Marine Vehicles Technologies Affecting Autonomy*. 2016. URL: https://oceanai.mit.edu/ivpman/pmwiki/pmwiki.php?n=Helm.MarineTechnologies (visited on 20/09/2016).

[20] M. R. Benjamin, H. Schmidt, P. M. Newman and J. J. Leonard. "Nested Autonomy for Unmanned Marine Vehicles with MOOS-IvP". In: *Journal of Field Robotics* 27.6 (Nov. 2010), pp. 834–875. ISSN: 15564959. DOI: 10.1002/rob.20370.

[21] S. P. Berge, M. Hagaseth and P. E. Kvam. "Hull-to-Hull Positioning for Maritime Autonomous Ship (MASS)". In: *18th Conferrence on Computer and IT Applications in the Maritime Industries*. ISBN 978-3-89220-709-2. 2019.

[22] S. P. Berge, P. E. Kvam and A. Rinnan. "Hull-To-Hull Concept Supporting Autonomous Navigation". In: *International Conference on Maritime Autonomous Surface Ships*. ISBN 978-82-536-1628-5 (pdf). 2018.

[23] V. Bertram. *Unmanned Surface Vehicles – A Survey*. Skibsteknisk Selskab. Copenhagen, Denmark, ENSIETA, 2008, pp. 1–14. URL: https://www.researchgate.net/publication/228393498_Unmanned_Surface_Vehicles-A_Survey.

[24] J. L. Beveridge. *Design and performance of bow thrusters*. Tech. rep. Washinton DC, United States: Naval Ship Research and Development Center Bethesda, Oct. 1971, pp. 1–39. URL: http://resolver.tudelft.nl/uuid:3abba515-43fa-466d-b83d-dffcd77b0dde.

[25] Binnenvaart. *Magazine voor vervoer over water*. Tech. rep. 68. Blue Line Logistics lanceert nieuw schip vol palletten, p9–11. Binnenvaart, Oct. 2014. URL: https://www.binnenvaart.be/publicaties/magazine.

[26] M. Blanke, K. Lindegaard and T. Fossen. "Dynamic model for thrust generation of marine propellers". In: *Proc. 5th IFAC Conf. Manoeuvring Control Mar. Cr.* 2000.Mcmc (2000), pp. 363–368. ISSN: 1474-6670. DOI: 10.1016/S1474-6670(17)37100-8.

[27] M. Blanke. "Ship Propulsion Losses Related to Automatic Steering and Prime Mover Control". ISBN 87-87950-14-6. PhD thesis. Technical University of Denmark, 1981.

[28] G. Blauwens, P. D. Baere and E. van de Voorde. *Transport Economics*. Antwerp, De Boeck, 2008. ISBN: 978 90 306 9662 9.

[29] Blue Line Logistics. *Blue Line Logistics is an alternative logistical platform for palletized goods using inland waterways*. Online. May 2020. URL: http://www.bluelinelogistics.eu/.

[30] P. Boers. *Pallet Shuttle Barge (Zulu 01) on the canal Dessel-Turnhout-Schoten.* Owner Blue Line Logistics BvbA in Beveren-Kallo. Aug. 2018. URL: https://www.binnenvaart.eu/motorvrachtschip/37922-zulu-o2.html.

[31] M. Bonci, M. Viviani, R. Broglia and G. Dubbioso. "Method for estimating parameters of practical ship manoeuvring models based on the combination of RANSE computations and System Identification". In: *Appl. Ocean Res.* 52 (2015), pp. 274–294. DOI: 10.1016/j.apor.2015.06.005.

[32] G. Box. "Robustness in the Strategy of Scientific Model Building". In: *Robustness in Statistics*. Ed. by R. L. Launer and G. N. Wilkinson. Academic Press, 1979, pp. 201–236. ISBN: 978-0-12-438150-6. DOI: 10.1016/B978-0-12-438150-6.50018-2.

[33] P. Boyland. *Belgium Mobile Network Experience Report.* Tech. rep. OpenSignal, 2019. URL: https://www.opensignal.com/reports/2019/09/belgium/mobile-network-experience.

[34] M. A. Branch, T. F. Coleman and Y. Li. "A Subspace, Interior, and Conjugate Gradient Method for Large-Scale Bound-Constrained Minimization Problems". In: *SIAM J. Sci. Comput.* 20.1 (Dec. 1999), pp. 1–23. DOI: 10.1137/S1064827595289108.

[35] I. Brown. "A review of the 'looked but failed to see' accident causation factor". In: *Behavioural research in road safety: eleventh seminar*. ISBN: 1-85112-527-2. Feb. 2002, pp. 116–124.

[36] H. Bruyninckx. *Building Blocks for the Design of Complicated Systems featuring Situational Awareness*. Online book. Work in progress. Oct. 2020. URL: https://robmosys.pages.gitlab.kuleuven.be/.

[37] M. Caccia, M. Bibuli, R. Bono and G. Bruzzone. "Basic navigation, guidance and control of an Unmanned Surface Vehicle". In: *Auton. Robots* 25.4 (2008), pp. 349–365. ISSN: 09295593. DOI: 10.1007/s10514-008-9100-0.

[38] C. Cadena, L. Carlone, H. Carrillo, Y. Latif, D. Scaramuzza, J. Neira, I. Reid and J. Leonard. "Simultaneous Localization And Mapping: Present, Future, and the Robust-Perception Age". In: *IEEE Transactions on Robotics* 32 (June 2016). DOI: 10.1109/TRO.2016.2624754.

[39] S. Campbell, W. Naeem and G. W. Irwin. "A review on improving the autonomy of unmanned surface vehicles through intelligent collision avoidance manoeuvres". In: *Annu. Rev. Control* 36.2 (2012), pp. 267–283. ISSN: 13675788. DOI: 10.1016/j.arcontrol.2012.09.008.

[40] Captain AI. *Autonomous Ships for Autonomous Ports*. Online. 2020. URL: https://www.captainai.com/.

[41] A. Caris, S. Limbourg, C. Macharis, T. van Lier and M. Cools. "Integration of Inland Waterway Transport in the Intermodal Supply Chain: a Taxonomy of Research Challenges". In: *Journal of Transport Geography* (2014). DOI: 10.1016/j.jtrangeo.2014.08.022.

[42] P. M. Carrica, A. Mofidi, K. Eloot and G. Delefortrie. "Direct simulation and experimental study of zigzag maneuver of KCS in shallow water". In: *Ocean Eng.* 112 (2016), pp. 117–133. DOI: 10.1016/j.oceaneng.2015.12.008.

[43] CCNR. *Inland Navigation in Europe, Market Observation*. Annual Report 2020. Central Commission for the Navigation of the Rhine, 2020. URL: https://www.ccr-zkr.org/files/documents/om/om20_II_en.pdf.

[44] CCNR. *Inland Navigation in Europe, Market observation*. Annual Report 2017. Central Commission for the Navigation of the Rhine, 2017. URL: https://www.ccr-zkr.org/files/documents/om/om17_II_en.pdf.

[45] CCNR. *Listing of pilot and research projects in the field of automation in inland navigation*. 2020. URL: https://automation.ccr-zkr.org/1000-en.html.

[46] CCNR. *Reglement onderzoek schepen op de Rijn (in Dutch)*. Tech. rep. Central Commission for the Navigation of the Rhine, 2018, pp. 1–235. URL: https://wetten.overheid.nl/BWBR0025973/2018-10-07/0/afdrukken+informatie.

[47] CESNI. *European Standard laying down technical requirements for Inland Navigation vessels (ES-TRIN)*. Tech. rep. European Committee for drawing up Standards in the field of Inland Navigation, 2019.

[48] M. M. Chatzimichailidou and I. M. Dokas. "The Risk Situation Awareness Provision Capability and its Degradation in the Überlingen Accident over Time". In: *Procedia Engineering* 128 (2015). Proceedings of the 3rd European STAMP Workshop 5-6 October 2015, Amsterdam, pp. 44–53. ISSN: 1877-7058. DOI: 10.1016/j.proeng.2015.11.503.

[49] L. J. Clancy. *Aerodynamics*. London: Pitman Publishing Limited, 1975. ISBN: 0-273-01120-0.

[50] D. Clarke, P. Gedling and G. Hine. "Application of manoeuvring criteria in hull design using linear theory." In: *Trans. R. Inst. Nav. Archit.* 125 (1983), pp. 45–68. URL: http://resolver.tudelft.nl/uuid:2a5671ac-a502-43e1-9683-f27c50de3570.

[51] A. Colling and R. Hekkenberg. "Waterborne platooning in the short sea shipping sector". eng. In: *Transportation research. Part C, Emerging technologies* 120 (2020), p. 102778. ISSN: 0968-090X. DOI: 10.1016/j.trc.2020.102778.

[52] C. Collodi. *Le avventure di Pinocchio, Storia di un burattino*. R. Bemporad & figlio, 1902. URL: https://commons.wikimedia.org/w/index.php?title=File:Le_avventure_di_Pinocchio.djvu&page=44.

[53] C. M. Costa, H. M. Sobreira, A. J. Sousa and G. M. Veiga. "Robust 3/6 DoF self-localization system with selective map update for mobile robot platforms". In: *Robotics and Autonomous Systems* 76 (2016), pp. 113–140. ISSN: 09218890. DOI: 10.1016/j.robot.2015.09.030.

[54] G. Crompton. "The Tortoise and the Economy: Inland Waterway Navigation in International Economic History". eng. In: *Journal of transport history* 25.2 (2004), pp. 1–22. ISSN: 0022-5266. DOI: 10.7227/TJTH.25.2.1.

[55] J. Dang and H. Laheij. *Dynamic Positioning Conference, Session Thrusters/Propulsion*. Tech. rep. June. Drunen, The Netherlands: Wärtsilä Propulsion Netherlands BV (WPNL), Sept. 2004, pp. 1–32. URL: http://resolver.tudelft.nl/uuid:d8bede42-a95e-4ad6-9fc9-58282d6006e9.

[56] B.-E. Danielsen. "Sensemaking on the Bridge: A Theoretical Approach to Maritime Information Design". In: *IHSED 2018, AISC 876*. Vol. 876. Springer Verlag, 2018, pp. 76–81. ISBN: 9783030020521. URL: http://hdl.handle.net/11250/2583132.

[57] De Vlaamse Waterweg NV. *Autonoom Varen in de Westhoek*. Project funded by European Fund for Regional Development. 2019. URL: https://www.vlaamsewaterweg.be/autonoom-varen-de-westhoek.

[58] S. W. A. Dekker. "The danger of losing situation awareness". eng. In: *Cognition, technology & work* 17.2 (2015), pp. 159–161. ISSN: 1435-5566. DOI: 10.1007/s10111-015-0320-8.

[59] G. Delefortrie, M. Tello Ruiz and M. Vantorre. "Manoeuvring model of an estuary container vessel with two interacting Z-drives". In: *J. Mar. Sci. Technol.* 23.4 (Nov. 2018), pp. 739–753. ISSN: 09484280. DOI: 10.1007/s00773-017-0508-0.

[60] V. Desai-Patil, A. Ayare, B. Mahajan and S. Bade. "A Review of Azimuth Thruster". In: *Int. J. Mech. Eng.* 2.10 (Oct. 2015), pp. 38–41. DOI: 10.14445/23488360/ijme-v2i10p107.

[61] J. Dieudonné. *Collected French Papers on the Stability of Route of Ships at Sea, (Translated by H. E. Saunders and E. N. Labouvie)*. Tech. rep. Technical Report DTMB-246. Washington D.C.: Naval Ship Research and Development Center, 1953.

[62] H. Dinkelberg. *Bierboot – Beer Boat*. online. This boat uses the canal in the inner city of Utrecht to provide the bars with beer. 2008. URL: https://commons.wikimedia.org/wiki/File:Bierboot_-_Beer_boat.jpg.

[63] K. D. Do and J. Pan. *Control of Ships and Underwater Vehicles*. Springer, 2009. ISBN: 978-1-84882-729-5. DOI: 10.1007/978-1-84882-730-1.

[64] A. Dogrul, S. Song and Y. K. Demirel. "Scale effect on ship resistance components and form factor". eng. In: *Ocean engineering* 209 (Apr. 2020), p. 107428. ISSN: 0029-8018. DOI: 10.1016/j.oceaneng.2020.107428.

[65] H. Dyos. *British transport : an economic survey from the seventeenth century to the twentieth*. Harmondsworth ; Baltimore : Penguin Books, 1974. ISBN: 9780140217841.

[66] A. Eggers, G. Peeters, P. Slaets and M. Vanierschot. "Shallow water surge resistance identification for inland vessels". In: *5th MASHCON Proceedings*. 2019. URL: http://hdl.handle.net/1854/LU-8624686.

[67] M. Ejaz and M. Chen. "Sliding mode control design of a ship steering autopilot with input saturation". In: *International Journal of Advanced Robotic Systems* (2017). DOI: 10.1177/1729881417703568.

[68] K. Eloot. "Selection, Experimental Determination and Evaluation of a Mathematical Model for Ship Manoeuvring in Shallow Water". PhD thesis. Universiteit Gent, 2006, p. 415. ISBN: 90-8578-092-6. URL: http://hdl.handle.net/1854/LU-757846.

[69] M. R. Endsley. "Situation Awareness Misconceptions and Misunderstandings". eng. In: *Journal of Cognitive Engineering and Decision Making* 9.1 (2015), pp. 4–32. ISSN: 1555-3434. DOI: 10.1177/1555343415572631.

[70] M. R. Endsley. "Design and Evaluation for Situation Awareness Enhancement". In: *Proceedings of the Human Factors Society Annual Meeting* 32.2 (1988), pp. 97–101. DOI: 10.1177/154193128803200221.

[71] O. A. Enezy, E. van Hassel, C. Sys and T. Vanelslander. "Developing a cost calculation model for inland navigation". In: *Research in Transportation Business & Management* 23 (2017), pp. 64–74. DOI: 10.1016/j.rtbm.2017.02.006.

[72] B. H. Eriksen, M. Breivik, E. F. Wilthil, A. L. Flåten and E. F. Brekke. "The branching-course model predictive control algorithm for maritime collision avoidance". eng. In: *Journal of field robotics* 36.7 (July 2019), pp. 1222–1249. ISSN: 1556-4967. DOI: 10.1002/rob.21900.

[73] H. van Essen. *Sustainable Transport Infrastructure Charging and Internalisation of Transport Externalities*. Tech. rep. CE Delft, 2018. URL: https://ec.europa.eu/transport/sites/transport/files/2018-year-multimodality-external-costs-ce-delft-preliminary-results.pdf.

[74] H. van Essen, A. Schroten, M. Otten, D. Sutter, C. Schreyer, R. Zandonella, M. Maibach and C. Doll. *External Costs of Transport in Europe - Update Study for 2008*. Tech. rep. Publication code: 11.4215.50. CE Delft, 2011. URL: https://www.cer.be/sites/default/files/publication/2312_External_Costs_update_study_FINAL.pdf.

[75] European Commission. *Commission Directive 2008/126/EC amending Directive 2006/87/EC of the European Parliament and of the Council laying down technical requirements for inland waterway vessels*. Tech. rep. European Commision, 2008, pp. 1–70. URL: https://eur-lex.europa.eu/LexUriServ/LexUriServ.do?uri=CONSLEG:2006R1881:20100701:EN:PDF.

[76] European Commission. "Commission implementing decision (EU) 2019/1118 of 27 June 2019, on the Seine – Scheldt cross-border project on the North Sea – Mediterranean and Atlantic Core Network Corridors". In: *Official Journal of the European Union* (2019). URL: https://eur-lex.europa.eu/eli/dec_impl/2019/1118/oj.

[77] European Commission. *Handbook on the external costs of transport*. Version 2019. Publications Office of the European Union, 2019. ISBN: ISBN 978-92-79-96917-1. DOI: doi:10.2832/27212.

[78] European Commission. *Refit ex-post evaluation of Combined Transport Directive 92/106/EEC*. Final Report. Brussels, European Commission, Apr. 2016. URL: http://data.europa.eu/eli/dir/1992/106/oj.

[79] European Commission. *Regulation (EU) No 1315/2013 of the European parliamant and of the council*. Official Journal of the European Union. on Union guidelines for the development of the trans-European transport network and repealing Decision No 661/2010/EU. European Union, 2013. URL: http://data.europa.eu/eli/reg/2013/1315/oj.

[80] Eurostat. *Modal split of freight transport*. Tech. rep. Brussels, Belgium: European Comission, Apr. 2020. URL: https://ec.europa.eu/eurostat/data/database.

[81] O. Faltinsen. *Sea Loads on Ships and Offshore Structures*. Cambridge University Press, 1990. ISBN: 9780521458702.

[82] K. K. Fedyaevsky and G. V. Sobolev. *Control and Stability in Ship Design*. State Union Shipbuilding Industry Publishing House, 1964.

[83] FernBin. *Remotely controlled, coordinated driving in inland navigation*. Online. 2020. URL: https://www.irt.rwth-aachen.de/cms/IRT/Forschung/Forschungsprojekte-dyn-Liste-/~jiqiq/FernBin/.

[84] Flanders Investment & Trade. *Flanders: Dense network of ports, airports, roads, rail and waterways*. Online. URL: https://www.flandersinvestmentandtrade.com/invest/en/investing-in-flanders/how-flanders-infrastructure-connects-your-business-world.

[85] Flepos. *The Flemish Positioning Service*. 2019. URL: https://overheid.vlaanderen.be/flepos-algemeen.

[86] F. D. Foresee and M. T. Hagan. "Gauss-Newton approximation to Bayesian learning". In: *Proc. Int. Conf. Neural Networks*. 1997. ISBN: 0780341228. DOI: 10.1109/ICNN.1997.614194.

[87] T. I. Fossen. "Nonlinear Modeling and Control of Underwater Vehicles". PhD thesis. Norwegian Institute of Technology, 1991. URL: http://hdl.handle.net/11250/259415.

[88] T. I. Fossen. "A Nonlinear Unified State-Space Model for Ship Maneuvering and Control in a Seaway". In: *International Journal of Bifurcation and Chaos* 15.9 (2005), pp. 2717–2746. DOI: 10.1142/S0218127405013691.

[89] T. I. Fossen. *Guidance and Control of Ocean Vehicles*. John Wiley & Sons. Ltd., 1994. ISBN: 978-0-471-94113-2.

[90] T. I. Fossen. *Handbook of Marine Craft Hydrodynamics and Motion Control*. eng. Chichester, UK: John Wiley & Sons, Ltd, 2011. ISBN: 9781119991496.

[91] T. I. Fossen. *Marine Control Systems Guidance, Navigation, and Control of Ships, Rigs and Underwater Vehicles*. Marine Cybernetics, Trondheim, Norway, 2002, p. 570. ISBN: 82-92356-00-2.

[92] J. Fourdrinoy, C. Caplier, Y. Devaux, G. Rousseaux, A. Gianni, I. Zacharias, I. Jouteur, P.-M. Martin, J. Dambrine, M. Petcu and et al. "The naval battle of Actium and the myth of the ship-holder: the effect of bathymetry". In: *5th MASHCON International Conference on Ship Manoeuvring in Shallow and Confined Water*. Version with additional information, stored at: HAL Id: hal-02139218. Ostend, May 2019, pp. 104–133. URL: https://hal.archives-ouvertes.fr/hal-02139218.

[93] J. Gong, C.-y. Guo, C. Wang, T.-c. Wu and K.-w. Song. "Analysis of waterjet-hull interaction and its impact on the propulsion performance of a four-waterjet-propelled ship". eng. In: *Ocean Engineering* 180 (2019), pp. 211–222. ISSN: 0029-8018. DOI: 10.1016/j.oceaneng.2019.04.002.

[94] W. S. Grant, R. C. Voorhies and L. Itti. "Efficient Velodyne SLAM with point and plane features". In: *Autonomous Robots* 43.5 (Aug. 2018), pp. 1207–1224. ISSN: 15737527. DOI: 10.1007/s10514-018-9794-6.

[95] M. R. Grech, T. J. Horberry and T. Koester. *Human Factors in the Maritime Domain*. CRC Press, Taylor & Francis Group, 2008. DOI: 10.1201/9780429355417.

[96] Grolltech derived from Hengl, derived from B.S. Halpern. *Shipping density (commercial). A Global Map of Human Impacts to Marine Ecosystems, showing relative density (in color) against a black background.* Based on: Halpern, B.S., et al. 2008. A Global Map of Human Impact on Marine Ecosystems. Science 319(5865):948-952. https://dx.doi.org/10.1126/science.1149345. Mar. 2012. URL: https://commons.wikimedia.org/w/index.php?title=File:Shipping_routes_red_black.png.

[97] G. Grote, J. Weyer and N. A. Stanton. "Beyond human-centred automation - concepts for human-machine interaction in multi-layered networks". eng. In: *Ergonomics: Beyond Human-Centred Automation* 57.3 (2014), pp. 289–294. ISSN: 0014-0139. DOI: 10.1080/00140139.2014.890748.

[98] B. J. Guo, S. Steen and G. B. Deng. "Seakeeping prediction of KVLCC2 in head waves with RANS". In: *Appl. Ocean Res.* 35 (2012), pp. 56–67. ISSN: 01411187. DOI: 10.1016/j.apor.2011.12.003.

[99] B.-j. Guo and S. Steen. "Evaluation of added resistance of KVLCC2 in short waves". eng. In: *Journal of hydrodynamics. Series B* 23.6 (2011), pp. 709–722. ISSN: 1001-6058. DOI: 10.1016/S1001-6058(10)60168-0.

[100] C.-y. Guo, X.-h. Zhong, D.-g. Zhao, C. Wang, J.-f. Lin and K.-w. Song. "Propulsion performance of large-scale ship model in real sea environment". eng. In: *Ocean engineering* 210 (Apr. 2020), p. 107440. ISSN: 0029-8018. DOI: 10.1016/j.oceaneng.2020.107440.

[101] M. T. Hagan and M. B. Menhaj. "Brief Papers". In: *Brain Cogn.* 32.2 (1996), pp. 273–344. ISSN: 02782626. DOI: 10.1006/brcg.1996.0066.

[102] C. R. Harris, K. J. Millman, S. J. van der Walt, R. Gommers, P. Virtanen, D. Cournapeau, E. Wieser, J. Taylor, S. Berg, N. J. Smith, R. Kern, M. Picus, S. Hoyer, M. H. van Kerkwijk, M. Brett, A. Haldane, J. Fernández del Río, M. Wiebe, P. Peterson, P. Gérard-Marchant, K. Sheppard, T. Reddy, W. Weckesser, H. Abbasi, C. Gohlke and T. E. Oliphant. "Array programming with NumPy". In: *Nature* 585 (Sept. 2020), pp. 357–362. DOI: 10.1038/s41586-020-2649-2.

[103] S. A. Harvald. *Resistance and Propulsion of Ships*. Hoboken, New Jersey, United States: Wiley, Nov. 1983. ISBN: 0-89464-754-7.

[104] V. Hassani, A. M. Pascoal and T. F. Onstein. "Data-driven control in marine systems". eng. In: *Annual Reviews in Control* 46 (2018), pp. 343–349. ISSN: 1367-5788. DOI: 10.1016/j.arcontrol.2018.10.006.

[105] R. Hekkenberg. "Inland Ships for Efficient Transport Chains". PhD thesis. TU Delft, 2013. DOI: 10.4233/uuid:f2ead20f-80b5-4d92-818f-7586c7b85f76.

[106] E. R. Herrero and F. J. V. Gonzalez. "Two-step identification of non-linear manoeuvring models of marine vessels". In: *Ocean Engineering* 53 (2012), pp. 72–82. DOI: 10.1016/j.oceaneng.2012.07.010.

[107] M. Heymann and A. Degani. "Formal Analysis and Automatic Generation of User Interfaces: Approach, Methodology, and an Algorithm". eng. In: *Human Factors: The Journal of Human Factors and Ergonomic Society* 49.2 (2007), pp. 311–330. ISSN: 0018-7208. DOI: 10.1518/001872007X312522.

[108] A. Hindmarsh. "ODEPACK, a Systematized Collection of ODE Solvers". In: *Scientific Computing* 1 (Aug. 1983). edited by Robert Stepleman, Elsevier, pp. 55–64. ISSN: 978-0444866073. URL: https://computing.llnl.gov/casc/nsde/pubs/u88007.pdf.

[109] C. W. Hirt and B. D. Nichols. "Volume of fluid (VOF) method for the dynamics of free boundaries". In: *J. Comput. Phys.* 39.1 (Jan. 1981), pp. 201–225. ISSN: 0021-9991. DOI: 10.1016/0021-9991(81)90145-5.

[110] E. Hollnagel. "Designing for joint cognitive systems". In: *The IEE and MOD HFI DTC Symposioum on People and Sytems - Who are We Designing for?* Dec. 2005, pp. 47–51. ISBN: 0-86341-576-8. DOI: 10.1049/ic:20050450.

[111] E. Hollnagel and D. D. Woods. *Joint cognitive systems: Foundations of cognitive systems engineering*. CRC Press, Taylor & Francis Group, 2005. ISBN: 0-8493-2821-7.

[112] X. Hou, S. Guo, L. Shi, H. Xing, Y. Liu, H. Liu, Y. Hu, D. Xia and Z. Li. "Hydrodynamic Analysis-Based Modeling and Experimental Verification of a New Water-Jet Thruster for an Amphibious Spherical Robot". eng. In: *Sensors (Basel, Switzerland)* 19.2 (2019), p. 259. ISSN: 1424-8220. DOI: 10.3390/s19020259.

[113] C. M. Hsu and C. W. Shiu. "3D LiDAR-based precision vehicle localization with movable region constraints". In: *Sensors (Switzerland)* 19.4 (2019). ISSN: 14248220. DOI: 10.3390/s19040942.

[114] H.-M. Huang, E. R. Messina and A. S. Jacoff. "Performance measures framework for unmanned systems (PerMFUS): Initial Perspective". In: *Proceedings of the Performance Metrics for Intelligent Systems (PerMIS)*. Jan. 2009, pp. 65–72. ISBN: 9781605587479. DOI: 10.1145/1865909.1865923.

[115] H.-M. Huang, E. R. Messina, A. S. Jacoff, R. Wade and M. McNail. "Performance measures framework for unmanned systems (PerMFUS): models for contextual metrics". In: *Proceedings of the 2010 Performance Metrics for Intelligent Systems (PerMIS) Workshop*. 2010. DOI: 10.1145/2377576.2377581.

[116] Z. Huiqian. *18th-century representation of the Bagua diagram by Zhao Huiqian ("River Chart spontaneously [generated] by Heaven and Earth", 1370s)*. This image may in fact be a reproduction of the diagram by Hu Wei in his Yitu mingbian ("Clarification of the diagrams in the book of changes"), dated 1706. 1370. URL: https://commons.wikimedia.org/wiki/File:Bagua_Zhao_Huiqian.jpg.

[117] F. H. Imlay. *The complete expressions for "added mass" of a rigid body moving in an ideal fluid*. Tech. rep. Department of the Navy David Taylor model basin, Hydromechanics laboratory, 1961. DOI: 10.21236/ad0263966.

[118] International Maritime Organization. *Standards For Ship Manoeuvrability*. Tech. rep. 76. Resolut. MSC.137(76) (adopted 4 December 2002). International Maritime Organization, 2002. URL: https://wwwcdn.imo.org/localresources/en/KnowledgeCentre/IndexofIMOResolutions/MSCResolutions/MSC.137(76).pdf.

[119] International Towing Tank Conference. *Full Scale Manoeuvring Trials - ITTC*. Tech. rep. Zürich Switzerland: International Towing Tank Conference, Sept. 2017, pp. 1–18. URL: https://www.ittc.info/media/8179/75-04-02-01.pdf.

[120] International Towing Tank Conference. *ITTC Quality System Manual – Recommended Procedures and Guidelines*. Tech. rep. ITTC, 2017. URL: https://www.ittc.info/media/8153/75-03-01-01.pdf.

[121] ITF. *ITF Transport Outlook 2019*. OECD Publishing, 2019. ISBN: N 978-92-82-10388-3. DOI: 10.1787/transp_outlook-en-2019-en.

[122] M. Janjevic and A. B. Ndiaye. "Inland waterways transport for city logistics: a review of experiences and the role of local public authorities". In: *WIT Transactions on The Built Environment* 138 (2014). ISSN: 1743-3509. DOI: 10.2495/UT140241.

[123] W. Jiao, L. Cheng, D. Zhang, B. Zhang, Y. Su and C. Wang. "Optimal Design of Inlet Passage for Waterjet Propulsion System Based on Flow and Geometric Parameters". eng. In: *Advances in materials science and engineering* 2019 (2019), pp. 1–21. ISSN: 1687-8442. DOI: 10.1155/2019/2320981.

[124] S. Johansson, D. Malvius and M. Bergendahl. "Performance Evaluation of Complex Product Development". In: *ICED 09 - The 17th international conference on engineering design, vol 6, design methods and tools*. 2009, pp. 87–97. ISBN: 978-1-904670-10-0.

[125] M. Kalikatzarakis, R. D. Geertsma, E. J. Boonen, K. Visser and R. R. Negenborn. "Ship energy management for hybrid propulsion and power supply with shore charging". In: *Control Engineering Practice* 76.November 2017 (2018), pp. 133–154. ISSN: 09670661. DOI: 10.1016/j.conengprac.2018.04.009.

[126] S. Kallas. *Transport 2050: Commission outlines ambitious plan to increase mobility and reduce emissions*. Tech. rep. IP/11/372. Brussels: European Commission, Mar. 2011. URL: https://ec.europa.eu/commission/presscorner/detail/en/IP_11_372.

[127] T. Konrad, J.-J. Gehrt, J. Lin, R. Zweigel and D. Abel. "Advanced state estimation for navigation of automated vehicles". eng. In: *Annual Reviews in Control* 46 (2018), pp. 181–195. ISSN: 1367-5788. DOI: 10.1016/j.arcontrol.2018.09.002.

[128] M. Kotzé, A. Bin Junaid, M. R. Afzal, G. Peeters and P. Slaets. "Use of Uncertainty and Zones for Vessel and Operation in Inland and Waterways". In: *Journal of Physics: Conference Series*. 2019. DOI: 10.1088/1742-6596/1357/1/012031.

[129] Kräutler. *Saildrive engine SDK-ED 2.5 AC*. Online. Product sheet. 2020. URL: https://www.nauticexpo.com/prod/kraeutler-elektromaschinen/product-23207-213000.html.

[130] L. Kretschmann, Ø. Rødseth, B. S. Fuller, H. Noble, J. Horahan and H. McDowell. *Maritime Unmanned Navigation through Intelligence in Networks: D9.3: Quantitative assessment*. Tech. rep. CML, MRTK, UCC, 2015. URL: http://www.unmanned-ship.org/munin/wp-content/uploads/2015/10/MUNIN-D9-3-Quantitative-assessment-CML-final.pdf.

[131] H. O. Kristensen and M. Lützen. *Prediction of Resistance and Propulsion Power of Ships*. Project no. 2010-56, Emissionsbeslutningsstøttesystem Work Package 2, Report no. 04. Technical University of Denmark, 2013. URL: https://www.danishshipping.dk/services/

beregningsvaerktoejer/download/Basic_Model_Linkarea_Link/163/wp-2-report-4-resistance-and-propulsion-power.pdf.

[132] D. K. M. Kufoalor, T. A. Johansen, E. F. Brekke, A. Hepsø and K. Trnka. "Autonomous maritime collision avoidance: Field verification of autonomous surface vehicle behavior in challenging scenarios". eng. In: *Journal of field robotics* 37.3 (Oct. 2019), pp. 387–403. ISSN: 1556-4967. DOI: 10.1002/rob.21919.

[133] B. Laine, B. Hoornaert and D. Coraline. *Vooruitzichten van de transportvraag in België tegen 2040*. Tech. rep. December. Brussel: Federaal Planbureau, 2019, pp. 42–58. URL: https://www.plan.be/publications/publication-1862-nl-vooruitzichten_van_de_transportvraag_in_belgie_tegen_2040.

[134] H. Lamb. *Hydrodynamics*. C.J. Clay and Sons, Cambrigde University Press, 1895. URL: https://archive.org/details/hydrodynamics00lambrich.

[135] A. Lampe and R. Chatila. "Performance Measure For The Evaluation of Mobile Robot Autonomy". In: *Proceedings of the 2006 IEEE International Conference on Robotics and Automation*. 2006. DOI: 10.1109/ROBOT.2006.1642325.

[136] R. B. Langley. "RTK GPS". In: *GPS World* (1998), pp. 70–76. URL: http://www2.unb.ca/gge/Resources/gpsworld.september98.pdf.

[137] E. Lataire, M. Vantorre and G. Delefortrie. "The Influence of the Ship's Speed and Distance to an Arbitrarily Shaped Bank on Bank Effects". In: *Journal of Offshore Mechanics and Arcic Engineering* 140.2 (2018), p. 021304. ISSN: 0892-7219. DOI: 10.1115/1.4038804.

[138] B. Launder and D. Spalding. "The numerical computation of turbulent flows". In: *Comput. Methods Appl. Mech. Eng.* 3.2 (1974), pp. 269–289. DOI: 10.1016/0045-7825(74)90029-2.

[139] G. W. Lecky-Thompson. *Infinite Game Universe: Mathematical Techniques*. USA: Charles River Media, Inc., 2001. ISBN: 1584500581.

[140] M. Leshno, V. Y. Lin, A. Pinkus and S. Schocken. "Multilayer feedforward networks with a nonpolynomial activation function can approximate any function". In: *Neural Networks* 6.6 (1993), pp. 861–867. ISSN: 08936080. DOI: 10.1016/S0893-6080(05)80131-5.

[141] N. G. Leveson. *Engineering a safer world: Systems thinking applied to safety*. The MIT Press, 2016. ISBN: 9780262016629.

[142] X. Li, M. Ge, X. Dai, X. Ren, M. Fritsche, J. Wickert and H. Schuh. "Accuracy and reliability of multi-GNSS real-time precise positioning: GPS, GLONASS, BeiDou, and Galileo". In: *Journal of Geodesy* 89.6 (2015), pp. 607–635. ISSN: 14321394. DOI: 10.1007/s00190-015-0802-8.

[143] Z. Li and J. Sun. "Disturbance compensating model predictive control with application to ship heading control". In: *IEEE Trans. Control Syst. Technol.* 20.1 (2012), pp. 257–265. ISSN: 10636536. DOI: 10.1109/TCST.2011.2106212.

[144] C. C. Liang and W. H. Cheng. "The optimum control of thruster system for dynamically positioned vessels". In: *Ocean Eng.* 31.1 (2004), pp. 97–110. ISSN: 00298018. DOI: 10.1016/S0029-8018(03)00016-7.

[145] J. Liu. "Impact of Rudder Configurations on Inland Vessel Manoeuvrability". PhD thesis. Delft University of Technology, 2017. URL: https://doi.org/10.4233/uuid:bef6c12f-5804-407b-a4c6-f7949541f21c.

[146] J. Liu, R. Hekkenberg, F. Quadvlieg, H. Hopman and B. Zhao. "An integrated empirical manoeuvring model for inland vessels". eng. In: *Ocean Engineering* 137 (2017), pp. 287–308. ISSN: 0029-8018. DOI: 10.1016/j.oceaneng.2017.04.008.

[147] J. Liu, R. Hekkenberg, E. Rotteveel and H. Hopman. "Literature review on evaluation and prediction methods of inland vessel manoeuvrability". In: *Ocean Engineering* 106 (2015), pp. 458–471. DOI: 10.1016/j.oceaneng.2015.07.021.

[148] Z. Liu, Y. Zhang, X. Yu and C. Yuan. "Unmanned surface vehicles: An overview of developments and challenges". eng. In: *Annual Reviews in Control* 41 (2016), pp. 71–93. ISSN: 1367-5788. DOI: 10.1016/j.arcontrol.2016.04.018.

[149] C. B. Luce. *Stuffed Shirts*. H. Liveright, Incorporated, 1931.

[150] D. J. C. Mackay. "Probable networks and plausible predictions — a review of practical Bayesian methods for supervised neural networks". In: *Netw. Comput. Neural Syst.* 6.3 (1995), pp. 469–505. DOI: 10.1088/0954-898X_6_3_011.

[151] D. J. C. MacKay. "A Practical Bayesian Framework for Backpropagation Networks". In: *Neural Comput.* 4.3 (1992), pp. 448–472. ISSN: 0899-7667. DOI: 10.1162/neco.1992.4.3.448.

[152] S. N. MacKinnon, Y. Man and M. Baldauf. *Maritime Unmanned Navigation through Intelligence in Networks, D8.8: Final Report: Shore Control Centre*. Tech. rep. CTH, HSW, 2015. URL: http://www.unmanned-ship.org/munin/wp-content/uploads/2015/09/MUNIN-D8-8-Final-Report-Shore-Control-Centre-CTH-final.pdf.

[153] P. B. D. Maere. *View on the "Korenlei" and "Graslei" in Ghent*. Painting. 18th century. URL: https://stamgent.be/nl_be/collectie/kunstwerken/A59_3.

[154] J. Maes, C. Sys and T. Vanelslander. *Vervoer te water: Linken met stedelijke distributie? (in Dutch)*. Tech. rep. Steunpunt Goederen- en personenvervoer, 2012. URL: https://medialibrary.uantwerpen.be/oldcontent/container33836/files/Beleidsondersteunende_papers/BP2012_12_vervoerwater.pdf.

[155] B. Magyar, C. Hós and G. Stépán. "Influence of control valve delay and dead zone on the stability of a simple hydraulic positioning system". In: *Math. Probl. Eng.* 2010.July (2010). ISSN: 1024123X. DOI: 10.1155/2010/349489.

[156] S. Maitlis and M. Christianson. "Sensemaking in Organizations: Taking Stock and Moving Forward". In: *The Academy of Management Annals* 8 (June 2014). DOI: 10.1080/19416520.2014.873177.

[157] *Man and woman towing a cargo-boat through a ship-canal.* The Dutch Nationaal Archief. The Netherlands. Place unknown. No known copyrights. May 1931. URL: https://nl.m.wikipedia.org/wiki/Bestand:Trekkers_van_vrachtschip_Towing_a_ship.jpg.

[158] Y. Man, M. Lundh and T. Porathe. "Seeking harmony in shore-based unmanned ship handling – From the perspective of human factors, what is the difference we need to focus on from being onboard to onshore?" In: *Proceedings of the 5th International Conference on Applied Human Factors and Ergonomics AHFE*. July 2014.

[159] Y. Man, M. Lundh, T. Porathe and S. MacKinnon. "From desk to field - Human factor issues in remote monitoring and controlling of autonomous unmanned vessels". In: *6th International Conference on Applied Human Factors and Ergonomics (AHFE 2015) and the Affiliated Conferences, AHFE 2015*. 2015. DOI: 10.1016/j.promfg.2015.07.635.

[160] Y. Man, R. Weber, J. Cimbritz, M. Lundh and S. N. MacKinnon. "Human factor issues during remote ship monitoring tasks: An ecological lesson for system design in a distributed context". In: *International Journal of Industrial Ergonomics* 68 (2018), pp. 231–244. ISSN: 0169-8141. DOI: 10.1016/j.ergon.2018.08.005.

[161] J. Manley. "Unmanned Surface Vehicles, 15 Years of Development". In: *OCEANS 2008*. 2008, pp. 1–4. ISBN: 9781424426201. DOI: 10.1109/OCEANS.2008.5152052.

[162] Marine Advance Robotics, inc. *Wave Adaptive Modular Vessel (WAM-V)*. Dec. 2020. URL: https://www.wam-v.com/.

[163] Matthew. *Gospel of Matthew, the New Testament, part of the Sermon on the Mount*. Fifth verse of the seventh chapter.

[164] V. Menkov. *The DHL floating service centre*. online. The world's first ever floating express distribution center in Amsterdam does the work of five DHL vans and saves over 3,000 liters of fuel a year. 2006. URL: https://commons.wikimedia.org/wiki/File:Amsterdam-DHL-boat-0524.jpg.

[165] N. Minorsky. "Directional stability of automatically steered bodies". In: *Journal of the American Society for Naval Engineers* (1922). DOI: 10.1111/j.1559-3584.1922.tb04958.x.

[166] P. Misuraca. *The Effectiveness of a Costs and Benefits Analysis in Making Federal Government Decisions: A Literature Review*. Tech. rep. Center for National Security, The MITRE Corporation, 2014.

[167] Mohamed Saad IBN Seddik. *GPS MOOS-Driver (iGPS)*. Software on Github. The MIT License (MIT), Copyright (c) IBN Seddik Mohamed Saad. Dec. 2015. URL: https://github.com/MOOS-drivers/iGPS.

[168] S. Mohanty. "Artificial neural network based system identification and model predictive control of a flotation column". In: *J. Process Control* 19.6 (2009), pp. 991–999. ISSN: 09591524. DOI: 10.1016/j.jprocont.2009.01.001.

[169] L. Moreira, T. I. Fossen and C. Guedes Soares. "Path following control system for a tanker ship model". eng. In: *Ocean engineering* 34.14 (2007), pp. 2074–2085. ISSN: 0029-8018. DOI: 10.1016/j.oceaneng.2007.02.005.

[170] D. Moreno-Salinas, D. Chaos, J. M. de la Cruz and J. Aranda. "Identification of a Surface Marine Vessel Using LS-SVM". In: *Journal of Applied Mathematics* 2013 (2013). Article ID 803548. DOI: 10.1155/2013/803548.

[171] A. Morrall. *1957 ITTC model ship correlation line values of frictional resistance coefficient*. NPL Ship Report 142. Zürich Switzerland: ITTC, 1957. URL: http://resolver.tudelft.nl/uuid:16d77473-7043-4099-a8c6-bf58f555e2e7.

[172] S. Motora. "On the measurement of added mass and added moments of intertia for ship motions (in Japanese)". In: *J. Soc. Nav. Archit. Jpn.* 105 (1959), pp. 83–89. DOI: 10.2534/jjasnaoe1952.1960.107_83.

[173] H. Mousazadeh, H. Jafarbiglu, H. Abdolmaleki, E. Omrani, F. Monhaseri, M. reza Abdollahzadeh, A. Mohammadi-Aghdam, A. Kiapei, Y. Salmani-Zakaria and A. Makhsoos. "Developing a navigation, guidance and obstacle avoidance algorithm for an Unmanned Surface Vehicle (USV) by algorithms fusion". In: *Ocean Eng.* 159 (2018), pp. 56–65. ISSN: 00298018. DOI: 10.1016/j.oceaneng.2018.04.018.

[174] MUNIN. *Maritime Unmanned Navigation through Intelligence in Networks (MUNIN)*. 2016. URL: http://www.unmanned-ship.org/munin/.

[175] NAIADES-II. *Greening the fleet: reducing pollutant emissions in inland waterway transport (Commission Staff Working Document)*. SWD(2013) 324 final. European Comission, 2013. URL: https://ec.europa.eu/transport/modes/inland/promotion/naiades2_cs.

[176] A. Neely, M. Gregory and K. Platts. "Performance measurement system design: A literature review and research agenda". In: *International Journal of Operations & Production Management* (Dec. 1995). DOI: 10.1108/01443579510083622.

[177] Neptec. *User Manual and Guide OPAL Perfomande Series 3D LiDAR Scanner*. Tech. rep. May. Neptec, 2019, pp. 1–26. URL: http://www.neptectechnologies.com/downloads/.

[178] IW-NET. *The IW-NET Project*. online. This project has received funding from the European Union's Horizon 2020 research and innovation programme under grant agreement No 861377. 2020. URL: https://www.isl.org/en/projects/iw-net.

[179] J. N. Newman. *Marine Hydrodynamics*. eng. Cambridge: The MIT Press, 2018. ISBN: 9780262344999.

[180] P. M. Newman. *MOOS - Mission Orientated Operating Suite*. Software. Cambridge, MA: Department of Ocean Engineering Massachusetts Institute of Technology, 2005.

[181] T. Nguyen, C. P. Lim, N. D. Nguyen, L. Gordon-Brown and S. Nahavandi. "A Review of Situation Awareness Assessment Approaches in Aviation Environments". In: *IEEE SYSTEMS JOURNAL* 13.3 (June 2019), pp. 3590–3603. DOI: 10.1109/JSYST.2019.2918283.

[182] F. Nietzsche. *Götzen-Dämmerung; oder, Wie man mit dem Hammer philosophirt*. 1889.

[183] K. Nomoto, T. Taguchi, K. Honda and S. Hirano. "On the Steering Quality of Ships". In: *International Shipbuilding Progress, ISP* 4 (1957), pp. 354–370.

[184] D. Norman and D. A. "Human-centered design considered harmful". In: *interactions* 12 (June 2005), pp. 14–19. DOI: 10.1145/1070960.1070976.

[185] N. Norrbin. "Theory and observation on the use of a mathematical model for ship maneuvering in deep and confined waters." In: *Proceedings of the 8th Symposium on Naval Hydrodynamics*. Pasadena, CA, 1971, pp. 807–904. URL: http://resolver.tudelft.nl/uuid:75736a6f-66e1-4c00-b3bc-897a19a232ea.

[186] NOVIMAR. *NOVIMAR researches a new system of waterborne transport operations*. Ongoing project. 2020. URL: https://novimar.eu/.

[187] A. Ogawa and H. Kasai. "On the mathematical model of manoeuvring motion of ships". In: *International Shipbuilding Progress* 25.292 (Dec. 1978), pp. 306–319. DOI: 10.3233/ISP-1978-2529202.

[188] OpenFOAM. *OpenFOAM: Open source CFD : Documentation*. Tech. rep. Online documentation. OpenFOAM, 2021. URL: https://www.openfoam.com/documentation/guides/latest/doc/index.html.

[189] OpenStreetMap Contributors. *OpenStreetMap*. 2019. URL: https://www.openstreetmap.org/.

[190] G. A. Osga and M. R. McWilliams. "Human-computer interface studies for semi-autonomous unmanned surface vessels". In: *6th International Conference on Applied Human Factors and Ergonomics (AHFE 2015) and the Affiliated Conferences, AHFE*. 2015. DOI: 10.1016/j.promfg.2015.07.154.

[191] G. Osga, M. McWilliams, D. Powell, J. Kaiwi and A. Ahumada. *Unmanned Surface Vehicles Human-Computer Interface for Amphibious Operations*. Tech. rep. SSC Pacific, Aug. 2013.

[192] A. Palmer, G. E. Hearn and P. Stevenson. "Modelling Tunnel Thrusters for Autonomous Underwater Vehicles". eng. In: *IFAC Proceedings Volumes* 41.1 (2008), pp. 91–96. ISSN: 1474-6670. DOI: 10.3182/20080408-3-IE-4914.00017.

[193] A. Papanikolaou. *Ship Design*. Springer, 2014, pp. 1–16. ISBN: 978-94-017-8750-5. DOI: 10.1007/978-94-017-8751-2.

[194] G. Peeters, M. R. Afzal, M. Vanierschot, R. Boonen and P. Slaets. "Model Structures and Identification for Fully Embedded Thrusters: 360-Degrees-Steerable Steering-Grid and Four-Channel Thrusters". In: *Journal of Marine Science and Engineering* 8.220 (2020). DOI: 10.3390/jmse8030220.

[195] G. Peeters, R. Boonen, M. Vanierschot, M. DeFilippo, P. Robinette and P. Slaets. "Asymmetric Steering Hydrodynamics Identification of a Differential Drive Unmanned Surface Vessel." In: *IFAC*. Vol. 51. 29. Elsevier, 2018, pp. 207–212. DOI: 10.1016/j.ifacol.2018.09.494.

[196] G. Peeters, T. Catoor, M. R. Afzal, M. Kotzé, P. Geenen, S. Van Baelen, M. Vanierschot, R. Boonen and P. Slaets. "Design and build of a scale model unmanned inland cargo vessel: Actuation and control architecture". English. In: *MTEC/ICMASS 2019*. Vol. 1357. 1. Institute of Physics Publishing, 2019. DOI: 10.1088/1742-6596/1357/1/012016.

[197] G. Peeters, A. Eggers, R. Boonen, P. Slaets and M. Vanierschot. "Surge Resistance Identification of Inland Vessels by CFD". In: *OCEANS 2018*. Kobe: IEEE, 2018. DOI: 10.1109/OCEANSKOBE.2018.8559048.

[198] G. Peeters, A. Eggers, R. Boonen, P. Slaets and M. Vanierschot. *Surge Resistance Identification of Inland Vessels by Computational Fluid Dynamics.* Presented at the VSC User Group Meeting, Brussels. May 2018.

[199] G. Peeters, M. Kotzé, M. R. Afzal, T. Catoor, S. Van Baelen, P. Geenen, M. Vanierschot, R. Boonen and P. Slaets. "An unmanned inland cargo vessel: Design, build, and experiments". In: *Ocean Eng.* 201.107056 (2020), p. 17. DOI: 10.1016/j.oceaneng.2020.107056.

[200] G. Peeters and P. Slaets. *Automated Inland Shipping: The Challenges on the Inland Waterways.* Presented at the Ocean Week, Trondheim, Norway. 2018.

[201] G. Peeters and P. Slaets. *Intelligent Autonomous Shipping.* Presented at the Unmanned Cargo Ship Conference, Venlo, Netherlands. June 2017.

[202] G. Peeters and P. Slaets. *Towards Autonomous Inland Shipping in Flanders.* Presented at the MOOS Development and Applications Working Group, Cambridge MA. Aug. 2017. URL: https://oceanai.mit.edu/moos-dawg17/pmwiki/pmwiki.php?n=Talk.07-Peeters.

[203] G. Peeters, S. Van Baelen, G. Yayla, T. Catoor, M. R. Afzal, C. Christofakis, R. Louw, Y. Singh, M. Vanierschot, R. Boonen and P. Slaets. "Decoupled Hydrodynamic Models and Their Outdoor Identification for an Unmanned Inland Cargo Vessel with Embedded Fully Rotatable Thrusters". In: *Journal of Marine Science and Engineering* 8.889 (2020). DOI: 10.3390/jmse8110889.

[204] G. Peeters, G. Waeyenbergh and P. Slaets. *Stimulating Innovation Through Projects in Engineering Education: The Growth and Success of the Ecorace-Challenge Project.* Presented at the European Battery, Hybrid & Fuel Cell Electric Vehicle Congress, Geneva, Switzerland. 2017.

[205] G. Peeters, G. Yayla, M. R. Afzal, S. Van Baelen, T. Catoor, M. Vanierschot, R. Boonen and P. Slaets. "Additional Test Manoeuvres for Autonomous Inland Vessels". In: *Proc. of ICMASS 2020*. 2020. DOI: 10.1088/1757-899X/929/1/012024.

[206] G. Peeters, G. Yayla, T. Catoor, S. Van Baelen, M. R. Afzal, C. Christofakis, S. Storms, R. Boonen and P. Slaets. "An Inland Shore Control Centre for Monitoring or Controlling Unmanned Inland Cargo Vessels". In: *Journal of Marine Science and Engineering* 8.758 (2020). With joined first authors G. Peeters and G. Yayla. DOI: 10.3390/jmse8100758.

[207] J. Petrich. “Improved Guidance, Navigation, and Control for Autonomous Underwater Vehicles: Theory and Experiment”. PhD thesis. Virginia Polytechnic Institute and State University, 2009. URL: http://hdl.handle.net/10919/27222.

[208] G. Pillonetto, F. Dinuzzo, T. Chen, G. De Nicolao and L. Ljung. “Kernel methods in system identification, machine learning and function estimation: A survey”. In: *Automatica* 50.3 (2014), pp. 657–682. ISSN: 0005-1098. DOI: 10.1016/j.automatica.2014.01.001.

[209] A. Pocora, S. Lupu and K. Cosmin. “Simulated propeller walk on a 13.300 TEU container ship”. In: *Naval Academy Scientific Bulletin* XVIII.2 (Dec. 2015), pp. 55–59.

[210] P.-J. Pompée. “About modelling inland vessels resistance and propulsion and interaction vessel - waterway. Key parameters driving restricted/shallow water effects”. In: *Proceeding of Smart Rivers 2015, Buenos Aires, Argentina*. Vol. 2015. September. 2015, pp. 7–11.

[211] T. Porathe, J. Prison and Y. Man. “Situation awareness in remote control centres for unmanned ships”. In: *Proceedings of Human Factors in Ship Design & Operation*. 2014, p. 93. ISBN: 9781909024243.

[212] S. S. Potter, D. D. Woods, E. M. Roth, J. Fowlkes and R. R. Hoffman. “Evaluating the Effectiveness of a Joint Cognitive System: Metrics, Techniques, and Frameworks”. In: *Human Factors and Ergonomics Society Annual Meeting Proceedings* 50.3 (2006), pp. 314–318. ISSN: 978-190504055-1. DOI: 10.1177/154193120605000322.

[213] Prepare Ships. *Prepare Ships is creating a smart positioning solution by developing and demonstrating a data fusion of different sensor and signal sources to enable a robust navigation application.* online. 2020. URL: https://prepare-ships.eu/.

[214] J. Prison, J. Dahlman and M. Lundh. “Ship sense—striving for harmony in ship manoeuvring”. In: *WMU Journal of Maritime Affairs* 12 (Apr. 2013). DOI: 10.1007/s13437-013-0038-5.

[215] J. Prison, M. Lützhöft and T. Porathe. “Ship sense - what is it and how does one get it?” In: *RINA, Royal Institution of Naval Architects International Conference - Human Factors in Ship Design, Safety and Operation*. London, Feb. 2009, pp. 127–130.

[216] Promotie Binnenvaart Vlaanderen. *Waterways according to the CEMR classification*. Online. Adapted figure. 2016. URL: https://www.binnenvaart.be/images/kaarten-CEMR/index.html.

[217] F. Quadvlieg, G. Delefortrie, J. Duffy, Y. Furukawa, P.-E. Guillerm, S.-Y. Kim, C. Simonsen, E. Tannuri and X. F. Mao. *Final Report and Recommendations to the 27th ITTC*. Tech. rep. Copenhagen: International Towing Tank Conference, 2014, pp. 128–194. URL: https://ittc.info/downloads/proceedings/27th-conference-copenhagen-2014/.

[218] M. A. Ramos, I. B. Utne and A. Mosleh. "Collision avoidance on maritime autonomous surface ships: Operators' tasks and human failure events". In: *Safety Science* (2019). DOI: 10.1016/j.ssci.2019.02.038.

[219] Rémih. *Horus*. Relief, Hatshepsut temple, Deir el-Bahari, Theban Necropolis, Egypt. This file is licensed under the Creative Commons Attribution-Share Alike 2.5 Generic, 2.0 Generic and 1.0 Generic license. June 2011. URL: https://commons.wikimedia.org/wiki/File:Hatshepsut_temple9c.jpg.

[220] Ricardo-AEA. *Update of the Handbook on External Costs of Transport. Final Report for the European Commission: DG Move. Ricardo-AEA/R/ED57769*. Tech. rep. Ref: ED 57769 - Issue Number 1. European Commission, 2014. URL: https://ec.europa.eu/transport/themes/sustainable/studies/sustainable_en.

[221] P. J. Roache. "Perspective: A Method for Uniform Reporting of Grid Refinement Studies". In: *Journal of Fluids Engineering* 116.3 (Sept. 1994), pp. 405–413. ISSN: 0098-2202. DOI: 10.1115/1.2910291.

[222] Ø. J. Rødseth and H. Burmeister. *D10 . 1 : Impact on Short Sea Shipping*. Tech. rep. MUNIN – FP7 GA-No 314286 D 10.1. MRTK, 2015. URL: http://www.unmanned-ship.org/munin/wp-content/uploads/2015/10/MUNIN-D10-1-Impact-on-Short-Sea-Shipping-MRTK-final.pdf.

[223] Ø. J. Rødseth and H. Nordahl. *Definition of autonomy levels for merchant ships, Report from NFAS, Norwegian Forum for Autonomous Ships, 2017-08-04*. Tech. rep. August. SINTEF Ocean AS, 2018. DOI: 10.13140/RG.2.2.21069.08163.

[224] A. Ross. "Nonlinear Manoeuvring Models for Ships: A Lagrangian Approach". PhD thesis. Norwegian University of Science and Technology, 2008. URL: http://hdl.handle.net/11250/259440.

[225] E. Rotteveel, R. Hekkenberg and A. van der Ploeg. "Inland ship stern optimization in shallow water". In: *Ocean Eng.* 141.February (2017), pp. 555–569. ISSN: 00298018. DOI: 10.1016/j.oceaneng.2017.06.028.

[226] J. D. J. Rubio, Z. Zamudio, J. Pacheco and D. Mújica Vargas. "Proportional derivative control with inverse dead-zone for pendulum systems". In: *Math. Probl. Eng.* 2013 (2013). ISSN: 1024123X. DOI: 10.1155/2013/173051.

[227] D. E. Rumelhart, G. E. Hinton and R. J. Williams. "Learning representations by back-propagating errors". In: *Nature* 323.6088 (1986), pp. 533–536. ISSN: 1476-4687. DOI: 10.1038/323533a0.

[228] J. Sandberg and H. Tsoukas. "Making sense of the sensemaking perspective: Its constituents, limitations, and opportunities for further development". In: *Journal of Organizational Behavior* 36.S1 (2015), S6–S32. ISSN: 0894-3796. DOI: 10.1002/job.1937.

[229] S. Savitz, I. Blickstein, P. Buryk, R. W. Button, P. DeLuca, J. Dryden, J. Mastbaum, J. Osburg, P. Padilla, A. Potter, C. C. Price, L. Thrall, S. K. Woodward, R. J. Yardley and J. M. Yurchak. *U.S Navy Employment Options for Unmanned Surface Vehicles*. Tech. rep. ISBN: 978-0-8330-8143-8. RAND, 2013, p. 119. URL: https://www.rand.org/content/dam/rand/pubs/research_reports/RR300/RR384/RAND_RR384.pdf.

[230] SBG. *Ekinox Surface Series Tactical Grade MEMS Inertial Sensors Hardware Manual*. Tech. rep. SBG, 2018, pp. 1–59. URL: https://www.sbg-systems.com/products/ekinox-series/#ekinox-e_inertial_navigation_system_gnss.

[231] Seafar NV. *Seafar NV is an independent ship management company, offering services to operate unmanned and crew-reduced vessels for ship owners and shipping companies*. Online. 2020. URL: www.seafar.eu.

[232] Sensing. *Your yachting experience: fully managed, Marinminds*. Online. 2020. URL: www.marinminds.com.

[233] Septentrio. *AsteRx-U User Manual*. Tech. rep. Leuven: Septenrio, 2017, pp. 1–84. URL: https://www.septentrio.com/en/products/gnss-receivers/rover-base-receivers/integrated-gnss-receivers/asterx-u-marine.

[234] V. Shigunov, O. el Moctar, A. Papanikolaou, R. Potthoff and S. Liu. "International benchmark study on numerical simulation methods for prediction of manoeuvrability of ships in waves". In: *Ocean engineering* 165 (2018), pp. 365–385. ISSN: 0029-8018. DOI: 10.1016/j.oceaneng.2018.07.031.

[235] M. Shiokari and S. Ota. "Considerations on the regulatory issues for realization of Maritime Autonomous Surface Ships". In: *Journal of Physics: Conference Series* 1357 (Oct. 2019), p. 012005. DOI: 10.1088/1742-6596/1357/1/012005.

[236] Shipping Technology. *The Black Box Pro*. Product. 2020. URL: https://shippingtechnology.com/products/.

[237] SIMMAN 2014. *Workshop on Verification and Validation of Ship Manoeuvring Simulation Models*. Experimental Towing Tank Data KVLCC2 tanker. Lyngby, Denmark: SIMMAN, Dec. 2014. URL: https://simman2014.dk/ship-data/.

[238] SINTEF. *The Hull-To-Hull (H2H) Project*. This project has received funding from the European GNSS Agency under the European Union's Horizon 2020 research and innovation programme grant agreement No 775998. 2020. URL: https://www.sintef.no/projectweb/hull-to-hull/.

[239] P. Slaets and G. Peeters. *A practical case study, automating the Scheldt - Rupel trajectory*. Online. Presented at the International Symposium on Autonomous Inland Shipping, Leuven. 2016. URL: https://lirias.kuleuven.be/retrieve/592545.

[240] P. Slaets and G. Peeters. *Demonstration of the first Autonomous Barge in Flanders*. Online. Presented at the International Symposium on Autonomous Inland Shipping, Antwerp. 2019. URL: https://lirias.kuleuven.be/retrieve/592543.

[241] P. Slaets and G. Peeters. *Intelligent autonomous shipping: a look at the future*. online. Presented at the International Symposium on Autonomous Inland Shipping, Leuven. 2017. URL: https://lirias.kuleuven.be/retrieve/592549.

[242] P. Slaets and G. Peeters. *Intelligent autonomous shipping: from concept to demonstration*. Online. Presented at the International Symposium on Autonomous Inland Shipping, Antwerp. 2018. URL: https://lirias.kuleuven.be/retrieve/592551.

[243] P. Slaets, G. Peeters and S. Van Baelen. *MOOS-IvP for Autonomous Inland Shipping: Challenges and Opportunities*. Presented at the MOOS-DAWG'19, Cambridge MA. Aug. 2019. URL: https://oceanai.mit.edu/moos-dawg/pmwiki/pmwiki.php?n=Talk.05-Slaets.

[244] A. I. Solzhenitsyn. *The Gulag Archipelago, 1918-1956: An Experiment in Literary Investigation*. Harper & Row, 1974. URL: https://books.google.be/books?id=3SXLvQEACAAJ.

[245] C. R. Sonnenburg. "Modeling, Identification, and Control of an Unmanned Surface Vehicle". PhD thesis. Virginia Polytechnic Institute and State University, 2012. URL: http://hdl.handle.net/10919/19240.

[246] C. R. Sonnenburg and C. A. Woolsey. "Modeling, Identification, and Control of an Unmanned Surface Vehicle". In: *Journal of Field Robotics* 30.3 (2013), pp. 371–398. ISSN: 1556-4959. DOI: 10.1002/rob.21452.

[247] O. J. Sørdalen. "Optimal thrust allocation for marine vessels". In: *Control Eng. Pract.* 5.9 (1997), pp. 1223–1231. ISSN: 09670661. DOI: 10.1016/S0967-0661(97)84361-4.

[248] SSAVE. *IMEC-SSAVE project*. online. Financing from IWT / VLAIO - iMinds / IMEC - ICON (main financing). Agentschap Innoveren &Ondernemen, Flemish level. 2019. URL: https://www.researchportal.be/nl/project/imec-ssave.

[249] N. A. Stanton, P. M. Salmon and G. H. Walker. "Let the Reader Decide: A Paradigm Shift for Situation Awareness in Sociotechnical Systems". eng. In: *Journal of Cognitive Engineering and Decision Making* 9.1 (2015), pp. 44–50. DOI: 10.1177/1555343414552297.

[250] C. Sys and T. Vanelslander. *Future Challenges for Inland Navigation : A Scientific Appraisal of the Consequences of Possible Strategic and Economic Developments up to 2030*. VUB University Press, 2011. ISBN: 978-9054878544.

[251] J. Tainmont. "Following in the footsteps of Vesalius around Brussels". In: *B-ENT* 5 (2009), pp. 283–291.

[252] N. N. Taleb. *Statistical Consequences of Fat Tails (Technical Incerto Collection) Real World Preasymptotics, Epistemology, and Applications*. STEM Academic Press, 2020. ISBN: 978-1544508054.

[253] T. Tango. *Repeated Measures Design with Generalized Linear Mixed Models for Randomized Controlled Trials*. Chapman and Hall/CRC, 2017. ISBN: 978-1498747899.

[254] E. Taniguchi, S. Kawakatsu and H. Tsuji. "New co-operative system using electric vans for urban freight transport". In: *Urban Transport and the Environment for the 21st Century* (2010), pp. 201–210. ISSN: 1-85312-823-6.

[255] R. Taylor. "Situational Awareness Rating Technique (SART): The Development of a Tool for Aircrew Systems Design". In: *Situational Awareness*. Ed. by E. Salas. First publised in 2011. Routledge: University ofCentral Florida, USA, 2017, pp. 111–128. DOI: 10.4324/9781315087924.

[256] TENtec. *Adapted from TEN-T Core Network Corridors (Freight and Passenger)*. Online. European Commission Mobility and Transport. 2020. URL: https://ec.europa.eu/transport/infrastructure/tentec/tentec-portal/site/en/maps.html.

[257] T. Tezdogan, A. Incecik and O. Turan. "Full-scale unsteady RANS simulations of vertical ship motions in shallow water". In: *Ocean Eng.* 123 (2016), pp. 131–145. DOI: 10.1016/j.oceaneng.2016.06.047.

[258] The Flemish government. *The ports of Flanders: key facts and figures*. Online. Department Mobility and Public Works. 2018. URL: https://www.vlaanderen.be/publicaties/the-ports-of-flanders-key-facts-figures.

[259] The Flemish Waterway provider (De Vlaamse Waterweg). *De Vlaamse Waterweg Corporate Brochure*. Brochure. 2020. URL: https://www.vlaamsewaterweg.be/publicaties/brochures.

[260] The pandas development team. *pandas-dev/pandas: Pandas*. Software, Zenodo. Version 1.0.3. Feb. 2020. DOI: 10.5281/zenodo.3509134. URL: https://doi.org/10.5281/zenodo.3509134.

[261] C. A. Thieme, I. B. Utne and S. Haugen. "Assessing ship risk model applicability to Marine Autonomous Surface Ships". In: *Ocean Engineering* 165 (2018), pp. 140–154. ISSN: 0029-8018. DOI: 10.1016/j.oceaneng.2018.07.040.

[262] S. Toxopeus. "Viscous-Flow Calculations for KVLCC2 in Deep and Shallow Water". eng. In: *MARINE 2011, IV International Conference on Computational Methods in Marine Engineering : Selected Papers*. Vol. 29. Computational Methods in Applied Sciences. Dordrecht: Springer Netherlands, 2013, pp. 151–169. ISBN: 9789400761421.

[263] N.-h. Tran, H.-s. Choi, S.-h. Baek and H.-y. Shin. "Tracking Control of an Unmanned Surface Vehicle". In: *AETA 2013: Recent Advances in Electrical Engineering and Related Sciences*. Vol. 282. 2014, pp. 575–584. ISBN: 978-3-642-41968-3. DOI: 10.1007/978-3-642-41968-3.

[264] M. S. Triantafyllou. "Steady and Unsteady Dynamics of an Azimuthing Podded Propulsor Related to Vehicle Maneuvering". PhD Dissertation. Department of Ocean Engineering, MIT: MIT, May 2004. URL: http://hdl.handle.net/1721.1/33164.

[265] J. Vallant and B. Hofmann-Wellenhof. "River Information Services". In: *Elektrotechnik und Informationstechnik* 125.6 (2008), pp. 238–243. ISSN: 0932383X. DOI: 10.1007/s00502-008-0539-7.

[266] J. Van Amerongen. "Adaptive steering of ships - A model reference approach". In: *Automatica* 20.1 (1984), pp. 3–14. ISSN: 0005-1098. DOI: 10.1016/0005-1098(84)90060-8.

[267] J. Van Amerongen. "Adaptive Steering of Ships". PhD thesis. Delft University of Technology, 1982, p. 156. URL: http://resolver.tudelft.nl/uuid:2edf96d7-ed7f-40a5-a927-72ff62dea72e.

[268] S. Van Baelen. "Modular Smart Terminal: Suggestions for Innovative Handling and Transshipment of Goods for Inland Navigation". MA thesis. KU Leuven, 2018.

[269] S. Van Baelen, H. Shin, G. Peeters, M. R. Afzal, G. Yayla and P. Slaets. "Preliminary results on increased situational awareness for inland vessels using onboard lidar." In: *Proc. of Oceans 2020*. In press, ISBN: 978-1-7281-5446-6. Singapore, 2020.

[270] G. Van Rossum and F. L. Drake. *Python 3 Reference Manual*. Scotts Valley, CA: CreateSpace, Oct. 2009. ISBN: 1441412697. URL: https://docs.python.org/3.6/reference/index.html.

[271] E. Verberght. *INN-IN: Innovative Inland Navigation*. Tech. rep. University of Antwerp, Department of Transport and Regional Economics, 2019. URL: https://hdl.handle.net/10067/1571790151162165141.

[272] E. Verberght. "Innovation in Inland Navigation: Failure and Success". PhD thesis. University of Antwerp, 2020. URL: https://hdl.handle.net/10067/1659200151162165141.

[273] E. Verberght and E. van Hassel. "The automated and unmanned inland vessel". In: *Journal of Physics: Conference Series*. IOP Publishing, 2019. DOI: 10.1088/1742-6596/1357/1/012008.

[274] K. Vicente and J. Rasmussen. "Ecological interface design: theoretical foundations". In: *IEEE transactions on systems, man, and cybernetics* 22.4 (1992), pp. 589–606. ISSN: 0018-9472. DOI: 10.1109/21.156574.

[275] L. da Vinci. *Vitruvian Man*. Circa 1492. Photo from www.lucnix.be. 2007-09-08 (photograph). Photograpy: Luc Viatour. URL: https://commons.wikimedia.org/wiki/File:Da_Vinci_Vitruve_Luc_Viatour.jpg.

[276] P. Virtanen, R. Gommers, T. E. Oliphant, M. Haberland, T. Reddy, D. Cournapeau, E. Burovski, P. Peterson, W. Weckesser, J. Bright, S. J. van der Walt, M. Brett, J. Wilson, K. J. Millman, N. Mayorov, A. R. J. Nelson, E. Jones, R. Kern, E. Larson, C. J. Carey, İ. Polat, Y. Feng, E. W. Moore, J. VanderPlas, D. Laxalde, J. Perktold, R. Cimrman, I. Henriksen, E. A. Quintero, C. R. Harris, A. M. Archibald, A. H. Ribeiro, F. Pedregosa, P. van Mulbregt and SciPy 1.0 Contributors. "SciPy 1.0: Fundamental Algorithms for Scientific Computing in Python". In: *Nature Methods* 17 (Mar. 2020), pp. 261–272. DOI: 10.1038/s41592-019-0686-2.

[277] Vision++. *Vision++, Computer Vision Experts*. Online. 2019. URL: http://visionplusplus.com/.

[278] M. Wahlström, J. Hakulinen, H. Karvonen and I. Lindborg. "Human Factors Challenges in Unmanned Ship Operations – Insights from Other Domains". In: *Procedia Manufacturing* 3 (2015). 6th International Conference on Applied Human Factors and Ergonomics (AHFE 2015) and the Affiliated Conferences, AHFE 2015, pp. 1038–1045. ISSN: 2351-9789. DOI: 10.1016/j.promfg.2015.07.167.

[279] WAMIT. *The state of the art in wave interaction analysis*. Software. Accessed October 19. Oct. 2020. URL: https://wamit.com/index.htm.

[280] L. Wang, P. D. Groves and M. K. Ziebart. "Multi-Constellation GNSS Performance Evaluation for Urban Canyons Using Large Virtual Reality City Models". In: *The Journal of Navigation* 65.3 (2012), pp. 459–476. ISSN: 0373-4633. DOI: 10.1017/s0373463312000082.

[281] Watertruck+. *Watertruck+: the future of inland navigation*. 2020. URL: http://www.watertruckplus.eu/.

[282] Y. Wei, M. Fu, J. Ning and X. Sun. "Quadratic Programming Thrust Allocation and Management for Dynamic Positioning Ships". In: *TELKOMNIKA Indones. J. Electr. Eng.* 11.3 (2013), pp. 1632–1638. ISSN: 2302-4046. DOI: 10.11591/telkomnika.v11i3.2318.

[283] K. E. Weick. *Sensemaking in Organizations*. SAGE Publications, 1995. ISBN: 9780803971776.

[284] F. H. Weißbach. *The Statue of Marduk depicted on a cylinder seal of the 9th century BC Babylonian king Marduk-zakir-shumi I*. Online. 1903. URL: https://commons.wikimedia.org/wiki/File:Marduk_and_pet.jpg.

[285] H. G. Weller and G. Tabor. "A tensorial approach to computational continuum mechanics using object-oriented techniques". In: *Comput. Phys.* 12.6 (July 1998), pp. 620–631. DOI: 10.1063/1.168744.

[286] B. Weyts. *Beleidsnota 2014-2019: Mobilieit en Openbare Werken (in Dutch)*. Tech. rep. Flemish Government, 2014. URL: https://www.vlaanderen.be/publicaties/beleidsnota-2014-2019-mobiliteit-en-openbare-werken.

[287] B. Wiegmans and R. Konings. "Inland waterway transport : challenges and prospects". In: London: Taylor & Francis Group, Routledge, 2017. Chap. Managing capacity in the inland waterway sector : to intervene or not to intervene?, pp. 71–98. ISBN: 9781315739083. DOI: 10.4324/9781315739083.

[288] Wikipedia. *Brussels–Scheldt Maritime Canal*. Online. Accessed on 09/12/2020. 2020. URL: https://en.wikipedia.org/wiki/Brussels%E2%80%93Scheldt_Maritime_Canal.

[289] Wikipedia. *Pallet Shuttel Barge*. Online. Dec. 2019. URL: https://en.wikipedia.org/wiki/Pallet_Shuttle_Barge.

[290] Wikipedia. *PID controller, History: Origins*. Online. Accessed on 09/12/2020. 2020. URL: https://en.wikipedia.org/wiki/PID_controller#Origins.

[291] World Maritime University. *Transport 2040: Autonomous ships: A new paradigm for Norwegian shipping - Technology and transformation.* Tech. rep. Malmö: World Maritime University, 2019. DOI: 10.21677/itf.20190715.

[292] K. Wróbel, J. Montewka and P. Kujala. "Towards the development of a system-theoretic model for safety assessment of autonomous merchant vessels". In: *Reliability Engineering and System Safety* (2018). DOI: 10.1016/j.ress.2018.05.019.

[293] Z. Xu, M. Haroutunian, A. J. Murphy, J. Neasham and R. Norman. "A comparison of functional control strategies for underwater vehicles: Theories, simulations and experiments". eng. In: *Ocean engineering* 215.107822 (2020). ISSN: 0029-8018. DOI: 10.1016/j.oceaneng.2020.107822.

[294] Y. Yao, L. Rosasco and A. Caponnetto. "On Early Stopping in Gradient Descent Learning". In: *Constr. Approx.* 26.2 (2007), pp. 289–315. ISSN: 1432-0940. DOI: 10.1007/s00365-006-0663-2.

[295] G. Yayla, C. Christofakis, T. Catoor, G. Peeters, S. Storms, M. R. Afzal, P. Pilozzi, Y. Singh, S. Van Baelen and P. Slaets. "A field study for accuracy and safety evaluation in unmanned ship handling using sensory information through a shore control center". In: *Proc. of the 12th AHFE Conference series.* Accepted. New York, 2020.

[296] G. Yayla, G. Peeters, M. R. Afzal, S. Van Baelen, T. Catoor, S. Storms and P. Slaets. "Impact of a navigation aid on unmanned sailing in inland waterways: Design and evaluation challenges". In: *Proc. of Oceans 2020.* In press, ISBN: 978-1-7281-5446-6. Singapore, 2020.

[297] G. Yayla, S. Van Baelen, G. Peeters, M. R. Afzal, T. Catoor, Y. Singh and P. Slaets. "Accuracy Benchmark of Galileo and EGNOS for Inland Waterways". In: *Proceedings of the International Ship Control Systems Symposium (iSCSS).* In press. Virtual online conference, 2020.

[298] D. R. Yoerger, J. G. Cooke and J.-J. Slotine. "The influence of thruster dynamics on underwater vehicle behavior and their incorporation into control system design". In: *IEEE J. Ocean. Eng.* 15.3 (1990), pp. 167–178. ISSN: 0364-9059. DOI: 10.1109/48.107145.

[299] M. S. Young, K. A. Brookhuis, C. D. Wickens and P. A. Hancock. "State of science: mental workload in ergonomics". eng. In: *Ergonomics* 58.1 (2015), pp. 1–17. ISSN: 0014-0139. DOI: 10.1080/00140139.2014.956151.

[300] E. Zereik, M. Bibuli, N. Mišković, P. Ridao and A. Pascoal. "Challenges and future trends in marine robotics". eng. In: *Annual reviews in control* 46 (2018), pp. 350–368. ISSN: 1367-5788. DOI: 10.1016/j.arcontrol.2018.10.002.

[301] J. Zhang and S. Singh. "Low-drift and real-time lidar odometry and mapping". In: *Auton. Robots* 41.2 (2017), pp. 401–416. ISSN: 15737527. DOI: 10.1007/s10514-016-9548-2.

[302] W. L. Z. Zhang. "Modeling of Ship Maneuvering Motion Using Neural Networks". eng. In: *Journal of marine science and application* 15.4 (Aug. 2016), pp. 426–432. ISSN: 1671-9433. DOI: 10.1007/s11804-016-1380-8.

[303] H. Zheng, R. R. Negenborn and G. Lodewijks. "Trajectory tracking of autonomous vessels using model predictive control". eng. In: *Proceedings of the 19th World Congress. The International Federation of Automatic Control*. Cape Town, South Africa., Aug. 2014, pp. 8812–8818. DOI: 10.3182/20140824-6-ZA-1003.00767.

[304] Z. Zhou, S. Yan and W. Feng. "Manoeuvring prediction of multiple-purpose cargo ships (in Chinese)". In: *Ship Eng.* 6 (1983), pp. 21–36.

Publications

Journal articles

G. Peeters, S. Van Baelen, G. Yayla, T. Catoor, M. R. Afzal, C. Christofakis, R. Louw, Y. Singh, M. Vanierschot, R. Boonen and P. Slaets. "Decoupled Hydrodynamic Models and Their Outdoor Identification for an Unmanned Inland Cargo Vessel with Embedded Fully Rotatable Thrusters". In: *Journal of Marine Science and Engineering* 8.889 (2020). DOI: 10.3390/jmse8110889

G. Peeters, G. Yayla, T. Catoor, S. Van Baelen, M. R. Afzal, C. Christofakis, S. Storms, R. Boonen and P. Slaets. "An Inland Shore Control Centre for Monitoring or Controlling Unmanned Inland Cargo Vessels". In: *Journal of Marine Science and Engineering* 8.758 (2020). With joined first authors G. Peeters and G. Yayla. DOI: 10.3390/jmse8100758

G. Peeters, M. R. Afzal, M. Vanierschot, R. Boonen and P. Slaets. "Model Structures and Identification for Fully Embedded Thrusters: 360-Degrees-Steerable Steering-Grid and Four-Channel Thrusters". In: *Journal of Marine Science and Engineering* 8.220 (2020). DOI: 10.3390/jmse8030220

G. Peeters, M. Kotzé, M. R. Afzal, T. Catoor, S. Van Baelen, P. Geenen, M. Vanierschot, R. Boonen and P. Slaets. "An unmanned inland cargo vessel: Design, build, and experiments". In: *Ocean Eng.* 201.107056 (2020), p. 17. DOI: 10.1016/j.oceaneng.2020.107056

Conference proceedings

G. Yayla, C. Christofakis, T. Catoor, G. Peeters, S. Storms, M. R. Afzal, P. Pilozzi, Y. Singh, S. Van Baelen and P. Slaets. "A field study for accuracy and safety evaluation in unmanned ship handling using sensory information through a shore control center". In: *Proc. of the 12th AHFE Conference series*. Accepted. New York, 2020

G. Peeters, G. Yayla, M. R. Afzal, S. Van Baelen, T. Catoor, M. Vanierschot, R. Boonen and P. Slaets. "Additional Test Manoeuvres for Autonomous Inland Vessels". In: *Proc. of ICMASS 2020*. 2020. DOI: 10.1088/1757-899X/929/1/012024

S. Van Baelen, H. Shin, G. Peeters, M. R. Afzal, G. Yayla and P. Slaets. "Preliminary results on increased situational awareness for inland vessels using onboard lidar." In: *Proc. of Oceans 2020*. In press, ISBN: 978-1-7281-5446-6. Singapore, 2020

G. Yayla, G. Peeters, M. R. Afzal, S. Van Baelen, T. Catoor, S. Storms and P. Slaets. "Impact of a navigation aid on unmanned sailing in inland waterways: Design and evaluation challenges". In: *Proc. of Oceans 2020*. In press, ISBN: 978-1-7281-5446-6. Singapore, 2020

G. Yayla, S. Van Baelen, G. Peeters, M. R. Afzal, T. Catoor, Y. Singh and P. Slaets. "Accuracy Benchmark of Galileo and EGNOS for Inland Waterways". In: *Proceedings of the International Ship Control Systems Symposium (iSCSS)*. In press. Virtual online conference, 2020

G. Peeters, T. Catoor, M. R. Afzal, M. Kotzé, P. Geenen, S. Van Baelen, M. Vanierschot, R. Boonen and P. Slaets. "Design and build of a scale model unmanned inland cargo vessel: Actuation and control architecture". English. In: *MTEC/ICMASS 2019*. Vol. 1357. 1. Institute of Physics Publishing, 2019. DOI: 10.1088/1742-6596/1357/1/012016

M. Kotzé, A. Bin Junaid, M. R. Afzal, G. Peeters and P. Slaets. "Use of Uncertainty and Zones for Vessel and Operation in Inland and Waterways". In: *Journal of Physics: Conference Series*. 2019. DOI: 10.1088/1742-6596/1357/1/012031

A. Eggers, G. Peeters, P. Slaets and M. Vanierschot. "Shallow water surge resistance identification for inland vessels". In: *5th MASHCON Proceedings*. 2019. URL: http://hdl.handle.net/1854/LU-8624686

G. Peeters, R. Boonen, M. Vanierschot, M. DeFilippo, P. Robinette and P. Slaets. "Asymmetric Steering Hydrodynamics Identification of a Differential Drive Unmanned Surface Vessel." In: *IFAC*. vol. 51. 29. Elsevier, 2018, pp. 207–212. DOI: 10.1016/j.ifacol.2018.09.494

G. Peeters, A. Eggers, R. Boonen, P. Slaets and M. Vanierschot. "Surge Resistance Identification of Inland Vessels by CFD". in: *OCEANS 2018*. Kobe: IEEE, 2018. DOI: 10.1109/OCEANSKOBE.2018.8559048

Abstracts/Presentations/Posters

P. Slaets and G. Peeters. *Demonstration of the first Autonomous Barge in Flanders.* Online. Presented at the International Symposium on Autonomous Inland Shipping, Antwerp. 2019. URL: https://lirias.kuleuven.be/retrieve/592543

P. Slaets, G. Peeters and S. Van Baelen. *MOOS-IvP for Autonomous Inland Shipping: Challenges and Opportunities.* Presented at the MOOS-DAWG'19, Cambridge MA. Aug. 2019. URL: https://oceanai.mit.edu/moos-dawg/pmwiki/pmwiki.php?n=Talk.05-Slaets

P. Slaets and G. Peeters. *Intelligent autonomous shipping: from concept to demonstration.* Online. Presented at the International Symposium on Autonomous Inland Shipping, Antwerp. 2018. URL: https://lirias.kuleuven.be/retrieve/592551

G. Peeters, A. Eggers, R. Boonen, P. Slaets and M. Vanierschot. *Surge Resistance Identification of Inland Vessels by Computational Fluid Dynamics.* Presented at the VSC User Group Meeting, Brussels. May 2018

G. Peeters and P. Slaets. *Automated Inland Shipping: The Challenges on the Inland Waterways.* Presented at the Ocean Week, Trondheim, Norway. 2018

G. Peeters and P. Slaets. *Towards Autonomous Inland Shipping in Flanders.* Presented at the MOOS Development and Applications Working Group, Cambridge MA. Aug. 2017. URL: https://oceanai.mit.edu/moos-dawg17/pmwiki/pmwiki.php?n=Talk.07-Peeters

G. Peeters and P. Slaets. *Intelligent Autonomous Shipping.* Presented at the Unmanned Cargo Ship Conference, Venlo, Netherlands. June 2017

P. Slaets and G. Peeters. *Intelligent autonomous shipping: a look at the future.* online. Presented at the International Symposium on Autonomous Inland Shipping, Leuven. 2017. URL: https://lirias.kuleuven.be/retrieve/592549

G. Peeters, G. Waeyenbergh and P. Slaets. *Stimulating Innovation Through Projects in Engineering Education: The Growth and Success of the Ecorace-Challenge Project.* Presented at the European Battery, Hybrid & Fuel Cell Electric Vehicle Congress, Geneva, Switzerland. 2017

P. Slaets and G. Peeters. *A practical case study, automating the Scheldt - Rupel trajectory.* Online. Presented at the International Symposium on Autonomous Inland Shipping, Leuven. 2016. URL: https://lirias.kuleuven.be/retrieve/592545

FACULTY OF ENGINEERING TECHNOLOGY
DEPARTMENT OF MECHANICAL ENGINEERING
INTELLIGENT MOBILE PLATFORMS
Willem de Croylaan 56
B-3001 Leuven
gerben.peeters@kuleuven.be
https://www.mech.kuleuven.be/imp/